NUMERICAL MODELING OF DIELECTROPHORETIC EFFECT FOR MANIPULATION OF BIO-PARTICLES

A thesis submitted for the degree of Doctor of Philosophy

By

Branimir Malnar

School of Engineering

Brunel University

August 2009

To my wife, mother and brother, for their immense support throughout this journey, and

To my father, for whom I wish would still be with us to see where I've come.

Acknowledgements

I am very grateful to my mentor Prof Wamadeva Balachandran for his extraordinary mentorship throughout the years of this research, and for all of the valuable advices he shared with me and the guidance he provided, both in research and writing up this thesis. I am thankful to CVCP for awarding me with ORS, thus making my studies in the UK possible. I also wish to thank Mr Beresford Malyan for all of the fruitful discussions we had on dielectrophoresis, and the experimental work that is a significant part of this thesis. Last but not least, I cannot find words to express my gratitude to my family, for all of their care and support that is with me every day of my life, in anything I do.

Table of contents

Abstract

This text describes different aspects of the design of a Doctor-on-a-Chip device. Doctor-on-a-Chip is a DNA analysis system integrated on a single chip, which should provide all of the advantages that stem from the system integration, such as small sample volume, fast and accurate analysis, and low cost. The text describes all of the steps of the on-chip sample analysis, including DNA extraction from the sample, purification, PCR amplification, novel dielectrophoretic sorting of the DNA molecules, and finally detection.

The overview is given of the technologies which are available to make the integration on a single chip possible. The microfluidic technologies that are used to manipulate the sample and other chemical reagents are already known and in this text they are analyzed in terms of their feasibility in the on-chip system integration. These microfluidic technologies include, but are not limited to, microvalves, micromixers, micropumps, and chambers for PCR amplification.

The novelty in the DNA analysis brought by Doctor-on-a-Chip is the way in which the different DNA molecules in the sample (for example, human and virus DNA) are sorted into different populations. This is done by means of dielectrophoresis – the force experienced by dielectric particles (such as DNA molecules) when subject to a non-uniform electric field. Different DNA molecules within a sample experience different dielectrophoretic forces within the same electric field, which makes their separation, and therefore detection, possible.

In this text, the emphasis is put on numerical modelling of the dielectrophoretic effect on biological particles. The importance of numerical modelling lies in the fact that with the accurate model it is easier to design systems of microelectrodes for dielectrophoretic separation, and tune their sub-micrometre features to achieve the maximum separation efficacy. The numerical model described in this text is also experimentally verified with the novel microelectrodes design for dielectrophoretic separation, which is successfully used to separate the mixture of different particles in the micron and sub-micron range.

Nomenclature

t_d	diffusion time
x_d	diffusion length
D	diffusion coefficient
Δp	pressure drop across the pumping chamber
ξ	pressure loss coefficient
ρ, ρ_m	mass density of the fluid
$\hat{u}$	mean fluid velocity
η	diffuser efficiency ratio
q	electric charge
E	electric field strength
P	polarization factor
F	force (dielectrophoretic force on a particle)
p	dipole moment of a polarized particle
v	volume of a particle
T	dielectrophoretic torque on a particle
Z	impedance
ω	angular frequency
C	capacitance of a capacitor
A	surface area of a parallel plate capacitor
ε	permittivity
$\tilde{\varepsilon}$	complex permittivity
ε_0	permittivity of vacuum
ε_r	relative permittivity of material
σ	conductance of material
$\tilde{\alpha}$	effective polarisability
f_{CM}	Clausius-Mossotti factor
τ_{MW}	Maxwell-Wagner relaxation frequency
γ_{12}	ratio between the outer and the inner shell radius for homogenous sphere
Re	real part of a complex value
Re	imaginary part of a complex value
Φ	electric potential
$\tilde{\phi}$	complex value of electric potential
Φ_R	real part of electric potential
Φ_I	imaginary part of electric potential
$\tilde{E}$	complex value of electric field
E_{RMS}	root mean square value of electric field
$\langle F_{DEP} \rangle$	time averaged value of DEP force

k	Boltzmann constant
T	temperature in the system of microelectrodes
g	acceleration under gravity
v	velocity of a particle
u	velocity of the fluid in the channel
Q	total volume flow rate
p_0	pressure drop across the flow through separation system
l, w, h	length, width and height of the flow through separation system
f	body force on the fluid in Navier-Stokes equation
Re	Reynolds number
η	fluid viscosity
ρ_c	charge density
c_p	specific heat of fluid at constant pressure
F_η	viscous drag force on particle suspended in fluid
f	friction factor
m	particle mass
v_{DEP}	velocity of particle in suspending medium under influence of DEP force

Chapter 1. Introduction

Over the past decade, the research and development in the area of microfluidics opened a new era in molecular biology, chemistry and medicine [e.g. 1-34]. System integration, as the most important topic in microfluidics studies, brings many advantages over standard laboratory techniques in aforementioned scientific and commercial areas. The market value for MEMS devices for fluid regulation has reached 9 billion dollars in the year 2000, and this figure does not include many systems that were still in the prototype stage [7-9]. Clearly, the "lab on a chip" vision is the main driving force for the research in microfluidics, as the integration will inevitably lead to cheap, disposable and reliable mass-produced systems for chemical analysis, delivery of drugs, bioreactors, medical analysis, and so forth.

Another important scientific field that received a significant boost with the development of the microfabrication technology is particle handling utilizing electric fields [e.g. 35-60]. Particular to the effect of dielectrophoresis, it was thought that controllable manipulation of particles in the submicron range is impossible, because high electric fields required would generate liquid flow that would overcome the dielectrophoretic force [15]. However, the developments in the micro- and nano-fabrication technology have made it possible to generate electric fields in the order of MV/m utilizing microelectrodes with applied voltages as low as 1 V. Relatively low power dissipation in such systems of microelectrodes allows controllable manipulation of particles as small as spheres with 14 nm radius [e.g. 188].

Doctor-on-a-Chip is an integrated micro system that combines a microfluidic network and a system of microelectrodes to analyze DNA from a biological sample [202-203]. The microfluidic network is used to extract, purify and amplify DNA from the sample, and the microelectrodes sort different DNA fragments (if present in the sample) and transport them to the detection points utilizing dielectrophoresis. There, the DNA is analyzed to provide the answer about presence of a certain pathogen or virus within the sample. Virus detection methods based on detection of their DNA have many advantages compared to other methods of detecting viruses [279]. These other methods include:

- Multiplication of the virus in a suitable cell culture and detection of the virus based on the effects it caused,
- Serology, i.e. a method which detects the virus based on its interaction with the antibody directed specifically against it, and
- Direct method of detecting the virus by using electron microscopy (optical microscopes are unable to detect viruses due to their small size).

All of these methods have significant disadvantages compared to DNA detection based methods, in terms of scaling for commercial purposes, speed of the analysis, cost, and accuracy [279]. This makes the methods based on DNA detection more suitable for commercial applications, both in standalone hand-held devices and standard laboratory tests and equipment.

Compared to standard analysis performed in a laboratory on a larger scale, integration of DNA analysis onto a single chip has many advantages [6]:

- Capability of microfluidic devices to reliably manipulate even picolitre volumes significantly reduces sample and reagents volumes and therefore costs of the analysis. Additionally, if only a small quantity of a sample is available, a network of microfluidic devices combined with the integrated PCR process can analyze the sample in a reliable manner,
- Small volumes usually decrease the time needed for DNA analysis. For example, integration of PCR reduces the volume and the thermal mass of a PCR mixture and therefore enables effective rapid thermal cycling,
- Integration and automation of DNA analysis decrease the possibility of contamination and potential human error, making the analysis more reliable, and
- Standard microfabrication technology allows mass production of inexpensive and disposable devices for DNA analysis.

1.1 Aims and objectives

Doctor-on-a-Chip can be functionally divided in three main parts based on the function they perform ([203], more details will be given later in chapter 4):

- A microfluidic network extracts DNA from a sample of blood or other body fluid introduced onto a chip, purifies the DNA and amplifies the target DNA to facilitate the detection.

- Microelectrodes of a suitable layout are used to sort the DNA into sub-populations utilizing dielectrophoresis.
- Following the dielectrophoretic sorting, the points of detection are investigated for the presence of pathogen DNA.

The research can be conducted on all three functional parts separately, bearing in mind the problems related to their integration onto the same chip, which is by no means a straightforward task.

The network of microfluidic devices must supply the purified DNA in sufficient amount for the subsequent detection to be highly reliable. The objectives of this part of the research are as follows:

- A microbiological protocol suitable for on-chip implementation needs to be clearly defined. As envisaged, Doctor-on-a-Chip will process samples originating at various biological sources: human, animal, plant, etc. Ideally, the protocol must be equally efficient on all of them, or otherwise different platforms and different chips must be developed for different applications.
- After the protocol has been defined, the physical properties of the liquids involved need to be summarized. Based on this, the conclusion will be drawn on which method of pumping and mixing is the most efficient by means of reliability, simplicity (and therefore the cost of production), time of completion, size, and power consumption (the temperature is a sensitive parameter in most biological applications).
- Based on the quantities and the properties of the liquids, the microfluidic network (channels, pumps and mixers) can be physically designed and tested for feasibility.
- External electric circuitry needs to be specified to drive the active elements on the chip (PCR heaters, pump, active mixers, etc.).

As stated above, the second functional part of the chip comprises of the microelectrodes for sorting the DNA into sub-populations according to their physical and dielectric properties. For this, the following objectives must be addressed:

- The method has to be defined which enables the sorting of the DNA fragments and their physical separation. This includes the design of the microelectrodes layout and how they are connected to a power supply (a

multi-phase versus a single-phase voltage, etc.). The size of DNA also has to be addressed as an important parameter. This is implemented through size of the primers for PCR amplification.

- To facilitate the microelectrodes design, a CAD tool needs to be developed for dielectrophoretic force calculation.
- To support the calculation and generally the estimation of behaviour of DNA when subjected to dielectrophoresis, the dielectric properties of the DNA and the suspending medium need to be known in a desired range of frequencies. These parameters need to be measured for different DNA molecules and for different mediums, and based on their values reasonable decisions can be made on the microelectrodes dimensions, the medium conductivity, the frequency of the applied voltage and other important parameters.

Finally, the third functional part of the chip detects the pathogen DNA if present within the sample. The method of choice needs to be suitable for integration with the microelectrodes and highly reliable. Ideally, the method does not need to detect the DNA sequence, but just the presence of the DNA molecules at the point of detection. In other words, PCR and the microelectrodes must serve as the filters for different DNA fragments separation, so that only specific pathogen DNA can find its way to specific detection points. If there is DNA at a given point of detection (i.e. the DNA passed through the aforementioned PCR/dielectrophoretic filters), we know which pathogen is in question.

The focus of this thesis will be on the concept of Doctor-on-a-Chip and the CAD tool for the dielectrophoretic force calculation. For the latter, the main objectives are:

- A review of forces that are relevant for a suspension of DNA molecules or any other particles at the micrometre scale,
- Implementation of a numeric algorithm for mesh generation for a structure of interest and calculation of the forces on particles,
- Viewing the simulation results in Matlab,
- Experimental dielectrophoretic separation of particles by using the novel method described in chapter 4. The experiments were performed in collaboration with Mr Beresford Malyan, to whom I am thankful for his most valuable contribution.

- Investigation of correlation between the experimental results and the simulation.

To achieve these objectives, a thorough review of available literature needs to be performed to investigate the existing technologies available to date for on-chip DNA analysis. Due to complexity of the analysis, theoretical background in several different fields needs to be obtained, namely biological concepts associated with DNA analysis, electrical and mechanical properties of DNA molecules relevant for this purpose, dielectrophoretic effect on small particles (including DNA molecules) on a micro- and nanoscale, and microfluidic technologies available to date for manipulation of DNA sample on a chip, including extraction, purification and multiplication of DNA molecules. The literature review of these and other relevant facts resulted in a proposal of Doctor-on-a-Chip concept, as will be shown in chapter 4. After developing the concept of the chip, the emphasis will be set on numerical modelling of dielectrophoretic effect on biological molecules subjected to electric field in a system of microelectrodes. The model will be written in the C++ programming language, with a simple user interface to describe the system and enter its geometry into the model. The program needs to generate a suitable mesh of points at which the field and the force will be calculated. The values in these points are stored in ASCII files, which can serve as an input to Matlab for easy viewing of the electric field distribution, dielectrophoretic force magnitude and direction, and other relevant effects and properties. After the model has been developed, the numerical modelling of dielectrophoresis can be compared with the real experimental data, which were generated by using a novel layout of microelectrodes for separation of small particles and molecules. This layout is used in Doctor-on-a-Chip for separation of DNA molecules into subpopulations for easy detection of pathogens in the sample. The numerical model will also be used to analyze other experimental results published elsewhere in literature.

1.2 Content of the thesis

Chapter 2 gives a literature review of biological concepts and some of the important technologies for DNA analysis relevant to Doctor-on-a-Chip. It starts with the general overview of a biological cell structure, and continues with emphasizing the differences between structures of viruses and bacteria and the most relevant

mechanical and electrical properties of DNA. This is followed by the overview of surface based and microfluidic based systems for DNA analysis. More emphasis is given on the microfluidic based systems, since Doctor-on-a-Chip also falls into that category. Hence, detailed description is given of microfluidic technologies available for controlling, mixing and transporting liquids on microfluidic chips. This is followed by the description of polymerase chain reaction method (PCR) for multiplication of targeted DNA molecules in the sample, and the technologies for performing PCR on microchips. The chapter concludes with the overview of various on-chip DNA detection methods that could be utilized with Doctor-on-a-Chip.

In chapter 3 different aspects of the dielectrophoretic effect are described. The chapter starts with the theoretical description of dielectrophoresis, and gives an overview of main mathematical equations that are later used for developing the numerical model. The theoretical description is followed by practical examples of using dielectrophoresis for separation of particles, which includes dielectrophoretic traps, travelling wave dielectrophoresis, electrorotation, and other methods. The chapter ends with the description of main fluid dynamics effects in microsystems with fluids and their relevant mathematical equations.

Chapter 4 presents the concept of Doctor-on-a-Chip as a total analysis system that integrates extraction and purification of DNA with PCR and dielectrophoretic separation and detection on a single chip. The novel system of microelectrodes used for DNA separation is also described, together with the overview of main building blocks of the chip, the tasks they perform, and how they are integrated with one another.

Chapter 5 describes the mathematical model for simulation of dielectrophoresis. It gives an overview of the main equations used in the numerical analysis of the dielectrophoretic force and the temperature distribution within the microchannel. This is followed by a more detailed overview of the program building blocks, and some of the more important concepts in developing the numeric algorithms, such as mesh generation and finite difference method for electric potential and temperature distribution calculation.

Chapters 6 and 7 show experimental verification of the numerical model on several dielectrophoretic separation methods. In chapter 6, the simulation of the castellated system of microelectrodes and travelling wave dielectrophoretic array is given, followed by the investigation of the dependence of the temperature within the

microchannel on the conductivity of the suspending medium. Chapter 7 shows the numerical analysis of the separation of two populations of latex spheres by using dielectrophoresis and fluid flow. The numerical results are compared and analysed together with the practical experimental results.

Chapter 8 covers the main conclusions drawn from this thesis, and the proposal for future work.

1.3. Contribution to knowledge and publications

This thesis presents a new concept of a microchip for DNA analysis. The microchip is capable of detecting pathogens within a sample, by performing all of the steps in the process of DNA analysis. These steps include DNA extraction, purification and PCR multiplication, followed by dielectrophoretic separation of different DNA sub-populations, and detection of the target DNA (if present within a sample).

The microchip utilizes known methods of DNA sample preparation, which includes the protocol for DNA extraction and purification, and multiplication of target DNA with PCR. The protocol is implemented on the chip by using already known microfluidic methods of pumping and mixing of the sample and the reagents needed to perform the chemical reactions for DNA isolation. Once the sample is prepared, it is amplified in the PCR chamber, again using already available methods. The multiplication of target DNA is followed by the novel method of DNA separation into different sub-populations, which is based on dielectrophoresis. This is done by using a new proposed and tested layout of microelectrodes, as described in chapter 4. After the DNA is separated, the pathogen DNA can be detected if present within the sample, by using a known method of impedance measurement. This provides the final answer about the presence of the pathogen within the sample, and thus completes the analysis.

In summary, the microchip utilizes already known methods and some original ones to perform complete sample analysis on-chip. The originality of this approach lies in the fact that the new dielectrophoretic method is used to separate the DNA, and that this new method is integrated with some other already known methods (DNA preparation and detection) to build the entire analysis system.

The second part of the thesis covers the numerical model for dielectrophoretic force analysis. The model is written from scratch in the C++ programming language, and allows the user to specify different layouts of microelectrodes through a simple user interface. In this way, the user can simulate different scenarios on the computer and come closer to the final setup of the system without going through the expensive process of trial and error and converging to the optimal setup by making many different prototypes. The model, which presents a unique method of simulating dielectrophoresis in the custom configurable software, is tested with several different configurations of microelectrodes and the results of the simulations have shown good correlation with the published experimental results.

This research produced the following publications:

- *Numerical modelling of dielectrophoretic effect for submicron particles manipulation*
  B. Malnar, W. Balachandran, and F. Cecelja
  IOP Conference Series, No. 178, 2004, 215-220

- *Separation of latex spheres using dielectrophoresis and fluid flow*
  B. Malnar, B. Malyan, W. Balachandran, and F. Cecelja
  IEE Proceedings on Nanobiotechnology, Vol. 150, No. 2, 2003, 66-69

- *3D simulation of travelling wave dielectrophoretic force on particles*
  B. Malnar, W. Balachandran, and F. Cecelja
  Proceedings of the ESA-IEEE Conference on Electrostatics, Vol. 1, USA 2003

- *Doctor on a Chip*
  B. Malnar, B. Malyan, F. Cecelja, and W. Balachandran
  MIPRO Proceedings, 2005

Chapter 2. Miniature Systems for Microbiological Analysis

This chapter describes the miniature systems in the area of microbiological analysis that already exist and are being developed. The focus will be on DNA analysis systems, basic elements of microfluidic networks, and, what is also important in the case of Doctor-on-a-Chip, current state of the art PCR techniques on a micro scale. An overview of certain microbiological aspects (such as structures of biological cells and viruses, DNA molecules and their physical properties) is also given to better understand the idea behind Doctor-on-a-Chip.

2.1. Microbilological background of cells, viruses and DNA

This section gives a short overview of basic microbiological aspects of DNA technologies. The overview of cellular and viral structures is given, followed by the overview of the structure of a DNA molecule. Finally, some of the most important physical properties of DNA are also described, as they are important to better understand the techniques used in the DNA analysis methods described in chapter 2.

2.1.1. Cellular structure

A cell is the fundamental structural unit of all living organisms. A cell is a self contained unit separated from its surroundings by a cytoplasmic membrane that serves as a limiting boundary [35, 37]. The membrane regulates the passage of materials into and out of the cell. Such a regulation allows the cell to maintain a more organized internal state than the cell's external surroundings. Within the membrane, the cell contains a fluid called cytoplasm in which chemical reactions that transfer the energy and materials needed for the cell growth and reproduction take place. The cell's hereditary information is contained in molecules of DNA, which direct the activities of the cell and passes the hereditary information to succeeding generations.

Based on the two distinct organizational patterns within the cells, we can distinguish between the prokaryotic (eubacteria and archaebacteria) and eukaryotic cells (all the other living organisms). The difference between the two represents an important division of all living systems and their different forms of essentially the same physiological and reproductive functions [37].

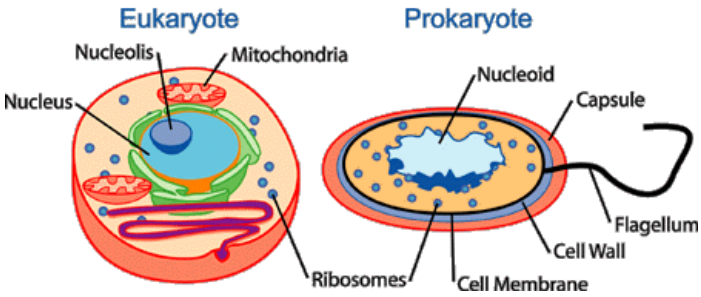

a)

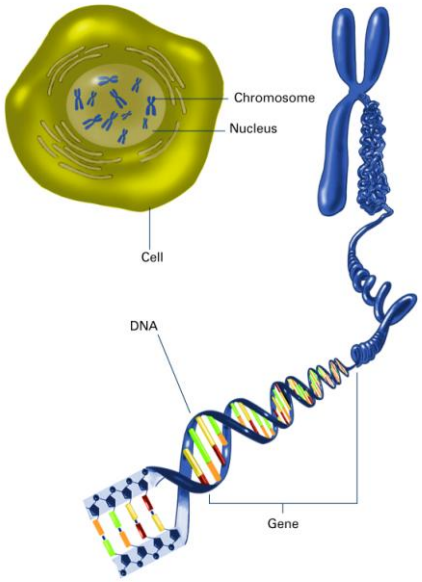

b)

Figure 2.1. a) Eukaryotic and prokaryotic cells structure, b) Cell structure with focus on chromosomes and DNA [37]

Structures of prokaryotic and eukaryotic cells are depicted in figure 2.1.a [37]. The prokaryotic cell is a simply organized cell and as such lacks specialized internal compartments known as organelles that characterize the more complex and large eukaryotic cell. One particular difference is of special importance: the DNA of a prokaryotic cell is not contained within the specialized organelle called the nucleus, which is a case for a eukaryotic cell. Figure 2.1.b shows another diagram of cell structure, but with focus on chromosomes and DNA. Inside the cell nucleus, DNA and proteins (which serve for packaging DNA and controlling its function) are packed into organized structures called chromosomes. The term chromosome is

loosely defined and can range from very long and complex structures that can be found in eukaryotic cells, to small and simple DNA structures containing no structural proteins that are typically found in viruses. Figure 2.1.b also shows a gene, which is the basic unit of heredity in a living organism. In general terms, a gene is a segment of nucleic acid that, taken as a whole, specifies a trait. All living things depend on genes, which hold the information to build and maintain their cells and pass genetic traits to offspring.

Protecting the cytoplasmic membrane against damage is essential for the survival of a living cell. The membrane is often surrounded by a protective layer, such as a cell wall. Different cells have walls with different structural and chemical compositions, based on the environment in which they usually exist. Some cells have walls that are protective against osmotic shock, some are typically protective against physical damage, and some cells do not have cell walls at all. The difference between the cell walls of different cells falls beyond the scope of this text and will not be discussed in more details.

2.1.2. Structure of viruses

Viruses do not have cells. Structurally, all viruses consist of a DNA or RNA genome surrounded by a protein coat capsid [37]. The capsid is composed of one or several different proteins and may be isometrically or helically symmetrical. A viral genome may consist of not only double helical DNA, but also of single-stranded DNA and double- and single-stranded RNA. A viral genome must be small and compact to fit within the viral capsid, which is 30-300 nm in diameter. Some viruses have a membrane layer called an envelope surrounding the outside of the capsid. The envelope of the virus can alter recognition by host defence mechanisms designed to destroy foreign substances, and may also have an important role in the initial attachment of a viral particle to the host cell in which it replicates.

Some of the virus structures are depicted in figures 2.2 and 2.3. Figure 2.2 shows a well studied Tobacco mosaic virus, with a helical capsid. Figure 2.3 shows a developed HIV virus, which falls under the category of enveloped viruses.

Viral replication begins with the attachment of a virus to the surface of a susceptible host cell, followed by the entry of the virus into the host cell. The entry may involve the transfer of only the viral genome across the cytoplasmic membrane,

or the transport of the entire virus (including an envelope and a capsid). The viral nucleic acid then codes the alternation of the normal cell metabolism and the production of viral proteins and nucleic acid. Thus the virus replicates, with many viruses being produced within a single host cell and released together [37, 39].

A virus can replicate only in certain cells, which are termed permissive or compatible. Some viruses replicate only in bacterial cells and are called bacteriophage. Other viruses replicate only within animal cells (so called animal viruses), or within plant cells (plant viruses).

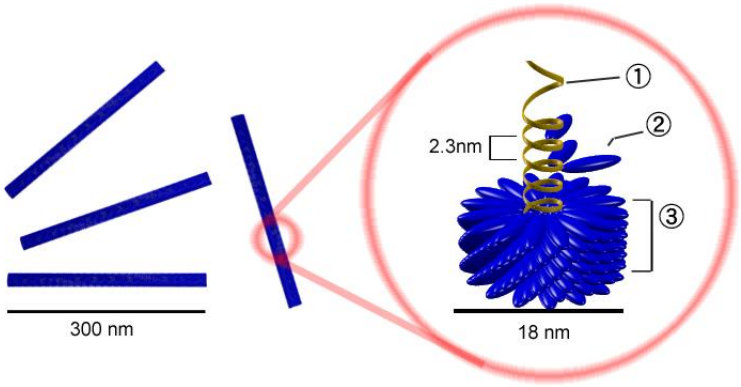

Figure 2.2. Tobacco mosaic virus with helical capsid [37]

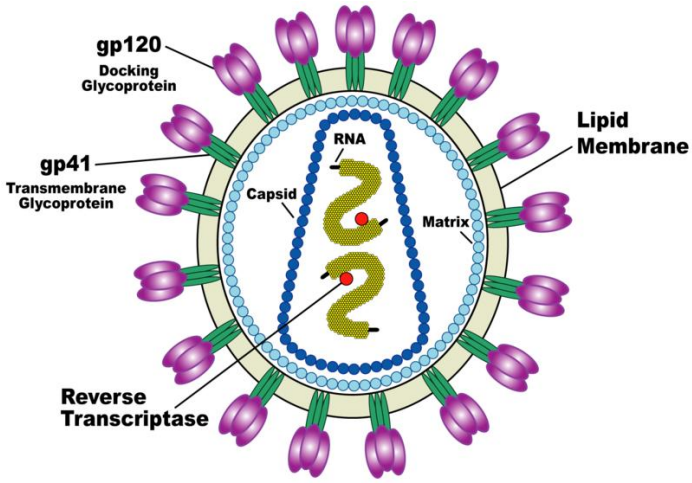

Figure 2.3. HIV virus [37]

2.1.3. Structure of nucleic acids

The chemical components of nucleic acid had been determined by Phoebus A. T. Levene in the 1920s [38]. He discovered two types of nucleic acids: ribonucleic acid (RNA) and deoxyribonucleic acid (DNA). Levene's analysis

revealed that both nucleic acids contain three basic components illustrated in figure 2.4: (i) a five carbon sugar, which could be ribose (in RNA) or deoxyribose (in DNA); (ii) a series of phosphate groups (i.e. chemical groups derived from phosphoric acid molecules); and (iii) four different compounds containing nitrogen and having the chemical properties of bases.

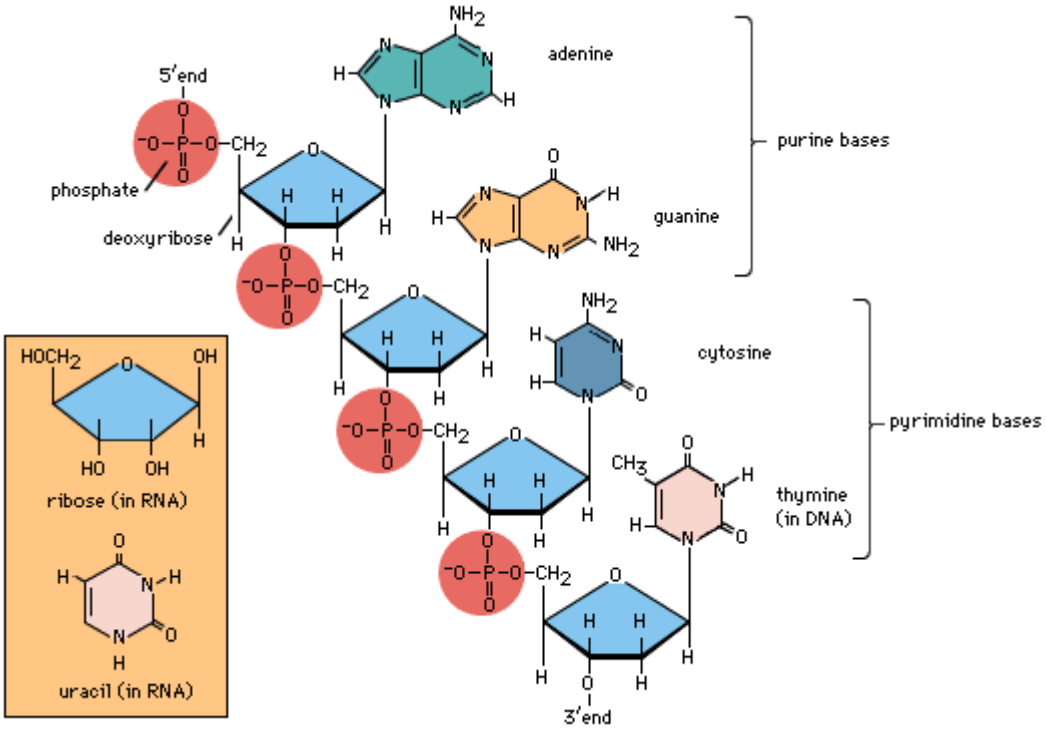

Figure 2.4. DNA polynucleotide chain [37]

In DNA the four bases are adenine (A), thymine (T), cytosine (C) and guanine (G), while in RNA uracil (U) replaces thymine (i.e. the four bases in RNA are A, U, C and G). A and G are double-ring molecules known as purines, while C, T and U are single-ring molecules called pyrimidines. They are also depicted in figure 2.4 above.

Figure 2.5 shows the structure of DNA molecule, which was discovered in the early 1950s by James Watson, Francis Crick, Rosalind Franklin and Maurice Wilkins [37]. A DNA molecule exists as a double helix, and is comprised of two strands running anti-parallel to each other and held together by non-covalent hydrogen bonds. One unit of DNA comprises a phosphate group, a sugar and a base and is known as nucleotide. Bases are attached to a sugar molecule (deoxyribose) and each sugar molecule is joined with adjacent sugar molecules through a

phosphate group. Thus one strand (or a polynucleotide chain) is formed. Non-covalent hydrogen bonds, that hold two strands together in a double helix, are formed between bases (A, T, G and C), where adenine bonds with thymine and guanine bonds with cytosine. One segment of a double stranded DNA is shown in figure 2.5.

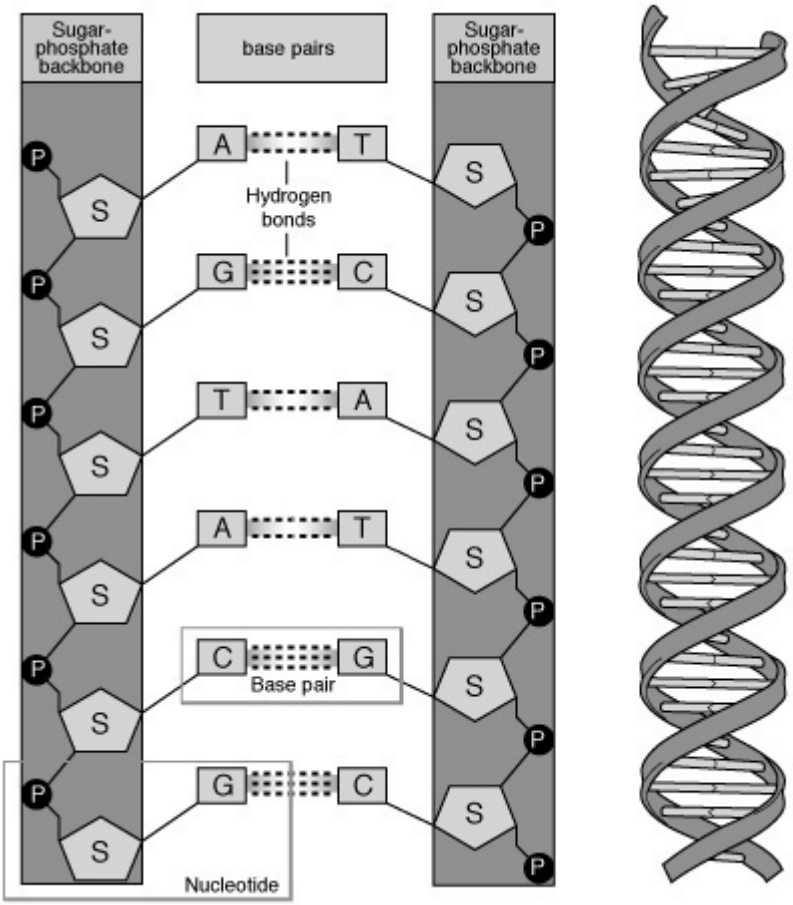

Figure 2.5. DNA double helix

Since in a double stranded DNA molecule A always bonds with T and G always bonds with C, the two strands are complimentary with each other. Therefore, by knowing the sequence of one strand, the sequence of the other strand is also immediately known. This feature makes possible the multiplication of a known DNA sequence, which will be described in section 2.3.

2.1.4. Physical properties of DNA

In this section, some of the physical properties of DNA will be described. For the purpose of this thesis, some of the important properties are:

- Mechanical properties, as DNA will be transported on a chip and the efficiency of this transport depends upon the DNA's mechanical properties (among other factors).
- Electrical properties, as DNA will interact with the surrounding medium and other molecules, and be subjected to electric field.
- Dielectric properties, as DNA will be subjected to dielectrophoresis, which is an effect that depends on its dielectric properties.

Mechanical properties of DNA

The mechanical properties of DNA are closely related to its molecular structure. When compared to the strength of the bonds within each strand, the hydrogen bonds and electronic interactions that hold strands of DNA together are relatively weak [38]. Furthermore, the hydrogen bonds between the strands of the double helix are weak enough that they can be easily separated by enzymes. Enzymes known as helicases unwind the strands to facilitate the advance of sequence-reading enzymes such as DNA polymerase - the unwinding requires that helicases chemically cleave the phosphate backbone of one of the strands, so that it can swivel around the other. The strands can also be separated by gentle heating, as used in PCR [36], provided they have fewer than about 10,000 base pairs (10 kilobase pairs, or 10 kbp). The intertwining of the DNA strands makes long segments difficult to separate.

When the ends of a piece of double-helical DNA are joined so that it forms a circle, as in plasmid DNA, the strands are topologically knotted. This means they cannot be separated by gentle heating or by any process that does not involve breaking a strand. The task of unknotting topologically linked strands of DNA falls to enzymes known as topoisomerases. Some of these enzymes unknot circular DNA by cleaving two strands so that another double-stranded segment can pass through. Unknotting is required for the replication of circular DNA as well as for various types of recombination in linear DNA.

The most important forces that hold the double helix together come from the stacked base pairs, which form van der Waal contacts in the interior of the molecule [38]. In addition, an induced-dipole effect enhances stacking interactions. The strength of these interactions is base dependent. Furthermore, calculations of

stacking energies show that stacking interactions involving G/C base pairs are stronger than those involving A/T base pairs. Consequently, DNA rich in G+C is more stable than DNA with lower G+C content. Although the forces between stacked bases are individually weak, they are additive; thus, in DNA molecules, which may contain millions of base pairs, stacking interactions are an important source of stability. Hydrogen bonding capacity contributes little to the energy of stabilization, but it is important because of its directionality, which ensures that the two strands are complementary to each other, and positions the bases correctly for stacking.

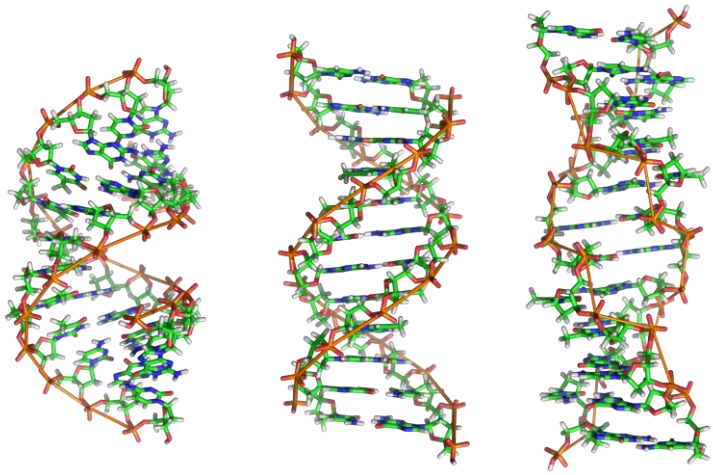

Figure 2.6. A, B and Z forms of DNA [39]

The DNA helix can assume one of three slightly different geometries, known as A, B, and Z form [39]. The "B" form described by James D. Watson and Francis Crick is believed to predominate in cells. It is 2.37 nanometres wide and extends 3.4 nanometres per 10 bp of sequence. This is also the approximate length of sequence in which the double helix makes one complete turn about its axis. This frequency of the twist (known as the helical pitch) depends largely on stacking forces that each base exerts on its neighbours in the chain. The B form of the DNA helix twists 360° per 10.6 bp in the absence of strain. The two other known double-helical forms of DNA (A and Z) differ modestly in their geometry and dimensions. The A form appears likely to occur only in dehydrated samples of DNA, such as those used in crystallographic experiments, and possibly in hybrid pairings of DNA and RNA strands. Segments of DNA that cells have methylated for regulatory purposes may adopt the Z geometry, which has a longer and thinner structure that the B DNA and

its phosphate backbone has a zigzag appearance. Figure 2.6 shows A, B, and Z forms of DNA.

Electrical properties of DNA

DNA electrical properties are of fundamental interest in life sciences and nanotechnology. DNA is the carrier of genetic information for all living species, and investigation of DNA by electrical field based methods has been around for decades [40]. On the other hand, the self-recognition and self-assembling properties of DNA make it a very interesting molecular bio-material, and recently (starting with the late 20^{th} and early 21^{st} century) a lot of research has been done in the field of so called DNA electronics [37-39].

Researchers started to look at the DNA electrical properties soon after discovery of the double helix structure of DNA, and with the recent advancements in the technology, the field has drawn many researchers' attention, as measurements on single DNA molecules were made possible [40]. The findings regarding DNA electrical properties are controversial. Some reports suggest that DNA is a conductive molecular wire, or semiconductor. Others, however, report that DNA behaves as an insulator. DNA electrical properties and its physical mechanism are still open problems. Experiments are underway to study the mechanisms that underlie charge transport in DNA [276-278].

From the application point of view, there are two major fields of science in which electric properties of DNA are of the utmost importance. One is DNA detection and usage of different DNA detection methods based on the DNA molecule charge. The other is usage of DNA as a material for building electrical circuits, where the most interesting DNA electrical property is the ability of DNA to conduct electric current [55-58, 276-278].

A DNA molecule carries negative charge. As stated in section 2.1.3, the DNA molecule comprises of two strands running in opposite directions, and those strands are made of sugar-phosphate backbones and A, T, C and G bases. The phosphate groups in DNA are highly charged: each one carries a unit of negative charge, which means that a DNA molecule carries 2 units of negative charge per base pair [e.g. 37]. This property of DNA has mostly been used in the process called electrophoresis. Since both the DNA molecule charge and the dynamics of DNA in

the suspension (i.e. the molecule size and shape) have an impact on DNA electrophoretic separation, it would be wrong to single out the charge as the only property of DNA that is crucial in electrophoresis success [124, 143]. Apart from electrophoresis, DNA charge is also used for DNA detection based on hybridization of DNA to probes, which causes the difference in charge distribution within the system of microelectrodes by changing the surface potential of one of the microelectrodes where the probes are attached [115-120]. This change of charge distribution can be measured through changes in capacitance and conductivity between the microelectrodes. The technique will be described in more details in section 2.4.

Another interesting electrical property of a DNA molecule is its apparent ability to conduct electric current. This has not yet been utilized in commercial applications, unlike the fact that a DNA molecule carries negative charge. However, recently numerous researchers have studied the mechanisms and means of control of the electric current flow, as well as control over building the DNA wires in a predictable and repetitive manner [276-278]. Current flows in DNA due to two different mechanisms of electrons transport, namely tunnelling and thermal hopping. Tunnelling is a process that consists of electron transfer from a donor to an acceptor. This process is said to be "coherent" in the sense that the electron does not exchange any energy with the molecule during the transfer, and the electron is never localized. The rate of such reactions decreases exponentially with the distance between donor and acceptor. Therefore, for the electron transfer over very long distances, this coherent rate is expected to be insignificant on any reasonable timescale. Thermal hopping, on the other hand, is a possible mechanism for long-distance electron transfer. In this incoherent process, the electron is localized on the molecule and exchanges energy with it. Electron transfer proceeds in a multi-step fashion from donor to acceptor. Such hopping processes can transfer charge over far longer distances than the coherent tunnelling process, and the motion can be thought of as diffusive. Both tunnelling and thermal hopping have been verified with experiments, although it seemed that the results were contradictory, as some researchers classified DNA as a conducting element, some as an insulator, and some as a semiconductor. It is not yet clear whether these opposing results are due to possible artefacts in some experiments, or if they reflect the broad range of many different DNA samples (by means of sequences and sizes) used in different experiments. Possible

differences could be due to the base sequence or the length of the DNA, or the properties of the buffer solution in which the DNA is kept. Other factors include the ambient surroundings (whether the experiments are conducted in liquid, air or vacuum), the structural form of the DNA and its organization (whether the bulk material is studied versus bundles or single DNA molecules), and the electrode-molecule interface and so on. The current status of the field imposes a particularly heavy responsibility on experimentalists. It is very important to devise careful control experiments and for all the findings to be thoroughly reproducible, to make progress on the potential usages of DNA conducting/semiconducting.

2.2. Overview of miniature systems for DNA analysis

At the beginning of the 21st century, the DNA technology has become an inseparable part of our everyday's life. The public has witnessed many new ways for improving pharmaceutical yields, diagnosing and treating diseases, controlling food and environment, and creating new products for home and industry – all based on DNA technology and its staggering potential [38].

The techniques for DNA analysis lie in the origin of all this. The large amount of information contained in DNA requires that the technology gives results rapidly, affordably and reliably [e.g. 7-9, 37-38]. Obviously, microfabrication technology presents an excellent platform for developing miniature integrated analysis systems with short cycle times, reduced sample volume requirements, and high cost efficiency.

Based on the concept of fluidics involved in the process, these microchip systems can be classified in two broad categories: surface microarray based and microfluidics based microdevices [40]. The first are arrays of minute spots of immobilized biological material. The sample is washed over the array, and locations where hybridization occurs are analyzed, generally by fluorescent measurements. On the other hand, in microfluidic systems, material is transported within microstructures where reactions, separations and analysis can occur. The following sections give a short overview of both surface based and microarray based devices.

2.2.1. Surface based microarray systems

The simplest form of surface based microarray systems is so-called DNA microarray, which allows scientists to analyze the presence, activity or sequence variations of thousands of genes simultaneously [40, 41]. The fabrication of a microarray starts with a piece of glass, silicon or plastics, the size of a microscope slide or smaller. Thousands of patterns of single stranded DNA molecules called probes are fixed on the substrate, each spot measuring 20 to 200 μm across. The location and identity of each spot of DNA are known ahead of time. The target DNA is labelled with fluorescence markers, washed over the array and hybridized to any single stranded probe that has a complimentary sequence to its own. A scan of the array with an excitation (usually laser) forces any DNA that has found a tagged match to fluoresce. The light is collected by a detector (a CCD or a photomultiplier tube) and the image fed to a computer for the analysis. Because the identity of the array's DNA is known, the identity of any captured DNA is also known. A schematic of the DNA detection process is shown in figure 2.7. There, the DNA of normal cells and the DNA of drug-treated cells have been washed over a microarray with the DNA probes attached. After hybridization, it is possible to relatively easy detect different DNA sequences.

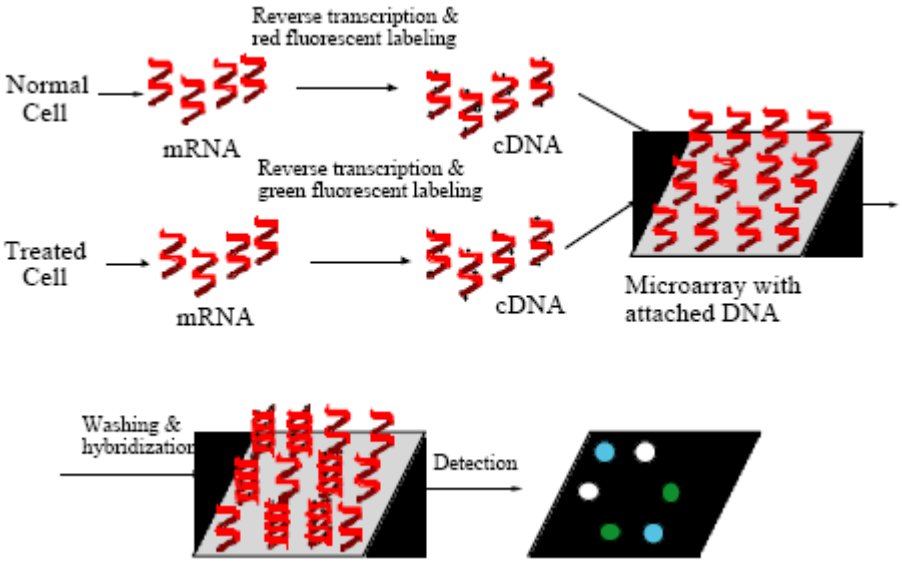

Figure 2.7. Surface based microarray system [40]

The disadvantage of DNA microarrays is that they do not have an integrated microsensor detection system, but they usually have a separate and relatively large detection system which is only suitable for laboratory based research applications

[266, 267]. Another disadvantage is possible contamination between different spots, and therefore one chip is to be used for only one sample. It would be possible to enable parallel analysis of different samples by using a microfluidic network, which directs different samples to different individual dots. However, such system would become much more complex in terms of fabrication and handling.

To allow isolation of analytes in picolitre volumes with low cross-contamination risk, small open surface based vials can be formed (etched or drilled) in the substrate [270-272]. Vials are used as sample containers for electrokinetic injection of DNA samples prior to capillary electrophoresis separation. The further improvement is achieved if the surface separating the vials is coated with hydrophobic film. The main disadvantage of a vial is its large surface area to volume ratio, which linearly increases the rate of evaporation. This can be reduced by several methods, which in return make the analysis more complex. Such methods include coating the vial with a membrane lid, increasing humidity in the working environment, increasing concentration of glycerol, etc [40]. Sometimes, however, evaporation is helping the analysis, if the concentration of the target DNA in the sample is low, and evaporation means increasing the DNA concentration and facilitating detection.

Gel pad arrays can be used for the same purposes as DNA microarrays, with the additional improvement in a sense that gel pad arrays form a three-dimensional system with greater capacity for immobilization compared to two-dimensional microarrays [40]. Such porous and aqueous environments brought by the gel pads also allow novel applications, with the capacity for immobilization increased by a factor of 100 compared to the microarrays. This in turn increases the sensitivity of the measurement. The manufacturing of these chips consists of three steps. Firstly, the gel pads (with dimensions of 10x10x5 microns or larger) are immobilized on a glass slide by photopolymerization. Secondly, the probes are added selectively to gel pads. To avoid cross-contamination, the pads are usually separated by a hydrophobic glass surface. In the third and final process of the chip manufacturing, the probes are covalently immobilized within the pads. During operation, to reduce evaporation of the sample, the chips can either be placed in the environment with 100% humidity, or they can be covered by a glass cover slip or an oil layer.

In general, although the DNA microarrays had a tremendous impact on the DNA technologies, they suffer from the complex fabrication needs, which greatly

increase production costs. Some of the features of the microarrays that increase the fabrication complexity include the relatively large size of the microarrays, and the fabrication protocol changes that are needed when any of the probe sequences in the array need to change [266]. An alternative to the microarrays is the approach based on DNA probes bound to microspheres. This process is well established and less costly then the microarrays fabrication, although the analysis itself is more complex. For identification purposes, each bead in the solution is encoded by chemical, spectrometric, electric or physical means [267].

There is also a possibility to combine the best features of microarrays (relatively easier detection) and DNA bound to microspheres (relative simplicity of fabrication), by using self-assembled array of beads bound to the substrate [39, 41]. The substrate can consist of many fiber-optic bundles, where each bundle consists of as many as 50000 individual fibers per 1 mm of bundle diameter. If these bundles are dipped into a chemical solution, a well will be etched at the end of each fiber. The fabrication process is tuned in a way that each of these wells can hold one microsphere about 3 microns in diameter [274, 275]. In a separate process, single stranded oligonucleotide probes are bound to optically encoded beads, and then randomly distributed across the array surface. Upon drying, the beads are held firmly in the wells on the fibers and are ready for analysis. The surface is then dipped into the sample solution, and the sample strands can found their matches on the beads. Since the bead array was assembled in a random manner, it first needs to be decoded (prior to the sample analysis), so that we know which beads occupy which fibers. This enables the sample strands to be simply detected by shining a laser through the fiber-optic and capturing the emitted light by a CCD device attached to a microscope. Such bead arrays allow much higher package densities than the DNA microarrays described above (due to the smaller feature size), without introducing complexities into the fabrication process. The analysis therefore has much higher throughput, and if different beads are desired for different analysis, it is easy to replace the current set with the new one. Another practical advantage of this method is that the bead array can be brought to the sample, rather than bringing the sample to the array, which is the case for the DNA microarrays [40].

To summarize, the main advantage of the open surface based DNA analysis systems is the ease with which samples and reagents can be added to and withdrawn from the system. Another big advantage is the relatively large number of detection

spots that can be created on a single chip, without the need for interconnections. The main disadvantages include evaporation of the sample due to small volumes (nano- or picolitres), and the risk of contamination (dust and biological material) due to the open environment in which the analysis is performed.

2.2.2. Microfluidic systems for genomic analysis

Microfluidic systems are microfabricated devices in which the material is transported through miniature channels. In literature, many different microfluidic devices can be found, ranging from simple PCR micro-chambers to entire analysis systems [40-74]. Microfluidic networks on these devices offer better control of sample and reagents manipulation, compared to the surface based systems, and hence greater diversity.

There are many different advantages of microfluidic systems compared to other methods for genomic analysis. These are stated in table 2.1 [40]. For these reasons, the usage of microfluidic systems is also recommended in Doctor-on-a-Chip, as will be presented in chapter 4. In general, the reduction in sizes of samples and reagents leads to less material consumption, which means that the fabrication of such systems will be more economically advantageous compared to the traditional methods of analysis. Other advantages result from the scaling of the system, giving dramatically increased performance. For example, the smaller thermal mass of the system allows for faster heating and cooling, which improves the speed of PCR, as the cycles of this process can be completed in a shorter period of time. As another example, greater voltage gradients may be used in the process of electrophoretic separation of DNA particles, without Joule heating of the system. Hence, greater electric field strength is produced, and it is possible to separate different DNA particles in a relatively short channel (compared to traditional electrophoresis). All of these advantages stem from the fact that microfluidic systems use small volumes of samples, which simplifies all of the steps in the analysis from DNA extraction through PCR to separation and detection of DNA molecules.

In this section, a more detailed overview of the microfluidic technologies will be given, as the Doctor-on-a-Chip device described in this paper incorporates a microfluidic network as a backbone for DNA transport. Typically, a microfluidic network comprises of channels, pumps, mixers, nozzles, and valves, and serves for

liquid injection, transportation, mixing, and filtrations. There is also a separate field of research regarding the handling and transport of particles within microfluidic systems.

Property	Advantage Confirmed	Reason
Reagent Consuption	Reduced consumption and less reagent requirement.	Reduced size requires less material.
Mass Transfer (Diffusion)	More rapid across the width of channels.	The effective diffusion time across the channel is proportional to d^{-2} (d is the channel diameter).
Heat Transfer	More rapid, improving heating and cooling times.	Effective rate of thermal dissipation is proportional to d-2. Therefore, it increases as d decreases, and higher voltages can be used.
Separation Efficiency	Improved separation speeds.	Higher voltage gradients may be deployed, hence faster separation.
Flow	Generally laminar (see later in the text).	Reynolds number is proportional to d. In microfluidic systems, it is usually 1-200, and the flow is laminar while < 2000.
Material Transport	Often less pumping required, less valves used.	Electroosmotic control of fluid motion allows for valve-less systems.
Portability	Improved.	Smaller systems, no external pumps required.
Parallelization	Readily achieved.	Single chip with multiple microfluidic networks can be designed for parallel analysis.
Disposability	Improved.	Single-use systems readily produced with low cost.

Table 2.1. Advantages of microfluidic systems [40]

Depending on the actual application of the device, the combination of the microfluidic elements as well as their mode of operation might vary. These

differences and the variety of elements will be described in this section. The main idea of a microfluidic network in Doctor-on-a-Chip is to implement the microbiological protocol of DNA isolation, purification, and amplification, so that it is suitable for on-chip detection for the purpose of detecting pathogens and virus within sample. This will be presented in more details in chapter 4. Hence, the description of the microfluidic basic elements that exist today will be given in the context of usability of those elements for such applications.

2.2.2.1. Valves

In literature, many different valves are described. In general, the valves can be divided into active and passive valves, where the former include some sort of actuation principles, and the later do not [75-77]. Within these two categories, the valves can be further divided into non-mechanical and mechanical valves.

Passive valves do not include any actuation, and are usually designed in such a way that the flow rate is high in one direction, and rather small in the opposite direction. The typical passive valve is a cantilever valve, depicted on the left side in figure 2.8 [290]. In general, such a valve consists of a thin flap sitting on top of a duct. The flap controls the flow through the valve system based on the difference in pressure on both sides. If the pressure difference across the flap is such that it is pressed against the seat, the flow through the valve is zero. In the opposite case, when the flap bends as depicted in the figure, the valve is open.

This type of valve can be produced either microscopically with cutting tools or by using micromachining. Both techniques yield similar working principles and performances, but micromachining allows for production of smaller devices, with feature size in sub-millimetre and even micrometer range. Different fabrication principles have been in details reported in the literature [41], but their description falls out of the scope of this text.

The second type of a passive valve works on a very similar principle, but it controls the flow by using a diaphragm instead of a cantilever. This type of valve is shown on the right side in figure 2.8. The diaphragm is either pressed against a rim, or the rim is attached to the diaphragm and pressed against the substrate. This type of valve is produced by using either surface micromachining or bulk micromachining. Either way, the process is much more complicated than in the case

of the cantilever valve. However, the valves with diaphragms show much higher throughput, when compared to the cantilever valves, for the same pressure difference across the valve. In addition to that, the leakage flow in the opposite direction (when the valve is closed) is of the same order of magnitude.

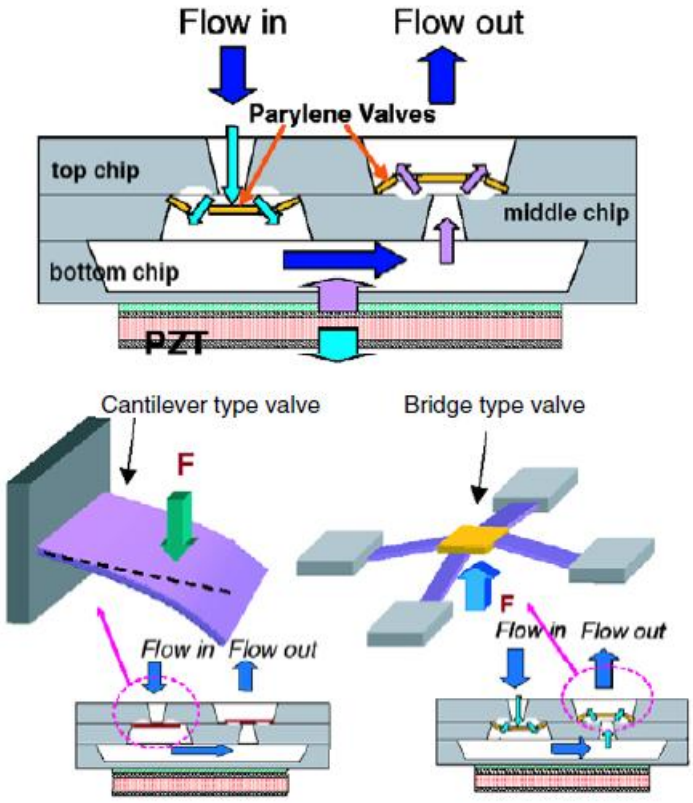

Figure 2.8. Cantilever valve (left) and membrane valve (right) [290]

The two types of valves described above are considered mechanical passive valves. The third and final type of passive valves described in this text is a so called diffuser/nozzle valve, which falls into the category of non-mechanical valves, since it contains no moving parts. Unlike all other valves, this type does not offer a large difference between the forward and reverse flow rates [75, 90]. The forward to reverse ratios are typically 10:9 and smaller compared to the other passive valves described above. For a given diffuser/nozzle valve, its behaviour is dependent upon the angle between two sides of the valve. If the taper angle is small (around 3 degrees), the diffuser direction is preferred. If the angle is enlarged, the nozzle direction is preferred. Figure 2.9 shows the flow rate versus the pressure difference for a diffuser/nozzle with the taper angle of 35.3 degrees. Over the whole pressure

range, the flow through the diffuser is smaller compared to the nozzle, as expected from the theoretical description [75]. Thus, the directional property of the valve is established. It will be shown in section 2.2.2.2 how even such a small forward to reverse flow rate ratio can be utilized for the production of fluid micropumps. The fabrication process depends upon the angle of the diffuser/nozzle. The results are published in the literature for dry etching of silicon and sealing with Pyrex for small angles, and anisotropic etching of silicon for larger angles [75].

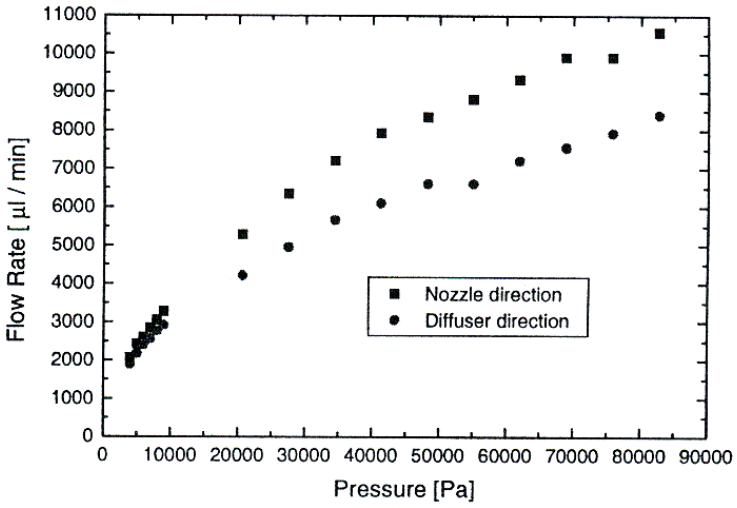

2.9. Pressure versus flow rate for diffuser/nozzle [90]

As stated above, active mechanical valves use some sort of actuation and the flow control is done via valve's moving parts. The basic principle is similar for all of the reported active mechanical valves: an actuator is used to control a flap and thus the fluid flow by opening and closing the valve. These valves can be further divided based on the actuation principle used to control the flow, as described in figure 2.10. Most common principles of actuation are electromagnetic, electrostatic, piezoelectric, bimetallic, thermopneumatic, and shape memory alloy actuation [291].

The magnetic valves can either utilize external magnetic fields, or have integrated inductors [291]. In the case of the former, a permanent magnet can be mounted on the movable membrane, and the valve can be closed or opened through the interaction of this magnet with external coils. In the opposite case, the coil can be fixed on the membrane and interact with the external permanent magnet. In both cases, the valve can be impractical for integration on a handheld microfluidic chip due to the need for external magnetic field.

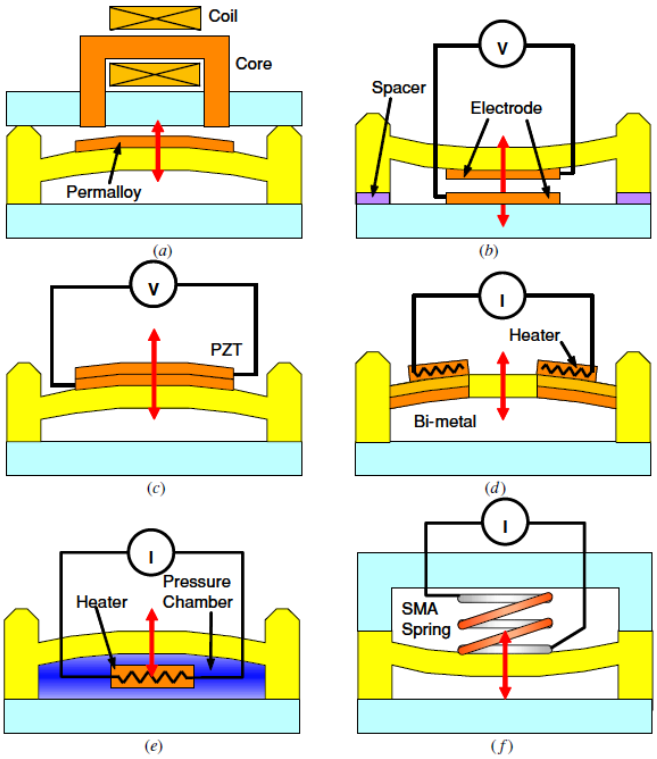

Figure 2.10. Various actuation principles of active mechanical valves: a) electromagnetic, b) electrostatic, c) piezoelectric, d) bimetallic, e) thermopneumatic, and f) memory shape alloy actuation [291]

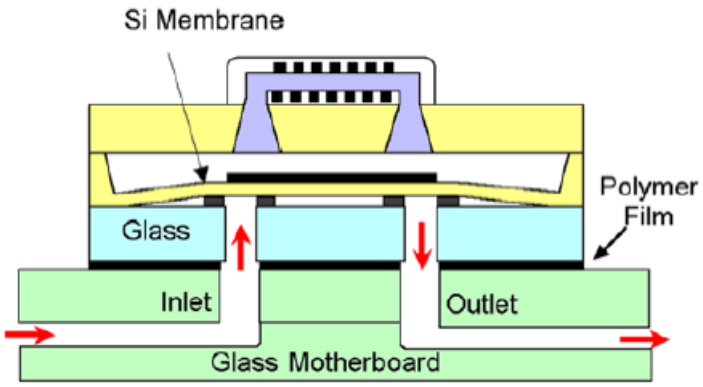

Figure 2.11. Magnetic valve with integrated inductor [79]

In the case of the integrated inductor, as shown in figure 2.10.a, there is no need for external magnetic field. Another schematic representation of such a valve is shown in figure 2.11. It consists of an integrated inductor, a deflectable silicon membrane with NiFe thin film and a stationary inlet/outlet valve seat [79]. These components were fabricated individually and bonded together using a low temperature bonding technique. The inductor acts as a flux generator and produces

sufficient magnetic forces to pull the silicon membrane by magnetically coupling with the NiFe permalloy electroplated on the silicon membrane. The membrane pulled up and removed itself from the valve seats, thus opening the valve and allowing the fluid flow if there is sufficient pressure difference between the inlet and outlet.

The electric valves can generally be divided into electrostatic and piezoelectric valves, as depicted in figures 2.10.b and 2.10.c. An example of an electrostatic valve is shown in figure 2.12 [41]. A flap sitting on top of a duct is the first electrode, while the second electrode is embedded in the valve seat. By applying the electric field between the two electrodes, the flap is moved either towards or away from the top wafer electrode, which in turn opens or closes the valve. The maximum pressure reported is 16 kPa, and a gas flow of up to 3 ml/min can be controlled at a switching frequency of around 2.5 kHz.

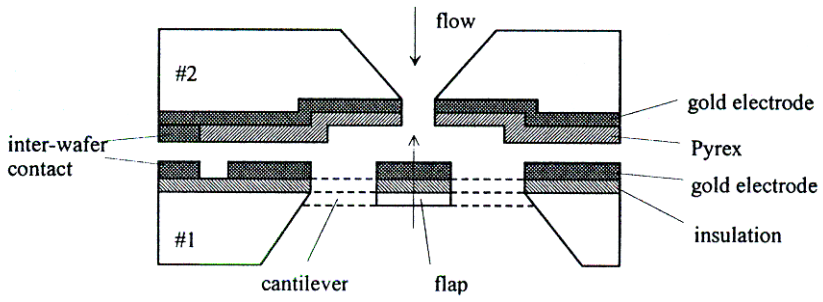

Figure 2.12. Active valve with electrostatic actuation [41]

An example of a piezoelectric valve is given in figure 2.13. The valve is designed in low temperature co-fired ceramic (LTCC) and manufactured using standard processes [292]. Actuation of the valve is based on a piezoelectric unimorph with a diameter of 15mm and thickness of 0.35mm glued onto the fired LTCC substrate. Under the applied electric field, transversal expansion and contraction of the piezoelectric layer together with the passive layer creates internal bending moment and deflection of the structure. Measurements of the valve revealed a flow of 143 ml/min under 1 bar pressure, leakage levels of 4%, valve displacement of 1.3 μm, and closing times less than 30 ms.

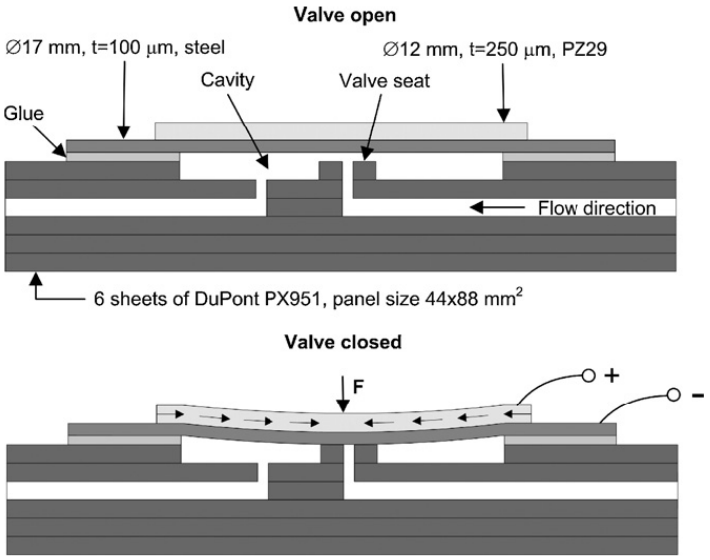

Figure 2.13. Piezoelectric valve [292]

Active mechanical microvalves can also use bimetallic actuation, as depicted in figure 2.10.d. Here, the flap is bimetallic and heated to open or close the valve. The valve operates with gas flows up to 150 ml/min and pressures between 7 and 344 kPa [77, 79], with the switching time around 100 milliseconds. Although the main drawbacks of these valves include relatively slow actuation speed and high power consumption due to temperature changes, thermal actuation schemes are attractive because of the simplicity in microstructures. However, due to temperature changes of the sample, these valves are not suitable for those microbiological applications in which the sample under investigation is sensitive to temperature changes and can thus be affected simply due to the working principle of the valves.

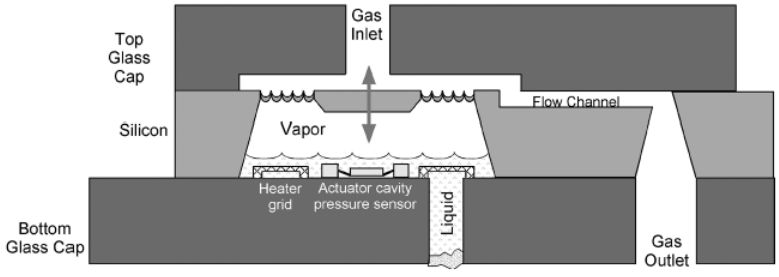

Figure 2.14. Thermopneumatic valve [293]

Another type of valve with actuation based on temperature changes is thermopneumatic valve, which is schematically depicted in figure 2.10.e. This valve

operates on the principle of volumetric thermal expansion, which is coupled to diaphragm deflection and thus opens or closes the valve [291]. One example of such a valve is depicted in figure 2.14. The valve consists of top and bottom glass caps, between which a sealed cavity fabricated in silicon contains a volatile fluid. The vapour pressure of the fluid can be increased by resistive heating, thus deflecting the diaphragm upwards and closing the valve. The valve also contains a capacitive pressure sensor located on the floor of the cavity, which allows direct and accurate monitoring of the cavity pressure. The valve generated a 16 Pa pressure rise with 500 mW of power, while closing of the membrane was maintained with a 30 mW steady input power. The flow rate through the valve was measured at 400 ml/min under 11.3 Pa differential pressure, while the leakage was measured as low as 1 µl/min.

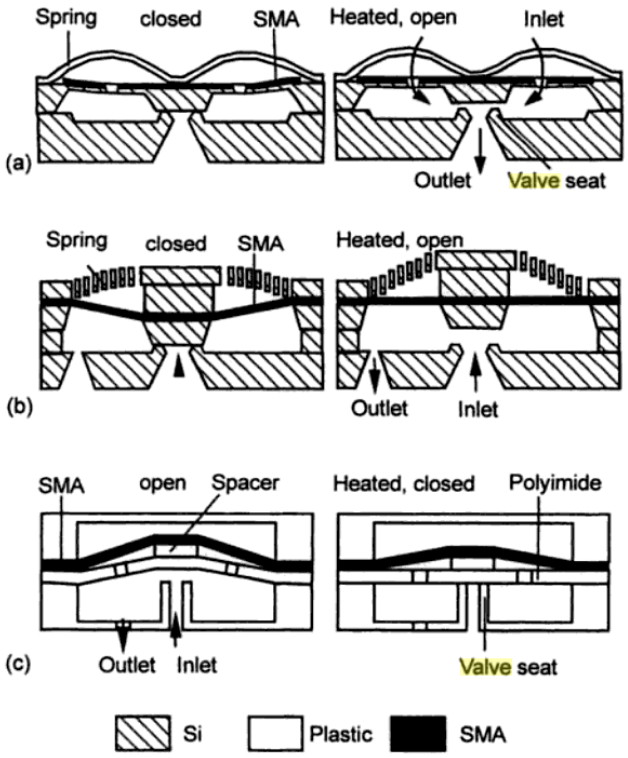

Figure 2.15. Different type of SMA valves: a) beryllium-copper (external) spring, b) silicon spring , and c) polymer spring [294]

Another type of thermally actuated valve is shape-memory alloy (SMA) valve depicted in figure 2.10.f. This type of valve is made of materials such as titanium/nickel alloy, which, once mechanically deformed, return to their original un-deformed shape upon a change of temperature [294]. SMA undergoes a phase

transformation from a “soft” state at low temperatures to a “hard” state at higher temperatures. Since the alloy structure represents an electrical resistor, passing a current through it generates heat. The advantages of SMA valves are high force and large stroke, while the main disadvantages include low efficiency and operation bandwidth (typically 1.5 Hz). Figure 2.15 depicts several typical SMA microvalves. All of the variations have a spring that either keeps the valve initially closed (a and b) or open (c). Heating the alloy brings the valve to the opposite state, and upon eliminating the heat, the spring brings the valve back to the original state. The springs can be made of different materials, based on the fabrication methods, and here we show an example with springs made of beryllium-copper (external spring), silicon, and polymer.

In summary, this section gives an overview of the microfluidic valves available in state of the art microfluidic chips for manipulation and analysis of fluid samples on micro- and nano-liter scale. From the point of view of Doctor-on-a-Chip application, the most important aspects are simplicity from the manufacturing standpoint, ease of use, robustness, and cost. The valves that operate based on any significant temperature change, such as bimetallic and thermopneumatic, are probably not suitable for DNA based applications due to the fact that DNA molecules are sensitive to temperature changes and the valve operation can potentially change the sample properties and affect the analysis. For similar reasons, electrostatic valve can also potentially affect the sample with DNA molecules due to the fact that they carry negative charge and can thus be trapped by the electric field produced for valve operation. The electromagnetic valves would be expensive to manufacture, which would increase the overall cost of production and eventually the analysis system. Of all the active valves presented in this section, piezoelectric valves are probably the most suited for controlling the fluid network that analyzes DNA sample, because of their simplicity and low impact on the sample under analysis. As far as the passive valves are concerned, they seem more attractive in general due to the fact that their manufacturing process is likely much simpler than for active valves. Cantilever and membrane valves are potentially problematic due to the fact that they are susceptible to clogging when the fluid carries particles through the valve. Diffuser/nozzle valve on the other hand has great potential, because it is very simple to manufacture, has good characteristic, and does not impact the sample in any way. In fact, in chapter 4 later in the text, the diffuser/nozzle concept is used

as a part of the pumping mechanism on the chip. As shown in figure 2.23 in section 2.2.2.2, the piezoelectric micropump based on diffuser/nozzle principle eliminates the need for valves elsewhere on the chip, because the pump itself serves the purpose of directing the fluid in the desired direction.

2.2.2.2. Micromixers

Mixing on the microscale is one of the key technologies for miniaturized integrated analysis systems. Miniaturization brings important advantages over macroscale for wide variety of fields, including, but not limited to, chemical industry, pharmaceutical industry, analytical chemistry, and biochemical analysis [295]. However, due to dominant surface effects, miniaturization also brings challenges that do not exist at the macroscale. For example, since the microchannel dimensions and the fluid flow rate in a microfluidic device are very small, the Reynolds number is low and the flow is dominantly laminar [88, 96]. Therefore, turbulence, which is used at the macroscale, is not possible at the microscale, and over the years a number of different techniques were investigated to improve mixing [295]. In general, they can be divided into two categories: passive mixing (without introducing external energy) and active mixing (with external energy input to enhance the mixing effect).

Passive mixing of two liquids is primarily relied on molecular diffusion that occurs when they come to a physical contact, i.e. they are introduced to the microchannel at the same time. A simple relation between the diffusion time t_d and the average diffusion length x_d can be found from Fick's second law of diffusion [88]:

$$t_d = \frac{x_d^{\,2}}{2D} \tag{2.1}$$

Here, D is the diffusion coefficient typically in the order of 10^{-3} mm^2/s. The process of diffusion is very slow. For example, if two microchannels carrying the fluid would simply be linked together by means of a Y-mixer, mixing of 100% would occur only after 13.3 m at flow rate equal to 4 μl per second and with a typical diffusion coefficient. Therefore, it is necessary to increase the active area for diffusion, which can be done by splitting the main flow of the liquid into a certain

number of branches prior to mixing. There are several reported designs that have successfully utilized this approach [41, 97]. Fundamentally, they are all very similar and one of them will be described here as an example. The principal design is depicted in the following figure [97]:

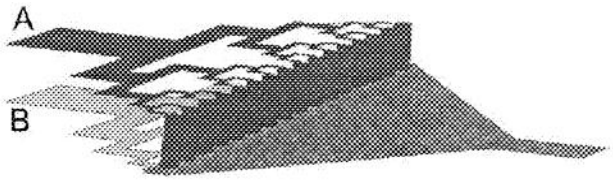

Figure 2.16. Passive micromixer [97]

The reported micro-total-analysis-system comprising this mixer is composed of three Pyrex wafers attached by fusion bonding. The mixer is produced by etching the middle wafer on both sides. As shown above, the incoming fluids A and B are gradually split into 16 smaller channels before mixing. The dimensions of the channels in the last level are limited by technological restrictions. For example, if the channels are 50 μm deep, the narrowest channel obtained is 110 μm wide, of which 10 μm are needed for the mask opening and 100 μm results from under-etching. In the mixer, the fluid A comes from the wafer topside through small holes and fluid B stays at the bottom side. They are combined in a triangular mixing chamber and the channel leading from the chamber contains the mixture of the two liquids. The performance of the mixer was reported to be highly satisfactory. The distance between the point where fluid A (and B) was split from one to two channels and the end of the triangular chamber is 7.5 mm, while the side of the triangular chamber on which the fluids come to contact is 10 mm long. Therefore, the effective area of the mixer is 75 mm^2. This type of mixer has certain disadvantages, such as sensitivity to clogging and gas bubbles, dependence on the mixing time and efficiency on the flow rates.

There have been several similar configurations reported, which work on a similar principle of mixing the fluids based on molecular diffusion [295]. They are shown schematically in figures 2.17 and 2.18.

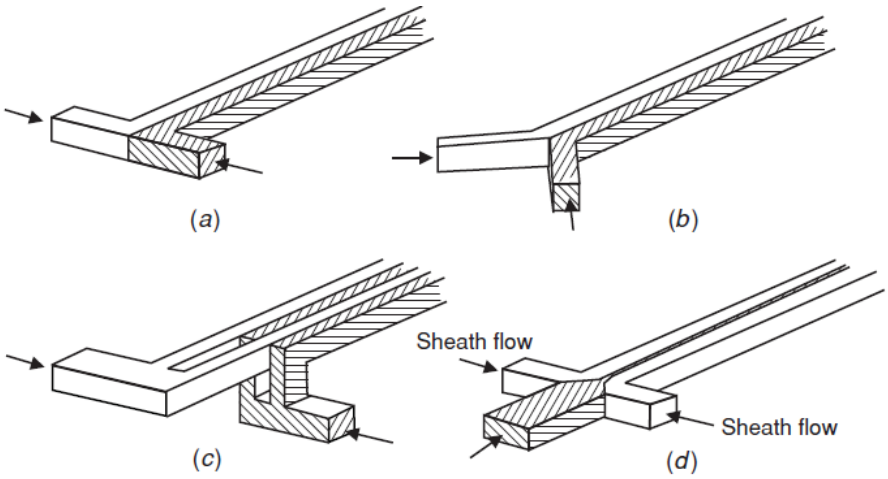

Figure 2.17. Parallel lamination mixers: a) T-mixer, b) Y-mixer, c) concept of parallel lamination, d) hydraulic focusing [295]

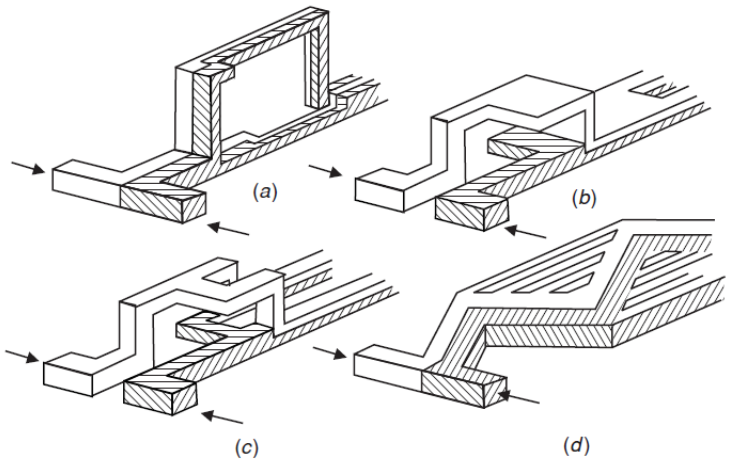

Figure 2.18. Serial lamination mixers: a) join-split-join, b) split-join, c) split-split-join, d) multiple intersecting microchannels [295]

In figure 2.17, basic T and Y mixers are shown in figures (a) and (b), respectively. Here, two different fluids enter the mixer at their dedicated inlets, and mixing based on molecular diffusion occurs across the length of the mixing channel. Similar concept is shown in figure (c), where the fluids enter the channel already split into two or more streams, which increases the surface between the two fluids and enhances the mixing effect. Figure (d) shows a mixer with three inlets, where the middle one is dedicated to one fluid, and the two inlets on the sides are dedicated to the other fluid.

Figure 2.18 shows schematic concepts of serial lamination mixers, where, similar to parallel lamination mixers, the mixing effect is enhanced by splitting and

joining the streams, and this action can occur multiple times across the mixing channel [295].

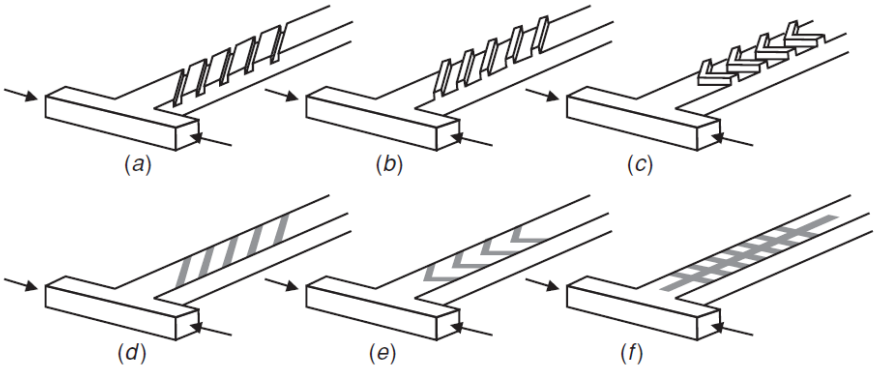

Figure 2.19. Chaotic advection for low Reynolds numbers: a) slanted ribs, b) slanted grooves, c) staggered-herringbone grooves, d-f) surface modifications [295]

Significant improvement of the mixing effect in passive micromixers can be achieved with chaotic advection [295-297]. This term refers to stretching, folding and breakup process caused by transverse flows. Generally, chaotic advection can be generated by special geometries in the mixing channel (passive micromixers), or induced by an external force (active micromixers). For the former, the basic idea is the modification of the channel shape for splitting, stretching, folding and breaking of the flow. Based on the Reynolds number, different techniques can be applied. Here, the techniques for low Reynolds number will be described, since they are most relevant in the case of Doctor-on-a-Chip. Some of these techniques are depicted in figure 2.19, where (a-c) show grooves with different patterns that were on the bottom of the wall by using laser a laser, and (d-f) show small surface modifications on the walls of the micromixers used together with electrokinetic mixing [295]. All of these techniques were shown to enhance the mixing effect via chaotic advection for flow rates as small as 100 μm/s and Reynolds number in the range between 1 and 100.

An active micromixer is defined as a mixer with external energy input to enhance the mixing effect. It should be tolerant of gas bubbles and the mixing effects should be controllable by changing the level of input energy. One example of an active micromixer employing piezoelectrically generated ultrasonic vibrations was presented in literature [41, 97-98, 299]. Its structure is shown in figure 2.20. A piece of lead-zirconate-titanate (PZT) was used as an active element and attached

directly onto the oscillating diaphragm using an epoxy resin. When the voltage is applied to the PZT piece, the mixing of liquids occurs in the chamber. Theoretically, this effect originates from the ultrasonic irradiation, not the diaphragm oscillation. Thus, the oscillating diaphragm is not a necessary part of the mixer. However, it was used here to prevent the ultrasonic radiation from escaping to the other parts of the device and to focus it onto the mixing chamber.

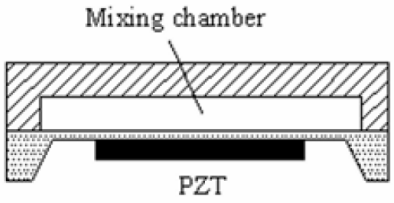

Figure 2.20. Piezoelectric micromixer [299]

It was shown that the turbulence occurs immediately after the ultrasonic vibration, and when the vibration was terminated the laminar flow resumed. The two liquids mixed rapidly and effectively. The frequency characteristic of the mixer was tested for up to 600 kHz of the driving voltage. There was no mixing for the frequencies below 8 kHz and then the mixing area gradually increased until the frequency reached 15 kHz. After that, it became stable with the slight drop between 90 and 130 kHz. The overall performances of the mixer were satisfactory, and the temperature rise was not significant (3˚C in this case, due to the good thermal conductivity of the silicon). However, it would be desirable to decrease the driving voltage to 10 or 15 V without deteriorating the mixing effect, so a more compact driver unit could be used.

There are other types of active micromixers described in the literature, which are schematically shown in figure 2.21 [295-296, 299]. In figure (a), the micromixer utilizes the pressure difference between two inlets in a Y-mixer. This difference is induced by pulsed flows of two fluids, which are subjected to external pumping forces. Figure (b) shows the Y-mixer with computer-controlled pressure disturbance induced at several places in the mixing channel. The frequency of the pressure disturbance can be tuned to maximize the mixing efficacy. Figure (c) shows a micromixer with a small micro-stirrer in the channel. The micro-stirrer consists of

magnetic beads, which are chaotically moved inside a channel by means of the induced magnetic field.

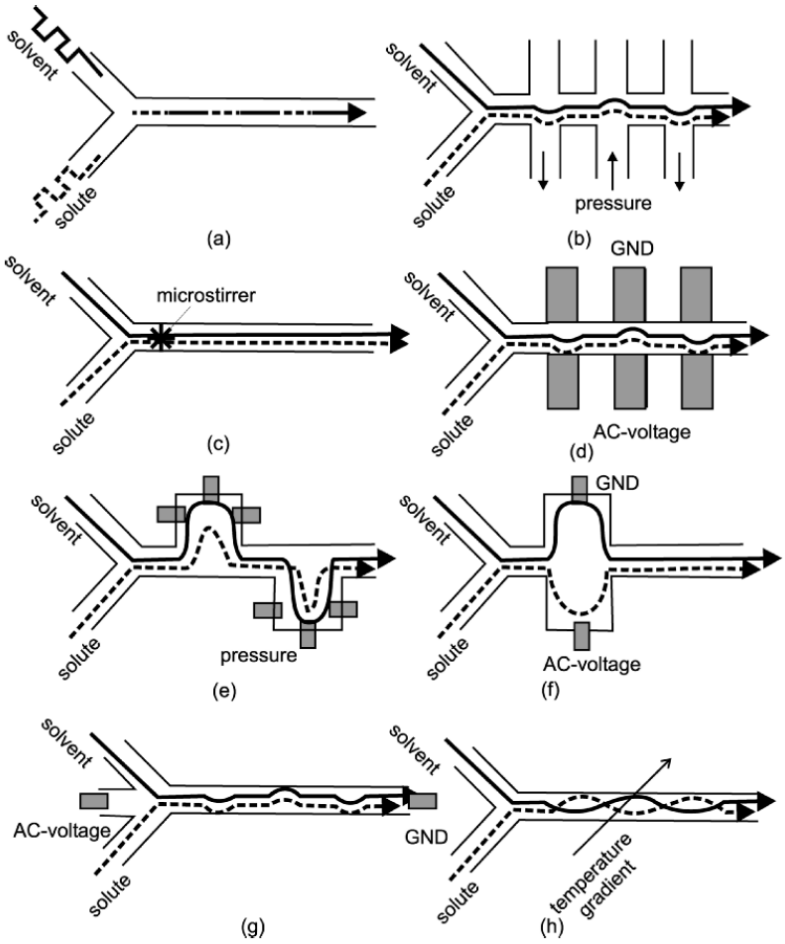

Figure 2.21. Active micromixers: (a) serial segmentation, (b) pressure disturbance along mixing channel, (c) integrated microstirrer in the mixing channel, (d) electrohydrodynamic disturbance, (e) dielectrophoretic disturbance, (f) electrokinetic disturbance in a mixing chamber, (g) electrokinetic disturbance in a mixing channel, and (h) disturbance caused by thermocapillary advection induced by a transverse temperature gradient [296]

Figure (d) shows electrohydrodynamic mixing, which is obtained by changing the amplitude and frequency of the voltage applied to the microelectrodes placed under the channel in the direction perpendicular to the fluid movement. Figure (e) shows the mixing effect based on dielectrophoresis. Here, dielectrophoretic force on the particles subjected to non-uniform electric field and suspended in liquid causes the particles to move to the regions of high or low electric field, and this movement of particles causes the mixing to occur. Figures (f) and (g) show electrokinetic mixing, where electrokinetic disturbance can take place

in a mixing chamber or all across the length of the channel, depending on the actual layout of microelectrodes. Finally, figure (h) shows the mixing effect based on the temperature gradient across the channel, which causes helical streamlines and thus chaotic advection.

In summary, this section gives an overview of the micromixer technologies for mixing fluids on a microscale. From the point of view of Doctor-on-a-Chip, mixing of fluids presents a significant challenge, because the DNA extraction, purification and amplification requires implementation of a relatively complex protocol, which requires several mixing steps, as described in chapter 4. Passive mixers are probably not suitable for this application, because of a very small Reynolds number in the system. The mixers based on chaotic advection should probably perform better, but that should be experimentally verified to ensure reproducibility of the mixing effect and thus reliability of the system. Active micromixers seem more attractive and more reliable. However, the mixers based on electrical fields (electrohydrodynamic, dielectrophoretic and electrokinetic mixers depicted in figure 2.21) could potentially interact with the sample, since DNA molecules are both charged and polarisable, and thus susceptible to both DC and AC electric fields. The mixers depicted in figure 2.21 (a)-(c), which operate based on serial segmentation, pressure disturbance and stirring on a micro scale, respectively, seem more suitable for Doctor-on-a-Chip due to low interaction with the sample, but the overall complexity of the system and cost of fabrication could make them less attractive. The piezoelectric active mixer seems attractive from the fabrication standpoint, as it is relatively simple to produce, and from the mixing efficiency standpoint, due to the fact that deflection of the oscillating membrane shows relatively good mixing characteristics compared to other types of mixers on such a small scale. In chapter 4 it will be shown that the proposed concept of Doctor-on-a-Chip utilizes a micropump based on the piezoelectric pumping effect, and that the pump is in fact also utilized as a mixer, as shown in figure 2.23. This is possible due to the fact that the pump has two inlets, and thus two different fluids are entering the pumping chamber at the same time. The membrane deflections cause the fluids to mix within the chamber, and the mixture is pumped out into the channel and towards the other parts of the chip.

2.2.2.3. Micropumps

Micropumps are essential components in microfluidic analysis systems because they must be able to handle fluids with wide variety of properties, i.e. viscosity, density, ion strength, pH, temperature, etc [41, 90-102]. The micropump's sensitivity to fluid properties is dependent on the principle used for fluid movement. Essentially, there are two kinds of micropumps: mechanical and non-mechanical. In this section, they will be described with more details.

Mechanical pumps

Most mechanical micropumps make use of an oscillating membrane, whose deflections change the pressure in a pumping chamber and thus pump the liquid [41]. That is why in the literature this group of pumps is also often referred to as membrane-actuated pumps.

When the chamber volume increases, the pressure drops and the fluid flows from the inlet into the chamber. When the chamber volume decreases, the pressure increases and the fluid is forced to flow out of the chamber through the outlet. A difference in the flow resistance between the inlet and the outlet for different flow directions is crucial for the pumping effect. The membrane can be actuated in different ways. The main principles described in the following text are summarized in [95] and depicted in figure 2.22.

- Pneumatic actuation is achieved by using an external pump for applying the pressure to one side of the membrane, and thus, the volume of the chamber is changed on the other side of the membrane. Because of the need for the external pump, it is virtually impossible to integrate this kind of pump with the rest of a microchip for microbiological and chemical analysis.
- Thermopneumatic actuation is achieved by heating and cooling the volume on one side of the membrane. The heating process increases the pressure in the volume and presses the membrane downwards, increasing the pressure in the pumping chamber and causing the fluid to flow out of the chamber and through the outlet. The opposite effect is achieved when the volume is cooled. If the heated volume is small enough, reasonable pumping frequency can be achieved.

- Piezoelectric actuation is achieved by attaching the piezoelectric layer on top of the membrane. The piezoelectric effect in the actuator causes the membrane to deflect, effectively pumping the fluid in and out of the chamber.

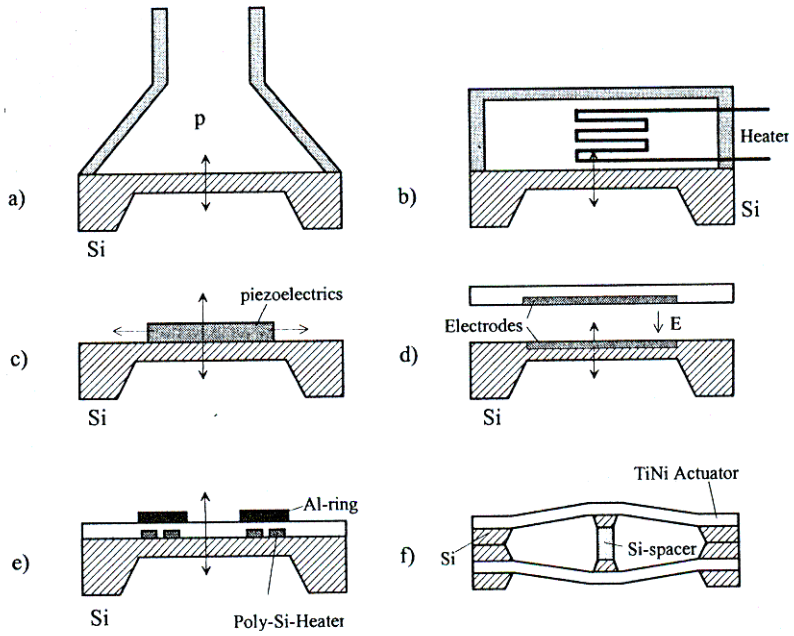

Figure 2.22. Different techniques for membrane actuation: (a) pneumatic, (b) thermopneumatic, (c) piezoelectric, (d) electrostatic, (e) bimetallic, and (f) shape-memory alloy [95]

- Electrostatic actuation is achieved by using two electrodes and applying an electric field between them. One electrode is embedded into the membrane, and the other electrode is fixed right above it. Depending on the polarity of the voltages applied to the electrodes, they will either attract or repulse, and thus the membrane changes the volume of the pumping chamber and pumps the fluid.
- Bimetallic actuation is achieved by applying a voltage to a poly-Si resistor, as shown in figure 2.22. Due to the bimetal effect between the resistor and the aluminium ring placed above it, the whole membrane is deflected and the fluid pumped through the chamber underneath it.
- Shape-memory effect is achieved with TiNi metal forming a membrane on two sides of the actuator, deflected in the centre by a spacer, as shown

in figure 2.22. When the top TiNi actuator is heated, the top membrane straightens and deflects the lower membrane further. Then the current through the top membrane is switched off, and applied through the bottom membrane. The deflection is then reversed, and the pumping effect is achieved.

The main advantage of all these different types of membrane pumps is their ability to pump almost any kind of liquid phase with a typical flow range between 1 and 100 μl per minute. Their main drawback is considered to be the fact that the generating flow is always pulsating, which can pose a problem in certain cases [41].

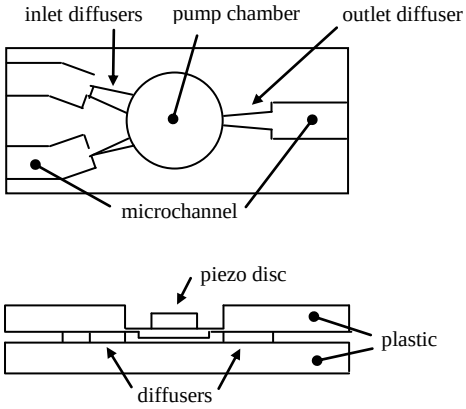

Figure 2.23. Piezoelectrically driven valve-less diffuser micropump with two inlet diffusers

The pumping principle will be in more details described on an example of a piezoelectrically driven micropump with passive diffuser/nozzle valves. Figure 2.23 depicts the principal design of the pump [107]. The key element is the diffuser, a flow channel with gradually expanding cross-section. The diffuser can have either rectangular or circular cross-section, but the rectangular one is chosen here because of a more compact design. The concept of a rectangular diffuser is shown in figure 2.24. This micropump was initially designed with only one inlet diffuser, but in this case this version is chosen as it allows the micropump to serve also as a mixer of two incoming liquids. This is based on the fact that the flow pattern inside the chamber is vortex-like, due to the diaphragm deflections. Therefore, if two liquids are pumped, each one coming from its own channel, it is possible to mix them utilizing the generated turbulence. This design effectively combines the pump and the active mixer into one pumping/mixing device [107]. The most interesting feature of the diffuser is the difference in its flow resistances in the forward (diffuser) and

reverse (nozzle) directions. The net flow resulting from this fact can be recognized from figure 2.25, where the size of arrows corresponds to the amount of the liquid pumped into the chamber in the supply mode and out of the chamber in the pump mode.

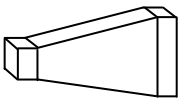

Figure 2.24. A rectangular diffuser

In the supply mode, the diaphragm deflection in the shown direction causes the fluid to be pumped into the chamber from both the pump inlet and outlet channels. The fluid coming from the inlet side has to flow through the diffuser to get into the pump chamber, while the fluid coming from the outlet side has to flow through the nozzle. The flow resistance that the fluid encounters coming from the inlet side is smaller (the flow resistance of the diffuser is smaller than that of the nozzle). Therefore the fluid volume introduced to the chamber from that side is greater than the one introduced from the outlet side, where the greater flow resistance is encountered.

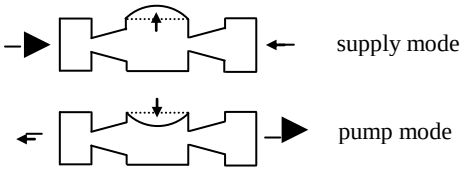

Figure 2.25. The diaphragm deflections in the supply and pump modes

In the pump mode, the diaphragm deflection causes the fluid to be pumped out of the chamber, again towards both inlet and outlet. In this case, the fluid flowing towards the inlet side encounters greater flow resistance and the greater volume is pumped towards the outlet side, where the flow resistance is smaller.

In conclusion, the pump diaphragm deflections cause the net flow of the fluid from the inlet side to the outlet side. The estimation of the pumping efficiency is based on the diffuser element efficiency ratio as follows [107]. For the diffuser element, the pressure drop in the diffuser and in the nozzle directions can be written as follows:

$$\Delta p_{diffuser} = \xi_{diffuser} * \frac{1}{2} \rho \hat{u}_{diffuser} \tag{2.2}$$

$$\Delta p_{nozzle} = \xi_{nozzle} * \frac{1}{2} \rho \hat{u}_{nozzle} \tag{2.3}$$

ξ is the pressure loss coefficient, ρ is the fluid density and $\hat{u}$ is the mean fluid velocity in the diffuser neck. The diffuser element efficiency ratio is then defined as

$$\eta = \frac{\xi_{nozzle}}{\xi_{diffuser}} \tag{2.4}.$$

The optimum efficiency is achieved when η is maximized. The experimental analysis showed that η is maximized for the angle between the diffuser walls equal to approximately 5° [41]. The diffuser angles in the above figures are drawn greater than 5° merely for the better representation.

The other mechanical pumps are described in details in the literature. However, this description falls out of the scope of this text. The pump above is presented with more details, as it was used as the pump of choice for the Doctor-on-a-Chip application described in [202], which will be described with more details in chapter 4.

Non-mechanical micropumps

The second mechanism used for micromachined pumps is the flow induced by electric fields [91-93]. These electric field actuated pumps are non-mechanical, i.e. they do not require any movable parts to pump fluids (one of the properties of these pumps is therefore a pulsation-free flow). A disadvantage is that they require relatively large voltages to produce reasonably high flow rates. These pumps work on a principle of the force experienced by the charged particles within the fluid when the electric field is applied. If the number of charged particles is large, the whole fluid is dragged along due to frictional forces. The electric field actuated pumps are categorized based on the mechanism used to generate charge within the fluid. Hence we have electrohydrodynamic and electroosmotic pumps.

The most significant research in the field of non-mechanical fluid pumping has been built up in the area of electroosmotic pumping [91]. The most interesting

features of electroosmotic pumps are the simple design without moving parts and the pulsation-free flow. The design without moving parts is advantageous because it simplifies both the fabrication and the operation of the device. The principal work of electroosmotic flow (EOF) pumps is electroosmosis, an effect due to the double layer in the pumping liquid. The mechanism of the electroosmotic flow is shown in the following figure.

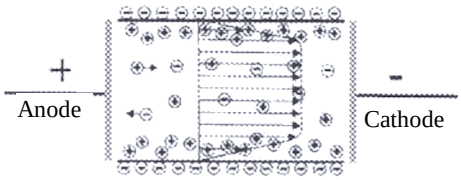

Figure 2.26. The mechanisms of electroosmotic flow [91]

Most surfaces obtain surface electric charge when they are brought into contact with polar medium. This may be due to ionisation, ion adsorption or ion dissolution [92]. The surface charge in turn influences the ion distribution in the polar medium forming the electric double layer (EDL). This situation is depicted in figure 2.26 with negatively charged channel walls. The counter ions from the bulk liquid (i.e. the positive ions) are attracted to the walls and shield the wall charges. Dissolved co-ions are likewise repelled from the wall. The ions in the inner layer of counter ions adjacent to the wall are immobile and called the Stern layer. The outer, diffuse part of the EDL is called the Gouy-Chapman layer and forms a net positive region that spans a distance on the order of the Debye length of the solution. When the external electric field is applied parallel to the wall, ions from the diffuse part of the EDL will move in response to the field and drag the surrounding medium with them. This ion drag causes a net motion of bulk liquid along the wall and it is called the electroosmotic flow [41]. Since the fluid motion is initiated by the electrical body force (the driving force) acting on the ions in the diffuse layer of the EDL, electroosmotic flow depends not only on the applied electrical field, but also on the net local charge density in the liquid. The detailed analysis of the electroosmotic flow and its dependence on the channel geometry, liquid properties and the applied voltage is given in [92, 93]. For high electric field strengths (27 – 163 V/cm) over a

165 mm long capillary, a moderate speed of 0.13 – 0.78 mm/s and flow rates of 3 – 18 nl/min have been achieved, with the channel dimensions of 5.6 x 66 μm.

The electroosmotic flow has one very important practical limitation, in a sense that it depends on the pumping fluid composition [41]. This means that when the carrier solution has a very high or very low pH, is a highly conductive saline or a non-conducting organic medium, the current levels are either excessive or inadequate to support significant electroosmotic. In order to utilize electroosmotic pumping in micro systems, it is preferable to separate the pumping device from the rest of the system (e.g. mixer), while maintaining the hydraulic connectivity between them.

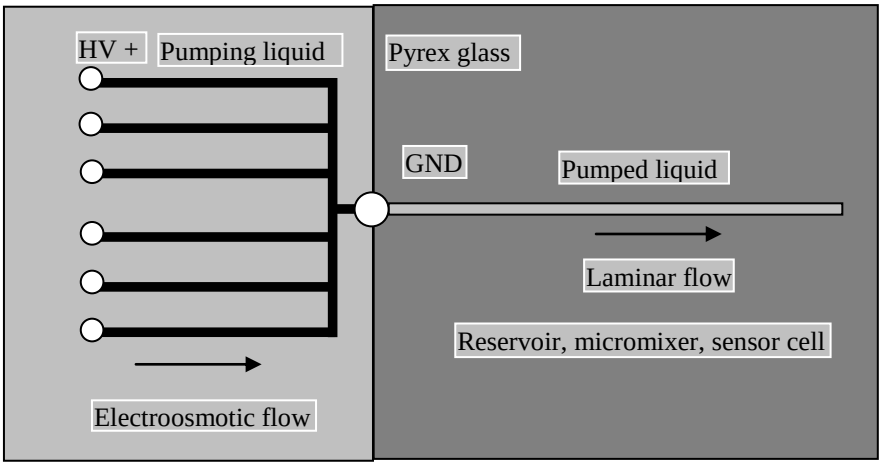

Figure 2.27. Electroosmotic pumping implemented on chip [41]

The schematic view of this principle is shown in figure 2.27. This electroosmotic micropump consists of a parallel arrangement of six microchannels. The liquid in these channels is the one suitable for electroosmotic pumping (for example 10 mM borax solution [ref 91]). When the voltage is applied to the channels, the flow is generated and the pumping fluid flows towards the container where the pumped liquid is previously introduced. The pumping liquid enters the reservoir and pushes the liquid out on the other side of the channel. The voltage applied to each pumping channel can be controlled separately and in this way the flow rate can be altered. It was shown that the liquid flow rate is directly proportional to the applied voltage. For example, the 10 mM solution of Borax and channels 300 μm wide and 50 μm deep resulted in the flow rate equal to 10 – 25 nl/s (depending on the number of pumping channels) for the applied voltage of 1000 V.

This approach to pumping the liquid on the chip can be impractical by means of area used for its implementation. In this example, the channels used for pumping the borax solution were each 83 mm long, making the total length of almost 500 mm (six channels). If a chip has to pump more than one or two liquids, the area used only for pumping could be too large for this pumping mechanism to be effective.

As far as the electrohydrodynamic pumps are concerned, they require fluids with conductivity between 10^{-8} and 10^{-10} S/cm in order to function. In general, the forces acting on a fluid are the electric field force, the dielectrophoretic force, the dielectric force, and the electrostrictive force. The equation describing these effects is given as:

$$\vec{F} = q * \vec{E} + \vec{P} * \nabla\vec{E} + \frac{1}{2} E^2 \nabla 2\varepsilon + \nabla(\frac{1}{2} \rho \frac{\delta\varepsilon}{\delta\rho} E^2) \tag{2.5}$$

Here, q is the electric charge, E is the electric field strength, ε is the permittivity of the material, P is the polarization factor, and ρ the mass density of the fluid. The last part of the equation representing the electrostrictive force is only important if the fluid under observation is compressible. Also, the dielectrophoretic part of the force is usually negligible, because it does not lead to a continuous flow for DC fields and is considerably smaller in cases of AC fields.

Conventional EHD pumps can be classified into injection EHD pumps and induction EHD pumps, based on the charge induction mechanism [104].

Injection EHD pumping starts with the formation of space charges through injection or electrolytic process at the boundary layers between the electrode and the liquid at high electric field strengths. In the case of intermediate electric field strengths, the charge creation within the liquid at one or both electrodes is achieved through dissociation or electrolytic processes within the liquid itself. The charges generated by electrolytic processes are of both polarities and are moved in opposite directions inside the liquid. For high field (higher than 100 kV/cm) the liquid is ionized at the electrode and ions are then injected into the bulk liquid. In that case, the injected charges are of the same polarity as the electrode from which they are injected. Both low and high electric fields can be employed for EHD pumping, and the voltage applied can be either DC or AC. Due to different electrochemical behaviour of the liquid at the two electrodes, one of them is favoured for creation of

ionic charges. This permits directional flow and thus pumping of the liquid. Moving the ionic charges and the friction process within the liquid then moves the whole liquid. The space charge around the electrode varies both with the distance between the two electrodes and with the liquid properties.

In induction EHD pumps, the charges are induced in the liquid. If a temperature gradient exists in a slightly conducting liquid, a conductivity gradient will be obtained as well. According to Maxwell's equations, a gradient in permittivity or conductivity is necessary to have free charges in the liquid. These free charges, and thus the whole liquid, can then be transported by using a constant electric field. In order to avoid the additional heat generation within the micropump, a second mechanism allows for the induction of charges within the liquid. Waves of electric fields travelling at the right angle to a liquid/solid interface induce free electric image charge in the liquid at the interface. These charges travel in synchronism with the potential waves, but lag behind because of charge relaxation effects. If the propagation velocity of the travelling wave is too slow, then very little charge is induced. If the propagation velocity is, on the other hand, too fast, the image charge is only slightly displaced from the potential waves. Thus there is an optimum velocity which produces maximum pumping.

A planar travelling-wave EHD pump has been fabricated by Bart [41]. It consists of polysilicon bars, which are 10 microns wide, 1.75 microns thick, and 10 microns spaced. Every third electrode is connected together, and the three-phase voltage is applied to the electrodes to produce a travelling electrostatic wave in a direction normal to the polysilicon bars. For silicone oil (σ = 10-12 S/m), pumping was visually observable at the frequencies below 2 kHz, and it was even greater at frequencies lower than that. Similar system of electrodes was reported by Fuhr, where a four-phase voltage was used to generate the travelling electric field above electrodes made of chrome and gold (gold or platinum is required in this case, to prevent electrolyte reaction on the electrodes in the aqueous salt solution).

In summary, this section gives an overview of the pumping technologies on the microscale. From the point of view of Doctor-on-a-Chip, the non-mechanical pumps depicted above probably do not meet the needs, because of the large area they occupy on the chip and the large voltage needed for operation. The large voltage is especially unsuitable for portable handheld devices, and it could also negatively impact the analysis due to interaction with the sample containing

negatively charged DNA molecules. As far as the active micropumps are concerned, those with actuation principles based on temperature changes (thermopneumatic and bimetallic) are not suitable due to the potential impact these temperature changes can have on the DNA molecules. For a similar reason, electrostatic pump might be unsuitable if the electric field used for deflecting the diaphragm ends up having an impact on the negatively charged DNA molecules in the sample (which might be the case if the pumping chamber is not completely isolated from the electric field). The micropump based on the pneumatic actuation principle is inadequate due to the need for an external pump to achieve diaphragm deflection, which complicates integration of this pump together with the rest of the analysis system on a single chip. The piezoelectrically driven micropump might be suitable due to the simplicity of the fabrication process and low interaction with the sample. In chapter 4, the micropump based on this actuation principle is chosen for Doctor-on-a-Chip, to achieve both pumping and mixing of the liquids at the same time (again, the pump has two inlets and is therefore capable of accepting two different liquids). In the pumping chamber, due to the diaphragm deflections, the liquids are mixed, and pumped out of the chamber and into the channel towards the areas of subsequent analysis steps. The pump is shown in figure 2.23, and has three diffusers/nozzles to ensure that liquid is pumped out of the chamber always in the same direction, while maintaining simple valve-less design that is relatively easy to manufacture.

2.3. Polymerase chain reaction (PCR)

This section gives an overview of polymerase chain reaction (PCR), which is a well known technique that allows reproduction of a single DNA strand to a billion of identical copies. The overview of the basic PCR techniques is followed by an overview of micro-systems for PCR analysis.

2.3.1. Overview of PCR

Polymerase chain reaction (PCR) multiplies a single DNA strand to a billion of identical copies in a short period of time, depending on the implementation of PCR and the volume of a sample [36]. It is a very sensitive process that can copy DNA in a sample of the density as low as a few copies of DNA per millilitre. PCR multiplication greatly increases reliability of the DNA analysis, and many DNA

techniques could not be imagined without it. PCR amplification requires target DNA, primers (or short single stranded DNA molecules that designate the sequence the PCR needs to copy), an enzyme, and a mixture of nucleotides or nuclear acid building blocks which are used to synthesize the new DNA.

Before the PCR process takes place, the primers of about 20 bases long have to be synthesized in order to define the sequence of the target DNA to be amplified in the process. This implies that the sequences that lie on both ends of the given region of interest have to be known prior to PCR, but we do not have to know the DNA sequence in between. With the careful design of the primers, the length of the sequence to be amplified and the size of the synthesized DNA particles can be defined. This can be useful in the subsequent steps of the analysis (for example the DNA separation by dielectrophoresis), as will be described in chapter 4.

Figure 2.28 shows three steps in PCR amplification that are repeated 30 to 40 times to achieve the multiplication factor of 10^6 to 10^9 [36]. Firstly, the PCR mixture is heated to about 95 ºC to denature the target DNA, i.e. to break the hydrogen bonds between the two strands and separate them. Secondly, the temperature is lowered to about 65 ºC to permit the primers to bind to their complementary sequences. It should be noted that the two complementary strands will always bind to the corresponding primers and not to each other, due to high concentration of the primers.

Finally, in the third step the temperature is raised to just over 70 ºC and the DNA polymerase catalyses the formation of the complementary strand between the two spots marked by the primers. The new strand, or the new nucleotide chain, is built out of the nucleotides from the mixture. The DNA polymerase used in PCR is a special heat-tolerant enzyme called Taq polymerase. As a result, after the third step, there are two double stranded DNA molecules, and each of those can serve as a template for the next cycle. The PCR amplification process is of exponential nature and theoretically the number of copies of the target sequence after n cycles is expressed by $(2^n - 2n)x$, where x is the number of copies of the original template. However, the amplification is never a 100% efficient process due to a number of factors that act against it. Therefore, as stated above, 30 to 40 cycles that are performed increase the number of target DNA molecules by a factor of 10^6 to 10^9.

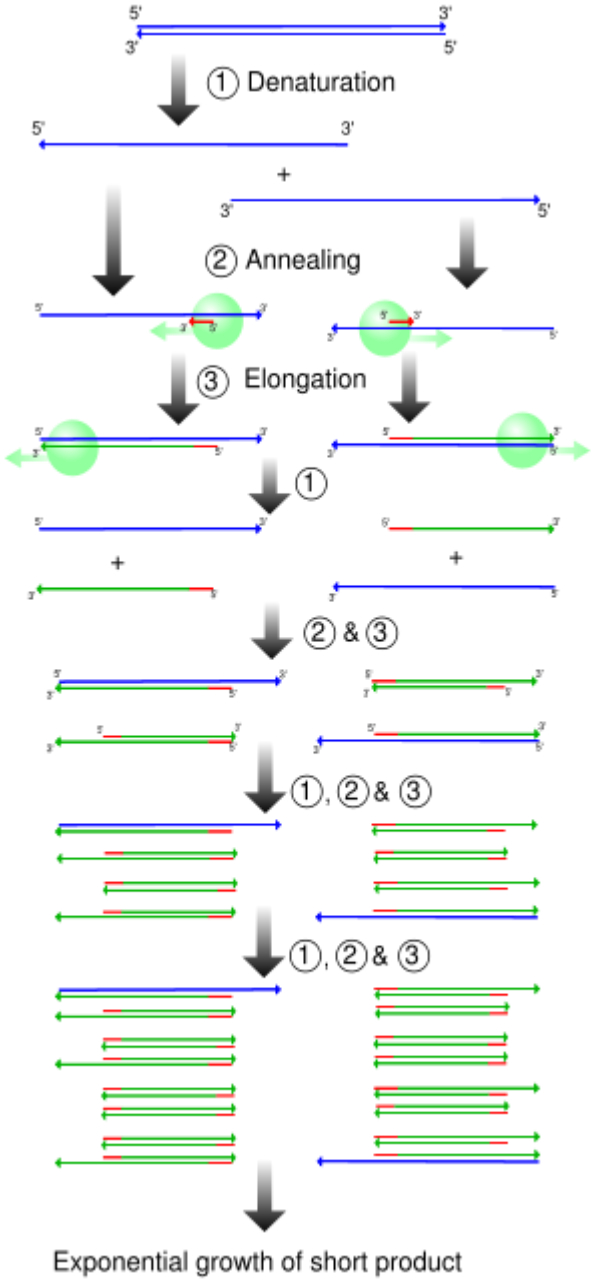

Figure 2.28. PCR multiplication : (1) Denaturing at 94-96°C, (2) Annealing at ~65°C, and (3) Elongation at 72°C [36]

It is also possible to target PCR multiplication of different DNA sequences at the same time in the same PCR chamber, by adding more primers to the reaction mixture to target each sequence [280-283]. This process is called multiplexing or multiplex PCR. The advantages of multiplex PCR are the ability to perform multiple PCR experiments on a small sample volume (sometimes there is not enough DNA available to perform multiple standalone PCR amplifications), low cost, and faster

overall analysis [281]. In reality, setting up multiplex PCR is a challenge, because the complexity of the amplification process increases exponentially with each additional primer. One of the most important requirements for multiplex PCR to work properly is compatibility of the primers in terms of their temperature of annealing and the complementarity of their sequences. The latter needs to be carefully taken into account to avoid excessive binding between primers instead of the target DNA and to avoid false negatives if different primers block each other during the target DNA amplification [281, 282]. In general, it is important to balance the concentration and size of the primers so that the PCR product also yields balanced concentrations of amplified target sequences. Moreover, if the PCR product is analyzed by using electrophoresis or dielectrophoresis, the primers need to be designed such that separation of different amplified target sequences is possible with sufficient accuracy [282].

Implementation of PCR onto a microchip has several advantages over standard laboratory PCR techniques. An example of a closed chamber PCR chip has been reported in [30]. There are also many other solutions, some of which will be described in section 2.3.2. The microfabrication technology allows the fabrication of a chamber with the volume in a submicron range, which in general increases the speed of PCR due to reduced thermal mass of the PCR mixture. It has been reported that it took a PCR chip with 1 μl chamber only 2.5 minutes to perform 30 cycles of PCR [29], which is very fast compared to tens of minutes for laboratory PCR. The mixture is heated with platinum heaters fabricated on the chip and placed underneath the bottom of the chamber. The heaters are driven by the outside circuitry with very low power consumption. All the materials used for the PCR chip fabrication have proved to be bio-compatible.

From a commercial standpoint, the disadvantage of PCR is that many existing patents surrounding this technology make other potential methods of DNA amplification very attractive as lucrative business ventures [284-286]. The most promising alternatives to PCR are isothermal DNA amplification methods, which have recently attracted many researchers [284-289]. The main advantage of these methods, as is apparent from their name, is the fact that the DNA amplification happens at a constant temperature, thus eliminating the need for thermal cycling and reducing complexity from the heating standpoint. The most common isothermal amplification methods are nucleic acid sequence-based amplification (NASBA),

strand displacement amplification (SDA), and loop-mediated isothermal amplification (LAMP). NASBA is geared more towards RNA amplification, as it is performed at a relatively low temperature of 37 °C, which is insufficient to denature the DNA double helix. SDA is performed at the same temperature, but is useful as DNA amplification method, as it uses a mixture of four primers and two specific enzymes to take advantage of the strand displacement effect for target DNA amplification. LAMP is the most popular of the isothermal DNA amplification techniques, and it is developed to overcome the relatively low target specificity of NASBA and SDA. LAMP is carried out at 65 °C, and uses a specific combination of primers and polymerases to increase the specificity of the amplification by recognizing six different sequences of the target DNA. Although isothermal amplification techniques show promise for the future commercial applications, the research is still undergoing to bring it up to speed with the PCR amplification methods [286-287]. The major disadvantages include low generality of the isothermal methods, lack of readily available kits, and much more increased complexity of the amplification process in the case of multiplex analysis, when compared to multiplex PCR.

In conclusion, PCR is nowadays the most common method for DNA amplification, and is used in many different scientific and commercial fields, such as medicine, environmental screening, forensics and others. Successful implementation of PCR on a portable chip, both as a standalone product and as a part of an integrated device, offers great market potential.

2.3.2. Microsystems for PCR

Miniaturized PCR has become very important and are widely used to replicate DNA, as described in section 2.3.1. Miniaturization of PCR devices leads to many improvements [47-74]:

- Decreased cost of fabrication and use,
- Decreased time of DNA amplification,
- Reduced consumption of biological sample necessary for PCR;
- Reduced production of PCR products;
- Increased portability and integration of the PCR device;
- Acceptable disposal of the PCR reaction vessel; and

- Avoidable cross-talk of the PCR reaction.

In addition, large numbers of parallel amplification analyses on a single PCR microfluidic chip can lead to more accurate information and greater understanding necessary for some particular bioassays, which are difficult, unpractical, or even impossible to perform on a macro-scale PCR device. Much smaller PCR reaction vessels can increase resolution while reducing the overall size of the PCR device, but effects related to the nonspecific adsorption of biological samples to the surfaces of the vessel may become significant as a result of the increased Surface-to-Volume Ratio (SVR) upon miniaturization, which may inhibit PCR amplification.

Most of the chips designed for PCR on a micro scale utilize either silicon or glass as the material for the substrate, in which the microfluidic network necessary for sample and reagents manipulation is built [e.g. 47, 73, and 75]. The reason these materials dominate the PCR microchips design is that there are well established methods of photolithography and chemical etching, which can be conveniently and effectively used to create microfluidic elements. Silicon is currently dominating as the material of choice for these applications, but there are also an increasing number of glass chips, due to some limitations in silicon [60]. For example, although silicon's ability to conduct heat very well is desirable for the PCR process (as the heat can be efficiently transferred from the heating elements to the chamber), it is also a drawback, because too large heat conductivity of the substrate may cause a significant drop of the PCR mixture temperature, which in turn requires additional isolation of the chamber and hence larger cost of production. Silicon is also a non-transparent material, which inhibits optical detection of the PCR product. If used in the combination with electrophoresis or electroosmotic pumping, silicon's electrical conductivity also presents a problem. Finally, it has been noted that, as a substrate material, silicon inhibits the PCR amplification process, and sometimes it is even possible that there won't be any amplification at all, due to the reaction at the silicon surface. All of these problems with silicon have raised the number of applications in which glass is used as a material of choice for PCR chip substrate. Glass has some advantages over silicon, such as well-defined surface chemistries, superior optical transparency, and good EOF characteristic, which has triggered the integration of PCR and capillary electrophoresis separation on a monolithic glass chip or on a hybrid silicon/glass chip.

However, the PCR microfluidics made of silicon or glass are not disposable due to the higher cost of fabrication [60]. Furthermore, the majority of problematical issues in silicon/glass microfabrication processing may ultimately hinder their wide use in commercial applications. Although no single substrate material can offer a preferable solution to all these restrictions including cost, ease of fabrication, disposability, biocompatibility, optical transparency, etc., polymers might show their superiority over silicon/glass and become the very promising substrate materials for PCR microfluidics [61-65]. Currently, many research groups have taken a great interest in the development of polymer-based PCR microfluidics, and therefore all kinds of polymer-based PCR microfluidics have been reported. Differences in production methods between glass, silicon and polymerase PCR chips is given in the literature, but it falls outside of the scope of this text.

As far as the PCR method on the chip is concerned, there have been several different approaches to heating and cooling reported [47-74]:

- Closed chamber PCR amplification works in the same manner as the conventional PCR devices, where the PCR solution is kept stationary and the temperature of the PCR reaction chamber is cycled between three different temperatures. After completion of the PCR reaction, the amplification products are recovered from the chamber for off-line detection or are detected in an on-line way. The heat is generated by microelectrodes placed just outside of the chamber. For example, in [52] they are placed underneath the bottom of the chamber. By applying the right voltage to the electrodes, the temperature inside the chamber is well controlled. This format of PCR microfluidics can be separated into two groups, namely *single* and *multi* chamber microfluidics. Single chamber devices can perform very well in terms of fluid and thermal control, and they present beneficial properties such as reduction of thermal and fluidic cross-talk between PCR reaction micro-chambers. However, they are not suitable for high throughput PCR. Instead, many sequential PCR experiments will be needed in case of a number of DNA samples to be amplified to meet the detection requirement. Furthermore, there is the risk of carry-over from one experiment to another, or, in other words, the possibility of incomplete

amplification or partial failure if these PCR amplifications are performed in the same chamber.

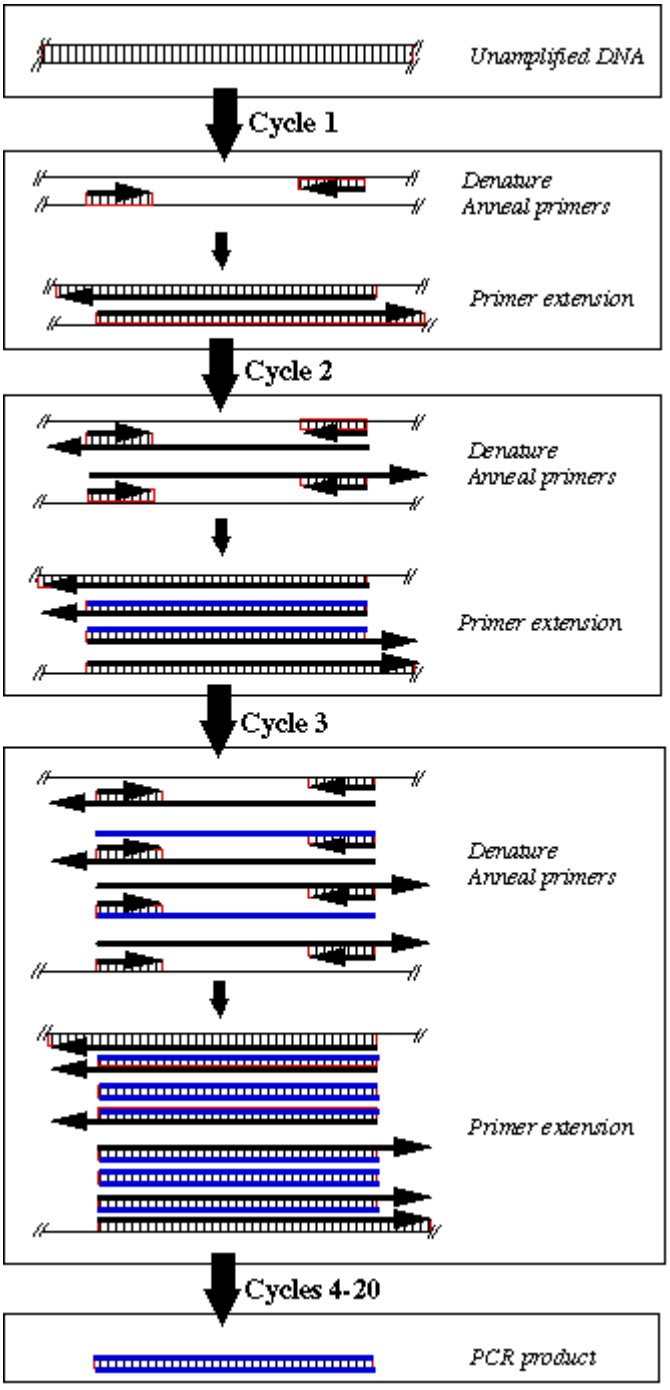

2.29. Thermal cycles in PCR [72]

On the other hand, multi-chamber PCR chips [48] improve the PCR throughput and reduce the analysis time, as well as the required labour (due to the introduction of a robot to inject the sample). Nevertheless, special care must be taken during the design of a chamber array in

order to acquire temperature uniformity between chambers. Without a careful design to assure temperature uniformity and the elimination of any possible differences in amplification, reliability, repeatability, sensitivity, efficiency and specificity of PCR amplification across the different chambers may be compromised. In addition, handling and processing of small sample volumes in the case of the increasing number of PCR reaction chambers on a single chip pose real challenges. The resulting issues are loss of sample on the walls of transferring devices, loss by evaporation, loss of components from the sample during manipulation, and possible loss of sample resulting from the immediate contact of the PCR solution with chamber walls.

- Continuous-flow PCR chips [72] address the problem of static closed chamber devices not being able to change the reaction rate, as there is always a certain amount of time needed to heat and cool the mixture. The continuous-flow devices are based on a time–space conversion concept, where, instead of being stationary in a chamber, the PCR solution is continuously and repeatedly flowing through the three different temperature zones necessary for PCR amplification. This is depicted in figure 2.30.

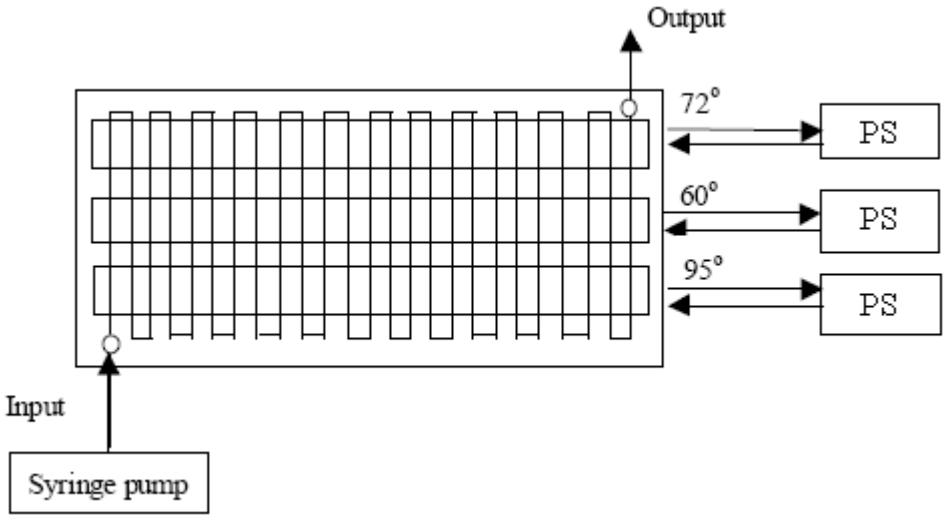

Figure 2.30. Diagram of a continuous-flow PCR chip [72]

The advantages of this concept are much faster amplification (order of minutes) due to rapid heat transfer, low possibility of cross-

contamination between samples, high potential for further development of a chip by incorporating many functionalities, etc. A significant limitation of this approach is the fixed number of cycles, which is dictated by the channel layout. Continuous-flow PCR devices might have different layout of microchannels, e.g. straight capillary channels, serpentine channels (such as shown in figure 2.30), or circular channels [72].

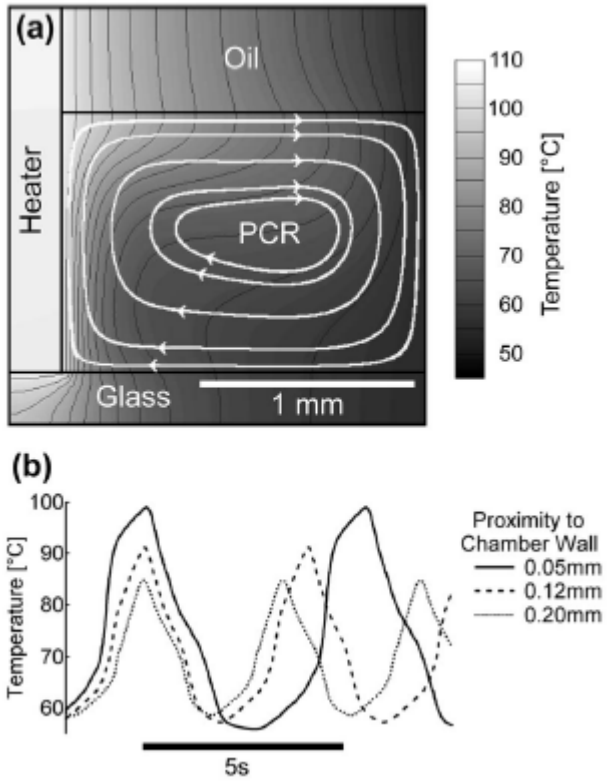

Figure 2.31. Thermal convection-driven PCR amplification process [73]

- Thermal convection-driven PCR chips [71] are similar to the continuous-flow chips described above in a sense that the PCR solution passes through different temperature zones to obtain heating and cooling cycles. However, instead of using a pump as the source of the external pumping force, the PCR solution is transported from one area of the chip to another by means of buoyancy forces. Because the external pumping is not necessary, the design is simpler and cheaper for mass production, and does not require any electronic control circuits, as cavity/loop is the only requirement. One example of a

device employing thermal convection-driven PCR method is shown in figure 2.31. The chip consists of an open vessel in which a micro immersion heater is dipped to heat the PCR solution. The convection chamber into which the heater is dipped consists of 1.75 mm thick silicone rubber sheet with a 4 mm hole. The chamber bottom is thermally connected to a temperature controlled aluminium stage. In figure 2.31.a, the heater is on the left hand side and next to it a simulated convection flow is drawn through the different temperature zones. In figure 2.31.b we can see that the reaction is relatively fast, as it takes only about 5 seconds for the complete cycle of heating and cooling.

For PCR chips, another important aspect is the ability to integrate the PCR method with other methods for manipulation, separation and detection of DNA molecules. One example of this is integration of PCR with DNA hybridization reaction, which is a selective reaction taking place between target DNA sample and a DNA probe [e.g. 46]. The probe is complementary in sequence to the fragment of DNA to be detected, and thus it can selectively hybridize to the correct fragment of DNA. The principle of DNA microarrays is that the advances in microfabrication technology have made it possible to miniaturize the DNA probe detection method. One obvious advantage of DNA microarrays is to allow thousands of specific DNA sequences to be detected simultaneously on a very small silicon/glass/polymer wafer. The fragment of DNA to be detected is usually first fluorescence-labelled and PCR amplified, and then hybridized with the probe by sample loading or microfluidic technology. To take advantages of the superiority of PCR microfluidics and DNA microarrays, a highly integrated microfluidic device has been developed on an 8 x 40 x 70 mm polycarbonate wafer smaller than a credit card, which is capable of extracting and concentrating nucleic acids from millilitre aqueous samples and performing microlitre chemical reactions, serial enzymatic reactions, metering, mixing and nucleic acid hybridization [46]. When PC is selected as a substrate material, the two ways have been taken into consideration: not only can it provide excellent thermal isolation to meet the requirement of independently controlling different temperature zones on a single chip but it can also be fabricated inexpensively as a low cost disposable thus avoiding any possibility of cross-talk

contamination. One of the parameters for optimal PCR process is the thickness of the PC wafer, which is optimized to achieve reasonable thermal cycling rates.

Another example of integration of PCR on a multi-process chip is PCR integration with sample preparation [62]. This kind of integration is regularly done to prevent failure of PCR due to chemical interference. Although an on-chip preparation step is not always necessary for successful PCR amplification, it is usually required when using environmental or otherwise complex samples, such as whole blood samples. This is because a variety of contaminants can inhibit PCR. It is noted, however, that only few attempts have been made to run PCR directly from crude blood and cell samples, lessening the need to integrate the sample preparation functionality with the PCR microfluidic module. On-chip sample preparation is much faster and requires smaller sample consumption over off-chip manual sample preparation, which is time-consuming, poorly portable and requires multiple expensive laboratory instruments. However, it still takes a longer time to perform on-chip sample preparation on a microfluidics chip, compared to performing the PCR and capillary electrophoresis on the same chip. Thus the PCR sample preparation may become a bottleneck. So far reported integrated chips include integrated dual-purpose chips for performing cell isolation and PCR. These were developed in glass-silicon hybrid chips, in which a series of 3.5 microns feature sized coiled/linear silicon microfilters with short flow paths were used to effectively separate white from red blood cells. They were then used for the amplification of a 202 base pairs sequence of exon 6 of the dystrophin gene directly from genomic DNA in filtered white blood cells. However, drawbacks of this system were that sample injection, cell isolation, and PCR amplification were not carried out on a single chip, thus resulting in the increased risk of sample loss or contamination. Moreover, some manual operations were still required for the analysis. The improvement of the same chip was Plexiglas-based module for the complete integration of blood sample preparation and PCR. This module simplified the nucleic acid analyses and it proved to be a simple way of assessing microfluidics prior to the microchip fabrication. There are also several ways reported on how to filter the PCR mixture to facilitate the amplification process and reduce the possibility of contamination. There are several methods for pre-PCR sample pre-preparation, which are all based on 3-D non-electrophoretic mechanical filtering methods [49-51, 55, 61]. For this purpose, electric fields can also be used. The

dielectrophoretic effect has been used as a selective filter for holding cells in a microsystem, so that the PCR inhibitors can be washed out of the system to increase the sensitivity of the PCR amplification. This method has been successfully used for the preparation of parasitized cell micro-samples related to malaria [70]. The combination of dielectrophoretic force and fluid flow fractionation is used to isolate malarially-infected erythrocytes from the other ones, so that only these will be subject to DNA isolation and purification. This will facilitate the PCR amplification process of the desired DNA sequence. The diagram of the chip is shown in figure 2.32.

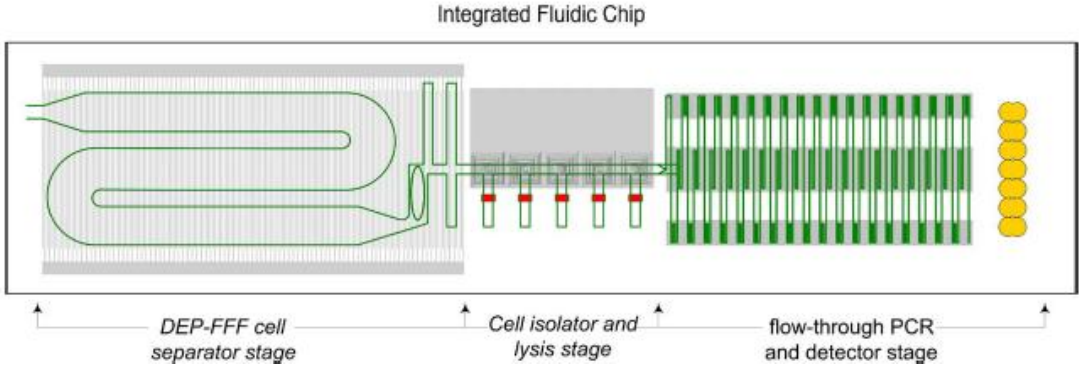

Figure 2.32. Integrated DNA isolation, purification, and PCR amplification [70]

The dielectrophoretic approach to selective filtration has several advantages: (1) there is no need for antibody and hence no changes of biological properties of cells due to the antibody reaction will occur, (2) the electric fields are non-destructive for cells, and the nature of cell growth and splitting will not alter, (3) the electric field strength, frequency and phase are easily controlled and thus the automation of the process is facilitated, and (4) dielectrophoresis can be coupled with other methods, such as fluid flow fractionation in this case, to acquire an optimized separation effect. Some disadvantages of dielectrophoresis are the limits imposed on conductivity and pH of the fluid carrying the cells (the dielectrophoretic flow has a huge dependency on the suspending medium), cell lysis or sample heating that may occur when applying the electric field (e.g. even cell destruction might occur if the setup is not right), and adhesion of cells to the electrodes.

Another and probably the most common operational component integrated with PCR on a single microfluidic chip is capillary electrophoresis, which forms the PCR-CE integrated microfluidic chip allowing for the on-line separation and

detection of PCR products [e.g. 55]. The theoretical advantages of performing CE in a miniaturized channel (or capillary) may be evaluated by the single determinants of separation efficiency given as $N / (t * d^2)$, where N is the so called "number of theoretical plates", t is the analysis time, and d is the capillary diameter. This means that the separation efficiency per unit time is inversely proportional to the square of the capillary diameter, and indicates the potential of microfluidic technologies to greatly improve the performance. There are many types of microfluidic devices with a certain degree of functional integration reported in the literature. They can be fabricated either on glass, polymers, silicon, or as hybrid chips (e.g. silicon and glass). There are several aspects to the PCR and CE integration. Firstly, the microheater and the temperature microsensor can be coupled to the PCR microchips leading to a decreased thermal mass of the system, as compared with commercial thermocyclers used in PCR-CE chips, allowing for the rapid heating rates of over 10 °C/s. Furthermore, the microfabricated resistance temperature detector can be placed within the reaction chamber, allowing for a more accurate temperature measurement. Another advantage is saving the total DNA analysis time by parallelizing or multiplexing the DNA amplification on a single micro-device. Also, the sensitivity of the PCR amplification of the total systems can be enhanced to the level of detecting a single DNA copy, which will facilitate studies of expression from individual cells and genetic heterogeneity. In addition to that, other functional components have been incorporated into PCR-CE systems to form a more complete analytical microfluidic chip, such as sample loading by valves and hydrophobic vents, cell lysis, and on-chip DNA concentration through a porous, semi-permeable polysilicate membrane, allowing further reduction of the analysis time by decreasing the number of thermal cycles. In addition, inexpensive polymeric materials may have taken an increasingly important role in fabricating PCR-CE integrated microfluidics, taking advantage of the superiority of polymeric materials in optics, electrical insulation, microchannel surface charge and fabrication cost.

2.4. On-chip DNA detection methods

This section covers the DNA detection methods suitable for integration onto microchips [113-142]. Traditionally, DNA detection was performed on a macro-scale in laboratories using well established optical read-out arrangements. These

techniques rely on experienced and well trained personnel to perform the read-out on extremely expensive laboratory equipment. With advances in microfabrication technologies, the emphasis of the research in DNA detection methods has shifted toward various techniques deployed on a microscale, which allows for integration of the detection method of choice into the system that already contains extraction, purification, PCR amplification and other analytical techniques in DNA analysis. Several different detection methods (with numerous variations) have been reported in the literature. Here, some of the most important concepts will be described.

Optical detection methods

Optical detection method reported in [128] relies on fluorescence microscopy. It is a well known and tested method heavily used on a macroscale, which allows efficient detection of a single DNA molecule in a sample volume of several femto-litres. Miniaturization of this method is not a straightforward task, because it requires ultra-sensitive low-noise photodiodes with on chip filters. In the literature, the fabrication of silicon-based photodiodes with on-chip interference filters have been integrated onto electrophoresis columns for detecting fluorescence signals from labelled DNA samples. The detectors were developed for DNA band detection in micro-electrophoresis columns and could detect double stranded DNA in concentrations up to 10 nanograms per microlitre. However, the detector sensitivity needs to be further improved in order to sense low concentrations of DNA while performing high-resolution separations or real time PCR. Diode response to fluorescent signals can be significantly improved by enhancing photocarrier generation in the active region and by increasing the collection efficiency of the generated photocarriers. The DNA analysis device consists of two parts:

- Silicon side which includes the heaters/temperature sensors and the photodetectors, and
- Glass side which has the fluidic network.

The glass side is glued onto the silicon side to render an integrated microfluidic device. Several photodetectors can thus be incorporated very close to the microfluidic channel at desired locations. Figure 2.33 shows the experimental setup for testing the device. Filtered (blue) light from a LED is used to excite DNA

samples (stained with fluorescence dyes) inside a microfluidic channel. The fluorescent light signal is collected by the photodiode in the silicon substrate. Photoinduced voltages were measured using a HP multimeter that was interfaced to a computer with a LabView program.

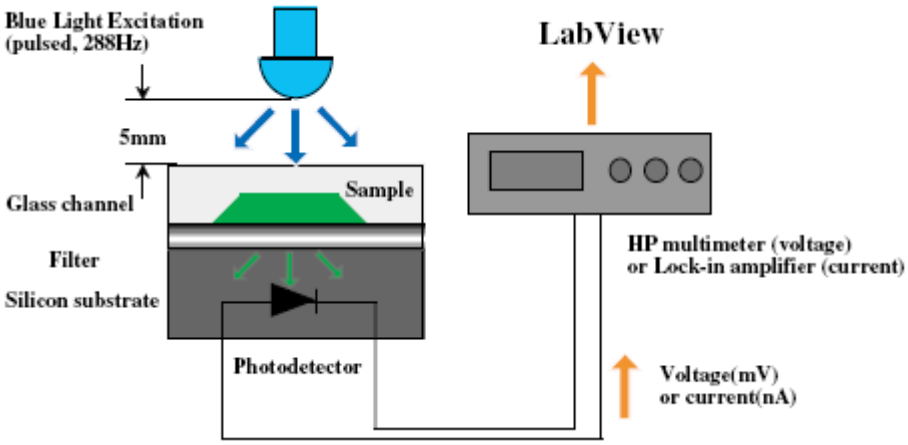

Figure 2.33. Experimental setup for on-chip fluorescence detection [128]

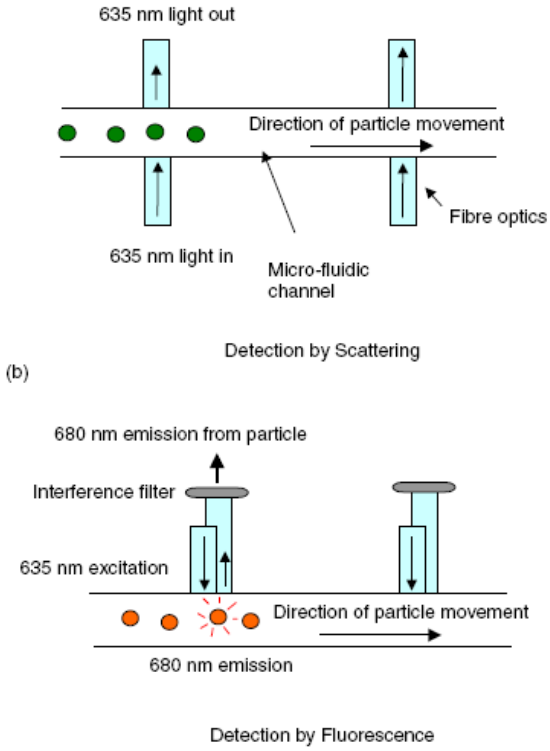

Figure 2.34. The principle of the particle detection system [139]

Another reported method for optical detection of DNA molecules based on fluorescence uses the travelling wave dielectrophoretic effect integrated with fiber

optics [139]. The schematic diagram of the method is shown in figure 2.34. The system can be used to detect the particles which are either fluorescent or not. If the particles are not fluorescent (figure 2.34.a), the light passes through the fiber optics and gets scattered when the particles are passing in the travelling electric field. The scattered light is detected by a photodiode.

In case of the fluorescent particles, they are excited by the light of an appropriate wavelength. The emitted light, which is of longer wavelength, is transmitted via a detection fibre and an interference filter (680 nm), to a photodiode for detection. In this way, the number of moving particles can be detected by looking at signals detected by the photodiode, providing that they do not overlap as they pass the detection point. If the time is measured for the particle to move from one detection point to the next, its velocity can be easily calculated. Figure 2.35 shows a schematic diagram of the particle analysis chip. A suspension of particles (cells or latex spheres) is suspended in a carrier medium and introduced into the device using a syringe pump. Under optimal conditions fractionation of the particles occurs. The optical fibers for interrogating the particles are embedded in channels fabricated in the base plane of the device as shown in the figure. The device is encapsulated with a transparent lid to assist with particle observation.

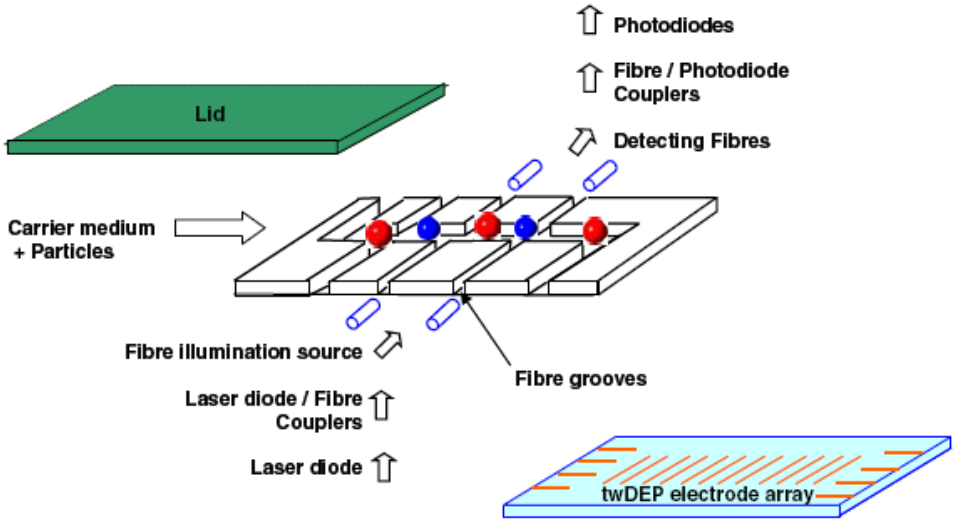

Figure 2.35. Schematic representation of the integrated particle analysis chip [139]

Impedance measurement methods

Another way of detecting particles in integrated micro-analysis systems is impedance measurement [137, 138, and 141]. In such systems, the particles under

observation are brought to the microelectrodes by means of the force acting upon them. The force in question can be dielectrophoretic in nature, and the electrodes that are used for impedance change measurement due to the arrival of particles can also be the source of the highly non-uniform electric field needed for the dielectrophoretic effect to occur. Such system is described in [137], where the authors refer to the method as DEPIM (dielectrophoretic impedance measurement). The positive dielectrophoretic force is utilized to capture suspended biological particles onto an interdigitated microelectrode array in the form of pearl-chains. Higher cell concentration results in faster development of the pearl-chains, which are electrically connected in parallel to the electrode gap and hence increase the conductance and the capacitance between the electrodes. By monitoring the temporal variation of the electrode impedance, it is possible to quantitatively evaluate the cell population according to a theoretical model of cell collection process. DEPIM can realize fast and simple bacteria inspection by using only electrical phenomena and instruments. The process of detection can also be made selective of the particle population if the dielectrophoretic force on the population of different particles is tuned in a way that only the desired population will be attracted to the microelectrodes and have impact on the change of impedance. The dielectrophoretic force in general also serves to improve the sensitivity of the detection system, as the greater number of gathered cells at the electrode edges mean the greater impedance change, and hence the easier detection.

The sensitivity of the system can also be improved by using electropermeabilization, which the effect defined as a transient increase in the membrane permeability for components of the cell interior and the extra cellular medium such as various ions, proteins, drugs, DNA and RNA. It is expected that the electrical conductance of one biological cell may transiently increase if the intracellular ions are released by electropermeabilization after DEP cell trapping in the DEPIM protocol. In the case of DEPIM, the same electric field used for generating the dielectrophoretic force is also used for electropermeabilization (it can, however, be even further increased to improve the effect of electropermeabilization). This is illustrated in figure 2.36, which shows a schematic diagram outlining the principle of the DEPIM combined with electropermeabilization. Figure 2.36.a shows the preliminary dielectrophoretic trapping of cells at microelectrodes, 2.36.b shows electropermeabilization under

increased electric field, and 2.36.c shows release of the intracellular ions through the perforated cell membrane.

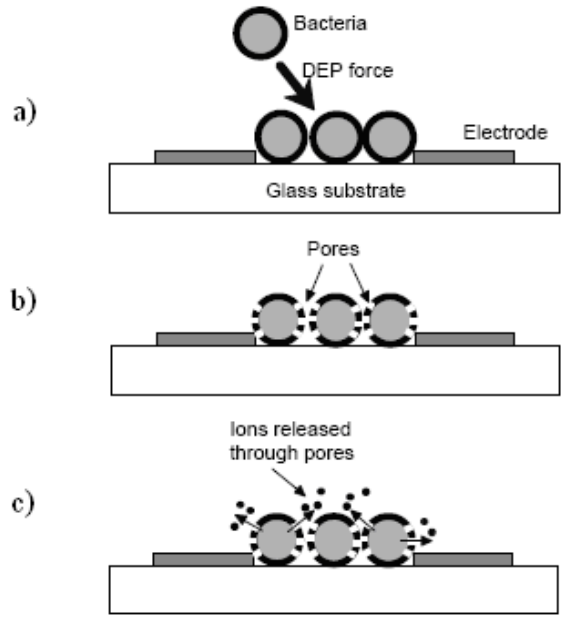

Figure 2.36. Schematic diagram of dielectrophoretic impedance measurement combined with electropermeabilization [137]

DNA detection based on amplification of gold nano-particles

Another method of detecting DNA is by labelling DNA with gold probes [e.g. 118, 120, 123, and 135]. The method of choice for detecting the labelled DNA in this case is the quartz crystal microbalance (QCM), which is a simple, cost-effective, high-resolution mass sensing technique, based upon the piezoelectric effect. In this case, the gold nanoparticles were used as mass amplifiers to improve the frequency signal of QCM detection of DNA.

As mass amplifier, gold nanoparticles can be linked to DNA by two approaches: one is the so-called direct labelling when nanoparticles are linked with thiol-modified oligonucleotides via Au–S bond. The other is indirect labelling when the nanoparticles are connected with DNA through a biotin–streptavidin conjugate. In the direct-labelling method, HSDNA is firstly incubated with nanogold and then hybridized with DNA probe immobilized on the gold surface of a quartz crystal. In

the indirect-labelling method, biotin–DNA is hybridized with a DNA probe on the gold surface of a quartzcrystal at first and then labelled with streptavidin–gold.

Both indirect and direct labelling of DNA probes with gold nanoparticles was studied in [135]. The frequency change of the indirect-labelling method achieved 105 Hz, and that of the direct-labelling method was about 39 Hz, which represents the difference of 2.7 times. Therefore, the frequency change of the indirect labelling method was much more significant than that of the direct-labelling method under the same hybridization conditions. The frequency decline of nonspecific adsorption was about 3 Hz.

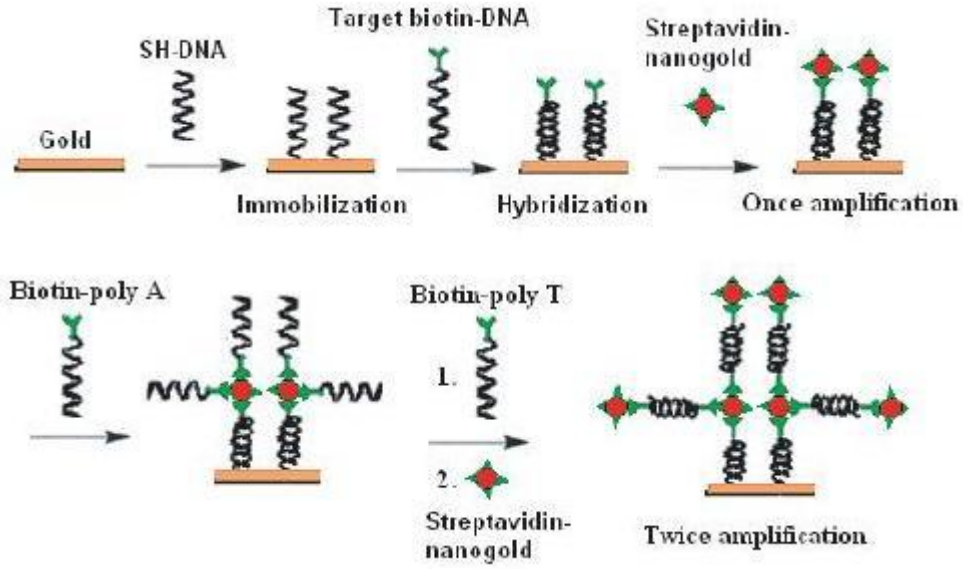

Figure 2.37. One-time vs. two-times amplification [135]

To further improve the frequency change signal, two-times hybridization amplification of gold nanoparticles was carried out. After one-time amplification of indirect-labelling hybridization, one layer of streptavidin–nanogold had been connected to the surface of the gold electrode. Then biotinpoly A (S1) was dropped to conjugate with streptavidin–nanogold at room temperature for 40 min. The second time of hybridization was performed by adding biotin-poly T (S2) solution onto the surface of a gold electrode. Finally, the second layer of gold nanoparticles was connected with streptavidin–nanogold conjugation. The sensitivity of two-times amplification detection proved to be one order of magnitude higher than that of one-time amplification detection. In the case of one-time amplification, the smallest detectable concentration of the target DNA was 100fM, and in the case of two-times

amplification it was as small as 10 fM. It was indicated that the two-times amplification detection can connect more gold nanoparticles and further improve the frequency decline signal, which results in the higher sensitivity. The schematic diagram of one-time versus two-times amplification is shown in figure 2.37.

Inductance based sensor for DNA detection

A method for DNA detection, which utilizes measurement of inductance change of the sample containing the target DNA due to the presence of magnetic beads, has been reported in [115]. The schematic diagram of such a sensor is shown in figure 2.38.

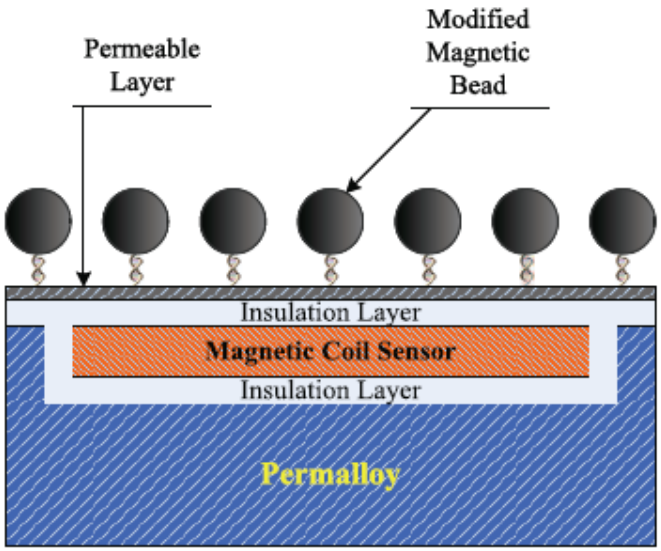

Figure 2.38. Schematic diagram of the sensor [115]

The core of the sensor is a planar spiral inductor, which is sandwiched between an insulating layer on the top and a layer of permalloy at the bottom. The probe DNA particles are attached to the surface and thus immobilized. When the target DNA with the magnetic beads attached to them is washed over the surface, the specific hybridization of the target DNA and the probes occurs. This will result in formation of an immobilized layer of magnetic beads right above this surface. This layer has high magnetic permeability and together with the underlying permalloy layer forms the magnetic core and completes the magnetic circuit. This in turn increases the coil inductance, which serves for detection of the hybridization process. In the paper, the numerical model of the sensor is presented and different

physical parameters were discussed in order to maximize the sensor sensitivity by optimizing the dimensions and thicknesses of different layers. This, however, falls outside the scope of this thesis.

To summarize the DNA detection methods from the point of view of Doctor-on-a-Chip, the methods which measure impedance and inductance changes in the system to detect DNA molecules are much more suitable compared to the optical detection methods, which require expensive equipment and thus increase both complexity and cost of the analysis. Measuring impedance or inductance changes should be simple to produce and integrate onto the chip that performs the analysis, and should also be sufficiently sensitive and robust to achieve dependability of the system. In the next chapter, the overview of the Doctor-on-a-Chip device is given with the proposal to use inexpensive and dependable method of detecting DNA molecules based on the measurement of impedance changes at the detection spots due to the presence of DNA molecules.

To summarize, this chapter gave the extensive overview of the microfluidic technology and, in particular, the aspects relevant to Doctor-on-a-Chip. The chapter started with the overview of the DNA analysis systems available to date, both surface based and microfluidic based. Since Doctor-on-a-Chip is a microfluidic chip, the extensive overview was given of different microfluidic components used for on-chip manipulation of liquid, such as mixers, valves, and pumps. Different methods of implementing PCR on a chip and different DNA detection methods suitable for on-chip integration were also analysed, to give a complete picture of microfluidic technologies crucial for Doctor-on-a-Chip concept development.

Chapter 3. Dielectrophoresis

This chapter gives an overview of the dielectrophoretic theory and practical examples of using dielectrophoresis for particles manipulation in microsystems. The first part of the chapter covers theoretical description of the dielectrophoretic effect, together with some of its most important aspects, such as dipole moment of the polarized particle, complex permittivity, and dielectrophoretic force and torque. The second part of the chapter gives an overview of practical examples of usage of dielectrophoretic traps, travelling wave dielectrophoretic arrays, electrorotation chambers, and other types of microelectrode systems that were successfully used to manipulate micro- and nano-particles in a repeatable and controllable manner.

As stated in chapter 1, the objective of this research is to investigate the possibility of manipulation of DNA molecules by using dielectrophoresis (DEP), and the possibility to integrate a system of microelectrodes for dielectrophoretic manipulation of DNA molecules onto a microfluidic chip, which would perform all of the steps in the analysis of a sample to detect pathogen DNA.

In general, one of the common and most important tasks in biochemical processes is manipulation, separation and/or concentration of sub-micron particles [145]. There are many techniques that can be used for this purpose, which include optical tweezers, lasers, magnetic sorting, filtration, and different approaches using electric fields [e.g. 143, 145]. Many of these techniques have already been implemented on microchips and used in research and commercial applications. Of the techniques using electric fields, the most common for many years have been electrophoresis and electroosmosis, which are based on DC electric fields. Only recently the effects of manipulating sub-micron particles in AC electric fields have drawn attention of researchers. The effect of dielectrophoresis has been described for the first time in 1970s [146], and then it was thought that the effect will not be usable for sub-micron particle manipulation due to high electric field strengths required in that case. As will be shown in section 3.1, the DEP force is proportional to the particle's volume, and until late 1990s the microfabrication technology was not capable of producing microelectrodes with such small features that the electric AC field strength of the order of magnitude of MV/m could be achieved with small

voltages. Hence, it was thought that any DEP effect would be masked inside the electric field due to induced electrohydrodynamic pumping of the suspending liquid.

However, with advances in microfabrication technologies, it is today possible to produce microelectrodes with spacing of order of magnitude of one micron and below. If two microelectrodes are spaced 1 micron apart and a voltage of 1V is applied between them, the electric field strength is 1 MV/m, which is shown to be sufficient to trap sub-micron particles with dielectrophoresis. Numerous publications have shown results of successful manipulation of genomic DNA, biological cells, viruses, bacteria, and artificial sub-micron particles in such small systems of microelectrodes [e.g. 143-211].

3.1. Theoretical background of dielectrophoresis

3.1.1. Dielectrophoretic force on a dipole

Dielectrophoresis (DEP) is the term used to define the translational motion of neutral matter caused by the polarization effects in a non-uniform electric field [15]. This effect is illustrated in figure 3.1, which compares the behaviour of the charged and neutral body in a non-uniform electric field.

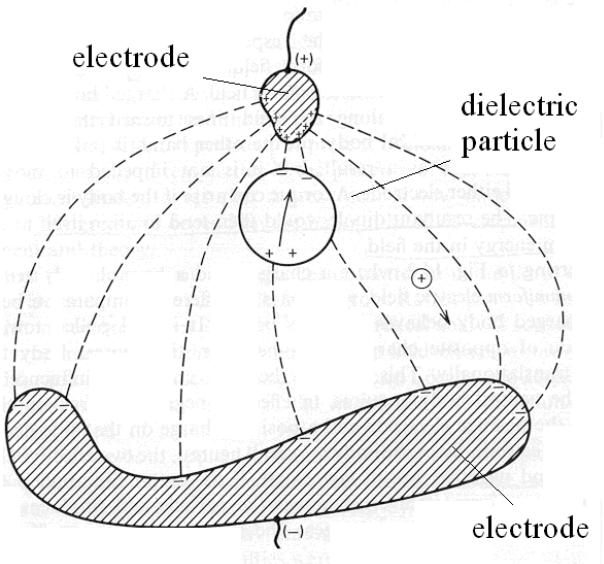

Figure 3.1. Dielectrophoretic effect [15]

If a charged body is placed inside the electric field, it experiences the force that tends to move the body towards the electrode with the opposite charge. The

neutral body, however, will experience the effect that is essentially different. Under the influence of the electric field, the neutral body becomes polarized (several types of polarization are described in the literature [e.g. 15]). In effect, it acquires the negative charge on the side nearest to the positive electrode and the positive charge on the side nearest to the negative electrode. Since the body is overall neutral, these charges are equal, and since the field is non-uniform and diverges across the particle, the forces on these two charges are unequal and the neutral body will tend to move. The direction in which the body will move does not depend on the electric field direction, so dielectrophoretic effect can be observed both in DC and AC electric fields. Usually, AC fields are used because in this way the influence of the polarisable particle's charge on its electrically induced movement is reduced [145].

As depicted in figure 3.1, the polarized body can be analyzed as a dipole, with equal and opposite charges $+q$ and $-q$ located a vector $\vec{d}$ apart. The dipole is located in a non-uniform electric field described with the vector $\vec{E}$. If we assume that the dipole does not influence the given value of the electrical field strength in its vicinity, the force on the dipole will be equal to the sum of the two forces acting on the positive and on the negative charge of the dipole:

$$\vec{F}(\vec{r}) = q\vec{E}(\vec{r} + \vec{d}) - q\vec{E}(\vec{r}) \tag{3.1}$$

Here, $\vec{r}$ is the position of the negative charge –q. If $\left|\vec{d}\right|$ is much smaller the characteristic dimension of the electric field non-uniformity, equation (3.1) can be simplified as follows. The electric field vector can be expanded about position $\vec{r}$ using the vector Taylor series expansion:

$$\vec{E}(\vec{r} + \vec{d}) = \vec{E}(\vec{r}) + \vec{d}\nabla\vec{E}(\vec{r}) + ... \tag{3.2}$$

In the previous equation, the additional terms, of order d^2, d^3, and so forth, have been neglected, so that equation (3.2) can be written as:

$$\vec{F} = q\vec{d}\nabla\vec{E}(\vec{r}) \tag{3.3}$$

The dipole moment of a polarized particle is given as

$$\vec{p} = q\vec{d} \tag{3.4}$$

By combining equations (3.3) and (3.4), the dielectrophoretic force on a particle with a dipole moment $\vec{p}$, which is placed in a non-uniform electric field $\vec{E}$ at the position given by a vector $\vec{r}$, equals

$$\vec{F} = \vec{p}\nabla\vec{E}(\vec{r}) \tag{3.5}$$

From equation (3.5), we can see that the dielectrophoretic force on a polarized particle is equal to zero if the electric field is uniform. This equation is an approximation of the DEP force on a particle, because we have neglected the size of the particle when compared to the characteristic dimension of the electric field non-uniformity. This approximation is sufficient for the imposed force calculation, because the assumption that we make about the particle size is valid in practice [146-147]. However, for situations in which we have a collection of particles that interact between them, the equation might lead to a significant error, because the non-uniformities of the electric field induced by the particles are comparable to their dimensions. Then the higher order effect must be taken into account [149-150, 153].

3.1.2. Dielectrophoretic torque on a dipole (electrorotation)

The effect of electrorotation occurs when a dipole moment vector of a polarized particle in the electric field does not align in parallel to the field vector [148]. This effect is due to torque that the particle exhibits around its centre. In accordance with figure 3.2, there are two contributions to this torque, one per each charge:

$$\vec{T} = \frac{\vec{d}}{2} x q\vec{E} + \frac{-\vec{d}}{2} x(-q\vec{E}) = q\vec{d}x\vec{E} \tag{3.6}$$

If we use the dipole moment vector equation given with equation (3.4), the torque on the particle is given by:

$$\vec{T} = \frac{\vec{d}}{2} x q\vec{E} + \frac{-\vec{d}}{2} x(-q\vec{E}) = \vec{p}x\vec{E} \tag{3.7}$$

From equation (3.7) we can see that the torque on a particle depends on the electric field vector curl, and not its gradient, which means that the torque can be present

even in a uniform electric field. The only requirement is that the dipole moment vector and the field vector are not in parallel. If that is the case, it will take a finite amount of time for a particle to re-align with the field vector if the direction of that vector changed. Hence, if the electric field vector constantly changes direction, it will cause the particle rotation, as its dipole moment will always tend to re-align with the field.

3.1.3. Complex permittivity

Complex permittivity describes the frequency dependent response of the dielectric particle to the electric field [147]. Some dielectric media are ideal, i.e. loss-free, and have a constant permittivity, but this is not true for most of them. The non-ideal dielectric media are called lossy, and their polarization depends on the frequency of the applied electric field. For a parallel plate capacitor with an ideal dielectric between its plates, the impedance is given by the following equation:

$$Z = \frac{1}{i\omega C} \tag{3.8}$$

Here, ω is equal to $2\pi f$, where f is the frequency of the electric field, i is $\sqrt{-1}$, and C is the capacitance of the dielectric. If the dielectric is lossy, the impedance is given by:

$$Z = \frac{1}{1/R + i\omega C} = \frac{R}{1 + i\omega RC} \tag{3.9}$$

Here, R is the resistance of the lossy dielectric, and the equation is the same as if it describes the resistance R connected in parallel with the ideal capacitance C, which is a common representation of a lossy dielectric. If we use the equation for a parallel plate capacitor whose capacitance is given by the plate surface area and the distance between the parallel, we get the following:

$$C = \tilde{\varepsilon}\frac{A}{d} \tag{3.10}$$

Here, A is the plate surface area, d is the distance between the plates, and $\tilde{\varepsilon}$ is the complex permittivity given by:

$$\tilde{\varepsilon} = \varepsilon_0 \varepsilon_r - i\frac{\sigma}{\omega} \tag{3.11}$$

Here, ε_0 is the absolute permittivity of vacuum, ε_r is the relative permittivity of the dielectric, and σ is the conductance of the dielectric. The equation for Gauss law of charge conservation is given for the lossy dielectric as:

$$\nabla\left(\varepsilon + \frac{\sigma}{i\omega}\right)\vec{E} = 0 \tag{3.12}$$

Here, ε is equal to $\varepsilon_0\varepsilon_r$ and represents the total permittivity of the dielectric. Since the electric field vector is complex, in general case, the permittivity should also be treated as complex wherever it makes sense to do so.

3.1.4. Induced effective dipole moment of particles

Real systems in which particles are manipulated by using electric fields often consist of a number of dielectrics with different electrical properties [e.g. 150, 153]. The dielectric particles are usually suspended within a dielectric fluid in such systems. When the electric field is applied, the surface charge accumulates at the boundaries of these different dielectrics due to their different dielectric properties [147]. Since the polarisabilities of the dielectrics are frequency dependent, the surface charge accumulation is also a frequency dependent effect. Hence the analysis of the overall force on particles and the calculation of the particles' effective dipole moment must be conducted by using complex permittivities.

The simplest case is that of a single homogenous dielectric sphere suspended in a homogenous dielectric medium. The derivation of the equation for the effective dipole moment of the particle in this case is given in [15]. The result is given by the following equation:

$$\vec{p} = 4\pi\varepsilon_m\left(\frac{\tilde{\varepsilon}_p - \tilde{\varepsilon}_m}{\tilde{\varepsilon}_p + 2\tilde{\varepsilon}_m}\right)a^3\vec{E} \tag{3.13}$$

Here, ε_m is the permittivity of the suspending medium (i.e. fluid), ε_p is the permittivity of the particle, a is the radius of the particle, and E is the electric field strength. It should be noted that the notation is different for real and complex

permittivities in this case: $\tilde{\varepsilon}_m$ is the complex value of the medium permittivity, and ε_m is the real part of that complex permittivity. The same notation will be used throughout the text.

Sometimes the equation for the effective dipole moment of a particle is simplified, and includes the volume of the particle. For example, for a spherical particle, the equation is given as:

$$\vec{p} = v\tilde{\alpha}\vec{E} \tag{3.14}$$

Here, *v* is the volume of the particle, and $\tilde{\alpha}$ is the effective polarisability of a sphere given as:

$$\tilde{\alpha} = 3\varepsilon_m \left(\frac{\tilde{\varepsilon}_p - \tilde{\varepsilon}_m}{\tilde{\varepsilon}_p + 2\tilde{\varepsilon}_m} \right) = 3\varepsilon_m \tilde{f}_{CM} \tag{3.15}$$

Here, f_{CM} is the Clausius-Mossotti factor, which is often used to describe the frequency dependence of the polarisability of particles.

$$\tilde{f}_{CM}\left(\tilde{\varepsilon}_p, \tilde{\varepsilon}_m\right) = \frac{\tilde{\varepsilon}_p - \tilde{\varepsilon}_m}{\tilde{\varepsilon}_p + 2\tilde{\varepsilon}_m} \tag{3.16}$$

Figure 3.2 shows the plot of the variation of the real and imaginary parts of the Clausius-Mossotti factor with the frequency of the applied voltage.

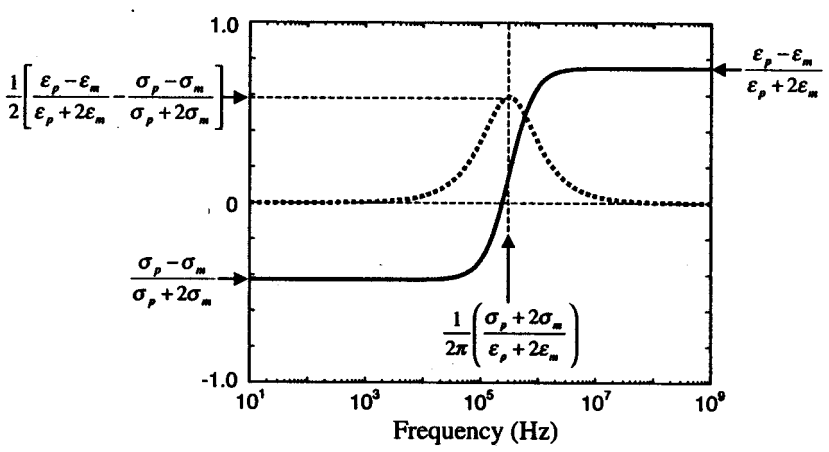

Figure 3.2. Real and imaginary parts of the Clausis-Mossotti factor [15]

The real part depends solely on the conductivity of the medium and the particles at low frequencies. At the high frequencies, the permittivities of the particles and the medium are the dominating factors. On the other hand, the imaginary part has a value of zero at low and high frequencies, but reaches a maximum at medium frequencies (order of MHz in figure 3.2). The reciprocal value of this frequency, also called the Maxwell-Wagner relaxation frequency, represents the relaxation time of the particles polarisability.

$$\tau_{MW} = \frac{\varepsilon_p + 2\varepsilon_m}{\sigma_p + 2\sigma_m} \tag{3.17}$$

Figure 3.2 shows the general case of a particle suspended in the medium with the AC voltage applied to a system of microelectrodes. In reality, the variation of the real and imaginary parts of the Clausius-Mossotti factor can show somewhat different shape when plotted against the frequency of the electric field. Figure 3.3 shows the case in which a latex sphere is suspended in water [146].

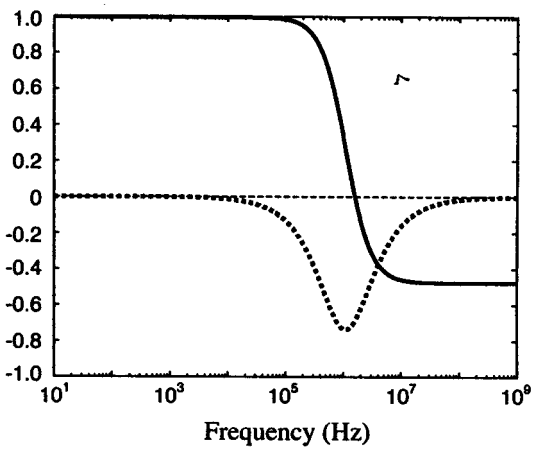

Figure 3.3. Real and imaginary parts of f_{CM} for a latex sphere suspended in water [15]

In this particular case, the particle conductivity is much larger than the medium conductivity, and the particle permittivity is much smaller that the medium permittivity. Therefore, the real part of the Clausius-Mossotti factor (solid line in figure 3.3) goes from the value of 1 at low frequencies to the value of around -0.5 at high frequencies. On the other hand, the imaginary part (dotted line in figure 3.3) is equal to zero at high and low frequencies, and the graph reaches minimum at about 1 MHz, where it is equal to around -0.75.

Similar to equation (3.15), which shows the effective polarisability of a sphere, equation (3.18) shows the effective polarisability of a homogenous dielectric ellipsoid with the half lengths of the major axes given as a_1, a_2, and a_3 [153-155]:

$$\tilde{\alpha}_n = 3\varepsilon_m \tilde{K}_n \tag{3.18}$$

Here, α_n is the effective polarisability given for each of the major axis, and therefore n can be equal to 1, 2, or 3. K_n is a frequency dependent factor similar to Clausius-Mossotti factor, and is given by:

$$\tilde{K}_n\left(\tilde{\varepsilon}_p, \tilde{\varepsilon}_m\right) = \frac{\tilde{\varepsilon}_p - \tilde{\varepsilon}_m}{3(A_n\tilde{\varepsilon}_p - \tilde{\varepsilon}_m) + 2\tilde{\varepsilon}_m} \tag{3.19}$$

Here, A is the depolarizing factor for the axis n, and is given by:

$$An = \frac{1}{2}a_1a_2a_3\int_0^\infty \frac{ds}{(s + a_n{}^2)B} \tag{3.20}$$

Here, s is the arbitrary distance for integration, and B is given as:

$$B = \sqrt{(s + a_1{}^2) + (s + a_2{}^2) + (s + a_3{}^2)} \tag{3.21}$$

Given equation (3.14) for the effective dipole moment and equation (3.19), the following equation can be used to calculate the effective dipole moment of ellipsoids:

$$\vec{p} = \frac{4\pi a_1a_2a_3}{3}\varepsilon_m\left(\frac{\tilde{\varepsilon}_p - \tilde{\varepsilon}_m}{\tilde{\varepsilon}_p + A_n(\tilde{\varepsilon}_p - \tilde{\varepsilon}_m)}\right)\vec{E} \tag{3.22}$$

More details about the behaviour of the ellipsoidal dielectric particles in AC fields, such as the particle orientation in the field due to torque, can be found in the literature [e.g. 161].

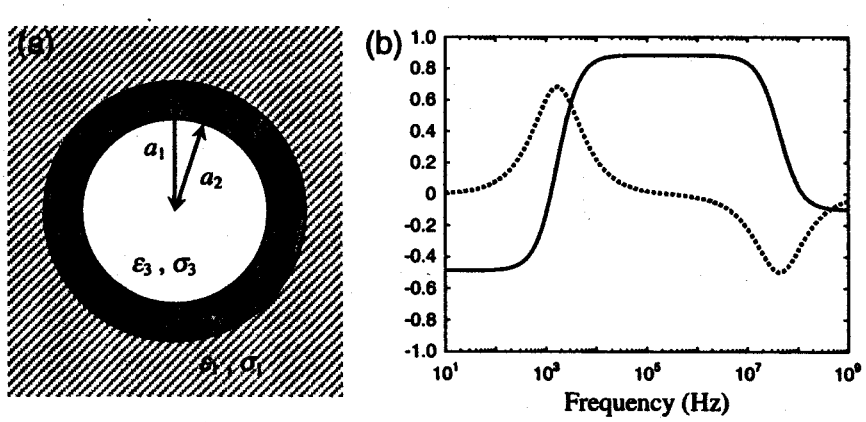

Figure 3.4. a) Schematic of a spherical particle with a single shell, b) The frequency variation of the equivalent f_{CM} with $a_1 = 2.01\text{x}10^{-6}$ m, $a_2 = 2.0\text{x}10^{-6}$ m, $\varepsilon_1 = 78.5\varepsilon_0$, $\varepsilon_2 = 10\varepsilon_0$, $\varepsilon_3 = 60\varepsilon_0$, $\sigma_1 = 10^{-4}$ Sm^{-1}, $\sigma_2 = 10^{-8}$ Sm^{-1}, $\sigma_3 = 0.5$ Sm^{-1} [161]

The two models given above for spherical and ellipsoidal particles in AC fields are not sufficient for modelling some biological particles with complex internal structures, such as cells and some viruses [161]. The most common approach in the literature is to model these particles by using shell models, in which particles are represented as concentric multi-shells surrounding each other. Each of these shells has different properties, and the boundaries between them represent the boundaries inside the cells where two different biological materials get into contact. The simplest shell model is shown in figure 3.4, where the particle is represented as consisting of two different types of materials and surrounded by a suspending medium. This shell model has two relaxation frequencies, one for each interface. The effective polarisability and the effective dipole moment are given by the following two equations:

$$\tilde{\alpha} = 3\varepsilon_m \left(\frac{\tilde{\varepsilon}_{12} - \tilde{\varepsilon}_m}{\tilde{\varepsilon}_{12} + 2\tilde{\varepsilon}_m} \right) = 3\varepsilon_m \tilde{f}_{CM} \tag{3.23}$$

$$\vec{p} = 4\pi\varepsilon_m a^3 \tilde{f}_{CM} \vec{E} \tag{3.24}$$

These equations are very similar to those equations above describing the spherical dielectric particles, but instead of the complex permittivity of a homogenous sphere, a more complex expression is used in the Clausius-Mossotti factor calculation, where the particle is represented by the following formula for complex permittivity:

$$\tilde{\varepsilon}_{12} = \tilde{\varepsilon}_1 \left[{\gamma_{12}}^3 + 2\left(\frac{\tilde{\varepsilon}_2 - \tilde{\varepsilon}_1}{\tilde{\varepsilon}_2 + 2\tilde{\varepsilon}_1} \right) \right] / \left[{\gamma_{12}}^3 - \left(\frac{\tilde{\varepsilon}_2 - \tilde{\varepsilon}_1}{\tilde{\varepsilon}_2 + 2\tilde{\varepsilon}_1} \right) \right] \tag{3.25}$$

Here, γ_{12} is the ratio between the outer and the inner shell radius, i.e. $\gamma_{12} = a_1/a_2$. The plots of the real and imaginary factors of the Clausius-Mossotti factor are shown in figure 3.4.b. As stated above, this shell model has one relaxation frequency per interface, and hence the real part graph (solid line in figure 3.4.b) shows two inflection points, and the imaginary part graph (dotted line in the figure) has one local maximum and one local minimum at these relaxation frequencies.

More complex shell models with two or more interfaces between different biological materials inside the particles can be found in the literature [161, 164-170], but fall out of the scope of this text.

3.1.5. Dielectrophoresis in AC fields

Compared to DC fields, dielectrophoresis in AC fields has several advantages [162, 172-181]. The most notable one is that AC fields of a sufficient frequency generate much less fluid pumping than DC fields of similar magnitudes. In practice, all of the experiments reported to have successfully manipulated particles in micron and sub-micron range have used AC fields. Therefore, the discussions in the following text will presume the usage of AC fields, and not DC fields.

If the voltage applied to the microelectrodes has a single frequency ω, all of the time dependent values in the system can be represented by phasors. At any point in space, the potential is given by:

$$\phi(\vec{x}, t) = \mathrm{Re}\left[\tilde{\phi}(\vec{x}) e^{i\omega t}\right] \tag{3.26}$$

Here, the vector *x* represents the position in space, and *Re* denotes the real part of the complex phasor of the potential, which is given by:

$$\tilde{\phi} = \phi_R + i\phi_I \tag{3.27}$$

Here, Φ_R and Φ_I are the real and the imaginary parts of the complex potential, respectively. Similarly, we can write the equations for the electric field:

$$E(\vec{x},t) = \mathrm{Re}\left[\tilde{E}(\vec{x})e^{i\omega t}\right] \tag{3.28}$$

Here, the tilde denotes the complex value of the electric field phasor given as:

$$\tilde{E} = -\nabla\tilde{\phi} = -(\nabla\phi_R + i\nabla\phi_I) \tag{3.29}$$

If the phase is constant across the system, the imaginary part can be neglected. In that case, by using the equations (3.5) and (3.14), the time-averaged DEP force becomes [e.g. 184]:

$$\langle F_{DEP}\rangle = \frac{1}{2}v\,\mathrm{Re}[\tilde{\alpha}]\nabla\left|\vec{E}_{RMS}\right|^2 \tag{3.30}$$

Here, E_{RMS} is the root mean square value of the electric field. Instead of the RMS value, we can use the amplitude of the electric field. Equation (3.30) shows that the DEP force is proportional to the volume of the particle and the gradient of the field magnitude squared. The force is also dependent on the permittivity and conductivity of the medium and the particle (through the effective polarisability given by equation (3.15) in the case of the spherical particle).

The real part of the effective polarisability defines the frequency dependence and the direction of the force. It can be shown that if the polarisability of the particle is greater than the polarisability of the medium, the real part of the effective polarisability (i.e. Clausius-Mossotti factor) is positive and the particles therefore move to the regions of high field strength. If the polarisability of the particle is less than the polarisability of the medium, the real part of the effective polarisability is negative, and hence the particles move towards the regions of the low field strength. These effects will be shown in section 3.2, when some practical experiments and results will be shown and analyzed.

In the case where multiple voltages with different phases are applied to the electrodes, the DEP force expression becomes more complex, as the imaginary part of the electric field cannot be neglected [184]. In that case, the equation for the DEP force calculation becomes:

$$\langle F_{DEP}\rangle = \frac{1}{2}v\,\mathrm{Re}[\tilde{\alpha}]\nabla\left|\vec{E}\right|^2 - \frac{1}{2}v\,\mathrm{Im}[\tilde{\alpha}]*\{\nabla x(\mathrm{Re}[\tilde{E}]x\,\mathrm{Im}[\tilde{E}])\} \tag{3.31}$$

Here, *Im* denotes the imaginary part of the complex value, in this case the effective polarisability. It is clear from equation (3.31) that if the imaginary part of the electric field phasor equals zero, the entire second term on the right hand side of the equation becomes zero, and equation (3.31) is equal to the equation (3.30). It should be noted that the second term depends on the imaginary part of the Clausius-Mossotti factor, and hence its value equals zero at high and low frequencies, and reaches its maximum at the Maxwell-Wagner relaxation frequency [146].

If the electrodes are of a suitable layout, the second term on the right hand side of equation (3.31) can represent the travelling wave electric field. This leads to the effect of the travelling wave dielectrophoresis (TWD), which can be used for particle transportation along the electrodes [185]. Generally, both of the electric field components need to exist for TWD to be effective:

- The particle is levitated above the electrodes to the regions of low field strength (i.e. the real part of the Clausius-Mossotti factor is negative), and
- The imaginary part of the Clausius-Mossotti factor is non-zero, and hence the particles experience the force of the travelling field wave.

Another effect that occurs in the electric field with the spatially dependent phase is electrorotation. The particle's dipole moment always tends to align itself with the electric field that induced it. After the dipole has aligned and the electric field vector has changed the direction, it will take a finite amount of time for the dipole to align itself with the field again. If the field vector continuously changes direction, i.e. if it is rotating, the particle will also rotate with it, since it will experience the torque, as already mentioned in section 3.1.2. The time-averaged expression for the electrorotation torque is given as:

$$\Gamma_{ROT} = \frac{1}{2}\mathrm{Re}[\vec{p}x\vec{E}^*] = -v\,\mathrm{Im}[\tilde{\alpha}]\left|\vec{E}\right|^2 \tag{3.32}$$

Here, the star symbol denotes complex conjugate. Similar to TWD, the electrorotation effect reaches its maximum at the Maxwell-Wagner relaxation frequency, and equals zero at low and high frequencies of the applied voltage.

3.2. Practical dielectrophoresis applications

Ever since nanotechnology has evolved enough to produce small microelectrodes capable of generating relatively strong non-uniform electric fields on a micron and sub-micron scale, dielectrophoresis has been a research topic in many different areas which involve manipulation and characterization of very small particles [146-209]. As nanotechnology advances even further, the potential of applicability of dielectrophoresis on even smaller particles greatly increases. The goal of many of these research efforts is controllability and reproducibility of the particle manipulation. This requires understanding and elimination of certain masking effects already described in this text. In this section, the most up to date efforts in the area of dielectrophoresis will be addressed, and many methods of using the dielectrophoretic force in practice will be shown, together with certain obstacles that the researchers need to overcome to reach a high level of controllability of dielectrophoretic manipulation of particles.

3.2.1. Concentration of particles within solutions

Probably the oldest practical application of the dielectrophoretic effect is concentration of small particles suspended in the fluid [e.g. 173]. As discussed in section 3.1, the dielectrophoretic force on particles is proportional to the real part of the Clausius-Mossotti factor and the gradient of the electrical field squared. Based on the polarity of the real part of f_{CM}, the dielectrophoretic force will act either in the same direction as the gradient of the electrical field squared (if the real part of f_{CM} is positive), or in the opposite direction. The polarity of f_{CM} depends on the frequency of the applied voltage and the permittivities and conductivities of the particles and the suspending medium.

In order for the particle concentration to occur, the electric field local minimum or maximum must exist somewhere in the system of microelectrodes. In these areas the gradient of the electric field squared, as well as the dielectrophoretic force on particles, equals zero. This is a necessity if the goal is to concentrate particles in certain areas, as this is feasible only in the areas where the force on particles diminishes (otherwise, the particles are constantly moving and it is difficult to concentrate them). Therefore, a system of microelectrodes for concentrating

particles must be designed in a way to generate the dielectrophoretic force on particles acting towards the local electric field minimum or maximum. When the particles reach this area, the dielectrophoretic force approaches zero, and the particles stop moving. If we turn off the electric field in the system, the dielectrophoretic effect does not take place any more, and the particles would again disperse around the system due to diffusion and Brownian motion. However, as long as the electric field is on, the dielectrophoretic force effectively keeps a wall around the particles concentrated in the area of zero gradient of the electric field squared. Hence they stay trapped as long as the force is strong enough to overcome other forces on particles.

The typical arrangement of microelectrodes for concentrating small particles is shown in the figure 3.5. These are so-called castellated electrodes. Their layout is such that the electric field distribution contains areas of minimum electric field strength and areas of maximum electric field strength. The former are found near the inner edges of the electrodes, and the latter near the tips (corners) of the outer edge of the electrodes. The electric potential of both electrodes is of the same magnitude and frequency, but of the opposite polarity.

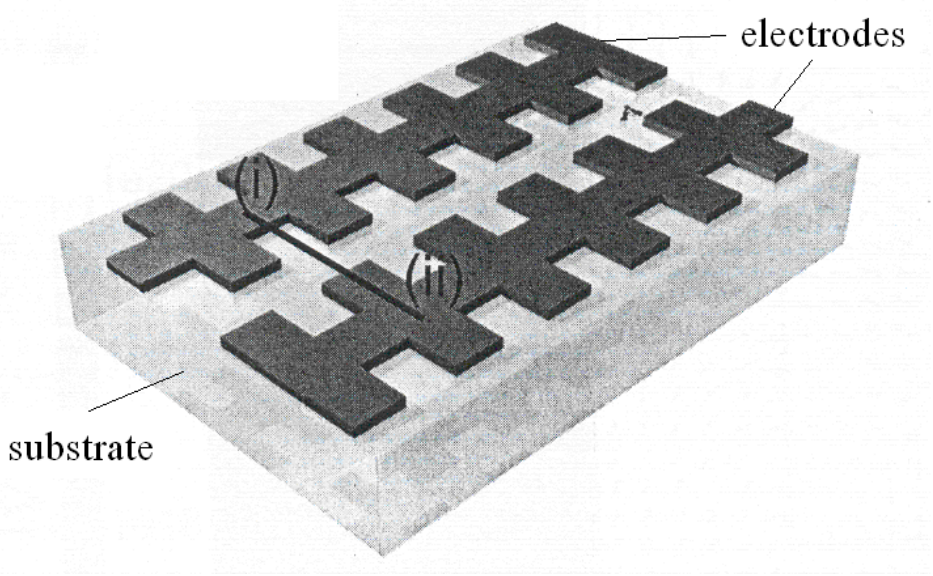

Figure 3.5. Castellated microelectrodes

The electric field distribution is shown in figure 3.6. In that figure, the distance between two electrodes is 5 microns, and the distance from the outer to the

inner edge of the same electrode is also 5 microns. The voltage between the electrodes is 1 volt, and the maximum electric field strength is about 0.5 MV/m.

Having both local minimums and maximums available in the resulting electric field distribution, this electrode arrangement is useful for separating different particles within the same mixture, and isolating a particle population from the others present within the same mixture. This method relies on the fact that, in general, different particles experience different dielectrophoretic forces, both in magnitude and direction. If the deterministic force on the particles (in this case the dielectrophoretic force) is dominant over the random forces (such as Brownian motion and the diffusion forces), the location of the particles is also deterministic, if all of the parameters defining the dielectrophoretic force are known.

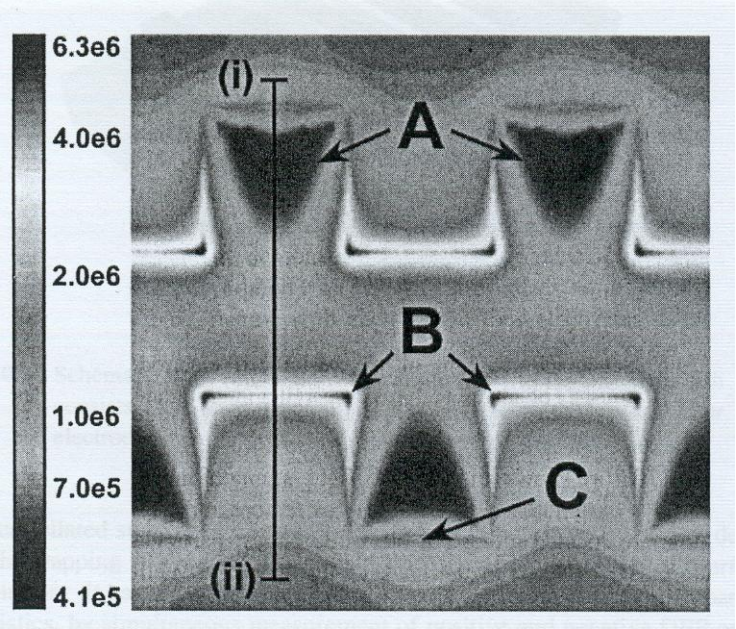

Figure 3.6. Electric field strength in V/m

Castellated microelectrodes have been successfully used for separation of two different particles populations in [194]. The experiments were performed within a system of gold microelectrodes fabricated on a glass surface. The particles in question were latex spheres 216 nm and 93 nm in diameter, which were suspended in 1 mM KCl suspending medium with the conductivity of 15 mS/m. An AC signal was applied to the electrodes to produce the dielectrophoretic effect. The voltage and frequency of the signal were variable. At frequencies above 500 kHz, the dominant force was the dielectrophoretic effect and the particles experienced the

positive dielectrophoretic effect. The fluid flow due to the electrohydrodynamic pumping was negligible at these frequencies, and the drag force on the particles was not observed. However, at the frequencies below 500 kHz, the fluid pumping became more apparent, with the schematic representation as shown in figure 3.7. The 216 nm particles were dragged towards the centre of the microelectrodes, as the fluid flow was perpendicular to the microelectrodes edges and perpendicular to the planar surface at the very centre of the microelectrodes. This effect became more apparent as the voltage was increased at the constant frequency, because the greater voltage means the greater fluid pumping force. The 216 nm particles were moving towards the regions were the dielectrophoretic force and the drag force (and possibly also the gravitational force) balanced each other. These particles were eventually pushed right in the centre of the microelectrodes at 100 kHz and 10 V peak to peak. At the same time, the smaller particles remained trapped at the microelectrodes edges, as in their case the dielectrophoretic force was dominant for the entire range of frequencies. This was due to the values of the Clausius-Mossotti factor for both populations.

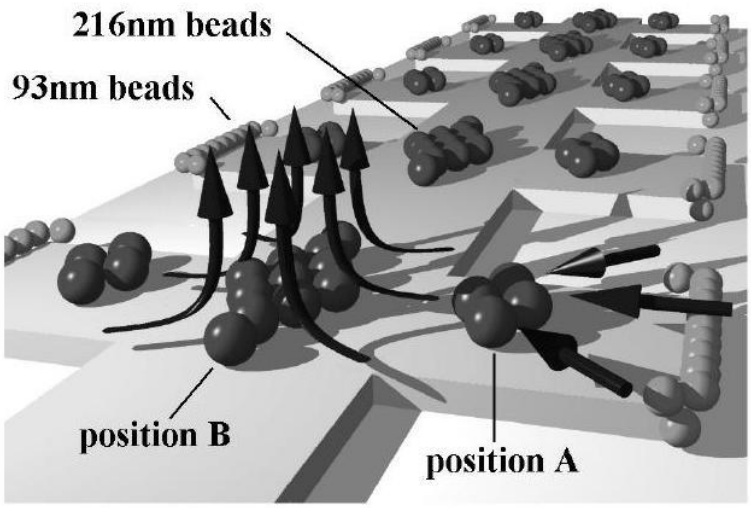

Figure 3.7. Separation of beads of different size [194]

Although the smaller particles have smaller volume and therefore would experience smaller dielectrophoretic force than the larger particles if all of the other factors in the equation for the force would be the same, they experience larger force due to the fact that their real part of the Clausius-Mossotti factor is about 20 times greater than in that of the larger particles, due to larger surface conductance. Overall,

the dielectrophoretic force on the smaller particles is approximately 1.5 times greater than in the case of the larger particles, and at the same time the drag force is about 2.5 times smaller. Therefore, the larger particles are dragged towards the centre of the microelectrodes and the smaller particles are trapped at the microelectrodes edges, resulting in the physical separation of the particles.

3.2.2. Dielectrophoretic trapping and manipulation of particles

As already stated many times in this text, the improvements of microfabrication technologies have enabled researchers to investigate sub-micron particles using dielectrophoretic techniques, as the microelectrodes can be fabricated with such small features that producing large enough electric field gradients is readily possible [145]. Certain microelectrodes configurations are capable of producing electric fields that can trap and manipulate single sub-micron and nanometre scale particles by using the negative dielectrophoretic effect. Such microelectrodes have a wide range of applications, such as viral infectivity studies, micromechanics, etc [145-147].

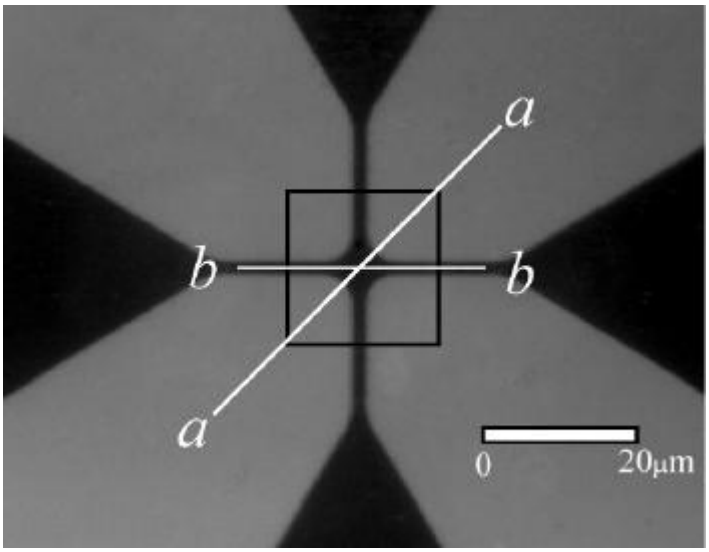

Figure 3.8. Dielectrophoretic trap [151]

Typical microelectrodes configuration for a dielectrophoretic trap is shown in figure 3.8. It consists of four electrodes, which in the centre can have a polynomial or a circular shape. These four electrodes are connected either to a four-phase voltage with each electrode having a unique phase applied to it, or a two-phase voltage such that two opposite electrodes share the same phase, while the

neighbouring electrodes have the opposite phases. In any case, a well defined region of potential energy minimum can be found at the centre of the trap, and the particles can be trapped there due to the negative dielectrophoretic force providing that the setup (the particles and suspending medium properties and the voltage frequency) ensures negative dielectrophoresis to occur.

An example of such setup of microelectrodes is reported in literature [151] to have been used for trapping the sub-micron particles such as herpes-simplex virion, herpes-simplex virus capsid, and a latex sphere. Their respective diameters were approximately 250 nm, 125 nm, and 93 nm. The microelectrodes were polynomial, with the 6 microns gap between the opposite electrodes and the 2 microns gap between the arms of the adjacent electrodes. The voltage applied to the microelectrodes was two-phase sine voltage with 5 V peak to peak and the frequency of 15 MHz. Such setup was used on all of the three collections separately, and when applied to the homogenous collection of particles, only a single particle was trapped after the voltage was applied. Although the voltage was still retained after that single particle was trapped, no other particle was observed to join it in the dielectrophoretic minimum (in all of the three experiments, different homogenous collections were used). The largest particle, herpes-simplex virion, was observed to stabilize at approximately 7 microns above the electrodes, probably due to the Brownian motion and the electrohydrodynamic pumping of the suspending medium (the EHD pumping was minimized with the usage of high frequency voltage, but was still present). In the case of the two smaller particles, herpes-simplex virus capsid and latex spheres, the isolated particle's position above the electrodes was impossible to measure accurately, as the particle was constantly moving within the minimum probably due to the two above-mentioned disruptive forces. The approximate z-position of the particles was estimated at 5-10 microns above the surface of microelectrodes.

To trap a particle successfully within the centre of the microelectrodes, the dielectrophoretic force on the particle must be strong enough to overcome any impulse that could potentially cause the particle to escape. The experimental method of trapping the particle was conducted in the way that the positive dielectrophoretic force was initially used to attract the particles within the medium towards the edges of the microelectrodes [151]. For this, the voltage frequency was set to 1 MHz. After the particles were concentrated in those areas, the voltage frequency would be

increased to 10 MHz, resulting in the negative dielectrophoretic force and trapping of the single particle at the centre of the microelectrodes. Due to the microelectrode configuration, the trap has an open top. In other words, if sufficiently lifted above the surface of microelectrodes, the particle could escape from the trap altogether. This is less likely to happen for larger particles (such as herpes-simplex virions in this experiment), as they are pulled down by the gravitational force. However, for smaller particles that experience neutral buoyancy (such as the latex spheres in this experiment), it is more likely that the particle could escape. The efficiency of the trap was discussed in the literature [151, 159] for the two distinctive cases: the trapped particle movement in the x-y plane, and its movement in the z-direction.

To estimate the movement in the x-y plane, two values are compared:

1) The time needed for the trapped particle to traverse a small region of thickness Δd over which the field gradient (and hence the dielectrophoretic force) is constant, and
2) The time needed for the particle to move the distance Δd due to the Brownian motion.

For the trap to be stable, the value under 1) should be significantly less then the value under 2). If we assume the factor of ten to render the trap stable, the value of Δd can be estimated by the following equation:

$$\Delta d > \frac{20kT}{F_{DEP}} \tag{3.33}$$

Here, k is the Boltzmann's constant and T is the temperature. For the spherical particle, the minimum particle radius for the trap to be successful can be estimated from the following equation:

$$r > \left(\frac{10kT}{\pi \varepsilon_m \Delta d \, \mathrm{Re}[K(\omega)] \nabla E^2} \right)^{1/3} \tag{3.34}$$

As usual, ε_m represents the medium permittivity and $Re[K(\omega)]$ represents the real part of the complex Clausius-Mossotti factor. It is obvious that the factors that contribute to the critical particle radius for stable trapping are the electrical field gradient and the distance across which the gradient exists, such that:

$$r \propto \frac{1}{\left(\Delta d \nabla E^2\right)^{1/3}} \tag{3.35}$$

In other words, the trapping efficiency is given as a maximum value of the function $\Delta d \nabla E^2$ for the particular trap.

Apart form the movement in the x-y plane, we can also observe the particle movement in the z-direction, perpendicular to the surface of the electrodes. The total force is given as:

$$F_{TOTAL} = F_{DEP} + F_{BROWNIAN} + F_{BUOYANCY} \tag{3.36}$$

In the case of stable trapping, the particle is forced upwards by the negative dielectrophoretic force, and pulled downwards by the gravitational force. The total force equals zero when these forces are in equilibrium. Since the total force is then a sum of the dielectrophoretic force and the buoyancy force, the following equation applies:

$$\mathrm{Re}\left[K(\omega)\right] 2\pi r^3 \varepsilon_m \nabla E^2 = \frac{4}{3}\pi r^3 \left(\rho_p - \rho_m\right) g \tag{3.37}$$

If the expressions on the right hand side and on the left hand side are reduced, equation (3.37) becomes:

$$\mathrm{Re}\left[K(\omega)\right] \nabla E^2 = \frac{2\left(\rho_p - \rho_m\right) g}{3\varepsilon_m} \tag{3.38}$$

Here, ρ_m and ρ_p are mass densities of the particle and the medium, respectively, and g is the acceleration under gravity. Equation (3.38) defines the condition which needs to be satisfied in order to lift the particle to a stable height within the trap. If the mass density of the particle is sufficiently high, the trap will be stable. However, if the medium density is comparable or greater than the particle's, the trap is unstable and it is possible that the Brownian motion would overcome the gravitational force and cause the particle to escape from the trap. To prevent that, sometimes the closed electrical field cages are used, such as described in the literature [174, 187].

3.2.3. Flow-through separation systems

The flow-through separation systems are used to separate different populations of particles from the mixture in the suspending medium. The particles and the medium enter the system of microelectrodes, and due to the differences in the dielectrophoretic force on the different particles, the separation occurs [172].

One example of such a system is depicted in figure 3.9. The two different populations of particles are suspended in the medium. This mixture has appropriate values of the particles and medium conductivity and permittivity, density and viscosity. The former two dictate the dielectrophoretic force on the particles, and the latter two dictate the sedimentation rate of the particles. If the setup is right, when the electric voltage is applied to the microelectrodes, one population of the particles will be pulled down towards the microelectrodes under the influence of the positive dielectrophoretic effect, and the other population will be subjected to the negative dielectrophoresis, pushed towards the middle of the channel, and carried out of the channel at the far end by the drag force of the moving liquid.

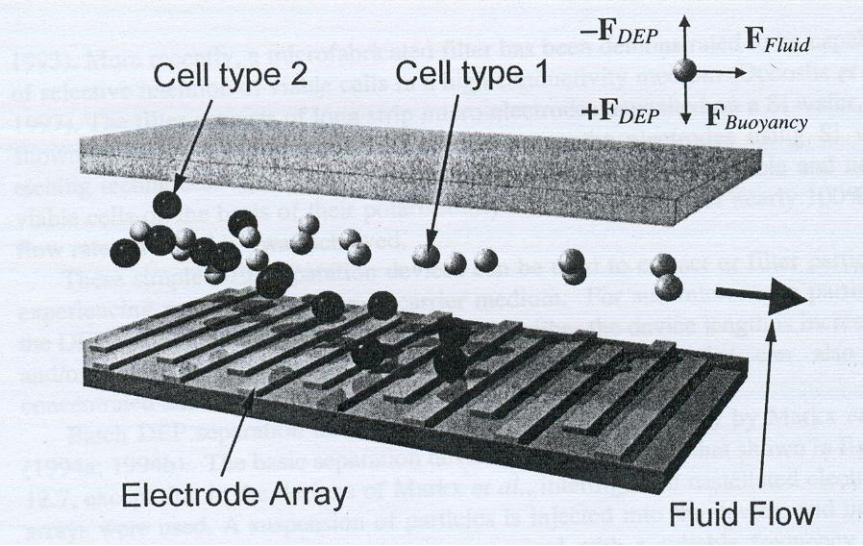

Figure 3.9. Flow through separation system [172]

This separation system is produced by depositing two different sets of microelectrodes onto the surface of the chamber, so that they form interdigitated arrays. The electric field distribution is such that the dielectrophoretic force decreases exponentially from the surface. The rate with which the particles accumulate at the electrodes due to positive dielectrophoresis is dependent upon the

dielectrophoretic force magnitude and the sedimentation rate. If the interactions between the particles themselves and the particles and the walls are ignored, the following equation describes the motion of the particles along the y axis:

$$m\frac{dv_y}{dt} = F_{DEP,y} + F_{Buoyancy} \tag{3.39}$$

In the x-direction (parallel to the surface of the microelectrodes), if the distance of the particles from the microelectrodes is sufficient, the only force acting on the particles is the Stokes force due to the movement of the fluid. It is reasonable to assume that the velocity of the particle equals the velocity of the medium at the location of the particle. The fluid flow profile adopts the parabolic shape. The total volume flow rate through the device is given in the literature as [172]:

$$Q = \frac{wh^3}{12\eta}\frac{p_0}{l_0} \tag{3.40}$$

Here, p_0 is the pressure drop and l_0, w and h are the length, width and height of the device, respectively. Ideally, all of the particles would be subjected to the same dielectrophoretic force and drag force, and hence gather at the same location within the system. In practice, the variations in the particles polarisability due to variations in the internal or surface properties lead to a distribution of the collection points across the different electrodes. Hence, any theoretical analysis of the particles trajectories should include a statistical component, which significantly affects the effort and the accuracy of the results.

Particle separators working on the abovementioned principles have clear limitations, such as limited throughput and the fact that the electric field extends only several microns or tens of microns into the carrier medium. Therefore, other methods for increasing the throughput have been investigated and developed. Some of them were based on different designs of microfabricated filters based on the dielectrophoretic effect. These filters were usually comprised of grid shaped microelectrode arrays [208] or long strip microelectrodes [212]. The latter were reported to have separated successfully viable and non-viable cells based on their polarisability, with the efficiency of nearly 100% at flow rates 100 ml/h.

However, the filter based separators do not work well in the case of sub-micron particles, as the dielectrophoretic force in these cases is much smaller and not sufficient enough for the filtering effect to take place. Hence, some alternative approaches have been reported. For example, batch dielectrophoretic separators were used to separate several different populations of particles mixed together in a single suspending medium. The approach is based on the interdigitated castellated microelectrodes. The particles were injected into the system and the fluid flow was turned off. The microelectrodes were energized and the frequency was tuned in a way that all the particles were attracted towards the microelectrodes under the influence of the positive dielectrophoretic effect. The fluid flow is then turned on and the frequency is swept until the value is reached for which only one population of the particles experienced the negative dielectrophoretic flow, while the other ones still experienced positive dielectrophoresis. The particles subjected to the negative dielectrophoretic force were pushed away from the microelectrodes and dragged from the system by the fluid flow. In this way, the first population of particles was separated from the rest of them. Then, the frequency was swept again until the value for which the next population of particles was subjected to the negative dielectrophoretic force, and in the same way as the first one, it was separated out from the system of microelectrodes. In this way, a whole range of micro-organisms can be successfully separated [193].

3.2.4. Fluid flow fractionation

The principle of separation of two or more populations of particles in the previous section was based upon one population of particles experiencing negative dielectrophoresis, and the other populations experiencing positive dielectrophoresis. The particles subjected to negative dielectrophoresis were pushed away from the microelectrodes and dragged away by the fluid flow. In the fluid flow fractionation system, the separation mechanism is based upon the fluid flow being the force for particle separation [e.g. 185]. In general, the particles are introduced into the medium in a channel, and the medium is moving through the channel from one end to another. The particles are distributed uniformly across the profile of the channel, providing there is no other force acting upon them. However, if the force is then applied upon the particles perpendicular to the flow, the equilibrium position is

disturbed and a new particles concentration profile is established. This new concentration is a function of some of the particles properties, such as charge, polarisability, etc (depending on the nature of the applied force).

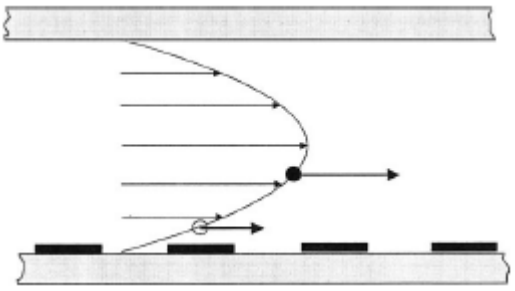

Figure 3.10. Dielectrophoretic force and fluid-flow-fractionation

If the dielectrophoretic effect is combined with the fluid flow fractionation, the process of particles separation is merely called the dielectrophoretic fluid flow fractionation, or DEP-FFF. In this case, a set of microelectrodes is deposited onto the bottom of the channel, as depicted in figure 3.10. An AC voltage is applied to the microelectrodes, and the polarisable particles suspending within the medium are suddenly subjected to the dielectrophoretic force. If the setup is such that the particles experience the negative dielectrophoretic effect, they will be pushed upwards and levitated. The fluid in motion will drag the particles outside of the channel, with the rate depending on the size of the particles and their height (as the fluid flow has a parabolic shape). Since the particles experience different dielectrophoretic and drag forces, they will be effectively separated at the channel exit. The advantages of such system when compared to the pure fluid flow fractionation are that the dielectrophoretic force on particles can be efficiently tuned with different physical properties of the medium (to increase the separation efficiency), and that the dielectrophoretic force levitates the particles above the surface of the microelectrodes, thus avoiding sticking of the particles to the surface.

If the dielectrophoretic force and the buoyancy force on the particles cancel each other to leave the particles in equilibrium, it can be shown that the height above the surface of the microelectrodes where the particle will be levitated can be calculated with the following equation:

$$y = \frac{d}{\pi} \ln\left[-\frac{24 V_0^{\,2} \varepsilon_m \,\mathrm{Re}\left[\tilde{f}_{CM}\right]}{\pi d^3 \Delta\rho g} \right] \tag{3.41}$$

Here, d is the distance between the interdigitated microelectrodes, and $\Delta\rho$ is the difference between the mass densities of the particles and the medium. This equation can be used to approximately calculate the needed physical properties of the setup to levitate the particles at a reasonable level.

The dielectrophoretic fluid flow fractionation method is suitable for larger particles, such as cells with relatively rapid sedimentation times, but is somewhat impractical for smaller particles such as viruses or micromolecules. To achieve the separation of such small colloidal particles, the dielectrophoretic force can be used to generate a flux of particles towards or away from the surface of the microelectrodes. This flux will be countered by a diffusion flux moving in the opposite direction, as the dielectrophoretic force increases the particles concentration in certain regions. In this was, the steady state particles distribution will be achieved, as shown in figure 3.11. The parabolic fluid flow profile will then fractionate the particles and separate them by the drag force towards one side of the channel [172].

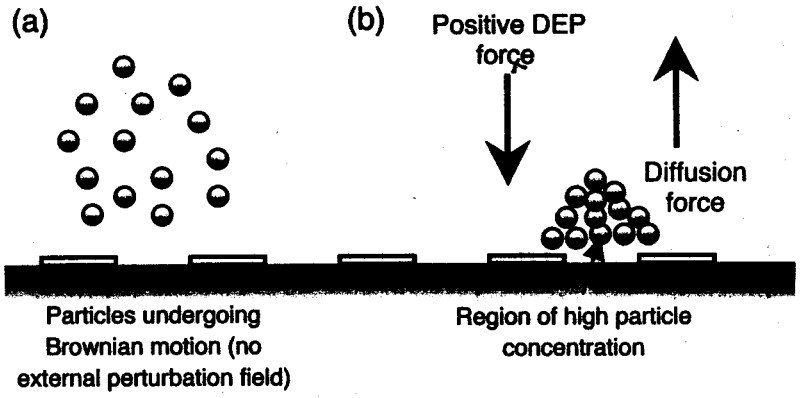

Figure 3.11. Illustration of the dielectrophoretic fluid flow fractionation method [172]

Similar to the dielectrophoretic field flow fractionation is the electrical field flow fractionation, or E-FFF. In this case, a DC field is used to perturbate the steady and random particles distribution by the electrophoretic force. However, this approach has several disadvantages compared to the dielectrophoretic field flow fractionation. For example, the voltage applied to the microelectrodes has to be low

to prevent electrical decomposition of the medium, and on top of that there is the voltage drop at the electrolyte-electrode interface, which reduces the force in the channel even more. Another disadvantage is that it is difficult to separate particles with the same charge of the opposite polarity, as they will be attracted towards the electrodes to the same height above them (one particle to the positive and one to the negative microelectrodes). On the other hand, the dielectrophoretic version of the separation process can be fine-tuned by adjusting the frequency of the applied field, so that one population experiences the negative and the other the positive dielectrophoretic force.

3.2.5. Travelling wave dielectrophoresis

One of the most popular separation techniques based on dielectrophoresis is the method with travelling electric fields. Many experiments were conducted and reported [232-247]. The example of the microelectrodes layout for travelling wave dielectrophoresis is depicted in figure 3.12.

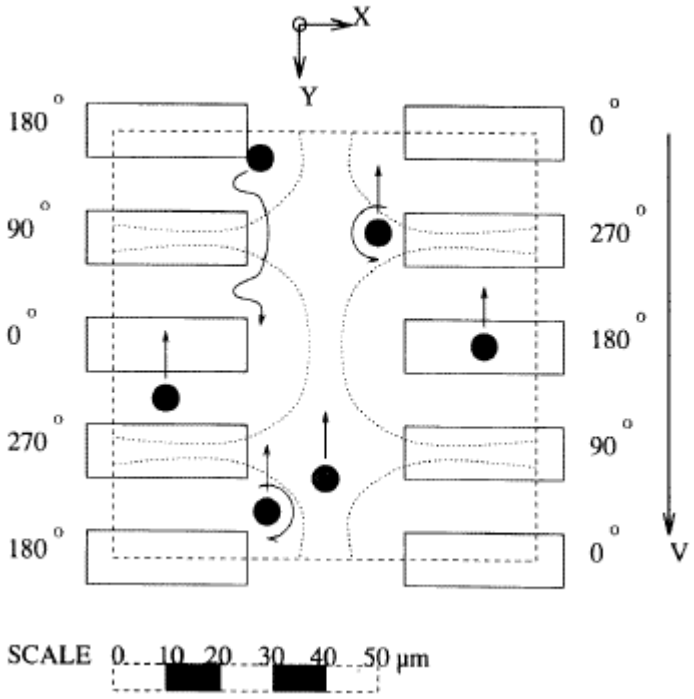

3.12. Travelling wave dielectrophoresis [237]

A four-phase voltage is applied to the interdigitated electrodes as depicted in figure 3.12. The travelling electric field is assumed to have been established in the

channel over the electrodes. Depending on the frequency of the applied voltages and on the conductivity of the suspending medium, the particles were moving along the centre of the channel in the direction opposite to that of the travelling electric field. The theoretical analysis of the experiment was restricted to the case of the particles located in the centre of the channel, to simplify the calculations and simulations. It was theoretically concluded that the velocity of the particle depends on the imaginary component of the induced moment, which is conventionally associated with electrorotation. This theoretical conclusion was also experimentally verified. For the particles to be repelled from the electrodes into the channel and undergo the linear motion, the necessary condition was that the induced dipole moment of the particles was negative, to induce the negative dielectrophoretic force. Particles located off the centre of the channel travelled with a spinning motion, as depicted in figure 3.12. As the frequency was increased to the region where the transition between negative and positive dielectrophoresis occurred, the particles were observed to travel in a 'zigzag' manner near the electrode tips in the same direction as the travelling field. After the frequency was further increased, the particles were trapped at the electrode tips under the influence of the positive dielectrophoretic force.

Several modifications were made to the original system to investigate dependencies of the particles behaviour on the physical parameters of the system. For example, when the gap between the neighbouring electrodes was decreased, the wavelength of the travelling wave is reduced. As expected from equation (3.31), both the travelling force and the trapping force increase in inverse proportion to the wavelength. It was also noted that the forces are greatest over closely spaced microelectrodes, corresponding to the smallest wavelengths. Therefore, the travelling fields are generated by adjacent electrodes, rather than by those opposite to each other across the channel. Another example of physical system alteration was moving the opposing electrode pairs closer together, reducing the channel width. Larger electric fields and hence larger travelling forces and larger trapping forces are thus produced. In other words, if either the electrode spacing or the channel width (or a combination of both) is decreased, it should be possible to use the amplified trapping force which exists at the points of shortest wavelength or narrowest channel width to manipulate a subpopulation of particles in a mixture selectively, either by trapping them or by directing them into or away from a channel constriction.

Interesting observations were also collected from an experiment in which two different voltages of different frequencies f_1 and f_2 were applied to this system of microelectrodes, with one voltage being applied to the electrodes on one side of the channel, and the other voltage to the opposing electrodes. The voltages were still four-phase. The forces above the electrodes resulting from this setup were found to be consistent with those already described above for each frequency, but at the centre of the channel the two force structures were found to be superimposed. In other words, the translational forces corresponding to signals f_1 and f_2 are generated independently of each other. In another experiment, the result of applying counter-directed travelling waves f_1 and f_2, on either side of the channel was investigated. If the frequencies were the same, stationary waves were established in the channel so that under conditions of negative dielectrophoresis, the particles formed stationary and slowly rotating aggregations at the sites of the electric field minima.

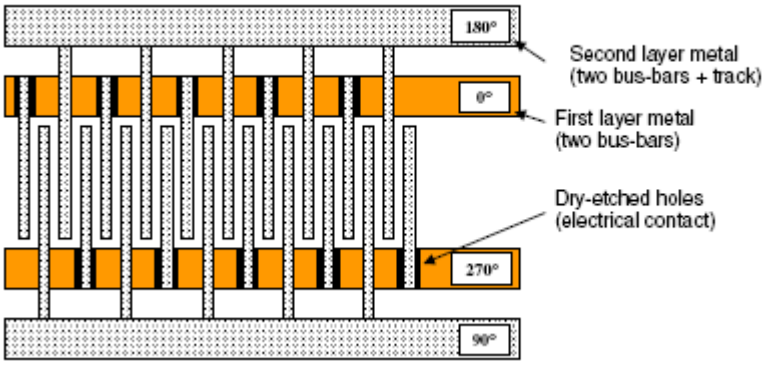

3.13. Four phase travelling wave dielectrophoresis separator [237]

Similar travelling wave dielectrophoretic separators were made with microelectrodes interleaved and parallel to each other. In this setup presented in figure 3.13, there is no channel in the middle of the structure, and all of the particles present inside such a system are effectively placed above the microelectrodes, regardless of their exact location. In the experimental setup presented in [237], the voltage applied to the microelectrodes was four-phase, with 2 volts peak to peak and the frequency of 1 MHz. Again, two adjacent electrodes had a phase difference of 90°, and the pattern was changing every four electrodes. The electrodes were 10 microns wide and the gap between them was also 10 microns. In the experiment, polystyrene spheres 10 microns in diameters were suspended in the liquid of 1

mS/m. After the particles were injected into the system, the voltage was applied to the electrodes and the motion of particles was clearly observable. It is also shown in figure 3.14, with screenshots of the experiment right before the voltage was turned on, and in 4 seconds intervals, until 20 seconds after turning on the voltage. The two circled dots represent the references against which the motion of particles can be clearly seen. The average velocity of the particles was between 6 and 8 microns per second.

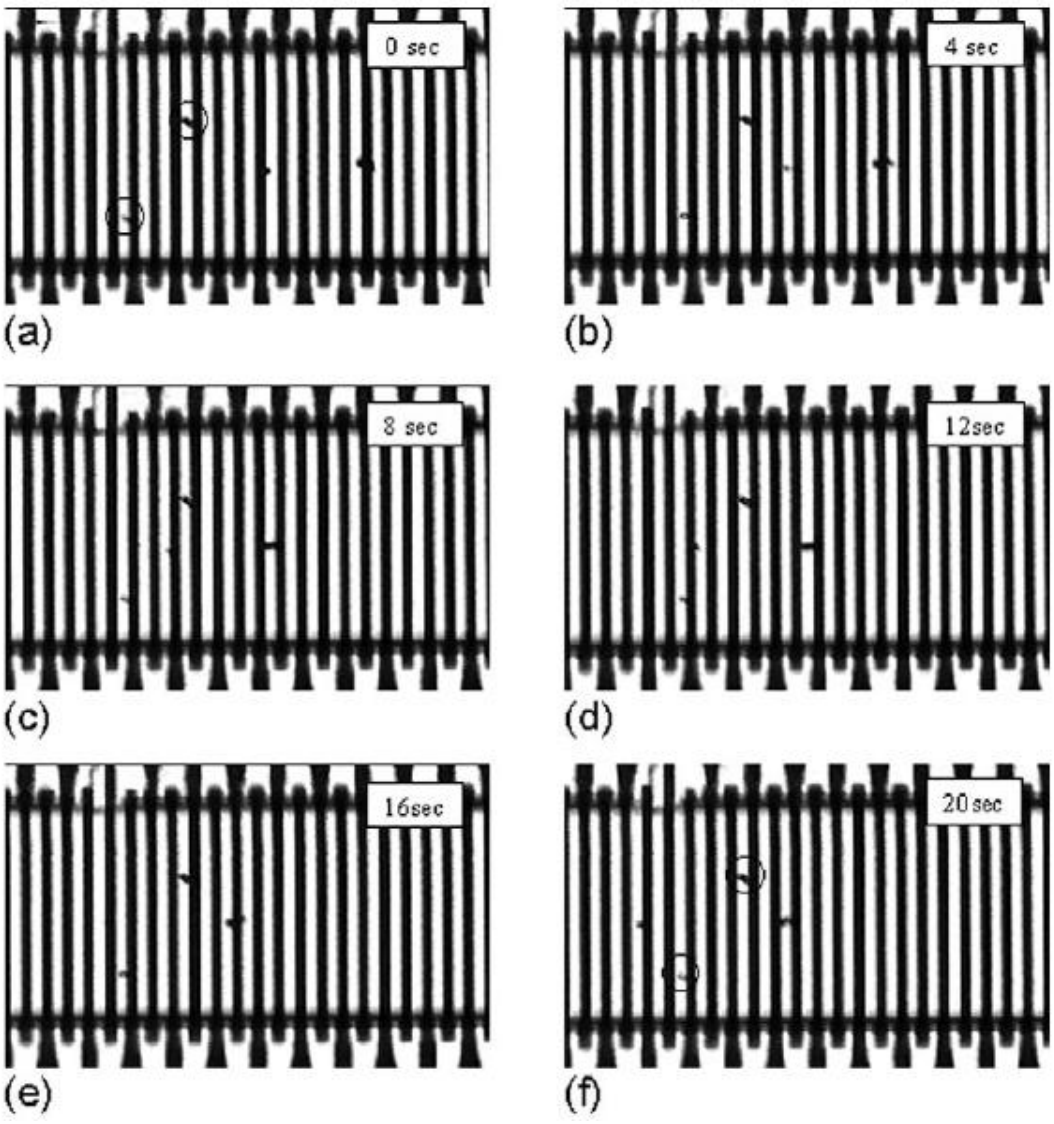

Figure 3.14. Screenshots of the experiment in 4 seconds intervals. (a) corresponds to turning on the voltage, and (f) corresponds to 20 s after that [237]

A similar method of generating travelling wave dielectrophoresis was used to experimentally show how different biological particles can be efficiently separated

[245]. For this purpose, 10 ml of fresh rabbit blood was prepared to get a suspension of erythrocytes and leukocytes of $5*10^7$ cells ml^{-1}. A large area separator with the electrodes layout as in figure 3.15 (there were 1000 electrodes in total to achieve better separation efficacy over a large area) was used with 10 V pp four-phase voltage with frequency of 500 kHz applied to the electrodes. At this frequency and voltage, there was a distinct difference between the velocities of different types of cells.

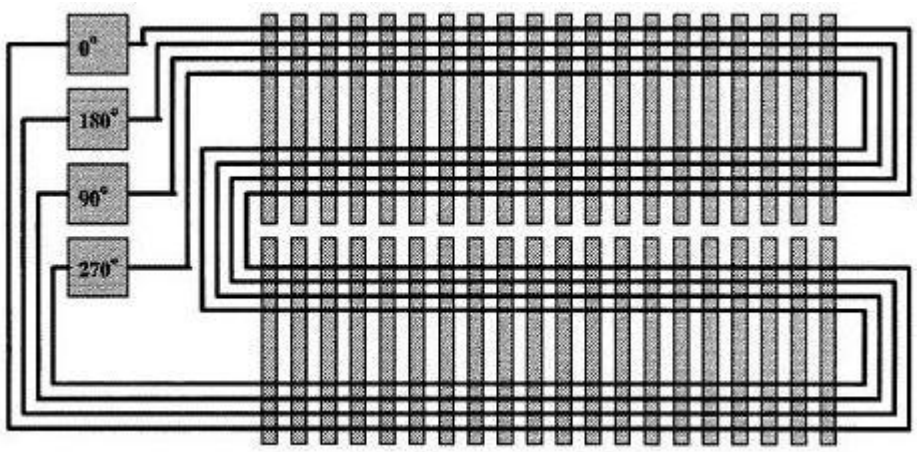

Figure 3.15. Travelling wave dielectrophoresis array [245]

Figure 3.16 shows a section of the TWD array with blood cells moving across the field of view from left to right. The four images were taken at 1 s intervals. During this time, the erythrocyte had moved 90 microns and the leukocyte had moved approximately 60 microns. The electrodes are out of focus in this figure owing to the fact that the cells are levitated by approximately 7 microns by the negative dielectrophoretic force [245]. The particles were moving in the direction opposite to the travelling electric field as predicted by theory. If the particles would travel with the same speed across the entire separator area from the entrance to the exit, there would be a path difference of 7.5 mm by the time the erythrocytes reach the end of the electrodes. The separation efficiency between two given particle types depends on the length of the array, with all other factors being equal. In this case, the erythrocytes and leukocytes would have separated into two homogeneous populations separated spatially by 1 mm after just 80 s (in that case the erythrocytes would have travelled 2.56 mm). If a concentration of cells was smaller, this would result in smaller band separations also being acceptable. Another important

theoretical and experimental observation is that smaller particle size also means smaller dielectrophoretic force. In other words, to achieve similar efficiency with smaller cells, larger electrical field needs to be generated. This is impractical for the frequencies over 20 MHz, as it is difficult to generate high stable voltages at those frequencies. The alternative is to decrease the spacing between the electrodes to increase the electric field strength. This is also possible with the advances in nano-fabrication technologies.

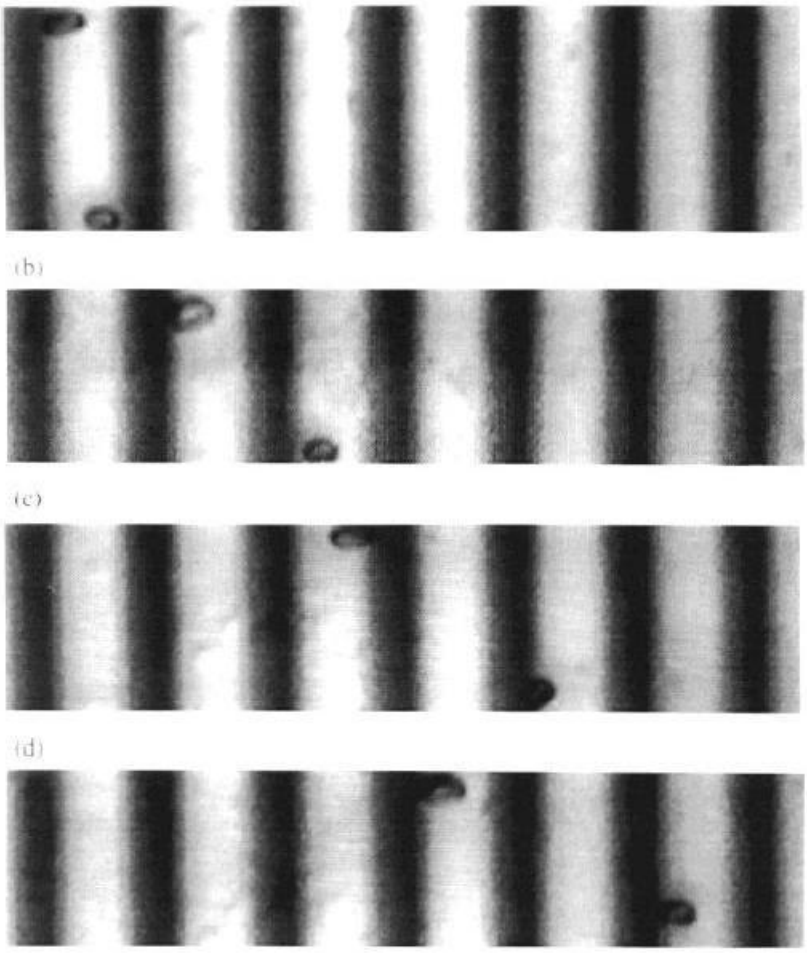

Figure 3.16. Blood cells moving across the array from left to right (screenshots taken at 1 second intervals) [245]

3.2.6. Electrorotation

Another important electrokinetic effect is electrorotation, which is the induced rotation of particles exposed to a rotating electric field. The theoretical and experimental aspects of electrorotation have been developed in several publications and it has been shown to be a sensitive method for monitoring the physiological

viability of cells [248-266]. The rotating electric field is usually generated using four electrodes positioned at right angles to each other and energized with four-phase signals of frequencies between 50 Hz and 100 MHz (see figure 3.8 earlier in this chapter about dielectrophoretic traps). The fact that travelling wave dielectrophoresis (TWD) and electrorotation (ROT) can be induced using similar electrical signals was efficiently deployed in [233], where these two phenomena were successfully integrated into a single microelectrode structure. Such a structure is shown in figure 3.17.

The TWD-ROT microelectrode design consists of four parallel spiral elements. These elements are energized using a four-phase sinusoidal voltage, as indicated by the figure. A travelling field propagates radially from the centre to the periphery of the device. At the centre, a clockwise rotating field is generated. If the phase sequence would be reversed, the generated electric fields would be opposite, i.e. the travelling wave would be directed towards the centre of the microelectrodes, and the rotating field in the centre would be anti-clockwise.

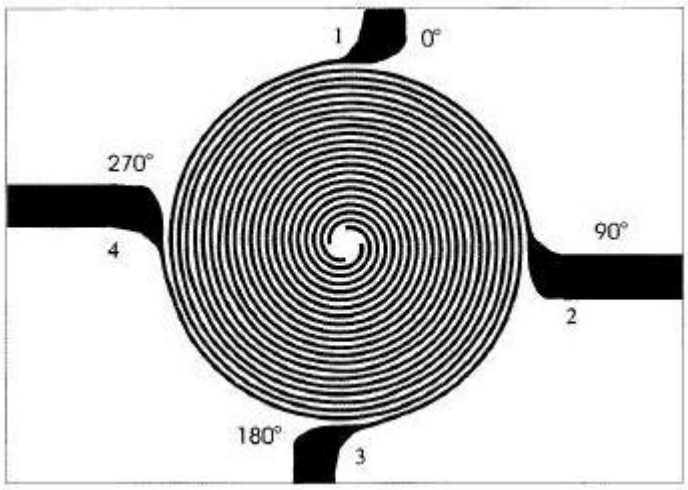

Figure 3.17. Combined TWD and ROT device [233]

In [233], the model microorganism used was the oocyst of Cryptosporidium parvum. The presence, even at very low concentrations, of these oocysts in drinking water has led to outbreaks of human infection (cryptosporidiosis), which occurs as a self-limiting diarrhoea in healthy adults but may lead to death in infants and immuno-compromised people. Because the oocysts do not multiply outside their hosts, they cannot be cultured in vitro. Current diagnostic techniques are based on

the filtration of large quantities of water followed by fluorescence microscopy and can be inaccurate. It was experimentally shown that travelling wave dielectrophoresis is very efficient for bringing the oocysts in the centre of the electrodes, as 51 of the estimated 55 oocysts in the suspension over the electrode array had been concentrated there some time after the electric field was applied. This collection efficiency of around 90% was reproducible. The concentration of oocysts was achieved by the negative dielectrophoretic force acting on them. The voltage applied was 2 V RMS and 60 kHz. After the voltage was adjusted to 1 V RMS and 1.5 MHz, the oocysts started to undergo electrorotation. At this frequency the oocysts experienced not only a clockwise rotating field, but also a positive dielectrophoretic force causing them to slowly move back towards the electrodes. If this effect interfered with the ROT analysis, the oocysts were redirected towards the centre by briefly reducing the frequency to 60 kHz. At the frequency of 1.5 MHz, the viable oocysts exhibit anti-field rotation, whereas non-viable ones rotate in a co-field sense. Of the 51 oocysts trapped in the centre of the electrodes, 27 exhibited anti-field (anti-clockwise) rotation and were deemed to be viable, while the remaining 24 oocysts rotated in a co-field (clockwise) sense and were considered to be nonviable. Although dipole–dipole interactions can influence the rotation rate, such interactions are not strong enough to reverse the sense of rotation.

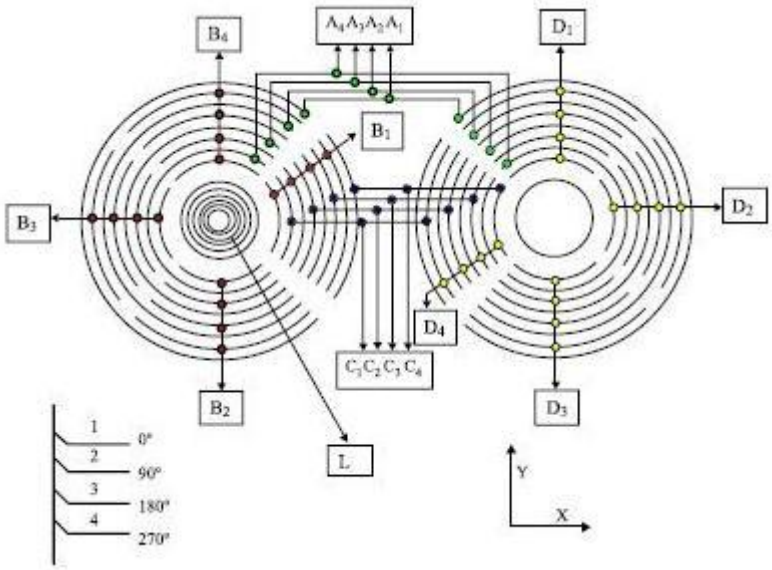

Figure 3.18. Electrode arrays for levitation and electrorotation of particles [244]

Another application of TWD and ROT forces for bio-particles manipulation and investigation is given in [244]. A set of microelectrodes as shown in figure 3.18 was successfully used to investigate different behaviour of viable and non-viable Daudi cells and multiple myeloma under the influence of dielectrophoretic forces. There are four sets of microelectrodes in this microchip, as shown in the figure. These are designated as A1 to A4, B1 to B4, C1 to C4, D1 to D4 and L. Electrode sets A and C consist of 80 individual electrodes, B and D consist of 160 electrodes, and L consists of 60 electrodes. Each set of electrodes is designed specifically for one of the electrokinetic techniques used for cells manipulation, and has the relevant electric field applied as required. The electrodes are used for the following purpose:

- Electrodes designated as L are used for levitation. The spacing between two adjacent electrodes is equal to 4 microns, and the electrodes themselves are 4 microns wide. Bonding pads are connected to the electrode in the centre and on rings 15, 30, 45 and 60, which provide external biasing. Internal biasing between any two adjacent sets of rings is provided by on-chip polysilicon resistors.
- Electrodes designated as A and C are used as travelling wave dielectrophoresis arrays. Each electrode is 4 microns wide, and the spacing between two adjacent electrodes is equal to 12 microns. Ten of these electrodes were connected together to one bonding pad. They are excited by externally applied four-phase signals, with the phase difference between any two adjacent electrodes equal to 90°. The generated travelling electric field propagates radially from the centre to the periphery.
- Electrodes designated as B and D are utilized for electrorotation measurements. Each electrode is 4 microns wide and spaced 12 microns from its neighbours. A sum of 40 electrodes is connected together to each pad, and an equivalent polynomial electrode configuration for electrorotation is formed. The connected signals generate counter clockwise rotating field.

In the frequency range of 10 kHz to 5 MHz, viable malignant cells travelled in the anti-field direction first and then changed to the opposite direction, while non-viable cells always travelled in the anti-field direction. It was possible to differentiate between the two populations, as the viable cells were stained with the dye eosin. Therefore, separation of viable and non-viable cells was obtained at

frequencies above 1 MHz. It was observed that the viable Daudi and NCIH929 cells adhered to the electrodes surface more readily than did nonviable cells. The physical differences between the two were also visible under a microscope. Based on the dielectrophoretic findings, the approximate dielectric properties of the cells were estimated from the experimental data and showed that low specific membrane capacitance can be one of the striking characteristics of malignant cells. Modelling of the frequency response was performed in Matlab, and a theoretical comparison between non-malignant and malignant character cells provided a strong theoretical base to use this method for the detection of malignant cells in the peripheral blood of patients. Cancer cells originating from different tissues may metastasize into peripheral blood during disease progression. For the most part, it has proved to be extremely difficult to detect rare cancer variants that invade the blood and mediate the spread of disease. The possibility exists that small numbers of circulating malignant cells may be detectable through their different frequency responses in a DEP field, enabling clinically useful devices for fractionation, enumeration and monitoring of metastatic spread.

3.3. Fluid dynamics

Fluid dynamics in microsystems plays an important role, as the particles suspended in the medium always experience some sort of a force due to the medium [e.g. 40]. For example, the particles moving through the medium experience a viscous drag force, as the medium is effectively opposing the movement. Another example is when the medium moves due to a force being applied upon it, and the static particles are dragged along and forced to move with the medium. The force on the medium can be either an external force applied by means of pumping, or the electrohydrodynamic force, due to the interaction between the applied electric field and the medium. In any case, to model the particles movement within the medium, the fluid dynamics effects should be taken into account.

3.3.1. Fluid dynamics governing equations

The local density of the fluid obeys the law of conservation of mass, which states that the rate of change of mass in an arbitrary volume is equal to the flux of

mass through the surface enclosing that volume [41]. This equation for mass continuity can be written as:

$$\frac{d\rho_m}{dt} + \rho_m \nabla \vec{u} = 0 \tag{3.42}$$

Here, ρ_m represents the mass density and u represents the velocity of the fluid. This equation can be further simplified for microfluidic systems. It has been noted [41] that the relative pressure difference in the fluid is proportional to the square of the ratio of the fluid velocity and the sound velocity in water. The typical velocities of fluids in microfluidic systems are about three orders of magnitude smaller than the sound velocity in water, and hence the relative pressure variations in the previous equation are negligible. In other words, the mass conservation equation comes down to:

$$\nabla \vec{u} = 0 \tag{3.43}$$

Another important equation in fluid dynamics describes the effect of momentum conservation and is called the Navier-Stokes equation [41]. For an incompressible fluid, this equation can be written as follows:

$$\rho_m \frac{\partial \vec{u}}{\partial t} + \rho_m (\vec{u}\nabla)\vec{u} = -\nabla p + \eta \nabla^2 \vec{u} + \vec{f} \tag{3.44}$$

Here, p is the pressure, η is the fluid viscosity, and f is the total applied body force. Similar to the mass conservation equation, this equation can also be simplified for microfluidic systems. Typical flow in microfluidic systems is laminar, with a low value for Reynolds number (<<1). This number is given as:

$$\mathrm{Re} = \frac{\rho_m u_0 l_0}{\eta} \tag{3.45}$$

Here, u_0 and l_0 are typical velocity and typical dimension of the system in question, respectively. In the case of the low *Re*, the second term on the left hand side of the equation above can be neglected:

$$\rho_m \frac{\partial \vec{u}}{\partial t} = -\nabla p + \eta \nabla^2 \vec{u} + \vec{f} \tag{3.46}$$

With the appropriate boundary conditions, which are difficult to specify for this problem, the solution of this differential equation is the velocity profile for the given body force on the fluid.

3.3.2. Fluid dynamics in microfluidic systems

Microfluidic systems typically have low values of Reynolds number, as the typical fluid velocity and typical dimensions are relatively small [88]. Typical velocity is in the order of mm per second, and typical dimension (such as the microchannel width or height) is in the order of micron or tens of microns. This results in *Re* being much lower than one, and the resulting flow is laminar and free of turbulence.

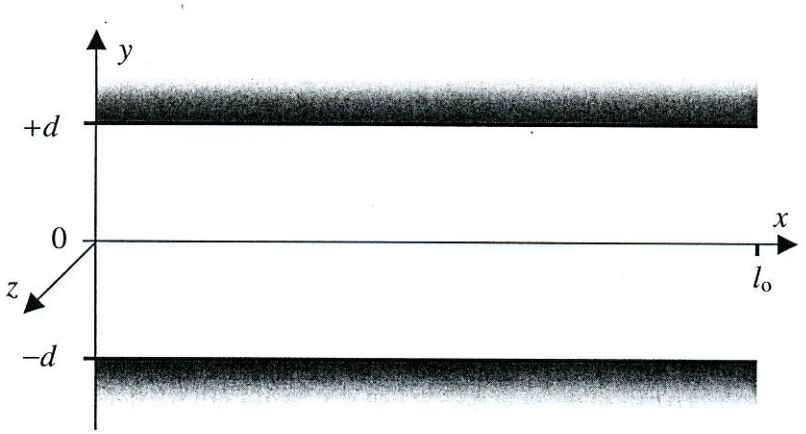

Figure 3.19. Long and narrow channel for 2D description of the fluid velocity profile [99]

However, the fluid flow is not entirely laminar, as some turbulence occurs at the entrance of the channel due to the channel geometries in that region [99]. This can be simply modelled by using a two-dimensional approach to describing the fluid velocity profile inside the channel. Figure 3.19 depicts a long and relatively narrow channel, into which the fluid enters on the left hand side at x = 0. In this case, we assume that in *z* direction the channel is much wider than in *y* direction, hence we can observe the problem in only two dimensions. The Navier-Stokes equation in that case becomes:

$$\rho_m \frac{\partial u_x}{\partial t} = -\frac{\partial p}{\partial x} + \eta \frac{\partial^2 u_x}{\partial y^2} \tag{3.47}$$

The following equation also applies:

$$\frac{\partial p}{\partial y} = \frac{\partial p}{\partial z} = 0 \tag{3.48}$$

The second equation implies that pressure is o dependent only on x and time t, but the first question also implies that the partial derivation of p with respect to x also depends on y (and t). In summary, the pressure drop along x depends only on t, and in the steady state it is constant along the chamber and equal to $-p_0/l_0$. The equation hence becomes:

$$\frac{\partial^2 u_x}{\partial y^2} = \frac{1}{\eta}\frac{\partial p}{\partial x} = -\frac{p_0}{\eta l_0} \tag{3.49}$$

By integrating this equation twice and applying the boundary conditions that u_x equals zero at the top and the bottom of the channel (where y equals d and $-d$), we get the following equation for the fluid velocity profile:

$$u_x = \frac{1}{2\eta}\frac{p_0}{l_0}(d^2 - y^2) \tag{3.50}$$

This equation actually represents a parabola, with the maximum and average values given with equations (3.51) and (3.52), respectively. The flow profile described with these equations is shown in figure 3.20.

$$u_{\max} = \frac{p_0 d^2}{2\eta l_0} \tag{3.51}$$

$$u_{avg} = \frac{d^2}{3\eta}\frac{p_0}{l_0} \tag{3.52}$$

There is a certain characteristic distance from the entrance to the channel in which the fluid flow profile can differ substantially from the parabolic flow described with the above equations. This characteristic distance is called the entry length. The detailed information and description of this effect can be found in the literature, but for the laminar flow in the microsystems, the entry length can usually

be ignored [41]. It can also be assumed that the flow profile takes the parabolic shape immediately at the entrance to the channel.

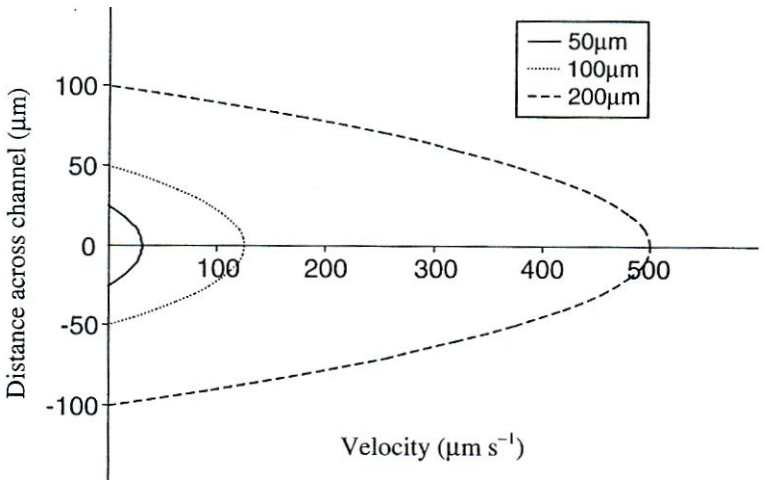

Figure 3.20. The fluid flow profile in the channel [99]

3.3.3. Electrical forces on fluid

When electric field is applied to a fluid, the body force is produced and the fluid generally moves [199, 226]. The stronger the electric field, the greater the force and the movement of the fluid. Therefore, in the microfluidic systems the electrical fields can cause greater force to be applied on the fluid, as the fields are generally stronger. Hence, the investigation of the impact of the fields on the fluid movement is important.

The electrical body force (i.e. the force on the fluid generated due to the applied electric field) is given by the following equation:

$$\vec{f}_e = \rho_c \vec{E} - \frac{1}{2}\left|\vec{E}^2\right|\nabla\varepsilon + \frac{1}{2}\left(\rho_m\left(\frac{\partial\varepsilon}{\partial\rho_m}\right)\left|\vec{E}^2\right|\right) \tag{3.53}$$

Here, ρ_c and ρ_m are the charge and mass densities, respectively. On the right hand side of equation (3.53), there are three distinct parts. The first is the Coulomb force, the second is the dielectric force, and the third is the electrostriction pressure. The latter can be ignored for the incompressible fluid.

Equation (3.53) effectively states how the body force on the fluid changes with the temperature distribution. That is because the localized heating of the fluid gives rise to the gradients of the fluid electrical properties, namely the conductivity

and the permittivity. These gradients cause the body force, as described above. To derive the equation for the force as the function of the fluid electrical properties, the following equation describing the Gauss law can be used:

$$\rho = \nabla(\varepsilon\vec{E}) = \nabla\varepsilon\vec{E}_0 + \varepsilon\nabla\vec{E}_1 \tag{3.54}$$

In equation (3.54), the electric field is described with two components denoted with indexes *0* and *1*, which represent the applied field and the perturbative expansion of the electric field due to the electric charge distribution within the fluid, respectively. The former is much greater than the latter.

If we neglect the third expression on the right hand side of equation (3.53), and use equation (3.54) to expand the first part in equation (3.53), we get:

$$\vec{f}_e = \left(\nabla\varepsilon\vec{E}_0 + \varepsilon\nabla\vec{E}\right)\vec{E}_0 - \frac{1}{2}\left|\vec{E}_0{}^2\right|\nabla\varepsilon \tag{3.55}$$

By using the charge conservation equation and by assuming the harmonic time varying field with the angular frequency ω, the following expression can be used to calculate the perturbative component of the electric field:

$$\nabla\vec{E}_1 = \frac{-\left(\nabla\sigma + i\omega\nabla\varepsilon\right)}{\sigma + i\omega\varepsilon}\vec{E}_0 \tag{3.56}$$

If we use this expression in the equation (3.55) to calculate the body force, and if we use the time averaged value of the force, the final expression for it becomes [228]:

$$\left\langle \vec{f}_e \right\rangle = \frac{1}{2}\mathrm{Re}\left[\left(\frac{\sigma\nabla\varepsilon - \varepsilon\nabla\sigma}{\sigma + i\omega\varepsilon}\vec{E}_0\right)\right]\vec{E}_0{}^* - \frac{1}{2}\left|\vec{E}_0{}^2\right|\nabla\varepsilon \tag{3.57}$$

Here, the star next to E_0 denotes the complex conjugate. Equation (3.57) describes the time averaged body force on fluid as the function of electric field and conductivity and permittivity gradients inside the fluid.

For an AC signal of a given frequency ω, the charge in the fluid will oscillate with the same frequency and the time dependent force will have two components: the steady time averaged component given by equation (3.57), and the oscillating component at twice the frequency of the AC signal applied (as the force is the product of the field and the charge distribution, and they both oscillate at the

frequency ω). Similar to the body force, the fluid velocity will also have the steady and the oscillatory terms. However, at sufficiently high frequencies, the oscillatory term is much smaller and can usually be neglected.

As discussed in the literature [228], the body force given by the equation (3.57) has two distinct limits. At low frequencies the dominating force is the Coulomb force given with the first term in the equation, and at high frequencies the dielectric force dominates, given by the second term in the equation. Typically, these two terms differ not only in the magnitude, but also the direction, changing the pattern of the fluid flow going from low to high frequencies and vice versa.

Generally, in the system where electrohydrodynamic effects take place, there is a coupling connection between the electric field, the temperature, and the fluid velocity profile. This connection is described with the temperature balance equation, given as [226]:

$$\rho_m c_p \frac{\partial T}{\partial t} + \rho_m c_p \vec{u} \nabla T = k \nabla^2 T + \sigma \left| \vec{E} \right|^2 \tag{3.58}$$

In this expression, c_p is the specific heat at constant pressure, k is the thermal conductivity, and the second term on the right hand side represents the Joule heating. To simplify the equation, we can neglect the first term on the left hand side and look at the steady state, if the frequency of the applied voltage is high enough, and it normally is in microfluidic systems. The second term on the left hand side (heat convection) can also be neglected when compared to the first term on the left hand side (heat diffusion), as it is about three orders of magnitude smaller in microfluidic systems [227]. In other words, the temperature distribution is much more affected by the heat diffusion, then the fluid motion. In this way, the temperature and the fluid problems are effectively decoupled. The electric field problem is also decoupled from the fluid motion problem, as the two are independent in a way that the fluid motion does not affect the electric field distribution profile. By taking all of the above into account, the temperature distribution is obtained from the diffusion equation with the heating coming from electric field, as in:

$$k \nabla^2 T + \sigma \left| \vec{E} \right|^2 = 0 \tag{3.59}$$

This equation is solved to obtain the temperature distribution in the fluid due to the electric field. Then, temperature dependent values of the electrical conductivity and permittivity of the fluid are calculated, and these values are used to calculate the body force on the fluid by using equation (3.57). From there, the fluid velocity profile can be calculated. The fluid drag force can then have an impact on the particle movement within the fluid, as will be described next.

3.3.4. Fluid drag force on particles

In a microfluidic system, if the electric field is applied to the fluid in which micro-particles are suspended, the fluid movement induced by the field can impact the particles movement within the fluid, as the particles will be subject to the drag force [226].

In general, when a particle is moving relative to the fluid, the viscous drag force on the particle is given by the following equation:

$$\vec{F}_{\eta} = -f\vec{v} \tag{3.60}$$

Here, f is the friction factor, which depends on the properties of the fluid and the particle, and v is the relative velocity of the particle. The negative sign implies that the force acts in the direction opposite to the movement of the particle.

In general, the relative velocity of the particle is given as a difference between the absolute velocity of the particle, v, and the absolute velocity of the fluid, u. If there is some arbitrary force (for example, the dielectrophoretic force due to the electric field) applied to the particle, its velocity can be calculated from the equation for Newton's second law:

$$m\frac{d\vec{v}}{dt} = \vec{F}_{arb} + f(\vec{u} - \vec{v}) \tag{3.61}$$

Here, m stands for the mass of the particle. The solution to this differential equation is given as:

$$\vec{v} = \left(\frac{\vec{F}_{arb}}{f} + \vec{u}\right)\left(1 - e^{-(f/m)t}\right) \tag{3.62}$$

The expression for the particle velocity in the previous equation is time-dependent. The characteristic time constant is given as the ratio of the mass and the friction coefficient. After the period of time much greater than this time constant, the particle velocity is given by the so-called terminal velocity, which is time-independent and given as:

$$\vec{v} = \left(\frac{\vec{F}_{arb}}{f} + \vec{u} \right) \tag{3.63}$$

If the fluid is not in motion, the particle velocity depends solely upon the applied force on the particle, and the friction factor. In the literature, friction factors can be found as functions of particles dimensions and the fluid viscosity [41]. There, the particles are assumed to be perfectly smooth at the surface, and neglecting that assumption complicates the calculation significantly. This, however, falls out of the scope of this text. Just as an example, the following equation shows the friction factor of a spherical particle:

$$f = 6\pi\eta a \tag{3.64}$$

Here, a is the radius of the sphere, and η is the fluid viscosity. In the case of the force applied to the particle being of the dielectrophoretic origin, the equation of the particle motion becomes:

$$m\frac{d\vec{v}}{dt} = \vec{F}_{DEP} - \vec{F}_{\eta} \tag{3.65}$$

With the assumption of steady state and with the particle velocity due to the dielectrophoretic force being directly proportional to the dielectrophoretic force, the total particle velocity can be written as:

$$\vec{v}_{DEP} = \frac{v\,\mathrm{Re}[\tilde{\alpha}]\nabla\left|\vec{E}\right|^2}{f} \tag{3.66}$$

For a spherical particle with the radius a, the equation above becomes:

$$\vec{v}_{DEP} = \frac{\pi a^3 \varepsilon_m \,\mathrm{Re}[\,\tilde{f}_{CM}\,]\nabla\left|\vec{E}\right|^2}{6\pi\eta a} = \frac{a^2 \varepsilon_m \,\mathrm{Re}[\,\tilde{f}_{CM}\,]\nabla\left|\vec{E}\right|^2}{6\eta} \tag{3.67}$$

If the dielectrophoretic mobility of the particle is defined as the ratio between the dielectrophoretic force and the square of the absolute value of the electric field, the equation below can be used to calculate that mobility:

$$\vec{v}_{DEP} = \frac{a^2 \varepsilon_m \,\mathrm{Re}[\,\tilde{f}_{CM}\,]}{6\eta} \tag{3.68}$$

This value shows that the mobility due to the dielectrophoretic force on a spherical particle with radius depends upon the particle radius, the permittivity and the viscosity of the suspending fluid, and the Clausius-Mossotti factor. This property of the particle can be used to estimate the response time of the particle when the electric field is turned on, and to compare the effect of the dielectrophoretic force and the fluid drag force, if the fluid is flowing inside the microchannel and the particles experience the drag force, together with the dielectrophoretic force.

In this chapter, an overview of dielectrophoresis was given in the context of manipulation of small particles suspended in a medium. Firstly, the theoretical background was presented, the main equations were stated and the most important concepts explained. In the second part of the chapter, an overview of practical applications of dielectrophoresis in particles manipulation was given, with the emphasis on dielectrophoretic traps, travelling wave dielectrophoresis, and electrorotation. In the final part of the chapter, the most important concepts in the theory of fluid dynamics were presented, with the emphasis on the interaction between small particles and fluids in which they are suspended.

Chapter 4. Proposal for Doctor-on-a-Chip

This chapter describes an overview of the Doctor-on-a-Chip device. The main components of the device are listed, and the main functionality of the device is described. The concept of the device is compared to an already existing proposal for DNA detection based on dielectrophoretic manipulation of cells.

4.1. Concept of Doctor-on-a-Chip

In this section, a proposal for Doctor-on-a-Chip will be described. This proposal describes the complete solution for a device that would take a sample of blood or any other bodily fluid, and perform the complete DNA analysis automatically on-chip, to provide an answer about the presence of a pathogen within the sample under investigation.

As depicted in figure 4.1, the device consists of four main building blocks, which perform the following functions:

1) DNA extraction from cells and purification
2) PCR amplification of target DNA
3) Separation of DNA by dielectrophoresis
4) DNA detection

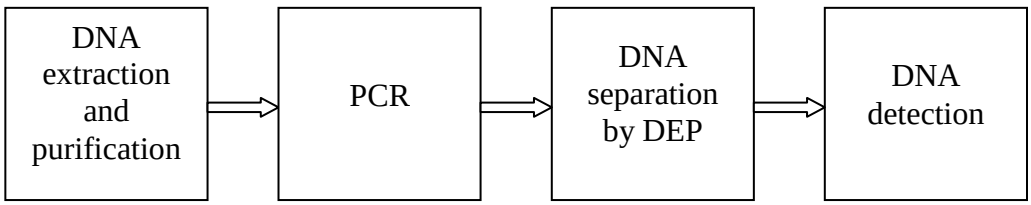

Figure 4.1. Block diagram of Doctor-on-a-Chip

The proposed layout of Doctor-on-a-Chip is given in figure 4.2. This figure shows how different building blocks depicted in figure 4.1 are realized on the chip. As described later in this section, the components to build Doctor-on-a-Chip are reviewed in chapter 2. The comprise the microfluidic pump, the PCR chamber for target DNA amplification, and detection chambers based on impedance measurement (sections 2.2.2.3, 2.3.2, and 2.4, respectively). Doctor-on-a-Chip also introduces a novel layout of microelectrodes for dielectrophoretic separation of DNA.

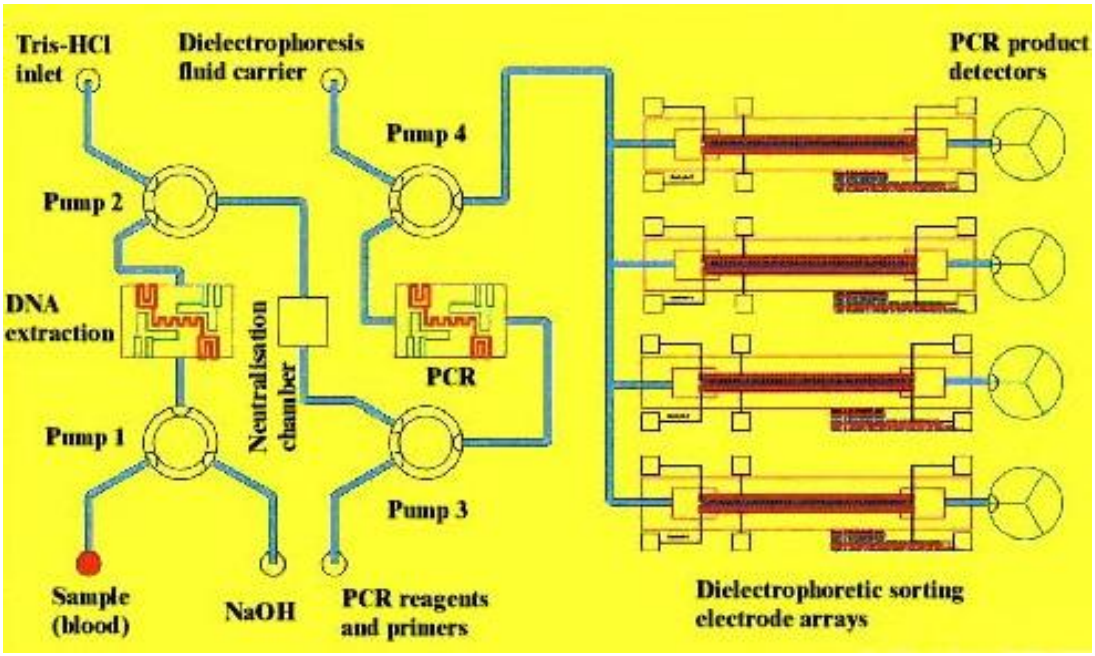

Figure 4.2. Proposed layout of Doctor-on-a-Chip

The first part of the chip consists of the microfluidic network for extraction and purification of DNA from the sample. This protocol is described in [204]. It consists of the following steps:

- Mixing the raw sample (for instance, 5µl whole blood) with 5µl of 10mM NaOH,
- Heating to 95°C for 1-2 minutes to lyse cells,
- Releasing DNA and denaturing proteins inhibitory to PCR,
- Neutralization of lysate by mixing with 5µl of 16mM tris-HCL (pH=7.5), and
- Mixing of neutralized lysate with 8-10µl of liquid PCR reagents and user-selected primers.

This protocol is implemented with the network of micropumps and heating chambers interconnected with the microchannels. The micropumps used are valve-less diffuser micropumps [107], as shown in figure 2.23 in chapter 2. They consist of a shallow pumping chamber, a piezoelectrically driven diaphragm, two inlet diffusers/nozzles, and one outlet diffuser/nozzle. All of the diffusers/nozzles have an optimal angle of approximately 5°. It should be noted that the pump has two inlets because it serves as a mixer as well as a pump (the pumping mechanism causes turbulence in the pumping chamber [107]).

The heating chamber is a simple well of a sufficient capacity to contain the mixture of the sample and the reagents needed for DNA extraction. The heaters are placed underneath the bottom of the chamber and driven by the outside circuitry.

The second step in the analysis is PCR. The PCR chamber is basically the same as the heating chamber for cell lysis. The heaters are placed underneath the bottom of the chamber and driven by the outside circuitry, which ensures that the temperature cycles are right for the PCR protocol. More details on PCR implementation on microchips can be found in section 2.3.

The third part of the chip comprises the microelectrodes [205], which are used to separate different populations of DNA molecules into groups and drive the desired DNA molecules towards the detection points at the right-hand side end of the chip in figure 4.2. The remaining DNA molecules, which are not allowed to reach the detection points, should remain in the microchannel, as the switching electric field does not produce the dielectrophoretic force of the sufficient strength for them to cross the entire channel length [205].

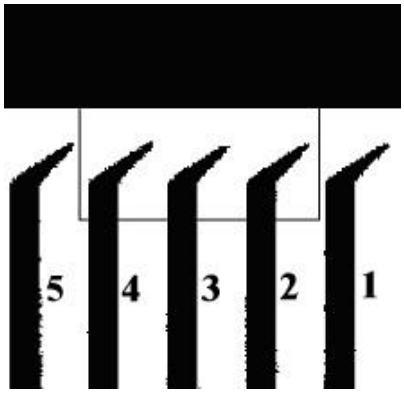

Figure 4.3. The microelectrodes for DNA separation [205]

Closer look of the microelectrodes is shown in figure 4.3. The black shapes in the figure are microelectrodes. There are 6 microelectrodes shown in the figure, five of which are designated with numbers 1 to 5, and one at the top (the black rectangle at the top of the figure). The separation mechanism is described in [205]. Two populations of particles of different size were introduced to the array on the right hand side of figure 4.3. Firstly, the voltage was applied to electrode 1, while all the other electrodes, including the top electrode, were grounded. The negative DEP force pushed the larger particles from electrode 1 to electrode 2, where they concentrated. Then the voltage was applied only to electrode 2, and the larger

particles were pushed towards electrode 3, and so forth. On the other hand, the smaller particles had lower dielectrophoretic mobility [205], and, as the voltage was switched between the electrodes, they were still left behind in the vicinity of electrode 1. This resulted in the larger particles being pushed from the right of the channel to the left, while the smaller particles remained to the left.

It should be noted that the proposed chip has four sets of microelectrodes, as shown in figure 4.2. The idea is that each set can be tuned for separation of a particular population of DNA molecules in the sample. Thus, the investigation of the presence of four different pathogens in the same sample could be done at the same time. Each set of microelectrodes should allow only DNA molecules of a single pathogen to go through towards the detection points on the right hand side of the chip. All of the other DNA molecules that enter that particular array should be trapped and they should not reach the corresponding detection point. In this way, the microelectrodes for dielectrophoretic separation should serve as filters, and the detection method used at the detection points on the right hand side of the chip should not depend on the sequence of DNA. Due to the fact that the microelectrodes act as filters, the presence of DNA at a particular detection points should be sufficient information for the observer to know which pathogen is detected in the sample (there is no need to analyze the DNA sequence).

After the DEP separation, the DNA detection is performed at the detection points to provide the answer about the presence or absence of a certain pathogen within the sample. The proposed detection method in this case is based on the impedance measurement. This method was described in section 2.4 and also in the literature [138]. The point of detection comprises of two electrodes connected to the AC voltage suitable to hold the particle at the tips of the electrodes utilizing DEP. If the particles reach the electrodes (i.e. they passed through the corresponding array) they will accumulate at their tips and change the impedance of the system. An AC bridge method to sense that change [138]. The impedance measurement method is quantifiable. However, in this case it is not important, because we are merely investigating the presence of the target DNA, and not its quantity. The assumption is that if the dielectrophoretic array of microelectrodes in figure 4.2 is well tuned, only the desired DNA particles (pathogen) can reach the detection point. All of the other DNA particles in the sample will remain in the microchannel and will not be detected at the detection points. This has to be verified in practice with great caution,

because if the dielectrophoretic array cannot perform reliable separation of the different DNA particles, false positive results might occur. This is highly undesirable and might force the DNA detection method to be able to detect the right sequence. This will also increase the complexity of the method, and hence the cost of fabrication and the analysis. However, for the commercial device such as Doctor-on-a-Chip, the accuracy and reliability are crucial performance factors.

4.2. Managing conductivity of suspending medium

As shown in figure 4.2, the separation of DNA molecules in Doctor-on-a-Chip is based on dielectrophoresis. The dielectrophoretic force on particles in a microchannel is given with equations (3.30) and (3.23) in chapter 3. The former shows the dependency of the force on the particle volume and polarisability and the electric field, while the latter additionally shows the dependency of the particle polarisability on the frequency and the complex permittivities of the particles and the suspending medium.

For the given particles and the layout of microelectrodes, it is apparent from equations (3.30) and (3.23) that the most suitable way to control the direction and magnitude of the dielectrophoretic force is by changing the value of the Clausius-Mossotti factor, which is dependent on the frequency of the applied voltage and the medium and particle permittivity and conductivity. The particles subject to dielectrophoresis are typically defined by the purpose for which dielectrophoresis is deployed, and therefore the conductivity and permittivity of the particles will not be considered as the means of changing the Clausius-Mossotti factor.

From many experiments described in the literature [e.g. 146-209], the medium conductivity is typically the parameter that is used more than the others in modifying the frequency response of the Clausius-Mossotti factor. The suspending medium in the dielectrophoretic applications, especially involving biological molecules and cells, is based on water. As described in section 4.1 and also in literature in several on-chip sample preparation systems [e.g. 306-308], the DNA extraction and purification protocols are very complex, and involve several different chemical reagents for cell lysis, denaturing of proteins, neutralization of lysate, etc. On top of that, in Doctor-on-a-Chip the resulting mixture from DNA purification is further combined with PCR reagents and primers. In figure 4.2, all of this is done by

using the micropumps designated as pumps 1 through 3. The third pump brings the mixture to the PCR chamber, where the target DNA is amplified.

At this point in the research, it is unclear how the mixture coming out of the PCR chamber, as defined by the DNA extraction protocol in 4.1, would behave in the dielectrophoretic arrays in figure 4.2. This is due to unknown conductivity of the medium coming out of PCR, and unknown dielectric properties of the DNA molecules that would be investigated on the device. However, the behaviour of the molecules with changes in the medium conductivity can be explained by using the following equation [172}:

$$f_0 = \frac{1}{2\pi}\sqrt{\frac{(\sigma_p - \sigma_m)(\sigma_p + 2\sigma_m)}{(\varepsilon_p - \varepsilon_m)(\varepsilon_p + 2\varepsilon_p)}} \tag{4.1}$$

Here, σ_p and σ_m are the conductivity of the particle and the medium, respectively, and ε_p and ε_m are their respective permittivities. The symbol f_0 stands for the cross-over frequency, which is defined as the frequency for which the dielectrophoretic force on the particle is zero. This is the case when the real part of the Clausius-Mossotti factor equals zero, since the effective polarisability of the particle is exactly the same as that of the suspending medium. By changing the frequency slightly at this point, the force becomes non-zero, i.e. it takes either positive or negative value, depending on the complex permittivities of the particle and the medium.

From equation (4.1) it is apparent that the cross-over frequency increases as the medium conductivity increases, with all other parameters in the equation being constant. Similarly, the cross-over frequency value decreases with decreasing the medium conductivity. This is a powerful method for modifying the direction of the dielectrophoretic force and defining whether the effect will be positive or negative. This obviously also depends on the properties of the particles, because for highly polarisable particles it would be necessary to significantly increase the medium conductivity to achieve positive dielectrophoresis. However, in that case the higher conductivity can lead to significant increase in the temperature of the medium and consequently fluid movement. High temperature can in some cases also affect the biological sample under investigation. In those cases, the possibilities of changing negative dielectrophoresis to positive are somewhat limited, and we should be aware

of those limitations when developing practical devices for dielectrophoretic manipulation of particles.

To address the conductivity issue and potentially change the conductivity of the suspending medium prior to dielectrophoresis, the Doctor-on-a-Chip device contains the fourth pump in figure 4.2. This pump forces the liquid designated as the dielectrophoretic fluid carrier to be mixed with the PCR products, and then pumps that new mixture towards the dielectrophoretic sorting arrays. Again, due to limited data on the actual polarisabilities of the protocol medium and the target DNA, it is unclear what would be the composition of the dielectrophoretic fluid carrier. Nevertheless, the idea is that with the fourth pump we should have a method for changing the medium conductivity and thus the frequency dependence of the Clausius-Mossotti factor and the cross-over frequency. The experimental methods, once conducted, should shed more lights on the actual medium of choice and its chemical composition.

4.3. DNA separation by dielectrophoresis

This section gives an overview of DNA manipulation methods and some experiments published in the literature. To better understand the possibility to manipulate DNA, it is important to understand the dielectric properties of DNA and their dependence on the frequency of the electric field.

The dielectric properties of any material are usually given as its permittivity and dielectric loss. In general, the complex permittivity comprising these two components is given as $\varepsilon^* = \varepsilon' - i\varepsilon''$, where ε' is the real part and corresponds to the dielectric constant in the physical model of a dielectric in a parallel plate capacitor, while ε'' is the imaginary part and corresponds to the dissipative loss in the material. Both values are frequency dependent, and therefore the complex permittivity can be expressed as a function of angular frequency as:

$$\varepsilon^*(\omega) = \varepsilon_\infty + (\varepsilon_s - \varepsilon_\infty)/(1 + i\omega\tau) \tag{4.2}$$

Here, ε_∞ is the permittivity at high frequencies where the polarisation mechanism cannot follow the electric field changes any more, ε_s is the static permittivity at very low frequencies, and τ is the relaxation time. The real and imaginary parts of the complex permittivity are similarly given as:

$$\varepsilon'(\omega) = \varepsilon_\infty + (\varepsilon_s - \varepsilon_\infty)/(1 + \omega^2\tau^2) \tag{4.3}$$

$$\varepsilon''(\omega) = (\varepsilon_s - \varepsilon_\infty)\omega\tau/(1 + \omega^2\tau^2) \tag{4.4}$$

These values are obtained through experimental measurements. In [309], the compilation of published data from various different sources is given. The diagram presenting all of those data is given in figure 4.4.

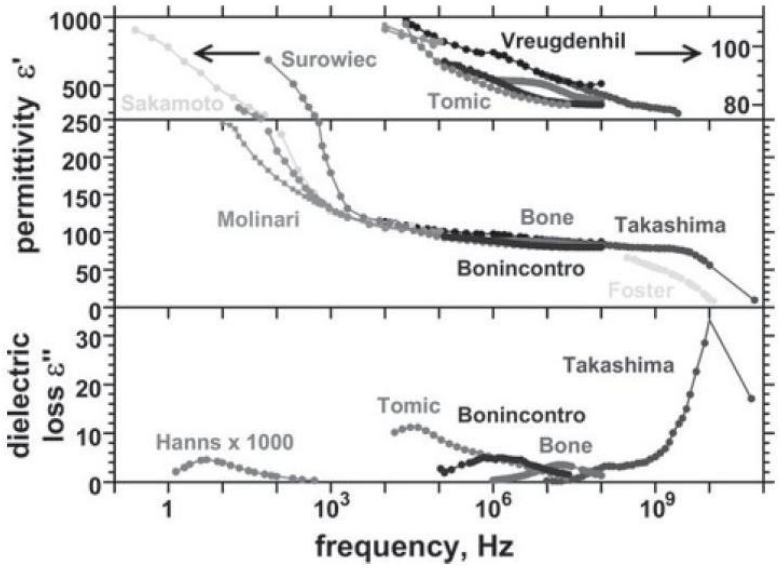

Figure 4.4. Permittivity and dielectric loss of calf-thymus DNA [309]

The data in figure 4.4 covers different sample preparation protocols, DNA length, suspending medium, and DNA concentration. It is apparent from the figure that there are at least four dispersions in the frequency range shown: one at the very low frequencies below 1 kHz, the second between 10 and 100 kHz, the third between 1 and 100 MHz, and the fourth above 1 GHz. In the figure, the dispersions are tagged with the names of researchers that gave explanation of the mechanisms responsible for dispersions [309]:

- The low frequency dispersion is interpreted as a rotation of the DNA molecule with a quasi-permanent dipole because of counterion fluctuations along the polymer backbone.
- The dispersion in the frequency range between 10 and 100 kHz is due to electrostatic interactions between fixed charges on the DNA with counterions and mutual interactions between mobile ions in the solution, which are redistributed by the DNA's fixed charges. The first effect

happens due to accumulation of counterions within a condensed layer around the DNA, while remaining mobile. For this to be possible, the Debye screening length must exceed the DNA radius, which is around 1 nm. The second effect is attributed to redistribution of mobile charges in the field of fixed DNA charges, which results in reduced interactions between these charges.

- The dispersion in the range between 1 and 100 MHz is attributed to free counterions, which hop between correlated DNA chains. It was initially thought that DNA base pair dipoles and Maxwell-Wagner interfacial polarisation are also causing this dispersion, but those theories were eventually ruled out.
- The high-frequency dispersion above 1 GHz is a result of the orientational polarisation of water molecules, which is centred around 17 GHz for pure water at room temperature. Relaxation frequency is only slightly shifted by the presence of DNA.

Many research activities that attempted to controllably manipulate DNA molecules by using dielectrophoresis have been published [e. g. 309-317]. The most obvious problem stems from the fact that the DNA molecules are very small, which not only makes the observation of experiments much more difficult, but also impacts controllability of the attempted dielectrophoretic manipulation. The latter is mostly due to Brownian motion, which increases for smaller particles, while the dielectrophoretic force decreases with the cube of the particle radius (i.e. with the particle volume).

In the literature, both negative [e.g. 317] and positive [e.g. 313 and 315] dielectrophoretic effects on DNA were reported. From the practical aspect, an interesting approach of measuring the DNA polarisability has been described in [315]. By measuring the initial collection rate of DNA molecules right after the dielectrophoretic force has been applied, the polarisability can be calculated at different frequencies of the applied voltage. In this experiment, the low frequency dielectrophoretic trapping force was not sufficient, which was attributed to electrophoretic and electrohydrodynamic forces that were masking the dielectrophoretic effect. At high frequencies (100 kHz to 10 MHz) there disruptive effects are smaller in magnitude, and most of the experimental work and theoretical

analysis was done in that frequency range. The frequency dependence of the DNA polarisability has been measured by taking the average of several repeated experiments. The repeatability of the experiments may find even more useful applications in the future devices for dielectrophoretic manipulation of DNA.

In [314], a study is given of the DNA polarisability as a function of frequency and magnitude of the applied voltage and the length of DNA molecules. This study seems to be highly relevant for attempting to separate different populations of DNA in Doctor-on-a-Chip, because it shows how polarisability, and therefore the dielectrophoretic force on DNA, changes those parameters, which can be modified for different DNA populations and different separation arrays (see figure 4.2). In terms of the voltage magnitude and frequency, the results were similar to above-mentioned measurement of DNA polarisability based on initial rate collection [315]. In other words, the polarisability of DNA molecules decreases with the frequency of the applied voltage, and hence higher voltages are needed for controllable manipulation of DNA at higher frequencies. With the magnitude of the voltage kept at a fixed value, more DNA molecules were collected near electrodes at lower frequencies. Dependence of DNA polarisability on the length of DNA is such that shorter DNA molecules had smaller polarisability than the longer ones, but the polarisability per base pair was higher for smaller molecules. This indicated that longer DNA molecules do not behave as rod-shaped objects under influence of dielectrophoresis, and that the polarization of DNA is related to the counterion cloud fluctuations [315].

In conclusion, separation of DNA molecules on a Doctor-on-a-Chip device is envisaged only conceptually, as shown in section 4.1, and has not yet been proven in practice. However, the published results from other researchers, some of which are described in this section, show that understanding of the effects and polarisation mechanisms in DNA in electric fields increases and polarisability of different DNA molecules can be measured with repeatable experimental methods. The qualitative diagram of DNA polarisability based on frequency has shown consistency between multiple independent experiments [313-315], and seems to have sound theoretical explanation. The overall dielectrophoretic force also depend on the size of the DNA [315], since total polarisability of the molecule and average polarisability of the molecule per base pair seem to be a function of the DNA molecule length, as describe in the text above. It is also reported that DNA

molecules experience both positive and negative dielectrophoresis, which presents another advantage of the method and potential usage in the dielectrophoretic separation of DNA. Different DNA populations under investigation in Doctor-on-a-Chip can have different sizes, based on the PCR amplification protocols and the sizes of the PCR primers of different types of DNA. This essentially means that we can potentially use PCR to get different polarisability values for different types of DNA, which can be used in the dielectrophoretic separation process.

The separation of latex spheres by using the electrodes as shown in figure 4.3 has been described in section 4.1 and also in [205]. The method is based on the negative dielectrophoretic effect, and the idea that different DNA molecules experience different force magnitude due to different polarisabilities. As described in section 4.1, by switching the voltage to different electrodes in a sequential manner, and by having different dielectrophoretic mobility for different types of DNA due to different sizes (both the drag force and the dielectrophoretic force depend on the size of the molecule), it could be possible to separate different DNA molecules by using this layout of microelectrodes. Obviously, the method needs to be proven by performing exhaustive experimental work to prove that all of these assumptions are valid in practice, and that it is indeed possible to separate DNA molecules in a highly reliable and repeatable manner.

4.4. Comparison with existing DNA detection device based on DEP

A device for preparation of DNA sample and hybridization analysis of the sample on a bioelectronic chip was published in [306]. The analysis has been performed on the same containing E. coli and human red blood cells. As a comparison, this section gives an overview of the publication and the differences between the Doctor-on-a-Chip concept and the method proposed in that publication.

The method described in [306] is done on two different chips. One chip is used for sample preparation and isolation of E. coli DNA/RNA from human blood cells. The second chip used in the analysis performed the function of hybridization of isolated DNA/RNA and detection based on biotinylated capture probes located on the surface of the chip. The transfer of DNA/RNA from one chip to the other was performed with additional steps of off-chip thermal denaturation and fragmentation. Although the analysis was performed by using two chips, as opposed to Doctor-on-

a-Chip concept which assumes only one chip for the entire analysis, this should not be taken as a significant difference between the two methods, because the two chips used in [306] could probably be integrated into one with the advances of the microfabrication technology in the past two decades. Therefore, in this text the fact that the analysis was done on two chips will not be given any significance from the comparison standpoint.

The first chip in [306] consists of microelectrodes for dielectrophoretic separation of E. coli cells and human red blood cells. The separation of two different types of cells is shown in figure 4.5. The microelectrodes are essentially located in the area of white dots in the figure, where the voltage applied to the electrodes caused the electric field maxima. The electric field minima are located in the areas between the electrodes.

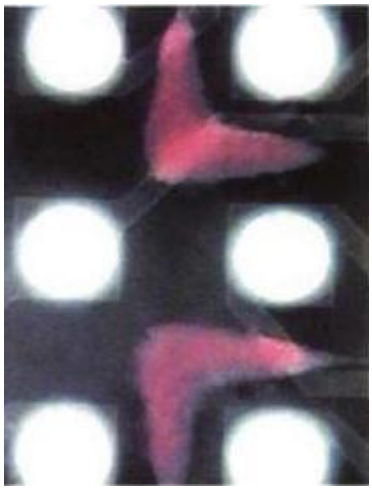

Figure 4.5. E. coli trapped in the areas of electric field maxima (white dots; on top of the microelectrodes), and human red blood cells trapped in the areas of electric field minima (red L-shaped concentrations of particles between the electrodes) [306]

By separating the cells as shown in figure 4.5, the red blood cells can easily be washed away from the chip by using a separation buffer, since they are held in the electric field minima by the relatively weak negative dielectrophoretic force. On the other hand, the E. coli cells remain trapped near the electrodes by the relatively strong positive dielectrophoretic force. Figure 4.6 shows that only the E. coli cells remained on the chip after the red blood cells were washed away.

After the dielectrophoretic separation, the E. coli cells were subjected to the electronic lysis process to break the cell walls and extract the DNA molecules. The

process consisted of a series of pulses applied between the microelectrodes (400 pulses of magnitude equal to 500V and duration equal to 50μs, with polarity altered every 20 pulses). The lysate mixture on the chip was incubated at 50 °C for 20 minutes, to allow for the proteins to be digested by proteinase K in the washing buffer. As the analysis showed, both DNA and RNA were released with no structural damage to the nucleic acids.

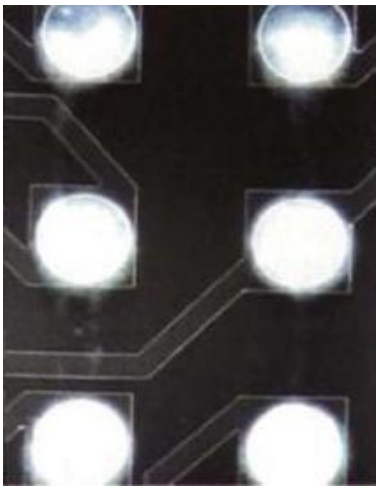

Figure 4.6. E. coli trapped in the areas of electric field maxima, with red blood cells washed away [306]

The next step in the analysis is removing the lysates from the first chip and transferring them to the second chip for hybridization, but only after they were diluted in hybridization buffer and thermally denatured. The second chip or the so-called assay chip was coated with streptavidin-agarose and loaded with biotinylated capture probes at specific microlocations above electrodes by using electronic addressing [306]. The target sequences, including both the lysate target and the model target, were examined by a "sandwich hybridization assay", in which the target DNA/RNA was caught first by an immobilized capture probe and then tagged by a second binding probe, i.e. reporter or signal probe, which contains a fluorophore. The chip was then examined with optical techniques to investigate hybridization of target DNA/RNA to known probes, and thus verify the analysis.

When comparing the device described in this section and [306] with Doctor-on-a-Chip proposed concept, the first thing that should be noted is that the two devices fall into two distinct categories of microsystems for the analysis of nucleic acids. As described in section 2.2, there are surface based and microfluidic based

systems for DNA/RNA analysis. Doctor-on-a-Chip falls into the second category, as the protocol implemented on the chip is using microfluidic elements (i.e. pumps, mixers and channels) to transfer and mix different liquids as described with the DNA extraction, purification and PCR amplification protocols. On the other hand, the device in [306] falls into the surface based category of microsystems, as the main method of detection includes the probes attached to the known locations on the surface of the microchip. After the mixture containing the DNA/RNA molecules is washed over that surface, hybridization occurs and the nucleic acids are attached to the probes of complementary sequence and tagged with fluorescent material to allow for the optical detection and analysis.

There are several advantages of Doctor-on-a-Chip over the surface based microsystems. Doctor-on-a-Chip is capable of using smaller quantities of target DNA and all of the ingredients necessary to implement the protocol for DNA extraction and purification. This makes the analysis cheaper and likely faster. The fact that smaller volumes are used in Doctor-on-a-Chip should not affect the quality and reliability of the analysis, since using PCR for target DNA amplification increases the number of DNA molecules and thus facilitates later steps in the analysis (dielectrophoretic separation and optical detection). PCR is another advantage over the device described in [306], which does not include PCR and therefore needs sufficient quantities of DNA for surface based analysis. The PCR amplification protocol could be integrated with the device in [306] between lysis and hybridization, but in this case it would probably be done by using the standard laboratory techniques (as there is no mention of PCR chips in the paper). This would increase the overall run time of the analysis, as on-chip PCR, such as the one incorporated into Doctor-on-a-Chip, is much faster due to smaller thermal mass of the sample (smaller volume).

Another advantage of Doctor-on-a-Chip over surface based microsystems for DNA analysis is the detection method. The impedance detection method described in sections 2.4 and 4.1 is very simple to implement and should be sufficiently sensitive and reliable for this application. As described in section 4.1, the fact that this method does not provide DNA sequence-based detection should not be of any particular importance, since the dielectrophoretic separation of DNA should be sequence-based and serve as a filter that separates the target DNA from any other DNA present in the sample, for each dielectrophoretic array shown in figure 4.2.

Compared to the impedance measurement method, the surface based microsystems regularly use optical methods for DNA detection, which are sequence specific due to the fact that we know the sequence of each probe at any particular microlocation on the chip surface, but their disadvantage is that they require expensive equipment and therefore are not suitable for any application outside of well equipped laboratories.

Finally, a significant difference between the two devices is how they use dielectrophoresis. Doctor-on-a-chip uses it for separation of DNA molecules into distinct populations, i.e. for filtering out the target DNA from the other DNA molecules in the sample. On the other hand, the device described in [306] uses the dielectrophoretic force to separate the cells of interest from the blood cells, and in this way making the cells ready for lysis without any noise being introduced into the analysis from unwanted DNA molecules (such as those from human blood). The usage of dielectrophoresis thus presents a fundamental difference between the two devices. In Doctor-on-a-Chip, the separation of DNA by the dielectrophoretic force presents a huge challenge, because it yet remains to be seen if it is possible to separate different DNA molecules in this way in a general purpose array such as the one shown in figure 4.2. On the other hand, the usage of the dielectrophoretic force on cells has already been thoroughly investigated and studied, and therefore it should be possible to separate the human blood cells from many different viral and bacterial cells by using the method proposed in [306] for separating E. coli. One potential advantage of the dielectrophoretic separation of DNA as proposed with Doctor-on-a-Chip, as opposed to the usage of dielectrophoresis in [306], is reducing the complexity of surface-based analysis microsystems. If dielectrophoresis proves to be a feasible method for precise manipulation of DNA and separation of different DNA molecules, the system based on that method should be much simpler and easier to produce and more affordable and easier to handle.

The chapter ends with the proposal for Doctor-on-a-Chip, which includes all the steps in the analysis of DNA, including extraction, amplification, and manipulation of DNA molecules with electric field, and finally DNA molecules detection. The proposal utilizes a novel method for separation of particles by dielectrophoresis, which allows investigation of multiple pathogens within the sample at the same time.

Chapter 5. Program for numerical modelling of dielectrophoresis

In this chapter, a more detailed description of the numerical algorithms for modelling the dielectrophoretic effects will be described. An overview will be given of the main equations used in the numerical analysis of the dielectrophoretic force and the temperature distribution within the microchannel. This will be followed by an overview of numeric methods for solving partial differential equations, and more detailed overview of the program building blocks.

As described in the paper [201], the assumption for the dielectrophoretic effect modelling is that the conductivity and permittivity of the suspending medium are temperature dependent values, and that the temperature depends on the electric field. The main equation for calculating the electric potential distribution is given in equation (3.12), which can be re-written in a slightly different form as:

$$\nabla\left[\left(\sigma + i\omega\varepsilon\right)\nabla\varphi\right] = 0 \tag{5.1}$$

In the general form of this equation, the electric potential φ is a complex value. Another equation describing the temperature dependency on the electric field strength is given as [199]:

$$\lambda\nabla^2 T + \sigma E^2 = 0 \tag{5.2}$$

Here, λ is the thermal conductivity of the suspending liquid. Since the conductivity and permittivity of the liquid are temperature dependent and used in equation (5.1) to calculate the electric potential distribution, and since the temperature profile is dependent upon the electric field as shown with equation (5.2), the two equations above are mutually dependent and are solved iteratively.

Both equations are solved by using the finite difference method, as will be described in sections 5.1 and 5.2. Equation (5.1) will be refereed to in the following text as an electrical problem, and equation (5.2) will be referred to as a thermal problem. Both programs need to have boundary conditions defined in order to converge. Typically, these boundary conditions are either Dirichlet or Neumann boundary conditions. Dirichlet boundary condition for partial differential equations specifies the values a solution is to take on the boundary of the domain. For example, a typical Dirichlet boundary condition in the electrical problem described

with equation (5.1) specifies that the values of the potential at the boundary occupied with the microelectrodes are equal to the voltage applied to these microelectrodes. On the other hand, a Neumann boundary condition specifies the values of the derivative of the solution at the boundary of the domain. For example, in the electrical problem described with equation (5.1) the Neumann boundary condition defines the values of the electric field at the boundary of the problem (since the differential equation is being solved for the potential, and the derivative of the potential is equal to the electric field).

The solution of the problem described with equations (5.1) and (5.2) starts with solving equation (5.1) by using the finite difference method. The values for conductivity and permittivity are temperature dependent and described with a set of equations, depending on the medium in question. At the beginning, a temperature of 300 K is assumed in all of the mesh points in the electrical problem. Hence, the conductivity and permittivity profiles are assumed to be constant during the finite difference solution of equation (5.1).

After the electric potential profile is obtained, the values of the electric field are calculated in all of the mesh points in the electrical problem. These electric field values are then used to calculate the temperature profile by using the finite difference method on equation (5.2).

After the temperature profile is obtained, the values for the conductivity and permittivity are calculated by using the temperature values in all of the mesh points. Then, equation (5.1) is solved again by using those updated values for the conductivity and permittivity. The new electric field distribution is again used to solve equation (5.2) for temperature, and the iterative process continues. The solution converges to the solutions of both electrical and thermal problems, but it never reaches exactly those solutions due to the inherent inaccuracy of the numerical model. The solution for the temperature profile is assumed to be sufficiently accurate when two successive temperature solutions differ for less than some specified value in all of the mesh points in the thermal problem (in all of the analyses in this chapter, the value of 0.001 is taken as a rule of thumb, which means that the thermal problem will be assumed to be solved when the difference in temperature in all of the mesh points is smaller than 0.001 K between two successive iterations). For that last thermal problem iteration, the electric potential

distribution is solved for once more, and the electric field profile resulting from that potential is taken as final.

The descriptions of the electrical and thermal problems are input into the program via a set of files, as will be described in section 5.2. The pseudo-algorithm of the program can be written as follows:

1) Read the input files describing the electrodes, voltage, mesh, and boundary conditions,
2) Set up the electrical and thermal problems by converting the user friendly parameters from the input files into an internal representation, which is more suitable for numerical calculation,
3) Calculate the first electrical potential distribution based on the constant values of the conductivity and permittivity,
4) Calculate the first temperature profile based on the first iteration of the electrical potential solution,
5) Update the values of the conductivity and permittivity, which are temperature dependent, and solve for the potential distribution again. Continue with the iterative process of the potential and the temperature calculations until the specified criterion is met for the thermal problem,
6) Solve for the last electric potential iteration and calculate the electric field and the dielectrophoretic force on the suspended particles.

The following section gives a short overview of some numeric methods available for solving partial differential equations, and describes why the finite difference method is chosen over other methods.

5.1. Numeric methods for solving partial differential equations

This section gives an overview of some of the most important methods in the numeric analysis and modeling of partial differential equations (PDE). Although there are many numeric methods available for solving PDEs in three dimensions, only a subset of applicable ones will be addressed here. They are finite difference method, finite element method, finite volume method, and boundary element method. Eventually, the finite difference method was taken as a method of choice and implemented in the program as a way to calculate electric potential and temperature distribution profiles.

Finite difference method

The finite difference method is a way to approximate the solution to differential equations by replacing derivative expressions with equivalent (approximate) differential quotients. By definition, the first derivative of a function *f* is given by the following equation:

$$f'(x) = \lim_{h->0} \frac{f(x) - f(x-h)}{h} \tag{5.3}$$

For some small value of *h*, a reasonable approximation of this equation can be given by the following equation:

$$f'(x) \approx \frac{f(x) - f(x-h)}{h} \tag{5.4}$$

This essentially means that the value of the derivative of the function *f* in the point *x* is given by the difference between the values of that function in the point *x* and an adjacent point, divided by the distance between these two points. There are three ways of representing the difference between two points: the forward difference, the backward difference and the central difference. They are represented by the following three equations, respectively:

$$\nabla_h[f](x) = f(x+h) - f(x) \tag{5.5a}$$

$$\nabla_h[f](x) = f(x) - f(x-h) \tag{5.5b}$$

$$\nabla_h[f](x) = f(x+\frac{1}{2}h) - f(x-\frac{1}{2}h) \tag{5.5c}$$

From these equations, the following three ways of representing the function derivatives can be deduced:

$$f'(x) = \lim_{h\to 0} \frac{f(x+h) - f(x)}{h} \approx \frac{f(x+h) - f(x)}{h} \tag{5.6a}$$

$$f'(x) = \lim_{h\to 0} \frac{f(x) - f(x-h)}{h} \approx \frac{f(x) - f(x-h)}{h} \tag{5.6b}$$

$$f'(x) = \lim_{h\to 0} \frac{f(x+\frac{1}{2}h) - f(x-\frac{1}{2}h)}{h} \approx \frac{f(x+\frac{1}{2}h) - f(x-\frac{1}{2}h)}{h} \tag{5.6c}$$

In a similar way, the second order derivative can be calculated from the first order derivatives using the finite difference approximation. For example, if the central difference method is assumed, the second order derivative can be approximated as:

$$f''(x) \approx f'(x+\frac{1}{2}h) - f'(x-\frac{1}{2}h) \tag{5.7}$$

If we substitute equation (5.6c) into equation (5.7), we get the following approximation for second order derivative of the function f:

$$f''(x) \approx \frac{f(x+h) - 2f(x) + f(x-h)}{h^2} \tag{5.8}$$

This equation can easily be expanded in the same way to approximate any order of the function derivative with the finite difference between adjacent points. Also, it should be noted that although the equations above describe the solution for a one-dimensional model, the finite difference method can be applied on a problem in any number of dimensions. For example, in a three-dimensional model, equation (5.4) would be separately applied on *x*, *y* and *z* derivatives of the function, by using six adjacent points surrounding the point in question for which we are calculating the value of the function derivative.

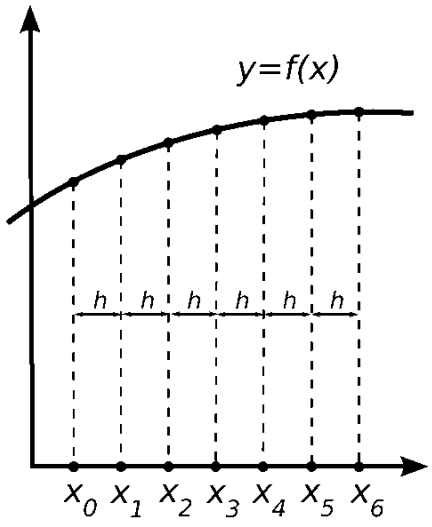

Figure 5.1. Mesh lines and mesh points for 1-D finite difference method

In order to use the finite difference method to solve a partial differential equation, the domain of the problem needs to be defined with a set of discrete

points. This is usually done by dividing the domain into a uniform grid, such that in each direction (for example *x*, *y* and *z* in a three-dimensional model) a certain number of mesh lines is defined, and the mesh points lie at the intersections of these mesh lines. For a one-dimensional domain, the problem is much simpler, as shown in figure 5.1.

It is obvious that the accuracy of this method depends mostly on the number of mesh points in the model, such that a higher number of mesh points (i.e. denser mesh) provides more accuracy. On another hand, the greater number of mesh points requires more compute power, because the function value must be solved separately in each mesh point and stored in the computer memory during the calculation. Therefore, a trade-off should be made between the required accuracy and the simulation time and system requirements, to achieve the most optimum setup.

It is also possible to use finite difference method in the case where the mesh is not uniform, i.e. the distance between the mesh lines is not constant. This is very valuable in large simulation domains that can be divided further into sub-domains, some of which do not require great accuracy because they are far away from the area of interest, and some of which require greater accuracy because we want to investigate, for example, the dielectrophoretic force magnitude in that area in more detail. In this case, the mesh lines would be sparser in the area of less interest (to reduce the need for compute power), and they would be denser in the area of high interest (to increase the accuracy). In this case, the first order derivative can be replaced with the following equation:

$$f'(x) \approx \frac{f(x+d_1) - f(x-d_2)}{d_1 + d_2} \tag{5.9}$$

Here, d_1 is a distance between the mesh point of interest and the adjacent mesh point to the right, while d_2 represents the distance to the adjacent point to the left. It should be noted that in this case the equations for approximation of the higher order derivatives become even more complex. This is because the number of variables and operations is increased in the case of the non-uniform mesh. For example, we are using two variables d_1 and d_2 in equation (5.9), instead of only one variable h in equation (5.4) that represents a uniform mesh. The increase in run time, however, could be offset by the decrease in the overall number of mesh points in the

areas of less importance, so the overall run time might actually decrease. The memory consumption also decreases, again due to the smaller number of mesh points.

For the purpose of simulating dielectrophoretic effect by using the program described throughout the rest of this chapter, the finite difference method is chosen primarily due to the fact that it is very simple and easy to set up, and uses regular mesh (either equidistant in terms of two adjacent mesh lines, or not). To achieve better accuracy with faster run times and less memory consumption, the non-uniform mesh is completely supported in the program. This allows the user to increase the number of mesh points near the tips of the microelectrodes, where the gradient of the electric field is greater, and so is the magnitude of the dielectrophoretic force. To compensate for this increase in the number of mesh points near the electrodes, the user can specify a sparse mesh in the areas away from the microelectrodes. This is explained in more details in section 5.2.5.

Finite element method

In the final element method the domain of the problem is divided into sub-domains or so called elements, with nodes located on interelement lines and/or inside the elements. The numerical solution takes on discrete values in these nodes, and in each element the solution is approximated by a simple geometrical shape. This is usually a polynomial function of the independent variables interpolating between the values in those nodes that belong to the same element.

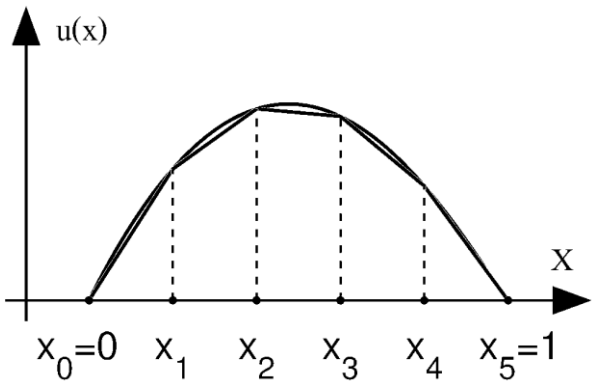

Figure 5.2. Finite element approximation of a function

Figure 5.2 shows an example of a one dimensional function approximated by pieces of straight line. This approximation can be expressed as a linear combination of basis function given with the following equation:

$$u(x) \approx \sum_{n=1}^{N} \varphi_n(x) u_n \tag{5.10}$$

Here, u_n is a value that the function u(x) takes in each of the N points in figure 5.2. The basis functions can be seen in figure 5.3. They are given for each x_n as a piecewise linear function between x_{n-1} and x_{n+1}. For example, for x_3, the function can be written as:

$$\varphi_3 = a_1 x + b_1, x_2 \le x \le x_3 \tag{5.11a}$$

$$\varphi_3 = a_2 x + b_2, x_3 \le x \le x_4 \tag{5.11b}$$

$$\varphi_3 = 0, elsewhere \tag{5.11c}$$

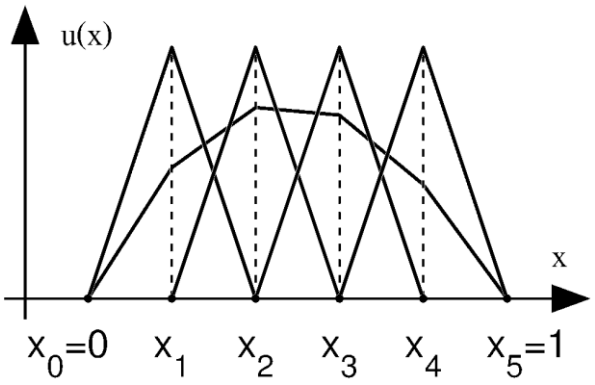

Figure 5.3. Basis functions for each element

In other words, for each node the basis function is defined in three domains. The first is between the node in question and the previous node, and for this segment the function is expressed as a line with parameters a_1 and b_1. Similar function with parameters a_2 and b_2 is defined for the second segment between the node in question and the next one. Elsewhere (i.e. outside of these two segments) the function is equal to zero. It is obvious from these equations that for any given node, only the basis functions of the elements that touch that node actually add to the value of the main function u(x) in that node, while the other elements do not. After obtaining the elemental equations, the assembly is performed. A simple way of assembly is to write equations for each element in the global form and then add each similar

equation of all the elements. The boundary conditions are applied to assembled equation and then are solved by a suitable solver. Then, post-processing is carried out to obtain the derivatives.

For example, this method can be used to solve the following problem in the domain between 0 and *l*:

$$-\frac{d^2U}{dx^2} = F(x) \tag{5.12}$$

$$U(0) = U(l) = 0 \tag{5.13}$$

Equation (5.13) represents boundary conditions. A simple application of the finite-element method is obtained by dividing the domain into N discrete elements of length Δx_n:

$$0 = x_0 < x_1 < ... < x_n < x_{n+1} < ... < x_{N+1} = l \tag{5.14}$$

By representing the solution by equation (5.10) and by using the Galerkin method [301], the Galerkin equations are found:

$$0 = \int \varphi_n (-\sum_m \frac{d^2\varphi_m}{dx^2} u_m - F) dx \tag{5.15}$$

Furthermore, function F(x) can be approximated in a similar fashion to equation (5.10):

$$F(x) \approx f(x) \approx \sum_{n=1}^{N} \varphi_n(x) f_n,\ fn \equiv F(x_n) \tag{5.16}$$

After evaluation of the integrals [301], the solution for node n is given by:

$$0 = \frac{u_{n-1} - 2u_n + u_{n+1}}{\Delta x^2} + \frac{1}{6}(f_{n-1} + 4f_n + f_{n+1}) \tag{5.17}$$

Here, the index *n* represents one node out of many used to approximate the solution with the finite elements. When the system of equations for all indexes is written out to be passed to the solver, the matrix of coefficient will be sparse, i.e. most of the elements in the matrix will be zero. This is similar to the finite difference method, because in both cases the solution in any given mesh point is only affected by the surrounding points (i.e. the points belonging to the same finite element in the finite element method).

Figure 5.4 shows a two dimensional case of the domain with a circular boundary. The domain is divided into triangular elements, which is a typical shape of an element for two dimensional problems. For such irregular boundaries, the finite element method is more suitable than the finite difference method, because it would be difficult to come up with a finite difference scheme over an irregular grid, and it is equally difficult to generate a regular grid over irregular boundaries. In general, the finite difference method in its basic form is restricted to handle rectangular shapes and their most basic alterations. However, for the purpose of solving electric potential and temperature distribution in the dielectrophoretic separation systems, the finite difference method can be a method of choice, due to the fact that it is simpler to implement, and it is probably accurate enough because most of the shapes in these systems are regular (i.e. rectangular).

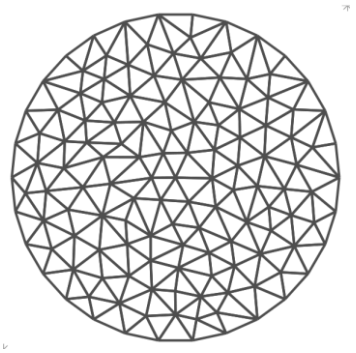

Figure 5.4. Triangular finite elements for two-dimensional problem [301]

In general, when deciding whether to use finite difference or finite element method in this program, one of the most important considerations was the simplicity of grid generation. In three dimensional domains, writing a general purpose engine for mesh generation for irregular boundaries naturally seems much more complex then generating a regular mesh such as the one used in finite difference method. It is estimated that in most case finite difference method with non-uniform grid (i.e. non-uniform distances between parallel mesh lines) should provide sufficient accuracy for modeling the dielectrophoretic effect.

Finite volume method

The finite volume method is a method for solving PDEs in the form of algebraic equations. Similar to the finite difference method, the values are calculated

at discrete mesh points. The most significant difference, however, between the finite volume method and the finite difference method is that the former uses the integral representation of the problem, while the latter uses the differential form. One of the main drawbacks of finite difference methods is their break down near discontinuities in the solution where the differential equation does not hold [302]. The finite volume refers to the small volume surrounding each node point on a mesh. Instead of pointwise approximations at mesh points, in the finite volume method the domain is broken into grid cells and approximate the total integral of the function over each grid cell. These values are modified in each time step by the flux through the edges of the grid cells, and the primary problem is to determine good numerical flux functions that approximate the correct fluxes reasonably well. Because the flux entering a given volume is identical to that leaving the adjacent volume, these methods are conservative. One of the most attractive features of the finite volume method is that, in general, it can easily be implemented on unstructured meshes [303].

The following paragraph shows an example of using the finite element method [303]. The partial differential equation in this example is Laplace's equation, which is one of the most studied elliptic PDEs. The problem is given as:

$$\nabla^2 u(x, y) = 0, (x, y) \in \Omega \tag{5.18}$$

The integral formulation of the equation is given by:

$$\int_{\Omega} \nabla^2 u d\Omega = \int_{\Gamma} \frac{\partial u}{\partial n} dS = 0 \tag{5.19}$$

Here, Ω is the volume, Γ is the surface, dS is the surface element, and n is the unit vector pointing outward on the surface of the element. In the case of simple regular grid points $(i\Delta x, j\Delta y)$, the control volume is a cell centered at $(i\Delta x, j\Delta y)$ with a size of Δx along x-axis and Δy along y-axis. Thus the boundary integral on any cell consists of four parts integrated on each of the four sides. We can use these simple approximations:

$$\frac{\partial u}{\partial x} = \frac{u_{i+1,j} - u_{i,j}}{\Delta x} \tag{5.20a}$$

$$\frac{\partial u}{\partial y} = \frac{u_{i,j+1} - u_{i,j}}{\Delta y} \tag{5.20b}$$

The solution then becomes:

$$\int_{\Omega i,j} \frac{\partial u}{\partial n} d\Omega = \frac{\Delta y}{\Delta x}(u_{i+1,j} + u_{i-1,j} - 2u_{i,j}) + \frac{\Delta x}{\Delta y}(u_{i,j+1} + u_{i,j-1} - 2u_{i,j}) = 0 \qquad (5.21)$$

Dividing both sides with $\Delta x \Delta y$ and letting $\Delta x = \Delta y = h$, we obtain:

$$(u_{i+1,j} + u_{i,j+1} + u_{i-1,j} + u_{i,j-1}) - 4u_{i,j} = 0 \qquad (5.22)$$

Equation (5.22) in many ways resembles the finite difference method, and actually represents the Laplace operator for a 5-point differencing scheme [303].

In literature, most of the problems solved by finite volume method have some kind of time dependence, such as computational fluid dynamics [302]. For solving equations such as (5.1) and (5.2), the finite volume method, according to equation (5.22), seems to be giving the same scheme as the finite difference method described earlier in the section.

Boundary element method

The boundary element method uses the integral form of partial differential equations, similar to the finite volume method. It is based on a reduction of a boundary value problem on a domain to an equivalent problem defined on the boundary [304]. The dimension of the problem is thus reduced by one. The boundary element method attempts to use the given boundary conditions to fit boundary values into the integral equation, rather than values throughout the space defined by a partial differential equation. This is in direct contrast to usual spatial domain methods (finite difference, finite element and finite volume), which use trial functions to satisfy the essential boundary conditions exactly, and then seek to satisfy the governing field equations approximately via minimizing an objective function [305]. In the boundary element method, once the boundary solution is obtained, post-processing can be done to calculate the values in any internal points in the domain. The method is very efficient in terms of computing power and simulation time, compared with the other methods, in the cases where surface to volume ratio is relatively small. However, for many problems the boundary element method seems to be much less efficient than the other methods described in this section. This is primarily due to the fact that this method results in fully populated

matrices once the solution is calculated in all of the mesh points internal to the domain. On the other hand, as mentioned earlier in this section, the spatial domain methods result in sparse matrices where most of the elements are equal to zero, because only the mesh points/elements in the immediate vicinity of the point/element in question have impact on its value. The compute power requirements are thus dramatically reduced.

Based on the preliminary investigation of the method, without going into too much details regarding its potential implementation in the program for general purpose of three dimensional simulation of dielectrophoresis, it seems that it is not suitable for this problem where the solution in the points internal to the domain are equally and often more important than the values on the boundary. The finite difference method seems again to be more usable in terms of simplicity of the implementation and compute power and simulation run time requirements.

5.2. Program building blocks

In this section, the algorithm to iteratively solve equations (5.1) and (5.2) by using the finite difference method is described with more details on the particular implementation. Each function of the program is described with the set of inputs and outputs, and the short description of the functionality it represents. The prototype of the function (i.e. the function declaration written in the C++ programming language) is given in appendix A. The names of the parameters are listed in this section in under input and output specification for easier cross-reference between this section and appendix A.

5.2.1. Function read_main_input_file

Input to the function:

- The name of the main input file (char fileName[]).

Outputs from the function:

- The dimensions of the overall structure (float &xWidth, float &yWidth, and float &zWidth),
- The mesh specification (float **xMesh, float **yMesh, float **zMesh),
- The specification of material interfaces (float **materialInterface),

- The specification of the area for the electric field calculation (float &xMinEl, float &xMaxEl, float &yMinEl, float &yMaxEl, float &zMinEl, and float &zMaxEl),
- The number of boundaries in the electric field calculation (int &numBoundsEl),
- The number of electrodes (int &numElecs),
- The number of different voltages applied to electrodes (int &numVoltages),
- The geometric specification of boundaries for electric field calculation, separately for the real (boundary **boundsEl_i) and imaginary (boundary **boundsEl_j) electric field components,
- The specification of the electrodes: the applied voltage, shape, size and location (electrode **elecs),
- The specification of the voltages: the amplitudes of the real and imaginary parts of the complex voltage (float **voltages), and
- The frequency of the applied voltage (float &freq)

Description:

The function read_main_input_file reads the main file, which contains values of the parameters necessary for electrical field calculation. In other words, this file is always required in order to run the program. Below is an example of a main input file for a castellated system of microelectrodes used in several references for dielectrophoretic manipulation of particles [e.g. 200]. The layout of the microelectrodes is shown in figure 5.5.

```
X_WIDTH 60
Y_WIDTH 30
Z_WIDTH 130
X_MESH 1 U 0 60 2
Y_MESH 1 U 0 30 2
Z_MESH 3 U 0 60 2 U 60 104 2 U 104 130 2
MATERIAL_INTERFACE 2 0 60 0 30 70 70 0 60 0 30 100 100
EL_PROBLEM 0 60 0 30 70 100
NUM_EL_BOUNDS 6
NUM_ELECTRODES 2
NUM_VOLTAGES 2
ELB1 0 60 0 0 70 100 N 0 N 0
```

```
ELB2 60 60 0 30 70 100 D 2 D 2
ELB3 0 60 30 30 70 100 N 0 N 0
ELB4 0 0 0 30 70 100 N 0 N 0
ELB5 0 60 0 30 70 70 N 0 N 0
ELB6 0 60 0 30 100 100 N 0 N 0
E1 R 0 20 0 30 70 70 1 300
E2 R 20 40 15 30 70 70 2 300
V1_i 10
V1_j 0
V2_i 0
V2_j 0
FREQ 10.0e6
```

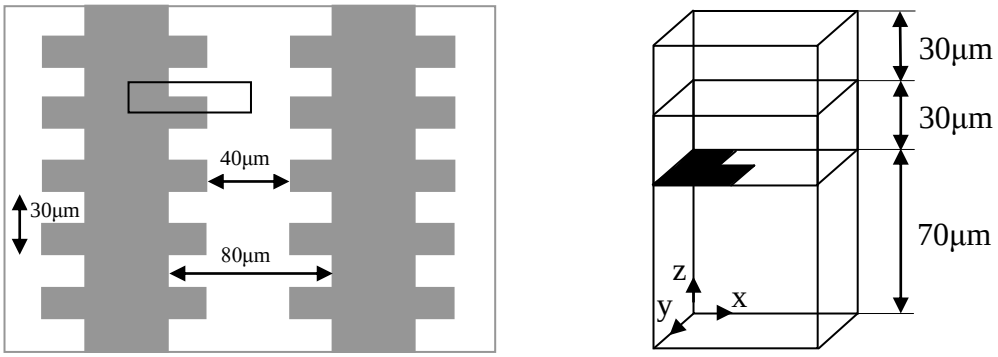

Figure 5.5 Top view and side view of castellated system of microelectrodes. The black rectangle on the left figure represents the cross-section given on the right figure

The problem is three-dimensional. The microelectrodes are fabricated on a glass substrate 70 microns thick. The microelectrodes are covered with another glass plate 60 microns thick. The microchannel 30 microns in depth is etched in the cover plate and the particles are suspended in the liquid inside the microchannel. Therefore, we have 70 microns thick glass, 30 microns deep microchannel, and 30 microns of glass covering the microchannel.

To describe the electrical problem, we have to define the boundaries, the mesh size, the microelectrodes, the voltage applied to the microelectrodes, and the frequency of the voltage. In the main input file, the first three lines always define the width of the overall structure in all three dimensions: X_WIDTH, Y_WIDTH and Z_WIDTH. In this case they are 60, 30 and 130 microns (the substrate plus the cover), respectively. It should be noted that in this case we will add the calculation

of the temperature distribution in the glass and liquid, and therefore the boundaries of the electrical problem do not correspond to the boundaries of the overall structure. This is because the electric field distribution is calculated only in the liquid, and the temperature distribution is calculated in both the glass and the liquid.

The next three lines define the mesh in all three directions: X_MESH, Y_MESH, and Z_MESH. The mesh can be defined as a uniform (the distance between the mesh lines is constant across an axis), or a non-uniform mesh. In the latter case, the distance between the mesh lines is not constant across the axis. For example, the mesh lines could be denser in the area where we want to increase the accuracy of the results, and sparser in the area where the accuracy is not critical. In this way we significantly improve the computation by means of memory usage and speed. The details about the mesh definition in this example will be discussed in more details in section 5.2.5.

The next line defines interfaces between the materials, in this case the glass and the liquid. There are two interfaces defined in this example: one is between the top of the substrate and the liquid, and the other one is between the liquid and the top of the microchannel. The material interfaces are only important in the calculation of the temperature, and therefore, we only look at the top and bottom interfaces (in x-y plane). Other interfaces (in x-z and y-z planes) are not important, because they are always described in the temperature calculation as boundaries with Neumann or Dirichlet boundary conditions. This line always starts with MATERIAL_INTERFACE, followed by the definitions of the interfaces. The first number denotes the number of interfaces (2 in this case), followed by sets of six numbers describing the start and end points in all three directions. The first six numbers are related to the first interface (i.e. the interface between the top of the substrate and the liquid) in the following way: (i) 0 and 60 denote that the first interface spreads between 0 and 60 microns in x direction; (ii) the following 0 and 30 denote that the first interface spreads between 0 and 30 microns in y direction; and (iii) the following 70 and 70 denote that the first interface is in x-y plane at the height of 70 microns. The following six numbers (0, 60, 0, 30, 100 and 100) are related to the second interface (i.e. the interface between the liquid and the top of the microchannel) in the same way.

The next line starts with EL_PROBLEM and defines the area for the electric field calculation. It goes from 0 to 60 microns in x direction, from 0 to 30 microns in

y direction, and from 70 to 100 microns in z direction. This apparently encloses only the liquid, because the glass is not included in electric field calculation, as will be described later in the text.

The following line starts with NUM_EL_BOUNDS and denotes the number of boundaries for electrical problem calculation. There are six boundaries in this example.

The next line defines the number of different voltages applied to the microelectrodes. For example, if there are four microelectrodes, each one of those can have a different voltage applied to it (e.g. 4-phase voltage in an electrorotation chamber), and four voltages would have to be specified in the main input file. In this example, we have two electrodes and two voltages with same amplitudes and opposite phases (the difference of 180º). Therefore, NUM_VOLTAGES equals 2.

The following lines ELB0 to ELB5 describe the boundaries of the area for the electric field calculation. The number of these lines (i.e. the number of boundaries) equals NUM_EL_BOUNDS, which equals 6 in this case. The first six numbers describe the width of a boundary in x, y and z directions. For example, the first boundary ELB0 spreads from 0 to 60 microns in x direction, from 0 to 0 in y direction, and from 70 to 100 microns in z direction. In other words, this is an x-z plane going from the bottom to the top of the microchannel. The physical description of a boundary is followed by the definition of its boundary condition for the electric field calculation, which can be Neumann (N) or Dirichlet (D). There are two electrical boundary conditions for each boundary: one for the real part of the complex potential value, and one for its imaginary part. It should be noted that we are working with voltages of sine wave, and each voltage is described with the amplitudes of their real (φ_R) and imaginary (φ_I) parts ($\varphi = \varphi_R + i\varphi_I$). In the case of ELB1 (the second electrode defined in the input file), we have Neumann boundary condition for both the real and the imaginary parts of the potential. The first 'N' is related to the real part and the second 'N' to the imaginary part. The zeros denote the values of the boundary conditions. In the case of ELB2 we have Dirichlet conditions for both the real and the imaginary parts of the potential. The number 2 associated to a Dirichlet boundary condition values denotes that the value of the boundary conditions equals the specification of voltage V2 (i.e. the second voltage in the list of defined voltages). In other words, the Dirichlet boundary condition for φ_R and φ_I equals 0 V for boundary ELB2.

After the specification of the boundaries, the electrodes have to be specified by means of their location, size, shape and the applied voltage. There are two electrodes in this example: E1 and E2. The first parameter specified in the electrode's definition is its shape. The electrodes can have one of the following geometrical shapes: rectangle (R), triangle (T), circle (C), ellipse (E) and a hyperbole (H). If an electrode has a more complex shape that can be described with a combination of the above mentioned shapes, a user can do so by specifying more than one electrode in the list to describe only one electrode. For example, if an electrode is of a general quadrangular shape, it can be specified by two electrodes of a triangular shape, which are connected to the same voltage and "glued" together to give the desired electrode. In this example E1 and E2 are rectangular electrodes. The numbers following the shape specification (in this case 'R') define the size and the location of the electrode. In this case the electrode E1 is rectangular, and spreads from 0 to 20 microns in x direction (the first two numbers following 'R'), from 0 to 30 in y directions (the next two numbers), and from 70 to 70 in z direction. In other words, E1 is located in x-y plane at 70 microns above the bottom of the substrate, and has zero thickness. The following number (1) denotes that the voltage applied to the electrode is specified in the list of voltages at the first place, i.e. it is V1 in the example file. In the same way, we define that the voltage applied to E2 is V2. The last number (300) defines the temperature of the electrode in Kelvin in the case when the electrode is assumed to be at the fixed temperature when calculating the temperature distribution in the liquid and glass. In temperature distribution calculation the electrodes can be assumed to have the fixed temperature of a certain value (in this case 300 K), or they can be neglected in the temperature distribution calculation. In any case, the temperature of the electrode has to be specified in the input file, and based on the value of the parameter isElectrodeThermTransparent defined in the thermal input file, it is decided in the program if this value is going to be used in the program or not.

Electrode shape specification

As already stated, the electrodes can have either a shape of a rectangle, triangle, circle, ellipse or a hyperbole. This example above shows how a rectangular electrode is specified: we have six numbers specifying the limits in all three

directions, and in this way we define the location and the size of the electrode. The following text explains how electrodes of the other four shapes are specified. The internal representation of the electrodes might not be based on the parameters specified in the input file, because there are several ways to geometrically describe the same geometrical shape and some are more suitable for certain mathematical problems, such as to determine if a mesh point lies on the electrode or not (which is important, because if a point lies on an electrode, its potential is known, and otherwise it has to be calculated with the finite difference method). More about internal representation of certain shapes of electrodes will be given in sections 5.2.14 and 5.2.15.

Each electrode specification line starts with E*n*, where *n* is the electrode's index. This is followed by the specification of the electrode's shape, which, as already stated, can be one of the following: R (rectangle), T (triangle), C (circle), E (ellipse) and H (hyperbole). The shape specification is followed by a set of numbers which specify the electrode's location and size, and the way this set is specified depends on the electrode's shape. The last two numbers in the electrode's specification always specify the same parameters, as described in the example file: the penultimate number specifies the index of the voltage (in the list of voltages in the main input file) which is connected to the electrode, and the last number specifies the temperature of the electrode for the temperature distribution calculation.

The following text specifies how the size and the location of the electrode are specified for all the shapes of the electrodes (the rectangular electrode is described in the example above, and we proceed with the four other shapes).

For a triangular electrode, the three points of the triangle are specified: x1, y1 and z1 for the first point, x2, y2 and z2 for the second point, and x3, y3 and z3 for the third point. The order in which the points are specified is not important. This representation is converted to another representation of the triangle within the program, and it will be described in more details in 5.2.14. It is important to note that the triangular electrode is limited in a way that the three angles of an electrode must all be less or equal to 90˚, or otherwise the program will not generate valid results. We can get around this problem by specifying two or more electrodes if an angle greater than 90˚ is needed. Here is an example of a triangular electrode specification:

```
E1 T 10 40 70 30 30 70 10 50 70
```

The letter *T* designates the electrode as triangular, and the numbers that follow are used to represent the three points enclosing the triangle. Each point is represented with three numbers, namely x, y and z coordinates, as stated in the previous paragraph. By looking at the numbers, it is apparent that the triangular electrode is in the x-y plane at 70 microns above the bottom of the structure, and with the vertices at the coordinates (10, 40), (30, 30), and (10, 50). All distances are in microns.

For a circular electrode, again three points are specified. It would be more straightforward to specify the circular electrode with a radius and the coordinates of the centre, but then it would not be possible to specify an electrode which is just a part of the circle, for example one quarter of a circle. The points we specify are the centre of a circle and two end points of an arc, see figure 5.10 in section 5.2.15. The order in which we specify the three points is important in this case, in a sense that the first specified point always represents the centre of the circle. The order of the other two points is not important. Similar to the triangular electrode specification, the circular electrodes are limited by means of a maximum portion of a circle that can be specified: the maximum is one quarter of a circle. If this constraint is violated, the program generates invalid results. If more than a quarter of a circle is needed, more than one electrode must be specified. For example, for a whole circle we would have to specify four quarters of a circle that make up a circle when glued together by the program. Below is an example of a circular electrode specification:

```
E1 C 10 10 70 20 0 70 20 20 70
```

The electrode is in the x-y plane at 70 microns height, the centre of the electrode is at the point (10, 10), and the two end points are at (20, 0) and (20,20). The order in which we specify the other two points apart from the centre of the circle is not important.

5.2.2. Function read_thermal_input_file

Input to the function:

- The name of the input file for temperature distribution calculation (char fileName[]).

Outputs from the function:

- The specification of the area for temperature calculation (float &xMinTh, float &xMaxTh, float &yMinTh, float &yMaxTh, float &zMinTh, float &zMaxTh),
- The number of boundaries for temperature calculation (int &numBoundsTh),
- The geometric specification of boundaries for temperature calculation (boundary **boundsTh),
- The switch (int &isElectrodeThermTransparent) defining the electrodes as being transparent for temperature calculation (equal to 1 in that case) or at the room temperature (equal to 0).

Description:

Function read_thermal_input_file reads the file which contains values of the parameters necessary for temperature calculation. This file does not need to be specified, because the temperature distribution is not required in order to calculate the electric field and the dielectrophoretic force. It is up to the user to decide if the temperature distribution has to be taken into account or not. The program reads this file and collects the parameters defined in it only if the switch CALCULATE_THERMAL_PROBLEM is set to 1 (true). Otherwise the function is not executed and later on the temperature is not taken into account when calculating the electric field.

Below is an example of a thermal problem file for the system of microelectrodes described in section 5.2.1.

```
TH_PROBLEM 0 60 0 30 0 130
NUM_TH_BOUNDS 6
THB1 0 60 0 0 0 130 N 0
THB2 60 60 0 30 0 130 N 0
THB3 0 60 30 30 0 130 N 0
THB4 0 0 0 30 0 130 N 0
THB5 0 60 0 30 0 0 D 300
THB6 0 60 0 30 130 130 D 300
IS_ELECTRODE_THERM_TRANSPARENT 1
TEMP_ERROR 0.05
```

As stated there, the main file always needs to exist and in that file we specify the parameters related to the overall problem (mesh specification, dimensions of the overall structure and material interfaces). Therefore, the thermal problem file needs only to specify the parameters of the thermal problem, i.e. calculation of the temperature distribution.

The first line describes the area for the temperature calculation. This line starts with TH_PROBLEM followed by six numbers. The first two specify the boundaries in the x direction (the area spreads from 0 to 60 microns in the x direction in this example), the middle two specify the boundaries in the y directions (between 0 and 30 microns in this example), and the final two specify the boundaries in the z direction (going from 0 to 130 microns in this example).

The next line starts with NUM_TH_BOUNDS and specifies the number of boundaries in the temperature distribution calculation. In this case the area has a shape of a rectangular parallelepiped, and hence there are six boundaries.

The following lines specify those boundaries. The lines start with THB1 to THB6. The following six numbers describe the width of a boundary in x, y and z directions. For example, the first boundary THB1 spreads from 0 to 60 microns in x direction, from 0 to 0 in y direction, and from 0 to 130 microns in z direction. This is therefore an x-z plane going from the bottom to the top of the structure. The physical description of a boundary is followed by the definition of its boundary condition for the temperature calculation, which can be Neumann (N) or Dirichlet (D). In the case of THB1, we have Neumann boundary condition, and its value equals 0. In the case of THB5 we have Dirichlet boundary conditions with the value of 300, which means that the temperature on this boundary is constant and equal to 300 K.

The next line defines the parameter, which specifies if the electrodes are transparent for the thermal problem calculation. This parameter, defined as a global configuration parameter, is called IS_ELECTRODE_THERM_TRANSPARENT. If it is equal to zero, the electrodes are assumed to be transparent for the temperature distribution calculation. If IS_ELECTRODE_THERM_TRANSPARENT is equal to 1, the electrodes are assumed to be at a fixed temperature.

The last line defines the parameter called TEMP_ERROR. It is used in the iterative calculation of the temperature distribution, as already described at the beginning of chapter 5. The first step in the calculation of the temperature and the electric field is the electric field calculation with the temperature assumed to be 300

K in all the mesh points throughout the structure. After the electric field distribution is obtained, the temperature distribution is calculated by taking into account the electric field distribution. Then the field is again calculated by taking into account the temperature and in this way the iterative steps are repeated. The difference in the temperatures between two successive iterations is calculated in all of the mesh points. If that difference is less than TEMP_ERROR in all of the points, the solutions for the electric field and the temperature are considered to be sufficiently accurate, and the iterative calculation is stopped.

5.2.3. Function read_fluid_input_file

Input to the function:

- The name of the input file for fluid flow calculation (char fileName[]).

Outputs from the function:

- The specification of the area for fluid flow calculation (float &xMinTh, float &xMaxTh, float &yMinTh, float &yMaxTh, float &zMinTh, float &zMaxTh),
- The number of boundaries for fluid flow calculation (int &numBoundsTh),
- The geometric specification of boundaries for fluid flow calculation (boundary **boundsFl_x, boundary **boundsFl_y, boundary **boundsFl_z, boundary **boundsFl_p

Description:

Function read_fluid_input_file reads the file, which contains values of the parameters necessary for fluid flow calculation. This file does not need to be specified, because the drag force on particles due to the fluid flow (of any origin) might in some cases be neglected when compared to the dielectrophoretic force. It is up to the user to decide if the drag force needs to be taken into account for better accuracy or not. The program reads this file and collects the parameters defined in it only if the switch CALCULATE_FLUID_PROBLEM is set to 1 (i.e. true). Otherwise the function is not executed and later on the fluid drag force is not taken into account when calculating the particles trajectories.

Below is an example of a fluid problem file for the system of microelectrodes described in section 5.2.1.

```
FL_PROBLEM 0 60 0 30 70 100
```

```
NUM_FL_BOUNDS 6
FLB1 0 60 0 0 70 100 N 0 N 0 N 0 N 0
FLB2 60 60 0 30 70 100 N 0 N 0 N 0 N 0
FLB3 0 60 30 30 70 100 N 0 N 0 N 0 N 0
FLB4 0 0 0 30 70 100 N 0 N 0 N 0 N 0
FLB5 0 60 0 30 70 70 D 0 N 0 N 0 N 0
FLB6 0 60 0 30 100 100 D 0 N 0 N 0 N 0
```

As stated in section 5.2.1, the main file always needs to exist, and there we specify the parameters related to the overall problem (mesh specification, dimensions of the overall structure and material interfaces). Therefore, the fluid problem file needs only to specify the parameters of the fluid problem, i.e. calculation of the fluid flow. These are described in the following text.

The first line describes the area for the temperature calculation. This line starts with FL_PROBLEM followed by six numbers. The first two specify the boundaries in x direction (the area spreads from 0 to 60 microns in the x direction in this example), the middle two specify the boundaries in the y directions (between 0 and 30 microns in this example), and the final two specify the boundaries in the z direction (going from 70 to 100 microns in this example).

The next line starts with NUM_FL_BOUNDS and specifies the number of boundaries in the temperature distribution calculation. In this case the area has a shape of a rectangular parallelepiped, and hence there are six boundaries.

The following lines specify those boundaries. The lines start with FLB1 to FLB6. The following six numbers describe the width of a boundary in the x, y and z directions. For example, the first boundary FLB1 spreads from 0 to 60 microns in the x direction, from 0 to 0 in y direction, and from 70 to 100 microns in z direction. This is therefore an x-z plane going from the bottom to the top of the microchannel. The physical description of a boundary is followed by the definition of its boundary conditions for the fluid flow calculation, which can be Neumann (N) or Dirichlet (D). There are four boundary conditions for each boundary. The first three are related to the x, y, and z components of the flow vector, respectively, and the last one is related to the pressure distribution. In the case of FLB1, we have Neumann boundary condition for all the flow vector's components and the pressure, and their values are all equal to 0. In the case of FLB4 we have Dirichlet boundary condition

for the x component of the flow vector with the value of 0, which means that it is constant and equal to 0 on this boundary.

5.2.4 Function rewrite_input_file

Inputs to the function:

- All the parameters read into the program from the main input file, and the parameters read from the thermal input file and the fluid input file, if those files are specified. The parameters in question include the overall dimensions of the structure, the boundaries for the electrical, thermal and fluid problems, the boundaries, the electrodes, the voltages applied to the electrodes, etc.

Output from the function:

- The file called rewritten_inputs.txt in the outputfiles directory. The file should resemble the input files (main, thermal and fluid altogether in one file) and it should be easy to visually inspect if all the parameters were successfully read into the program.

Description:

The purpose of this function is to create a file called rewritten_inputs.txt, which should serve to a user as a sanity check if all the parameters from the input files were successfully read into the program. This should reduce the possibility of getting false results by the program if a user makes a lexical mistake while typing the input files.

The rewritten_inputs.txt file for the example described in sections 5.2.1 through 5.2.3 is given below:

```
X_WIDTH 60
Y_WIDTH 30
Z_WIDTH 130
X_MESH 1 1 0 60 2
Y_MESH 1 1 0 30 2
Z_MESH 3 1 0 60 2 1 60 104 2 1 104 130 2
MATERIAL_INTERFACE 2 0 60 0 30 70 70 0 60 0 30 100 100
EL_PROBLEM 0 60 0 30 70 100
NUM_EL_BOUNDS 6
NUM_ELECTRODES 2
NUM_VOLTAGES 2
```

```
ELB1 0 60 0 0 70 100 N 0 N 0
ELB2 60 60 0 30 70 100 D 2 D 2
ELB3 0 60 30 30 70 100 N 0 N 0
ELB4 0 0 0 30 70 100 N 0 N 0
ELB5 0 60 0 30 70 70 N 0 N 0
ELB6 0 60 0 30 100 100 N 0 N 0
E1 R 0 20 0 30 70 70 0 300
E2 R 20 40 15 30 70 70 0 300
V1 10
V2 0
V3 0
V4 0
FREQ 1e+007
TH_PROBLEM 0 60 0 30 0 130
NUM_TH_BOUNDS 6
THB1 0 60 0 0 0 130 N 0
THB2 60 60 0 30 0 130 N 0
THB3 0 60 30 30 0 130 N 0
THB4 0 0 0 30 0 130 N 0
THB5 0 60 0 30 0 0 D 300
THB6 0 60 0 30 130 130 D 300
IS_ELECTRODE_THERM_TRANSPARENT 1
TEMP_ERROR 0.05
FL_PROBLEM 0 60 0 30 70 100
NUM_FL_BOUNDS 6
FLB1 0 60 0 0 70 100 N 0 N 0 N 0 N 0
FLB2 60 60 0 30 70 100 N 0 N 0 N 0 N 0
FLB3 0 60 30 30 70 100 N 0 N 0 N 0 N 0
FLB4 0 0 0 30 70 100 N 0 N 0 N 0 N 0
FLB5 0 60 0 30 70 70 D 0 N 0 N 0 N 0
FLB6 0 60 0 30 100 100 D 0 N 0 N 0 N 0
```

The first part of the file is an exact copy of the main input file described in section 5.2.1. It starts with the dimensions of the overall structure (X_WIDTH, Y_WIDTH and Z_WIDTH), and ends with the frequency of the applied voltage. In between there is also the definition of the mesh, the interface of materials, the dimensions of the electrical problem, the number of electrical boundaries, the

number of microelectrodes, the number of different voltages applied to the microelectrodes, the boundaries of the electrical problem, the microelectrodes, and the voltages.

The second part of the file is an exact copy of the thermal input file described in section 5.2.2. It starts with the dimensions of the thermal problem, followed by the number of the boundaries in the thermal problem, the specification of the boundaries (the shape and location), the parameter TEMP_ERROR, and the parameter IS_ELECTRODE_THERM_TRANSPARENT.

The final part of the file is an exact copy of the fluid input file described in section 5.2.3. It defines the dimensions of the fluid problem, the number of the boundaries for the fluid problem, and the location and shape of those boundaries.

5.2.5. Function create_mesh_lines

Inputs to the function:

- The mesh specification obtained from the main input files (float *mesh), and
- The name of the axis in question (char axis; this function is run three times: for x, for y and for z axis).

Output from the function:

- The locations of the mesh lines in microns (float **meshLines; each run of the function creates an array of mesh lines, and each axis is assigned a separate array, namely xMeshLines, yMeshLines and zMeshLines in the main function), and
- The file containing the locations of the mesh lines (each run of the function creates a separate file, and we have separate files for the three axis, namely mesh_lines_x.txt, mesh_lines_y.txt and mesh_lines_z.txt).

Description:

This function creates such a representation of the mesh, which is more suitable for the subsequent calculation and manipulation of the mesh points. The locations of the mesh lines are written into files and may be verified by the user. A typical mesh specification in the main input file described in section 5.2.1 could be as follows:

```
Z_MESH 3 N 0 60 3 2 U 60 104 2 N 104 130 2 3
```

This line defines the mesh in the z direction in the flowing way: the first number (3 in this case) specifies how many different sequences there are in which the mesh is specified differently. In this case there are three sequences, as will be described below. Each sequence is specified by a letter 'N' or 'U', followed by the coordinates of the endpoints of the sequence, followed by one or two numbers, as will be described below. The letter associated with a sequence denotes if the mesh lines are distributed in a way that the distance between the adjacent mesh lines is a constant, or changes linearly. In the former case, the sequence is designated with 'U', which stands for uniform, and in the latter case, the mesh is non-uniform and the sequence is designated with 'N'. In the specification above, the first and the last sequence are non-uniform, and the middle one is uniform.

For each sequence, the letter specifying the uniformity of the sequence is followed by the endpoints of the sequence. Thus the first sequence lies between 0 and 60 microns, the second one between 60 and 104 microns, and the third one between 104 and 130 microns.

The final parameter in a sequence specification is the distance between the mesh lines. For a uniform sequence, it is simply a distance in microns between the mesh lines. For example, in the case of the middle sequence listed above, it is 2 microns. For a non-uniform sequence, two numbers are specified: the first one denotes the distance between the mesh lines at the first end of the sequence, and the second one denotes the distance between the mesh lines at the other end. In the case of the first sequence, the first mesh line after the starting point of the sequence will be 3 microns away from the starting point, i.e. at the location where z equals 3 microns (0 + 3 microns). The last mesh line before the end of the sequence will be 2 microns away from the ending point of the sequence, i.e. at the location where z equals 58 microns (60 microns – 2 microns). Between 3 and 58 microns, the distance between the mesh lines decreases linearly, and falls in the range between 3 and 2 microns (why it sometimes does not will be explained in more details in the following text).

The mesh lines obtained from the specification above lie at the following locations:

```
0, 3, 5.95652, 8.86957, 11.7391, 14.5652, 17.3478, 20.087,
22.7826, 25.4348, 28.0435, 30.6087, 33.1304, 35.6087,
```

38.0435, 40.4348, 42.7826, 45.087, 47.3478, 49.5652, 51.7391, 53.8696, 55.9565, 58, 60, 62, 64, 66, 68, 70, 72, 74, 76, 78, 80, 82, 84, 86, 88, 90, 92, 94, 96, 98, 100, 102, 104, 106, 108.139, 110.417, 112.833, 115.389, 118.083, 120.917, 123.889, 127, 130.

Note that the distance between the mesh lines at 123.889 and 127 microns is 3.111 microns, i.e. greater than 3 microns, which should be an upper limit, as explained in the last paragraph. The reason for this discrepancy will be described in section 5.2.6, but for now it should be said that this does not affect the accuracy of the results, because it is irrelevant if the distance between the mesh lines equals 3 microns or slightly more or slightly less, due to the nature of the finite difference method. However, a user should be aware that a situation like this might occur.

5.2.6. Function create_nonuniform_mesh

Inputs to the function:

- The mesh specification obtained from the main input files (float *mesh), and
- The index of the mesh sequence within the array *mesh (int i). For example, the mesh specification in 5.2.5 (`Z_MESH 3 N 0 60 3 2 U 60 104 2 N 104 130 2 3`) would generate the values for I equal to 0, 1 and 2, for the first, second and third sequence, respectively.

Output from the function:

- The array of distances between the adjacent mesh lines within the sequence in question (float **array), and
- The integer nPart equal to the number of mesh lines minus 1 (int &nPart).

Description:

This function is called within the function create_mesh_lines. As stated above, create_mesh_lines rewrites the mesh specification in a way which is more suitable for use in the finite difference method and other algorithms. Create_nonuniform_mesh is called when the mesh specification that create_mesh_lines deals with is a non-uniform one, i.e. the distances between the adjacent mesh lines is not a constant. Such a representation exists in the example in section 5.2.5:

(…) `N 104 130 2 3`

As stated in that section, this specifies the mesh between 104 and 130 microns, in a way that the distance between the mesh lines at the left end is equal to 2 microns, the distance between the mesh lines at the right end is equal to 3 microns, and the distance between the mesh lines in between these endpoints increases linearly from 2 to 3 microns.

As stated above, this function returns the array of distances between the adjacent mesh lines (float **array), and the number of mesh lines minus 1 (int &nPart).

In the example above, we will use the following notation: x_1 = 104 microns, x_2 = 130 microns, y_1 = 2 microns and y_2 = 3 microns. The number of mesh lines n is equal to:

$$n = \frac{2*(x_2 - x_1)}{y_1 + y_2} + 1 \tag{5.23}$$

In the case above, this is equal to 11.4. Obviously, the number of mesh lines has to be an integer; hence we round the number to 11. There are therefore 11 mesh lines between 104 and 130 microns, including those two mesh lines at 104 and 130 microns. The integer nPart is equal to the number of mesh lines minus one, i.e. 10.

The distance between the mesh lines increases linearly from left to right, and therefore the location of mesh lines changes linearly. The distance between the first and the second mesh line is equal to y_1, i.e. 2 microns. The distance between the second and the third mesh line is equal to $y_1 + \Delta y$, where Δy is a constant for which the distance between the mesh lines changes (in this case decreases) going from the beginning to the end of the grid. The distance between the third and the fourth mesh lines is $y_1 + 2\Delta y$, and so forth. The distance between the penultimate and the last mesh lines is equal to $y_1 + (nPart - 1)\Delta y$, but also to y_2, i.e. 3 microns. Therefore, we can calculate Δy using the following equation:

$$\Delta y = \frac{y_2 - y_1}{nPart - 1} \tag{5.24}$$

Using the values for the necessary parameters as in the example above, Δy calculates to 0.111 microns. As described above, in general case we introduce an error to this calculation, because nPart does not always calculate to an integer, but

we round it to an integer. If we sum together all the distances between the mesh lines using the values for y_1, y_2, nPart and Δy, the result would be:

$$\Delta Y = nPart * y_1 + \frac{nPart(nPart-1)}{2}\Delta y \tag{5.25}$$

In the example above, this equals 25 microns. The correct result, however, is obviously equal to $y_2 - y_1$, which, in our example, equals 26 microns. The difference between the two is taken into account and added to Δy to eliminate the abovementioned error. If we denote this difference with D (in our example D equals 1 micron), then we add a portion of D to Δy for all of the distances between the mesh lines except for the first one and the last one (that is why the parameters y_1 and y_2 remain as defined in the specification, i.e. 2 and 3 microns, respectively). There are nPart-2 mesh distances to which we add this compensation, and therefore, its value can be calculated by using the following equation:

$$\Delta D = \frac{2D}{(nPart-1)(nPart-2)} \tag{5.26}$$

In our example, ΔD equals 0.0277 microns, and therefore the modified value for Δy equals 0.1388 microns. Compared to the old value of 0.111 microns, it is a change of 25%. As mentioned in the text above, we do not change the distance between the first and the second, and the penultimate and the last mesh lines – they remain as specified in the input file. That is the reason why some distances between the mesh lines may be greater then the upper limit, as mentioned in section 5.2.5, where the actual Δy increases above the value that compensates the rounding of number of the mesh lines.

5.2.7. Function calculate_number_mesh_points

Inputs to the function:

- The overall dimensions of the problem (float xWidth, float yWidth, float zWidth),
- The minimum and maximum co-ordinates for the electrical, thermal and fluid problems (float xMinEl, float xMaxEl, float yMinEl, float yMaxEl, float zMinEl, float zMaxEl, float xMinTh, float xMaxTh, float yMinTh, float

yMaxTh, float zMinTh, float zMaxTh, float xMinFl, float xMaxFl, float yMinFl, float yMaxFl, float zMinFl, float zMaxFl), and

- The arrays of mesh lines (float *xMeshLines, float *yMeshLines, float *zMeshLines).

Output from the function:

- The total number of mesh points (int &numPoints) and the number of points in the electrical, thermal and fluid problems (int &numPointsEl, int &numPointsTh, int &numPointsFl, respectively).
- The text file number_of_mesh_points.txt, which contains the values for the total number of mesh points and the number of points in the electrical, thermal and fluid problems.

Description:

This function calculates the total number of mesh points and the number of points in the electrical, thermal and fluid problems. We need these values simply because we need to calculate certain parameters in all of the mesh points, and we do this by using loops. Therefore, we need the number of mesh points to know how many times we need to repeat these loops in the program.

We calculate the number of mesh points within a 3D structure with a regular mesh simply by taking the number of mesh lines parallel to x axis, the number of mesh lines parallel to y axis, and the number of mesh lines parallel to z axis, and by simply multiplying those numbers. For example, if we are looking at the mesh 20 microns wide on all three axis and with the constant distance between the mesh lines of 2 microns, the total number of mesh points is equal to 11^3 or 1331.

5.2.8. Function calculate_number_mesh_lines

Inputs to the function:

- The range in which we are counting the mesh lines (float beginPoint, float endPoint), and
- The array of mesh lines (float *meshLines).

Output from the function:

- The number of mesh lines in the given array of mesh lines within the given range (the function returns this value).

Description:

This function simply counts all of the mesh lines in the given array of mesh lines that lie in the given range specified by two endpoints. For each mesh line, the function checks if it lies within the given range, and if it does, it increments the counter of mesh lines. Otherwise, the counter does not change.

5.2.9. Function create_mesh_distances

Inputs to the function:

- The total number of points (int numPoints),
- The overall dimensions of the problem (float xWidth, float yWidth, float zWidth), and
- The arrays of mesh lines on all three axis (float *xMeshLines, float *yMeshLines, float *zMeshLines).

Output from the function:

- The array that for each mesh point contains the distances of the adjacent mesh points in all three directions (float **meshDistances_fbrlud),
- The arrays of co-ordinates for all of the mesh points (float **x, float **y, float **z), and
- The text files that contain co-ordinates for all of the mesh points: x.txt, y.txt, and z.txt (all of the co-ordinates are written into separate files).

Description:

To calculate gradients of certain three dimensional variables in all of the mesh points, it is necessary to know not only the index of the mesh point in which we calculate the gradient, but also the distances between the mesh point in question and the mesh points in front of it, behind it, on the right hand side, on the left, above it, and under it. This function generates the array of those distances for all of the mesh points (six elements for each mesh point).

For example, a mesh point can be assumed with co-ordinates x = 10, y = 8, and z = 17 microns, and its index in the array of mesh points is 1922. If the mesh lines around this point are 1 micron away, the adjacent points have the following co-ordinates (the indexes are taken randomly for this example):

- (x, y, z) = (12, 8, 17) μm, index = 1921 (this point is “in front” of the given mesh point, because its y and z co-ordinates are equal, and its x co-ordinate is greater than the x co-ordinate of the mesh point in question),

- (x, y, z) = (10, 8, 17) μm, index = 1923 (this point is “behind” the given mesh point, because its y and z co-ordinates are equal, and its x co-ordinate is less than the x co-ordinate of the mesh point in question),
- (x, y, z) = (10, 9, 17) μm, index = 1998 (this point is “on the right” of the given mesh point, because its x and z co-ordinates are equal, and its y co-ordinate is greater than the y co-ordinate of the mesh point in question),
- (x, y, z) = (10, 7, 17) μm, index = 1846 (this point is “on the left” of the given mesh point, because its x and z co-ordinates are equal, and its y co-ordinate is less than the y co-ordinate of the mesh point in question),
- (x, y, z) = (10, 8, 18) μm, index = 2154 (this point is “above” the given mesh point (or “up”), because its x and y co-ordinates are equal, and its z co-ordinate is greaters than the z co-ordinate of the mesh point in question),
- (x, y, z) = (10, 8, 16) μm, index = 1690 (this point is “under” the given mesh point (or “down”), because its x and y co-ordinates are equal, and its z co-ordinate is less than the z co-ordinate of the mesh point in question).

For this mesh point with the index of 1922, number 1 (representing the distance of 1 micron to the adjacent mesh points) would be input six times to the array meshDistances_fbrlud, starting from the array index of 11532 (this is equal to 1922 * 6, because there are 1922 mesh points before this one with indexes from 0 to 1921, and for each of these mesh points we have to write 6 indexes for the 6 points that surround it). That means that the mesh point with the index equal to 1922 occupies the elements of the array from 11532 to 11537. The next element in the array belongs to the mesh point with the index equal to 1923.

The indexes of the surrounding points are always written in the same order, as shown here. This is also suggested by the name of the array – it contains fbrlud. It stands for f(ront), b(ack), r(ight), l(eft), u(p), and d(own).

This function also checks if the mesh point in question lies somewhere at the edge of the structure. For example, all of the points with the z co-ordinate equal to 0 do not have the adjacent mesh point under it (all of the co-ordinates are always positive and 0 represents the edge of structure). In this case, in place of the distance between the mesh points, we write -1. For example, if height of the structure in the example above would be 17 microns, then the point with co-ordinates (10, 8, 18) microns would not exist, and we would write the following to the array: 1921, 1923, 1998, 1846, -1, 1690.

Apart from the array meshDistances_fbrlud, this function also creates the arrays of co-ordinates of the mesh points, namely *x, *y and *z. These arrays contain as many elements as there are mesh points. For example, the first element in the array *x is the x co-ordinate of the mesh point that has the index equal to 0. What follows is the x co-ordinate of the mesh point with the index equal to 1, and so forth. The last element is the x co-ordinate of the point with the index equal to numPoints - 1. The same is the case for the arrays *y and *z.

5.2.10. Function create_relative_index

Inputs to the function:

- The number of points in the electrical, thermal and fluid problems (int numPointsEl, int numPointsTh, int numPointsFl, respectively),
- The arrays of co-ordinates of the mesh points (float *x, float *y, float *z),
- The overall dimensions of the problem (float xWidth, float yWidth, float zWidth),
- The arrays of mesh lines (float *xMeshLines, float *yMeshLines, float *zMeshLines), and
- The minimum and maximum co-ordinates for the electrical, thermal and fluid problems (float xMinEl, float xMaxEl, float yMinEl, float yMaxEl, float zMinEl, float zMaxEl, float xMinTh, float xMaxTh, float yMinTh, float yMaxTh, float zMinTh, float zMaxTh, float xMinFl, float xMaxFl, float yMinFl, float yMaxFl, float zMinFl, float zMaxFl).

Output from the function:

- The arrays that connect the indexes of the mesh points in the electrical, thermal and fluid problems (int **index_El_Th, int **index_El_Fl, int **index_Th_El, int **index_Th_Fl, int **index_Fl_El, int **index_Fl_Th – it will be described in more details in the following text), and
- The text files that store some of the abovementioned arrays, namely index_El_Th.txt (stores *index_El_Th), index_Fl_El.txt (stores *index_Fl_El), index_Fl_Th.txt (stores *index_Fl_Th) and index_Th_El.txt (stores *index_Th_El).

Description:

Overall, there are three problems to be solved: electrical, thermal and fluid problems. Some mesh points belong to all of these problems, and some do not, because the dimensions of the problems are different in general. That is why a single mesh point can have more than one index associated to it, depending on the problem being solved. For example, a mesh point that has the index of 1345 in the electrical problem might have the index of 2419 in the thermal problem. Therefore, it is important to know the relations of these indexes. For example, if a point has an index of 1346 in the thermal problem, what is its index in the electrical problem? We need this, for example, because the temperature distribution depends on the electrical field strength, and vice versa. In other words, the problems we are solving are interconnected.

This function creates six arrays that effectively represent connectivity between the electrical, thermal and fluid problems. As stated above, they are: index_El_Th, index_El_Fl, index_Th_El, index_Th_Fl, index_Fl_El and index_Fl_Th. The abbreviations El, Th and Fl correspond to the electrical, thermal and fluid problems, respectively. The contents of these arrays will be described in the following text.

The indexes of the array belong to the problem stated with the first abbreviation (El, Th or Fl) in the array name. The array values are indexes of the problem stated with the second abbreviation in the array name. For example, index_El_Th connects the electrical and thermal problems. If its 151st element has a value of 1650 (or in other words, index_El_Th[150] = 1650), that means that the point that has the index in the electrical problem equal to 150, has the index in the thermal problem equal to 1650. In the same manner, if index_Th_Fl[1500] = 125, that means that the point that has the index in the thermal problem equal to 1500, has the index in the fluid problem equal to 125.

By using these arrays, we can easily calculate different physical quantities in the same mesh point. For example, let's say that we are looking at the mesh point with the index in the thermal problem equal to 550, and that we have the array of values for the temperature in all the mesh points in the thermal problem (this array is called *temperature*), and the array of values for the electrical field strength in all the mesh points in the electrical problem (this array is called *field*). Because the dimensions of the thermal and electrical problems are not necessarily the same, the indexes of the same points in these two problems might be different in general case.

In other words, the mesh point with the index of 550 in the thermal problem might not have the index equal to 550 in the electrical problem. If we want to know the temperature in this point, it is simply equal to the value of 550^{th} element in the temperature array, i.e. temeperature[550]. If we want to know the value of the electrical field in that point, we can make use of the array index_Th_El. To get the index in the electrical problem of the point that has the index in the thermal problem equal to 550, we take the value of the 551^{st} element in the array index_Th_El. In other words, the electrical field strength in the point in question is equal to field[index_Th_El[550]].

5.2.11. Function find_type

Inputs to the function:

- The array of electrodes (electrode *electrodes) and the number of electrodes (int numElectrodes),
- The array of boundaries (boundary *bounds) and the number of bundaries (int numBounds),
- The co-ordinates of the point (float x, float y, float z), and
- The minimum and maximum co-ordinates (float xMin, float xMax, float yMin, float yMax, float zMin, float zMax).

Output from the function:

- The type of the mesh point: ‘O’, ‘E’, ‘N’, ‘D’, ‘B’, or ‘I’ (the function returns this value). The meaning will be described in the following text.

Description:

This function returns the value of the parameter called type of the mesh point. The type is determined according to the location of the mesh point, i.e. does it lie on the electrode, on the boundary, and so on. As stated above, the type of the mesh point might be one of the following: ‘O’, ‘E’, ‘N’, ‘D’, ‘B’, and ‘I’, as follows:

- ‘O’ denotes the mesh point which lies outside of the boundaries (minimum and maximum co-ordinates) passed to the function.
- ‘E’ denotes the mesh point which lies on an electrode.
- ‘N’ denotes the mesh point which lies on the boundary, and the boundary condition on this boundary is Neumann’s.

- ‘D’ denotes the mesh point which lies on the boundary, and the boundary condition on this boundary is Dirichlet’s.
- It is possible for a mesh point to be a part of two boundaries, or of one boundary and one electrode. An example of this situation is when two boundaries touch and therefore, share some points, or when an entire electrode lies on the boundary between the glass substrate and the suspending liquid. ‘B’ denotes the mesh point that falls in one of these two categories:
    - The mesh point lies on two boundaries and one of those boundaries has a Neumann boundary condition and the other boundary has a Dirichlet boundary condition (if the boundaries have the boundary condition of the same type, the mesh point is of type ‘D’ or ‘N’, and not ‘B’).
    - The mesh point lies on an electrode and on a boundary, which has a Neumann boundary condition (the combination of an electrode and a Dirichlet boundary condition would render a point ‘E’, not ‘B’).
- ‘I’ denotes the mesh point which lies inside the boundaries (minimum and maximum co-ordinates) passed to the function, but does not lie on any of the boundaries or electrodes.

5.2.12. Function iselectrode

Inputs to the function:

- The co-ordinates of the point (float x, float y, float z), and
- The array of electrodes (electrode *electrodes) and the number of electrodes (int numElectrodes).

Output from the function:

- The index of the electrode (member of the array *electrodes) on which lies the mesh point in question.

Description:

This function goes through all of the electrodes in the array *electrodes in search for the electrodes on which the mesh point in question lies. The function goes through each of the electrodes and looks at the type of the electrode to execute the piece of code for that particular electrode. There are separate blocks of code to

check for circular, triangular and rectangular electrodes. If the point in question lies on the electrode, it will have a fixed electric potential during the electrical potential distribution calculation.

5.2.13. Function isboundary

Inputs to the function:

- The co-ordinates of the point (float x, float y, float z), and
- The array of boundaries (boundary *bounds) and the number of bundaries (int numBounds).

Output from the function:

- The array of indexes of the boundaries (members of the array *bounds) on which lies the mesh point in question. The function returns the pointer on this array.

Description:

This function goes through the array of boundaries and looks if the given mesh point lies on any of the boundaries in the array. If it lies on one or more boundaries, it creates an array of indexes of those boundaries that contain the given mesh point and returns the pointer on this array.

For example, let's say that there are 6 boundaries with indexes equal to 0, 1, 2, 3, 4 and 5, and that the mesh point in question lies on 3 of those boundaries, with indexes 1, 3 and 4 (for example, this is possible for a corner of a cube, which always touches three boundaries of the cube). The array that the function returns always has the first element equal to the number of boundaries that the point belongs to. In this case, it is 3. The indexes of those boundaries follow, and the resulting array is [3, 1, 3, 4].

If the mesh point does not belong to any of the boundaries, the array returned by the function would be [0]. The first element is the number of boundaries the point belongs to, and it is equal to zero, and since there are no boundary indexes to add to the array, the first element is also the last.

5.2.14. Function convert_triangular_electrodes

Inputs to the function:

- The array of electrodes (electrode *electrodes) and the number of electrodes (int numElectrodes).

Output from the function:

- The array of electrodes (electrode *electrodes) in which the representation of triangular electrodes is changed in a way that is more suitable for calculation. The details will be described in the following text.

Description:

As stated in section 5.2.1, the shape and the location of the electrodes are specified in the main input file. One of the supported shapes of the electrodes is triangular. When specified, a triangular electrode is defined with the co-ordinates of the three points of the triangle. However, this representation of the triangle is useless in some cases. For example, if a triangle is defined by three points and if there is another point for which it needs to be established whether or not it lies within the triangle or not, the program must perform a certain amount of calculation. Instead of performing those calculations every time some colcaulations need to be done, it is easier to come up with a more suitable representation of a triangle, which eliminates the need for those calculations. This would save a significant amount of time during simulations.

The twelve different types of triangles are given in figure 5.6. Any triangle given by any three points in two-dimensional space can be put into one of those twelve categories. As stated in section 5.2.1, the electrodes of a triangular shape must not have an angle greater than 90°. If there is a need for such an electrode, the user should specify it by dividing it to two triangles that meet this constraint.

To simplify the problem of resolving whether a point lies inside a triangle or not, the representation of triangles by three points (P1, P2 and P3) is converted into representation by three lines that connect these points (Y1, Y2 and Y3). Each line can be described by one of the following equations in the x-y co-ordinate system:

$$y = ax + b \tag{5.27}$$

$$y = c \tag{5.28}$$

$$x = c \tag{5.29}$$

Equation (5.27) represents a general case, with *a* and *b* being any two real numbers. Here, *a* designates the slope of the line, which is positive if the gradient of the line is positive (the value of *y* rises as *x* rises), and it is negative if the gradient of the line is negative (the value of *y* falls as *x* rises). We will limit the parameter *a* to be non-zero ($a \neq 0$) in this case, to make a distinction between equation (5.27) on one hand, and equations (5.28) and (5.29) on the other hand. Equation (5.28) represents a line parallel to x axis, while equation (5.29) represents a line parallel to y axis.

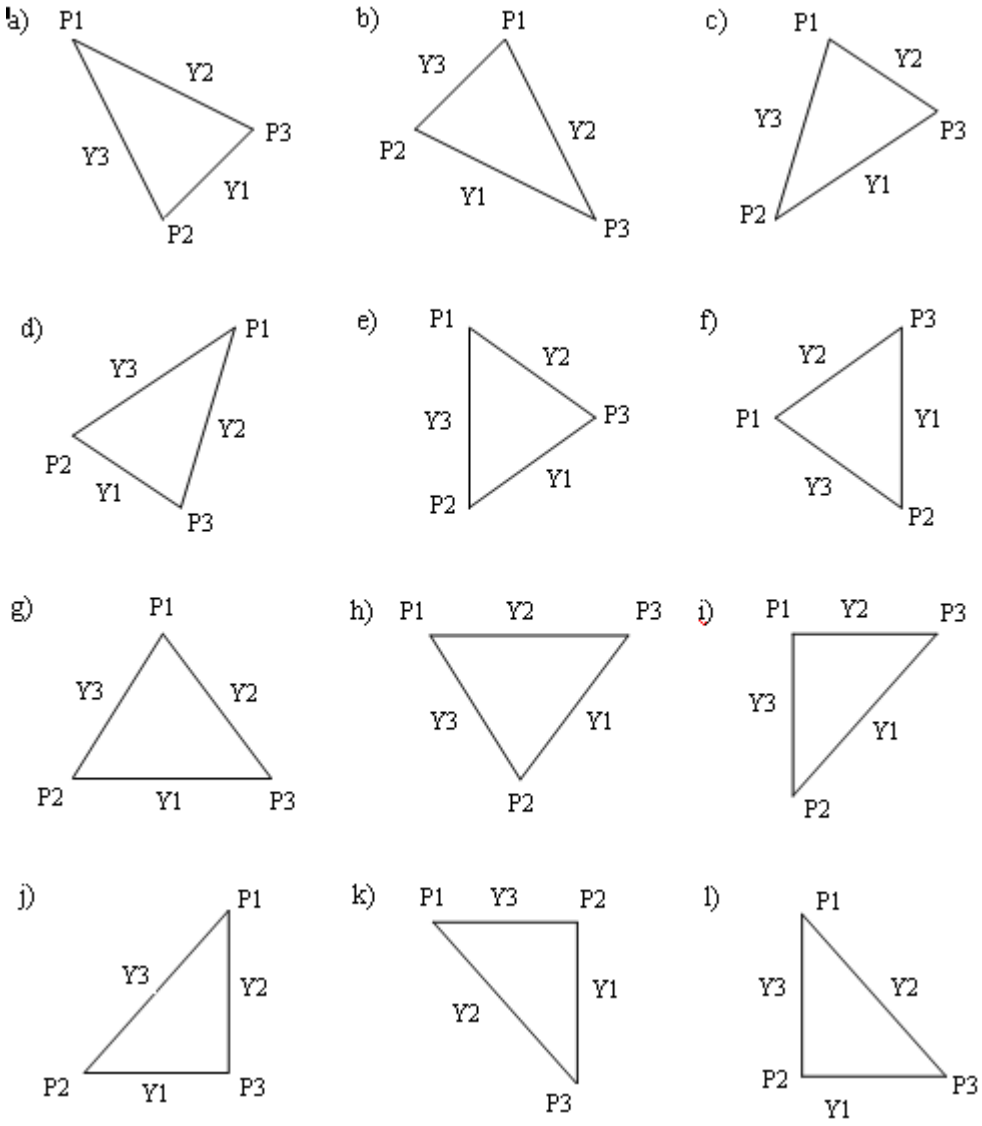

Figure 5.6. Triangular electrodes

From figure 5.2, it is apparent that the first four triangles have all three lines given by equation (5.27). The first two triangles a) and b) have two lines with

parameter *a* being negative and one line with *a* being positive, while c) and d) have two lines with *a* being positive and one with *a* being negative.

The next four triangles e), f), g) and h) have one line described by either equation (5.28) or (5.29), while the other two lines are described by equation (5.27), with one line having *a* as positive and the other one having *a* as negative. The last four triangles i), j), k) and l) have exactly one line described by all the three above equations. Those lines described by equation (5.27) can have a parameter *a* as either positive or negative.

When triangular electrodes are specified in the main input file, they are defined by the co-ordinates of three points: x_1, y_1, z_1, x_2, y_2, z_2, x_3, y_3, and z_3. After we call the function conver_triangular_electrodes, other parameters become important in describing the triangular electrode. They are: a_1, b_1, c_1, a_2, b_2, c_2, a_3, b_3, c_3, t_1, t_2, t_3, *s_point* and *t_type*. The parameters *a*, *b* and *c* are defined as floating point variables, the parameter *t* is a character, and *s_point* and *t_type* are integers. They are described in the following text.

- Parameters *a*, *b*, *c* and *t* are related to the lines of a triangle, and their roles can be understood by looking at equations (5.27) through (5.29). There are three lines in a triangle and therefore three sets of parameters *a*, *b*, *c* and *t*, where *t* basically defines with which equation (5.27) through (5.29) the line can be described, and *a*, *b* and *c* store the values based on parameter *t*.
    - If a line in question is described by equation (5.27), then *a* and *b* are calculated based on the co-ordinates of the end points, while the value of *c* is insignificant. The value of *t* depends on *a*: if *a* is greater than zero, *t* equals '+', and if *a* is less than zero, *t* equals '-'. In other words, *t* stores the sign of parameter *a*.
    - If a line in question is described by equation (5.28), meaning it is parallel to x axis, then *a* and *b* are insignificant, and *c* is calculated from the co-ordinates of the end points of the line. Parameter *t* stores 'Y' in this case, denoting that the equation describing this line is y = c.
    - If a line in question is described by equation (5.29), meaning it is parallel to y axis, then *a* and *b* are again insignificant as in the previous case, while *c* is calculated from the co-ordinates of the end

points of the line. Parameter *t* stores 'X' in this case, denoting that the equation describing this line is x = c.

- The order in which the points are specified in the main input file is irrelevant, as well as the order in which we assign the three lines of a triangle to the parameters *a*, *b*, *c* and *t*. However, to successfully manipulate with the triangle data, we need to have at least one point for which we know where it lies on the triangle. We call this point a significant point, or *s_point*. Obviously, exactly one point in any of the twelve triangles in figure 5.6 can be a significant point:
    - For triangles a) through d), exactly two lines have parameter *a* with the same sign, while the third one has a parameter *a* of the opposite sign. In this case, the significant point is the point where those lines with the same sign of *a* meet. For triangles a), b), c) and d), those points are P_1, P_3, P_2 and P_1, respectively.
    - For triangles e) through h), two lines are described with equation (5.27), and one line is described with either (5.28) or (5.29). A significant point is the point in which the lines that are described with equation (5.27) meet. For triangles e), f), g) and h), those points are P_3, P_1, P_1 and P_2, respectively.
    - For triangles i) through l), one line is described with equation (5.27), one is described with equation (5.28), and one with (5.29). A significant point is the point in which those lines described with (5.28) and (5.29) meet. For triangles i), j), k) and l), the significant points are P_1, P_3, P_2 and P_2.
- The parameter *t_type* denotes the type of triangle by means of different triangles described in figure 5.6. As stated above, if the constraint that all the angles are less or equal to 90˚ is met, any three points in a two-dimensional space will define a triangle that resembles one of the triangles described above and that can be defined with parameters *s_point*, t_*type* and three sets of parameters *a*, *b*, *c* and *t*. There are 12 types of triangles, and therefore *t_type* is an integer that takes the values from 1 to 12. If a triangle resembles the triangle in figure 5.6.a, *t_type* equals 1. If a triangle resembles the triangle in 5.6.b, *t_type* equals 2, and so forth. For example, if the points of a

triangle are (10, 10), (20, 10) and (20, 20) in x-y plane, *t_type* would have a value of 10, because the triangle resembles the triangle in 5.6.j.

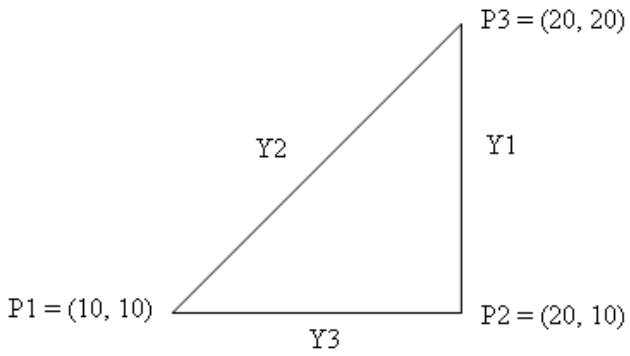

Figure 5.7. Example of a triangular electrode

Figure 5.7 shows an example of a trinagular electrode given with three points P_1, P_2, and P_3, and three lines Y_1, Y_2, and Y_3. The parameter *s_point* in this case would be 2 (the second point in the triangle definition P_2 is the significant point, with co-ordinates (20, 10)). The other parameters would be as follows:

- For Y_1: t_1 = 'X', c_1 = 20 (a_1 and b_1 are irrelevant),
- For Y_2: t_2 = '+', a_2 = 1, b_2 = 0 (c_2 is irrelevant), and
- For Y_3: t_3 = 'Y', c_3 = 10 (a_3 and b_3 are irrelevant).

5.2.15. Function convert_circular_electrodes

Inputs to the function:

- The array of electrodes (electrode *electrodes) and the number of electrodes (int numElectrodes).

Output from the function:

- The array of electrodes (electrode *electrodes) in which the representation of circular electrodes is changed in a way that is more suitable for calculation. The details will be described in the following text.

Description:

As stated before, the shape and the location of the electrodes are specified in the main input file. One of the supported shapes of the electrodes is circular. This function serves the similar purpose as the function convert_triagular_electrodes, i.e.

it converts the representation of the circular electrodes into a format that is more suitable in certain calculations. As stated in section 5.2.14, which covers the function convert_triangular_electrodes, one purpose of this new representation is to facilitate the calculation of whether or not a given point lies on a circular electrode, which is not easy if the circular electrode is defined by only the three points as in the main input file (i.e. the conversion is from a user-friendly format to a program-friendly format).

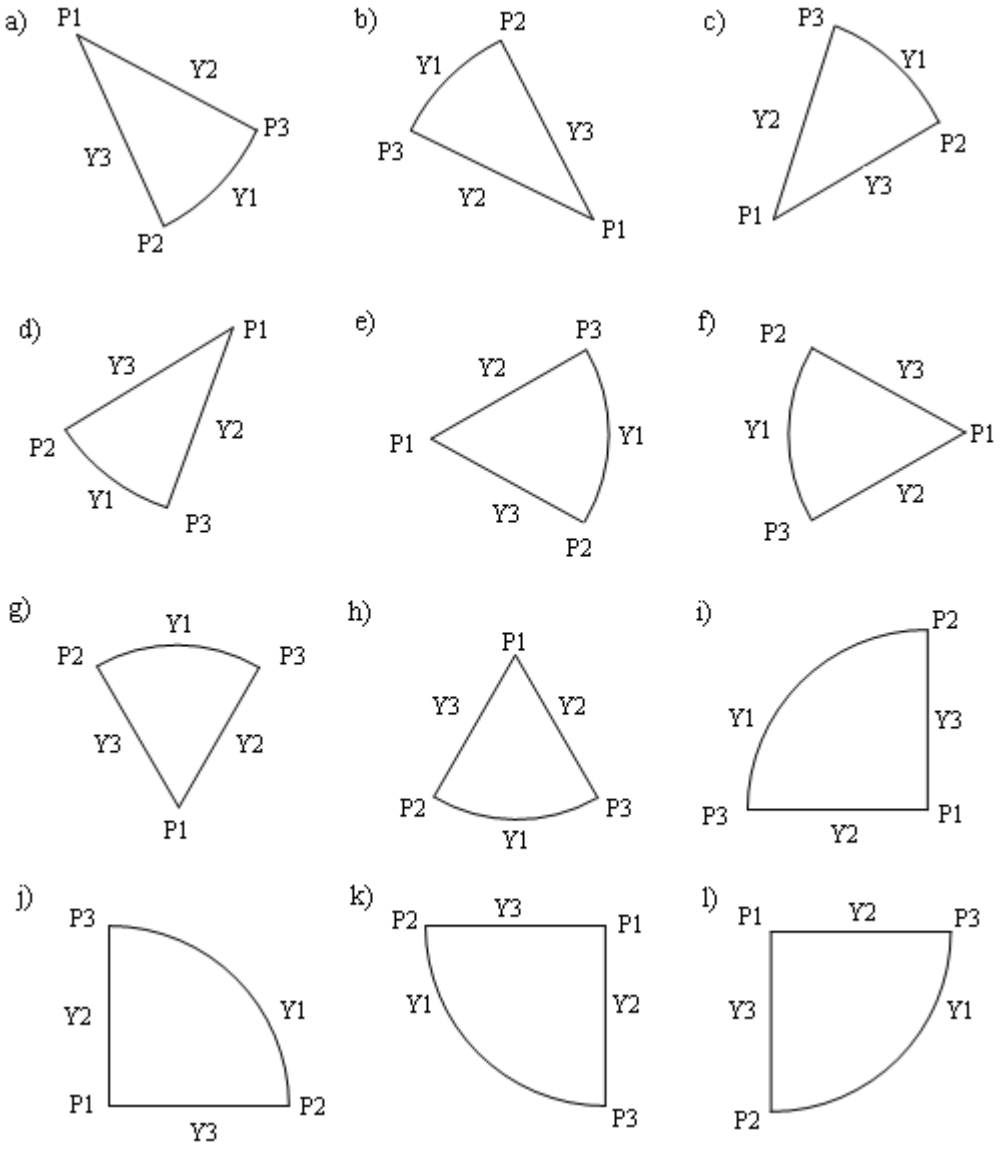

Figure 5.8. Circular electrodes

As stated in section 5.2.1, the circular electrode is specified by three points: the centre of a circle and the two endpoints of an arc. The points are specified in such an order that the first point is always the centre point, and the order of the

remaining two points is irrelevant. Another constraint when specifying the circular electrode is that the arc must be less than or equal to one quarter of the whole circle. If more than a quarter is needed, two electrodes must be specified. For example, if we need a portion of a circle that makes up 40% of a circle, or 144˚ in total, we can specify one electrode that would be one quarter of a circle, or 90˚ in total, and another electrode that would add another 54˚ to make the targeted 144˚.

The three points that are specified define two lines and one arc, as depicted in figures 5.8 and 5.9. The two lines are described with one of the equations (5.27) to (5.29), as in the case of triangular electrodes. Again, the program distinguishes between the different shapes of circular electrodes, as depicted in figures 5.8 and 5.9. Whichever three points we specify in the main input file, the circular electrode will resemble (by means of parameters *a* and *c*, as described in section 5.2.14) one of those depicted in figures 5.8 and 5.9.

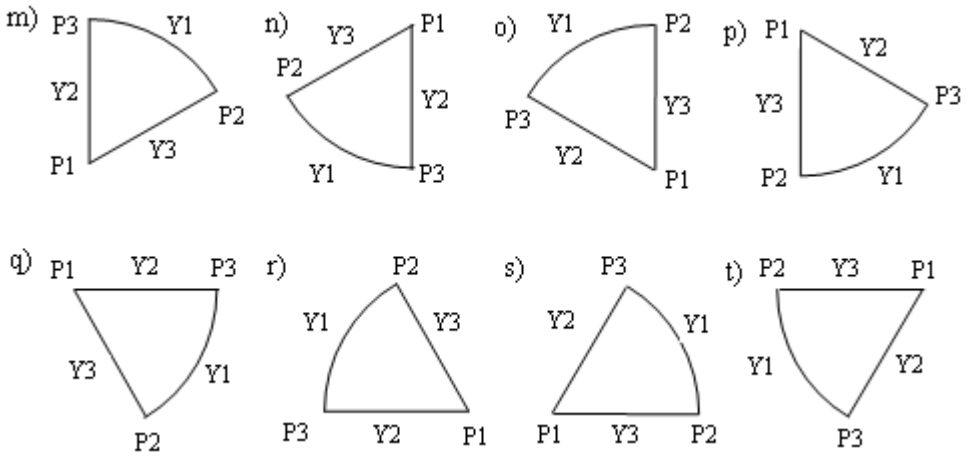

Figure 5.9. Circular electrodes – continued

Similar to the conversion of the triangular representation, the representation of a circular electrode by the three points P_1, P_2 and P_3 is converted by the program to the representation with parameters *a*, *b*, *c*, *t* and *s_point*. The meaning of the first four was described in section 5.2.14 (it is the same for the circular and the triangular electrodes). The parameter *s_point* has the same meaning and purpose as with the triangular electrodes, and here more details will be given on how *s_point* is determined for the electrodes in figures 5.8 and 5.9, as each one of them has a unique *s_point*, as was the case for the triangular electrodes. As already stated, the

first point in a circular electrode specification is the centre of an arc, and this point is denoted as P_1 for all the electrodes in the figures. The other two points can be specified in a random order, and one of them is always *s_point*, as follows:

- For the electrodes a) and b), the two lines are described with equation (5.27) and both have parameter *t* equal to '-'. In this case, *s_point* is the point with greater y co-ordinate. In case a) in figure 5.8 it is P_3, and in case b) it is P_2 (as stated above, P_1 can never be *s_point*).
- For the electrodes c) and d), the two lines are described with equation (5.27) and both have parameter *t* equal to '+'. Again, *s_point* is the point with greater y co-ordinate, which in case c) in figure 5.8 is P_3, and in case d) it is P_2.
- For the electrodes e) and f), the two lines are described with equation (5.27), with one of them having parameter *t* equal to '+', the other having *t* equal to '-', and with x co-ordinate of P_1 being either greater than or less than x co-ordinates of both P_2 and P_3. As in previous four cases a) thorugh d), *s_point* is the point with greater y co-ordinate, which in case e) in figure 5.8 is P_3, and in case f) it is P_2.
- For the electrodes g) and h), the two lines are described with equation (5.27), with one of them having parameter *t* equal to '+', the other having *t* equal to '-', and with y co-ordinate of P_1 being either greater than or less than y co-ordinates of both P_2 and P_3. Here, *s_point* is the point with greater x co-ordinate. In both of these cases in the figure, *s_point* is P_2.
- The electrodes i) thorugh l) are quarters of a circle, with one of the two lines described with equation (5.28) and the other with equation (5.29). One of the points P_2 and P_3 has x co-ordinate equal to x co-ordinate of P_1, while the other point has y co-ordinate equal to y co-ordinate of P_1. The point that has x co-ordinate equal to x co-ordinate of P_1 is taken as *s_point*. In cases i), j), k) and l) in the figure, these points are P_2, P_3, P_3 and P_2, respectively.
- The electrodes m) to t) have one line described with equation (5.27) and the other line described with either equation (5.28) or (5.29). One of the points has either x co-ordinate equal to x co-ordinate of P_1 (if one of the lines is described with equation (5.28)), or y co-ordinate equal to y co-ordinate of P_1 (if one of the lines is described with equation (5.29)). We always take the

other point to be *s_point*, i.e. the one that does not have any of the co-ordinates equal to any of the co-ordinates of P_1. For the electrodes m) to t), s_point is P_2, P_2, P_3, P_3, P_2, P_2, P_3 and P_3, respectively.

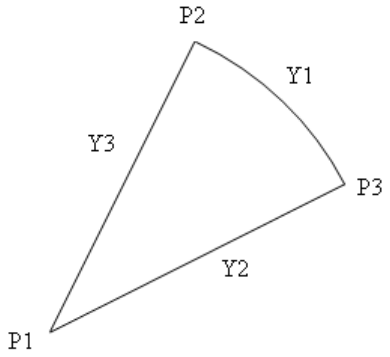

Figure 5.10. Example of a circular electrode

An example of a circular electrode specification is given in figure 5.10 with the following points: P_1 (10, 10), P_2 (15, 20) and P_3 (20, 15). The two lines of the triangle are described with equation (5.27) and both have parameter *t* equal to '+'. It is apparent from the figure that this electrode corresponds to the electrode c) in figure 5.8. The *s_point* parameter corresponds to P_2, because the y co-ordinate of P_2 is greater than the y co-ordinate of P_3.

5.2.16. Function create_electrical_problem

Inputs to the function:

- The array of electrodes (electrode *electrodes) and the number of electrodes (int numElectrodes),
- The array of boundaries of electrical problem (boundary *boundsEl) and the number of those boundaries (int numBoundsEl),
- meshDistances_fbrlud,
- The arrays of co-ordinates of the mesh points (float *x, float *y, float *z),
- The arrays of mapping the indexes between the electrical and the thermal problem (int *index_El_Th) and the thermal and the electrical problem (int *index_Th_El),
- The arrays of mesh lines (float *xMeshLines, float *yMeshLines, float *zMeshLines),

- The specification of the area of the electrical problem (float xMinEl, float xMaxEl, float yMinEl, float yMaxEl, float zMinEl, float zMaxEl),
- The number of mesh points in the electrical problem (int numPointsEl), and
- The array of the potentials (float *voltages),

Output from the function:

- The array describing the type of the point in the electrical problem (char **type_El),
- The indexes of the points surrounding any given point in the electrical problem (int **indexF_El, int **indexB_El, int **indexR_El, int **indexL_El, int **indexU_El, int **indexD_El),
- The potential coefficients of the points, used for weighted calculation of real and imaginary components of the potential by using the finite different method (float **potential_coefficients_fbrlud),
- The arrays of real and imaginary components of the potential in any given point in the electrical problem (float **potential_i, float **potential_j), and
- The arrays of real and imaginary components of the electric field in any given point in the electrical problem (float **field_i, float **field_j) and the field's root mean square (RMS) value (float **rmsField).

Description:

This is the main function that builds the electrical problem for the potential and the electric field calculation. The main idea behind this function is to build a structure that will allow the potential calculation through solving the differential equation for the potential using the finite difference method. For this calculation, it is required to calculate the potential gradient in all of the mesh points, and for this we need to know the indexes of the six points surrounding the given point in all six directions. These surrounding points are noted as F (front), B (back), R (right), L (left), U (up), and D (down). This naming convention is described with more details in section 5.2.9., together with the function create_mesh_distances. As with the mesh distances in the aforementioned function, if the given point lies at the edge of the electrical problem and does not have an adjacent point in any of the six directions, the corresponding index will have a value of -1.

The function starts with dynamic allocation of memory for all of the output arrays listed above, under "Outputs from the function". The allocated memory is

checked, and if any of the allocations was unsuccessful, the program will error out and throw a message to the user that the system memory is insufficient for this simulation. Obviously, apart from telling the user that the problem is too large for the computing system, dynamic allocation has another advantage when compared to the static memory allocation: the size of the problem does not need to be known in advance, and the program will still allocate just enough memory for the calculation, without wasting memory space if the size of the problem differs significantly from the predefined statically allocated memory.

After the successful memory allocation, the function proceeds with building the array of types of the points in the electrical problem. As stated in section 5.2.12., a point can be of one of the following types: 'O' (outside of the problem boundaries), 'E' (on an electrode), 'N' (on a Neumann boundary), 'D' (on a Dirichlet boundary), 'B' (on both Neumann and Dirichlet boundaries, i.e. on the intersection of two boundaries of a different type), and 'I' (inside of the electrical problem, not on any boundary or electrode). The function create_electrical_problem actually uses the function find_type described in the section 5.2.11., to resolve the type of the point in question. The type of a point dictates how the voltage and the electric field will be calculated at the point, and this function also initializes the voltage array for those points that lie on a Dirichlet boundary or on an electrode, because the voltage at this points is obviously constant throughout the simulation. If a point lies on both a Neumann and a Dirichlet boundary, it will have a constant value of the boundary condition of the corresponding Dirichlet boundary. The potential in all of the 'I' and 'N' points is initialized to zero, and it will be calculated later on using the finite difference method. The electric field in all of the points in the electrical problem is also initialized to zero.

It is important to initialize the unknown potential values to zero, because it will help the algorithm to converge to a final solution quicker. Generally speaking, when new variables are declared in a C++ program, they have random values before they are initialized. These random values can be way off the final solution of the potential, and hence the overall run time can be significantly worsened. It is practically impossible to envisage the situation in which the random values in the declared and not initialized variables would help the convergence more than initialization to zero of the unknown values of the potential.

After the array of types has been built and the arrays of potential and electric field preset to the initial solution, the function builds the structure of the electrical problem, namely the arrays **indexF_El, **indexB_El, **indexR_El, **indexL_El, **indexU_El, and **indexD_El. These arrays define the connectivity of the electric problem and allow the program to quickly find the surrounding points of any given point, once the electric problem has been built. The algorithm to find the surrounding points is largely based upon the functions find_index_forward and find_index_backward. These functions take two adjacent points that differ in only one co-ordinate (for example, their x and y co-ordinates are equal and their z co-ordinate differs by one distance between the mesh lines), and based on the index of one of the points, they calculate the index of the other point, by moving backward or forward and calculating the number of points they passed in the process of moving from one point (the known one) to the other one (with the unknown index). Performing such a search for any given point in the electrical problem is costly by means of the run time, but is necessary to build the connectivity between the points. By storing the indexes of the adjacent points for any given point, this search needs to be done only once.

During the same iteration that goes through all of the points and builds the connectivity, the so called potential coefficients are also calculated for any given point for which the potential is not constant (i.e. the point is either of a type ‘B’ or ‘I’). These coefficients are used in the finite difference method to account for the non-uniform mesh distances between a point and its neighbours.

5.2.17. Function create_thermal_problem

Inputs to the function:

- The array of electrodes and the number of the electrodes (electrode *elecs, int numElecs),
- The array of boundaries of the thermal problem, and the number of those boundaries (boundary *boundsTh, numBoundsTh),
- Float *meshIndexes_fbrlud,
- The arrays of co-ordinates of the mesh points (float *x, float *y, float *z),
- The arrays of mesh lines (float *xMeshLines, float *yMeshLines, float *zMeshLines),

- The dimensions of the thermal problem (float xWidth, float yWidth, float zWidth),
- The area of the thermal, i.e. minumum and maximum x, y, and z co-ordinates (float xMinTh, float xMaxTh, float yMinTh, float yMaxTh, float zMinTh, float zMaxTh), and
- The number of points in the thermal and electrical problems (int numPointsTh, int numPointsEl, respectively).

Output from the function:

- The array describing the type of the point in the thermal problem (char **type_Th),
- The indexes of the points surrounding any given point in the thermal problem (int **indexF_Th, int **indexB_Th, int **indexR_Th, int **indexL_Th, int **indexU_Th, int **indexD_Th),
- The potential coefficients of the points, used for weighted calculation of the temperature (float **temperature_coefficients_fbrlud),
- The arrays of the temperature values in the current and the previous iteration (float **temperature, float **temperature_prev),
- The values of conductivity, permittivity, and thermal conductivity in any given mesh point (float **conductivity, float **permittivity, float **thermal_conductivity), and
- The switch indicating if the microelectrodes are treated as transparent for the temperature distribution calculation, or not (int elThermTrans).

Description:

This is the main function that builds the thermal problem for the temperature distribution calculation. Similar to the function create_electrical_problem, this function builds a structure for temperature calculation through solving the differential equation for the temperature using the finite difference method. To calculate temperature in any given mesh point, we need to know the indexes of the six points surrounding the given point in all six directions. Similar to building the electrical problem, we again use six arrays of indexes denoted with the letters F (front), B (back), R (right), L (left), U (up), and D (down). We do not use the same arrays of indexes as in the electrical problem, because the dimensions of the thermal and electrical problem are not necessarily the same.

The function starts with dynamic allocation of memory for all of the output arrays listed above, under "Outputs from the function". The allocated memory is checked, and if any of the allocations was unsuccessful, the program will error out and print the message onto the screen that the system memory is insufficient for this problem. If the memory allocation was successful, the function proceeds with building the array of types of the points in the electrical problem. As stated in section 5.2.11., a point can be of one of the following types: 'O' (outside of the problem boundaries), 'E' (on an electrode), 'N' (on a Neumann boundary), 'D' (on a Dirichlet boundary), 'B' (on both Neumann and Dirichlet boundaries, i.e. on the intersection of two boundaries of a different type), and 'I' (inside of the thermal problem). Again, the type of a point dictates how the temperature will be calculated at that point. The function also initializes the voltage array for those points that lie on a Dirichlet boundary, because the temperature in those points is constant throughout the simulation. If a point lies on both a Neumann and a Dirichlet boundary, it will have a constant value of the boundary condition of the corresponding Dirichlet boundary. The temperature in all of the 'I' and 'N' points is initialized to zero, and it will be calculated by using the iterative finite difference method.

After the array of types has been built and the temperature values preset to the initial solution, the function builds the structure of the thermal problem, namely the arrays **indexF_El, **indexB_El, **indexR_El, **indexL_El, **indexU_El, and **indexD_El. As described above, these arrays define the connectivity of the thermal problem and allow us to quickly find the surrounding points of any given point, once that the thermal problem has been built. The process of building these arrays is exactly the same as in the case of the electrical problem (see section 5.2.16, function create_electrical_problem).

5.2.18. Function calculate_potential

Inputs to the function:

- The specification of material interfaces (float **materialInterface),
- The arrays of co-ordinates of the mesh points (float *x, float *y, float *z),
- The frequency of the applied voltage (float freq),

- The arrays of conductivity and permittivity values in all of the mesh points (float *conductivity, float *permittivity),
- The array of indexes (float *meshIndexes_fbrlud),
- The indexes of the points surrounding any given point in the electrical problem, for both real and imaginary potential calculation (int *indexF_El_i, int *indexB_El_i, int *indexR_El_i, int *indexL_El_i, int *indexU_El_i, int *indexD_El_i, int *indexF_El_j, int *indexB_El_j, int *indexR_El_j, int *indexL_El_j, int *indexU_El_j, int *indexD_El_j),
- The potential coefficients of the points, used for weighted calculation of real and imaginary components of the potential by using the finite difference method (float **potential_coefficients_fbrlud),
- The array of characters denoting the material in question in the electrical problem mesh points (char *material), and
- The array describing relations between the mesh points in the electrical and thermal problems (int *index_El_Th).

Outputs of the function:

- The array of electric potential values in all of the mesh points for both real and imaginary potential values (float *potential_i, float *potential_j).

Description:

This function calculates the electric potential in any given point in the electrical problem by solving equation (5.1) using the finite difference method. The method has been described with more details in section 5.1. It is important to remember that the electric potential is, in general, a complex value. Also, the values for the conductivity and permittivity are not constant in the three dimensional space, as they are temperature dependent, and the temperature profile varies with the non-uniform electric field. Hence, equation (5.1) can be further expanded into:

$$\nabla\left[\sigma\nabla\left(\varphi_r + i\varphi_i\right)\right] + i\omega\nabla\left[\varepsilon\nabla\left(\varphi_r + i\varphi_i\right)\right] = 0 \tag{5.30}$$

Here, indexes *r* and *i* denote the real and imaginary parts of the complex potential, respectively. By further expansion and by separating the real and imaginary parts of equation (5.30), which are both equal to zero, the following set of equations is obtained:

$$\nabla(\sigma\nabla\varphi_r) - \omega\nabla(\varepsilon\nabla\varphi_i) = 0 \tag{5.31a}$$

$$\nabla(\sigma\nabla\varphi_i) + \omega\nabla(\varepsilon\nabla\varphi_r) = 0 \tag{5.31b}$$

In this way, the problem for calculating the complex value of the electric potential has been represented by the set of two equations with two unknowns. These equations can be written in the finite difference form as:

$$\sigma_0\varphi_{r0} - \sum_k \sigma_k\varphi_{rk} - \omega\varepsilon_0\varphi_{i0} + \omega\sum_k \varepsilon_k\varphi_{ik} = 0 \tag{5.32a}$$

$$\sigma_0\varphi_{i0} - \sum_k \sigma_k\varphi_{ik} + \omega\varepsilon_0\varphi_{r0} - \omega\sum_k \varepsilon_k\varphi_{rk} = 0 \tag{5.32b}$$

Here, the index 0 denotes the mesh point in question for which the potential is calculated, and the index *k* denotes the surrounding mesh points. There are six surrounding mesh points in the three-dimensional problem (two points per direction x, y, and z). By combining equations (5.32a) and (5.32b), the real and imaginary potential can be separated as:

$$\left(\sigma_0 + \frac{\omega^2{\varepsilon_0}^2}{\sigma_0}\right)\varphi_{r0} = \sum_k\left(\sigma_k\varphi_{rk} - \omega\varepsilon_k\varphi_{ik} + \frac{\omega^2\varepsilon_0\varepsilon_i}{\sigma_0}\varphi_{rk} + \frac{\omega\varepsilon_0\sigma_i}{\sigma_0}\varphi_{ik}\right) \tag{5.33a}$$

$$\left(\sigma_0 + \frac{\omega^2{\varepsilon_0}^2}{\sigma_0}\right)\varphi_{i0} = \sum_k\left(\omega\varepsilon_k\varphi_{rk} + \sigma_k\varphi_{ik} - \frac{\omega\varepsilon_0\sigma_i}{\sigma_0}\varphi_{rk} + \frac{\omega^2\varepsilon_0\varepsilon_i}{\sigma_0}\varphi_{ik}\right) \tag{5.33b}$$

If the sums in equations (5.33a) and (5.33b) are represented as S_1 and S_2, and the inverse of the term in the bracket on the left hand side of the equation as *C*, the following equations are final for the real and imaginary potential calculation using the final difference method:

$$\varphi_{r0} = C * S_1 \tag{5.34a}$$

$$\varphi_{i0} = C * S_2 \tag{5.34b}$$

These equations are solved by using the iterative process. In each iteration the potential (real and imaginary part) is calculated by using the following formula:

$$\varphi_0(n) = \varphi_0(n-1) + \Omega\left[C * S - \varphi_0(n-1)\right] \tag{5.35}$$

Here, $\varphi_0(n)$ represents the new value of potential, and $\varphi_0(n-1)$ represents the value in the previous iteration. The value Ω is the convergence factor or acceleration factor, and it was set to 1.85, as a rule of thumb. In theory of iterative solutions for finite difference method, this factor can take any value that satisfies the constraints $0 < \Omega < 1$ or $1 < \Omega < 2$. The value of 1.85 was obtained through experimentation with different values. Equation (5.35) is used in the same manner for calculating the real and imaginary values of the potential, by utilizing equations (5.34a) and (5.34b). In each iteration the potential distribution is getting closer to the final solution, but it never reaches it. The program will perform as many iterations as needed to reach the exit criterion. The exit criterion indicates that the difference between two successive iterations has to be less than some predefined value in all of the mesh points in the electrical problem. When this criterion is satisfied, the assumption is that the current solution is sufficiently close to the real solution.

5.2.19. Function calculate_field

Inputs to the function:

- The number of points in the electrical problem (int numpointsEl),
- The array describing types of the mesh points in the electrical problem (char *type_El),
- The array describing material properties of the whole structure (char *material),
- The array of indexes (float *meshIndexes_fbrlud),
- The array describing relations between the mesh points in the electrical and thermal problems (int *index_El_Th),
- The array of electric potential values in all of the mesh points (float *potential), and
- The indexes of the points surrounding any given point in the electrical problem (int **indexF_El, int **indexB_ El, int **indexR_ El, int **indexL_ El, int **indexU_ El, int **indexD_ El).

Output from the function:

- The array of values of the electrical field in all of the mesh points (float *field).

Description:

This function calculates the electrical field in a mesh point, and stores these values in the array called *field*. The function is called twice within the main program: once with the real potential array *potential_i* to calculate the real electrical field *field_i*, and once with the imaginary potential array *potential_j* to calculate the imaginary electrical field *field_j*. These two arrays (*field_i* and *field_j*) are then used for calculation of RMS of the electrical field.

The function calculates the field by using the following algorithm: it goes through all of the mesh points and checks their types, and based on the type of the point, the types of the surrounding points, the boundary type etc., it calculates the electric field value for the mesh point in question.

- The electric field value in the mesh point is calculated by using the electric potential values of all surrounding mesh points and the distances to those points as defined in the array meshIndexes_fbrlud. In this case, the electric potential value in the given mesh point is taken as a linearly interpolated value based on the surrounding mesh points. The field components are calculated by using the following equations:

$$Fx = \frac{\phi_F - \phi_B}{mesh_F + mesh_B} \tag{5.36}$$

$$Fy = \frac{\phi_R - \phi_L}{mesh_R + mesh_L} \tag{5.37}$$

$$Fz = \frac{\phi_U - \phi_D}{mesh_U + mesh_D} \tag{5.38}$$

- If a mesh point is of a type ‘E’ (i.e. it resides on the microelectrode), one field component is always non-zero. Only one additional component might be non-zero (we are observing strictly rectangular mesh), if the mesh point resides on the boundary of the electrode. Thus, the electrical field in the mesh point is calculated based on the type of the surrounding points.

- If a mesh point is of a type ‘D’ (Dirichlet boundary), the field component perpendicular to the boundary is calculated by using only the potential and the mesh distance of the point which lies inside the electrical problem. This point’s “mirror” point is neglected, as it does not reside in the electrical problem and therefore its electric potential value is not known.
- If a mesh point is of a type ‘N’ (Neumann boundary), the field component perpendicular to the boundary is zero by default (according to the definition of the Neumann boundary).

5.2.20. Function calculate_rms_field

Inputs to the function:

- The number of points in the electrical problem (int numpointsEl), and
- The arrays of values of the real and imaginary electrical field components (float *field_i, float *field_j).

Output from the function:

- The array of the RMS values of the electrical field in all of the mesh points (float *rmsField).

Description:

This function calculates the RMS value of the electrical field in all of the mesh points in the electrical problem. Since all of the values of the electrical field are already calculated by using the function calculate_field (both the real and imaginary componenets), the RMS value of the field is simply calculated as follows:

$$E_{RMS} = \sqrt{E_i^{\,2} + E_j^{\,2}} \tag{5.39}$$

Here, E_i and E_j are the real and imaginary componenets of the field, respectively, and E_{RMS} is the RMS value of the field.

5.2.21. Function calculate_field_components

Inputs to the function:

- The array of voltages applied to the microelectrodes (float *currentVoltages),
- The array describing types of the mesh points in the electrical problem (char *type_El),

- The array describing material properties of the whole structure (char *material),
- The array of indexes (float *meshIndexes_fbrlud),
- The array describing relations between the mesh points in the electrical and thermal problems (int *index_El_Th),
- The array of electric potential values in all of the mesh points (float *potential), and
- The indexes of the points surrounding any given point in the electrical problem (int **indexF_El, int **indexB_ El, int **indexR_ El, int **indexL_ El, int **indexU_ El, int **indexD_ El).

Outputs from the function:

- The array of values of the electrical field in all of the mesh points (float *field),
- The array of values of the electrical field components in all of the mesh points (float **fieldComponents; the same array stores the values for x, y, and z components), and
- The array of values of the gradients of the electrical field components in all of the mesh points (float **gradFieldComponents; again, the same array stores the values for x, y, and z components).

Description:

This function takes as arguments the potential in all of the mesh points of the electrical problem, as well as the physical data regarding the mesh and the boundaries. It then calculates the electric field components in all of the points, the electrical field strength, and the electric field components gradients.

Similar to the previously described function calculate_field, this function also calculates the field of the boundary points based on the type of the boundary they are residing on, as not all of the points surrounding the point in question are inside the electrical problem. In other words, their potential value is unknown. However, the function still uses the same set of variables to calculate the electrical field for a given point, even if the point lies on a boundary. For example, if the point left to the point in question lies outside the electrical problem, the function will set the potential value of that point to be the same as the potential of the point at the right of the point in question (if the boundary in question is of Neumann type), or to

have the same absolute value, but the opposite sign (if the boundary in question is of Dirichlet type).

If we take into account the above, the *y* component of the electrical field is given as:

$$Fy = \frac{V_R - V_L}{y_R - y_L} \tag{5.40}$$

The same procedure applies if the boundary lies in one of the other two planes (in that case, *Fx* or *Fz* would be calculated by setting the potential of the point outside the problem to an already calculated value).

To calculate the gradient of the field components, we need to know the potential in all of the points surrounding the point in question – the same as in the electric field calculation. Again, for boundary points the function assigns a known value to the surrounding points outside the problem boundaries.

5.2.22. Function create_electrical_problem_files

Inputs to the function:

- The arrays of values of both real and imaginary components of electric potential (float *potential_i and float *potential_j, respectively),
- The arrays of values of both real and imaginary components of electric field (float *field_i and float *field_j, respectively),
- The arrays of values of x, y, and z components of both real and imaginary components of electric field (float *field_i and float *field_j, respectively),
- The array of values of electric field RMS (float *rmsField),
- The array of values of the voltages applied to the electrodes (float *currentVoltages),
- The indexes of the points surrounding any given point in the electrical problem, for both of the electrical problems solving the equations for the real and imaginary components of electric potential (int *indexF_El, int *indexB_El, int *indexR_El, int *indexL_El, int *indexU_El, int *indexD_El, int *indexF_El_j, int *indexB_El_j, int *indexR_El_j, int *indexL_El_j, int *indexU_El_j, int *indexD_El_j),
- The arrays of co-ordinates of the mesh points (float *x, float *y, float *z),

- The array of electrodes and the number of the electrodes (electrode *elecs, int numElecs),
- The array of boundaries of electrical problem for both of the electrical problems solving the equations for the real and imaginary components of electric potential, and the number of those boundaries (boundary *boundsEl, boundary *boundsEl_j, numBoundsEl),
- The arrays of mesh lines (float *xMeshLines, float *yMeshLines, float *zMeshLines),
- The specification of the area of the electrical problem (float xMinEl, float xMaxEl, float yMinEl, float yMaxEl, float zMinEl, float zMaxEl),
- The number of mesh points in the electrical problem (int numPointsEl), and
- The array of relative indexes between the mesh points in the electrical and thermal (int **index_El_Th).

Output from the function:

- The files with the following physical quantities per mesh point:
    - The real and imaginary values of electric potential,
    - The real and imaginary components of the electric field,
    - x, y, and z components of the real and imaginary electric field components,
    - RMS value of electric field, and
    - The real and imaginary components of the field used in the calculation of dielectrophoretic force on particles.

Description:

This function creates several files with the values of electric field and potential in any given mesh point of the problem. These files are created for two reasons. Firstly, the electrical potential and field distribution do not depend on the actual particles subjected to the DEP force, but only on the shapes and dimensions of the microelectrodes and the channel. Hence it is not necessary to calculate the field distribution every time we want to calculate the DEP force on different particles within the same system of microelectrodes. It is sufficient to calculate the field distribution once and store the values in the files on the hard disk, and when we want to reuse those values for calculating the DEP force on a different kind of particles, we can simply load these files into the program. The second reason for

storing the values into the files is to graphically show the distribution of the electric field and potential distributions. For this, we can use any program with two- or three-dimensional plotting capabilities, such as Matlab. Graphical representations of these physical values is very useful, as we can quickly and easily draw the first conclusion about the capabilities of our system of microelectrodes to move the particles around by using the DEP effect.

This function simply takes all of the abovementioned arrays of the electric field and potential values, and tries to open the corresponding files for writing. If successful, it goes through all of the points in the electrical problems, and stores the values into the files.

5.2.23. Function create_thermal_problem_files

Inputs to the function:

- The arrays of temperature values in all of the points in the thermal problem (float *temperature),
- The arrays of values of electrical conductivity and permittivity in all of the points in the thermal problem (float *conductivity and float *permittivity, respectively),
- The arrays of values of thermal conductivity in all of the points in the thermal problem (float *thermal_conductivity),
- The arrays of co-ordinates of the mesh points (float *x, float *y, float *z),
- The arrays of mesh lines (float *xMeshLines, float *yMeshLines, float *zMeshLines),
- The array of characters describing the material in the mesh point in question (char *material).

Output from the function:

- The files with the following physical quantities per mesh point:
    - Temperature (temperature.txt),
    - Electrical conductivity and permittivity (conductivity.txt and permittivity.txt, respectively), and
    - Thermal conductivity (thermal_conductivity.txt).

Description:

This function creates several files with the values of temperature, thermal conductivity, and electrical conductivity and permittivity in all of the mesh points in the thermal problem. These files are primarily used to visualize these physical values for better understanding on the electrical field and temperature distributions.

5.2.24. Function calculate_cond_perm

Inputs to the function:

- The total number of points in the thermal problem (int numPointsTh),
- The arrays of temperature values in all of the points in the thermal problem (float *temperature),
- The arrays of co-ordinates of the mesh points (float *x, float *y, float *z),
- The array of characters describing the material in the mesh point in question (char *material), and
- The array describing the points on the interface between the two materials (i.e. the boundary of the electrical problem, which would typically be the glass-liquid interface; float *materialInterface).

Output from the function:

- The arrays of values of electrical conductivity and permittivity in all of the points in the thermal problem (float *conductivity and float *permittivity, respectively),
- The arrays of values of thermal conductivity in all of the points in the thermal problem (float *thermal_conductivity),

Description:

This function calculates electrical conductivity and permittivity and thermal conductivity in all of the points in the thermal problem. These properties depend on the temperature at the point in question. There are predefined functions to be used for calculating these properties. For each material in the system, a separate function can be written to accommodate for the different parameters in the equation.

5.2.25. Function calculate_temperature_maxerror

Inputs to the function:

- The total number of points in the thermal problem (int numPointsTh), and

- The arrays of values of temperature in all of the points in the thermal problem, in the current and the previous iteration of the temperature calculation (float *temperature and float *temperature_prev, respectively).

Outputs of the function:

- The maximum difference in the values of temperatures between two consecutive iterations in the same mesh point (float &temperature_maxerror), and
- The maximum temperature in the system (float &max_temperature).

Description:

This function takes as a parameter the number of mesh points in the thermal problem and the arrays of temperatures in the thermal problem in the current and the previous iteration. It then goes through all of the points and calculates the maximum difference per point between the two iterations for the entire system. This value is used to control when the program will stop iterating, i.e. it will converge on the final solution for the electric potential distribution within the electrical system. When the difference between the two iterations in all of the points is less or equal than the specified maximum error allowed, the program stops converging towards the solution and the acceptable accuracy is assumed to be achieved.

Apart from calculating the maximum temperature difference between the two iterations, the function also reports the maximum temperature in each iteration. This value is not used for further calculations, but rather for a user to observe the trend of the temperature of the system and sanity check.

5.2.26. Function calculate_grad_rms_field

Inputs to the function:

- The total number of points in the electrical problem (int numPointsEl),
- The array of RMS of the electric field (float *rmsField),
- The array of indexes (float *meshIndexes_fbrlud),
- The indexes of the points surrounding any given point in the electrical problem (int **indexF_El, int **indexB_ El, int **indexR_ El, int **indexL_ El, int **indexU_ El, int **indexD_ El),
- The array describing relations between the mesh points in the electrical and thermal problems (int *index_El_Th), and

- The arrays of co-ordinates of the mesh points (float *x, float *y, float *z).

Outputs of the function:

- This function does not produce any variables as an output, but rather stores the caluclated data in the files. There are four files generated with the function:
    - grad_rms_field_x.txt
    - grad_rms_field_y.txt
    - grad_rms_field_z.txt
    - grad_rms_field.txt

  The following text describes the files in more detail.

Description:

This function calculates the gradient of the RMS values of the electric field in all of the points in the electrical problem. There are essentially four values that are calculated: the x, y and z components of the gradient, and the magnitude of the gradient (i.e. the root of the sum of the squares of the three aforementioned components).

During the iterative process that goes through all of the mesh points, the function looks at the adjacent points to the point for which the calculation is being performed. For example, if the x component of the gradient is being calculated, the algorithm looks at the two adjacent points of the point in question on the x axis. If the mesh point is not at the boundary, the gradient component is simply calculated by adding the distances of the point in question to the two points, and dividing the difference in the electric field RMS value between these two points by that number.

If the point is at the boundary for the particular axis, the two points that are used to calculate the gradient are one adjacent point and the point in question. In other words, the difference in electric field RMS values between the point in question and that one adjacent point is divided by the distance of the adjacent point from the point in question. The same algorithm is used for all the three axis and the values are stored in the files mentioned above. The magnitude of the gradient is stored in the last file on the list above.

5.2.27. Function calculate_ temperature

Inputs to the function:

- The total number of points in the thermal problem (int numPointsTh),
- The array of types of the mesh points in the thermal problem (char *type_Th),
- The potential coefficients of the points, used for weighted calculation of the temperature (float **temperature_coefficients_fbrlud),
- The indexes of the points surrounding any given point in the thermal problem (int **indexF_Th, int **indexB_Th, int **indexR_Th, int **indexL_Th, int **indexU_Th, int **indexD_Th),
- The arrays of co-ordinates of the mesh points in the thermal problem(float *xTh, float *yTh, float *zTh),
- The arrays of electrical conductivity (float *conductivity) and thermal conductivity values (float *thermal_conductivity) in the mesh points of the thermal problem,
- The array of values of the electric field RMS (float *rmsField), and
- The arrays of mapping the indexes between the electrical and the thermal problem (int *index_El_Th) and the thermal and the electrical problem (int *index_Th_El).

Outputs of the function:

- The array of temperature values in the mesh points of the thermal problem (float *temperature).

Description:

This function calculates temperature in all of the mesh points in the thermal problem. Temperature is calculated similar to electric potential, by using the finite difference method to solve the partial differential equation given by equation (5.2). Similar to equation (5.35), the new temperature in a mesh point is calculated based on the previous iteration and the current summation of the temperatures in all of the surrounding mesh points, multiplied by a factor that depends on the mesh distances between the adjacent points and the convergence factor applied in the equation (similar to Ω in equation 5.35). Similar to the algorithm for the electric potential calculation the iterative process stops when the difference between two successive iterations is smaller than some pre-defined value in all of the mesh points.

5.2.28. Function calculate_grad_temperature

Inputs to the function:

- The total number of points in the thermal problem (int numPointsTh),
- The array of temperature values in the thermal problem (float *temperature),
- The array of indexes (float *meshIndexes_fbrlud),
- The indexes of the points surrounding any given point in the thermal problem (int **indexF_Th, int **indexB_Th, int **indexR_Th, int **indexL_Th, int **indexU_Th, int **indexD_Th), and
- The arrays of co-ordinates of the mesh points (float *x, float *y, float *z).

Outputs of the function:

- The x, y and z components of the temperature gradient (float **gradTemperature_x, float **gradTemperature_y and float **gradTemperature_z, respectively).
- Files that store temperature gradients in x, y, and z direction, and the RMS value of the temperature gradient in any given point:
    - grad_temperature_x.txt,
    - grad_temperature_y.txt,
    - grad_temperature_z.txt, and
    - grad_temperature.txt.

Description:

This function calculates the temperature gradient in all of the mesh points in the thermal problem. This gradient is needed for calculation of the electrohydrodynamic force on the suspending medium. The temperature gradient is calculated in the same manner as the gradient of the RMS electric field, as described in the chapter above. Again, the approach is to look at the temperature values in all of the surrounding points, and calculate the gradient in the point in question by using these values.

5.2.29. Function calculate_cm_factor

Inputs to the function:

- The real part of the medium permittivity, the imaginary part of the medium permittivity, the real part of the particle permittivity, and the imaginary part of the particle permittivity (float permittivity_medium_i, float

permittivity_medium_j, float permittivity_particle_i, and float permittivity_particle_j, respectively).

Outputs of the function:

- The real and imaginary parts of the Clausius-Mossotti factor (float &cm_factor_i and float &cm_factor_j respectively).

Description:

This function calculates the real and imaginary parts of the Clausius-Mossotti factors from the complex permittivities of the particle and the medium. The equation used for this calculation is given by equation (3.16) in chapter 3.

5.2.30. Function calculate_dep_force_components

Inputs to the function:

- The number of points in the electrical problem (int numPointsEl),
- Electric field flow components (float *fieldComponents_i and float *fieldComponents_j),
- The arrays of co-ordinates of the mesh points (float *x, float *y, float *z),
- The real and imaginary components of the Clausius-Mossotti factor (float cm_factor_i, float cm_factor_j),
- First order derivatives of the electric field components (float ** fieldx_i_x through fieldz_j_z).
- The real component of the suspending medium permittivity (float permittivity_medium_i), and
- The array describing relations between the mesh points in the electrical and thermal problems (int *index_El_Th).

Outputs of the function:

- The dielectrophoretic force components in x, y and z directions (double **dep_force_1_x, double **dep_force_1_y, double **dep_force_1_z).
- The output file with the values of the dielectrophoretic force in the mesh points, ready for display and analysis in Matlab.

Description:

This function calculates the dielectrophoretic force on particles that have a spherical shape with radius *r*. Similar functions can easily be written for any other

shape of the particles that can be numerically modeled for the dielectrophoretic effect by means of their dipole moment.

The corner stones for this calculation are the equations (3.5), (3.13) and (3.30) from chapter 3. The equation for the dielectrophoretic force can be written in the following form:

$$\langle F_{DEP} \rangle = \frac{1}{2} \mathrm{Re}\left(4\pi\varepsilon_m r^3 f_{CM} \vec{E} \nabla \vec{E}^*\right) \tag{5.41}$$

Here, ε_m is the real component of the medium permittivity, r is the particle radius, f_{CM} is the Clausius-Mossotti factor, and E is a complex value of the electric field (the star denotes the complex conjugate). In equation (5.41), the following stands:

$$\vec{E} \nabla \vec{E}^* = (\vec{E} \nabla) \vec{E}^* \tag{5.42}$$

In other words, E and ∇ can be grouped together to form a 3x3 operator that can then be used on the complex conjugate to calculate the dielectrophoretic force. The matrix of that operator is given by the following equation:

$$\vec{E} * \nabla = \begin{bmatrix} Ex\frac{\partial}{\partial x} & Ex\frac{\partial}{\partial y} & Ex\frac{\partial}{\partial z} \\ Ey\frac{\partial}{\partial x} & Ey\frac{\partial}{\partial y} & Ey\frac{\partial}{\partial z} \\ Ez\frac{\partial}{\partial x} & Ez\frac{\partial}{\partial y} & Ez\frac{\partial}{\partial z} \end{bmatrix} \tag{5.43}$$

Then, equation (5.42) can be written as:

$$\vec{E} * \nabla \vec{E}^* = \begin{bmatrix} Ex\frac{\partial Ex^*}{\partial x} & Ex\frac{\partial Ex^*}{\partial y} & Ex\frac{\partial Ex^*}{\partial z} \\ Ey\frac{\partial Ey^*}{\partial x} & Ey\frac{\partial Ey^*}{\partial y} & Ey\frac{\partial Ey^*}{\partial z} \\ Ez\frac{\partial Ez^*}{\partial x} & Ez\frac{\partial Ez^*}{\partial y} & Ez\frac{\partial Ez^*}{\partial z} \end{bmatrix} \tag{5.44}$$

Equation (5.44) is then used in equation (5.41) to calculate the dielectrophoretic force on the particles.

5.2.31. Function calculate_dep_force_components

Inputs to the function:

- Electric field flow components (float *fieldComponents_i and float *fieldComponents_j),
- The arrays of co-ordinates of the mesh points (float *x, float *y, float *z),
- The frequency of the applied voltage (float freq),
- The number of points in the electrical problem (int numPointsEl),
- The array of indexes (float *meshIndexes_fbrlud),
- The indexes of the points surrounding any given point in the electrical problem, for both real and imaginary potential calculation (int *indexF_El_i, int *indexB_El_i, int *indexR_El_i, int *indexL_El_i, int *indexU_El_i, int *indexD_El_i, int *indexF_El_j, int *indexB_El_j, int *indexR_El_j, int *indexL_El_j, int *indexU_El_j, int *indexD_El_j), and
- The array describing relations between the mesh points in the electrical and thermal problems (int *index_El_Th).

Outputs of the function:

- First order derivatives of the electric field components (float ** fieldx_i_x through fieldz_j_z).

Description:

This function calculates the first order derivatives of the electric field components. There are real and imaginary electric fields, and they are three dimensional vectors. The components can be denoted as *field<M>_<N>*, where *M* denotes a direction of the particular component (one of: *x*, *y*, and *z*), and *N* denotes if the particular component is real or imaginary (one of: *i* and *j*). For example, *fieldz_j* denotes the component of the imaginary electric field in the z direction.

The derivatives of these components get an additional label, which denotes over which variable the component's derivative is calculated. For example, *fieldz_i_x* denotes the derivative over x of the z component of the real part of the field. Altogether there are 18 derivatives: there are 6 components of the field (x, y, and z of the real and imaginary components), and each one has three derivatives. The derivatives are used in the calculation of the dielectrophoretic force as follows.

The dielectrophoretic force is given by equation (5.41), and the differential equation portion of the equation can be substituted by equation (5.44). From the

latter, it is apparent that all of the possible combinations of the electric field components and the derivatives need to be calculated to numerically solve equation (5.41).

The basic equation for numerical solution of the derivatives is given by the following simple equation:

$$f'(x) = \lim_{h \to 0} \frac{f(x+h) - f(x-h)}{2h} \approx \frac{f(x+h) - f(x-h)}{2h} \tag{5.45}$$

From this equation it is apparent that the accuracy of the solution depends on the mesh density. In other words the smaller the distance between the adjacent points, the greater the accuracy. Equation (5.45) is called the central difference derivative and is more accurate than the equation for calculating only backward or forward differences. More details on these three types of finite differences can be found in section 5.1.

Similarly, the following equations show the second order derivative and the general equation for the *n*th order derivative, respectively:

$$f''(x) = \approx \frac{f(x+h) + f(x-h) - 2f(x)}{h^2} \tag{5.46}$$

$$\partial^n [f](x) = \sum_{i=0}^{n} (-1) i \binom{n}{i} f\left(x + \left(\frac{n}{2} - i\right)h\right) \tag{5.47}$$

By using equation (5.47), any order of the derivative of the electric field can be calculated, in order to account for higher order components of the dielectrophoretic force, as suggested by equation (3.2) in chapter 3. These higher order components are usually omitted from the calculations, as their impact is often negligible.

This chapter gave an overview of numeric methods for solving partial differential equations for electric potential and temperature distribution in the system of microelectrodes. An overview of numeric methods was given together with the reasons on why the finite difference method was chosen to implement the three dimensional program for the simulation. This was followed by the overview of main equations that are solved in the program, and the program building blocks.

Chapter 6. Results of numerical modelling of dielectrophoresis

This chapter shows the simulation results of the program described in chapter 5. The castellated microelectrodes and travelling wave dielectrophoretic array are described as examples of the simulation. The final section in the chapter gives the results of the simulation of dependency of the temperature in the channel on changes in the conductivity of the suspending medium.

6.1. Castellated microelectrodes

Figure 5.1 in section 5.2.1 shows a castellated system of microelectrodes that was successfully used for separation of small particles by utilizing the dielectrophoretic effect. In this section, this layout of microelectrodes will be used as an example of the numerical modelling of the dielectrophoretic effect by using the above program. Similar analysis has been done in [200]. For this model, the input files used to describe the system are the same as those described in sections 5.2.1 through 5.2.3.

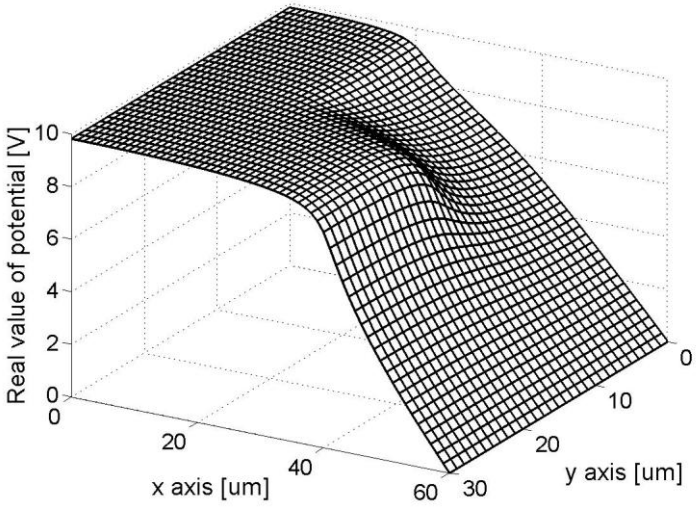

Figure 6.1a. Real value of the potential

Figure 6.1 shows the plot for the electric potential distribution, both the real and the imaginary components. It is apparent from the figure that the real value dominates over the imaginary value. This is expected, as the voltage applied to the microelectrodes is strictly real (the imaginary component is equal to zero as there is

only one phase of the voltage applied). The imaginary value of the potential is not zero due to the non-uniform temperature distribution, which results in the non-uniform distribution of the conductivity and the permittivity of the suspending medium. As described with equation (5.11), this results in the non-zero imaginary part of the potential.

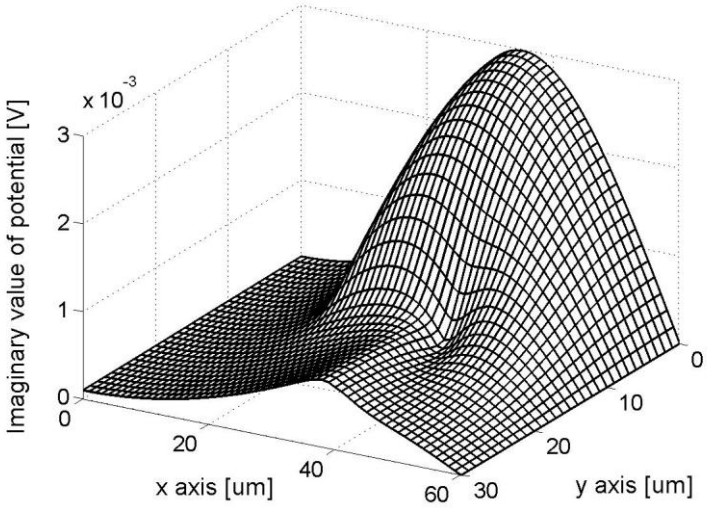

Figure 6.1b. Imaginary values of the potential

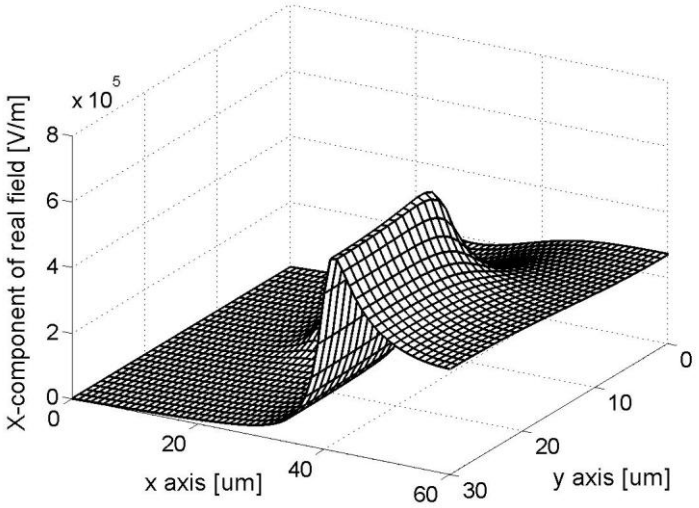

Figure 6.2. x-component of the real electric field

The field components can be calculated from the potential distribution using equations (5.18) through (5.20). The real components of the field are shown in

figures 6.2 through 6.4, and the imaginary components are shown in figures 6.5 through 6.7. It is apparent from the z axis (which represents the magnitude of the field components) that the real field components are stronger than the imaginary ones, which is expected, as the imaginary component of the applied voltage is equal to zero.

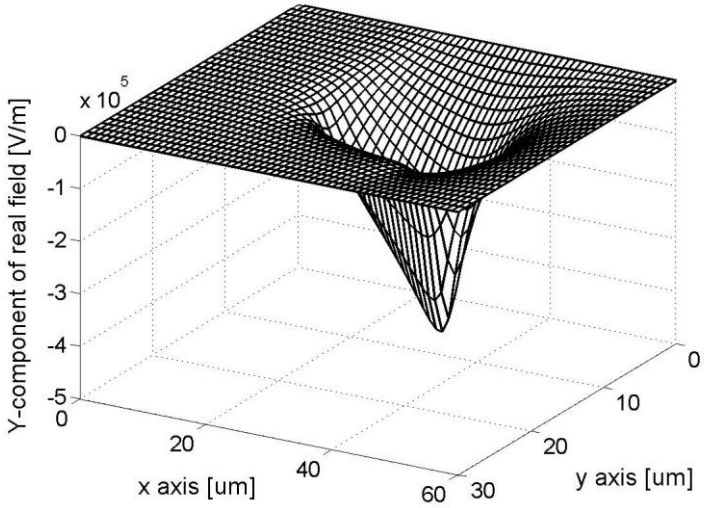

Figure 6.3. y-component of the real electric field

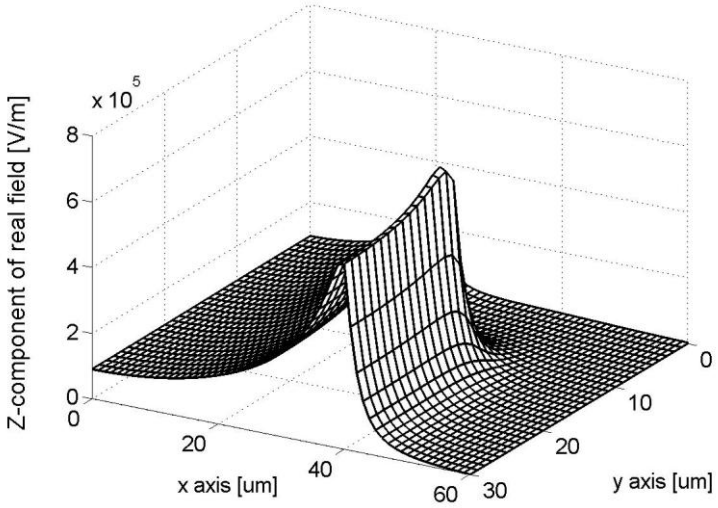

Figure 6.4. z-component of the real electric field

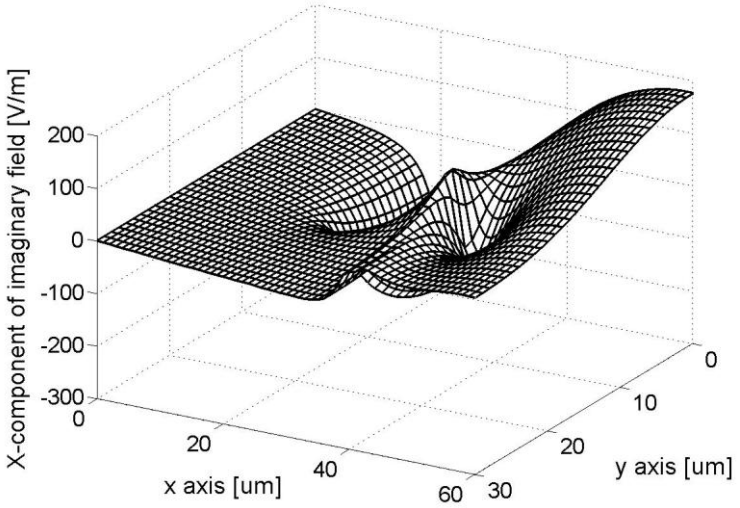

Figure 6.5. x-component of the imaginary electric field

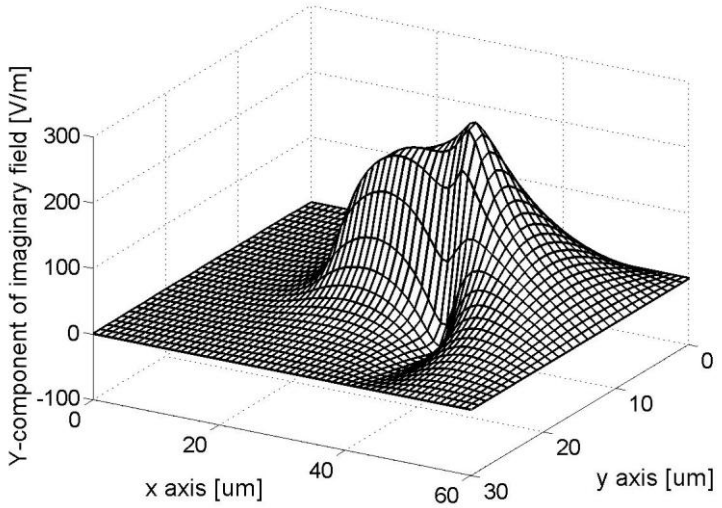

Figure 6.6. y-component of the imaginary electric field

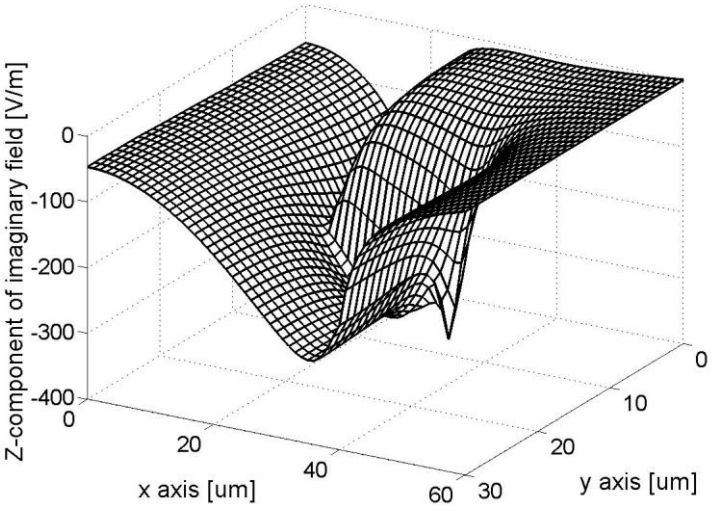

Figure 6.7. z-component of the imaginary electric field component

The electric field comprising of the real and imaginary components is shown in the next three figures. Figure 6.8 shows the real electric field, figure 6.9 shows the imaginary electric field and figure 6.10 shows the RMS value of the electric field. It is apparent from figure 6.10 that the RMS value of the electric field qualitatively (and quantitatively) corresponds to the real electric field component, as it is much more dominant than the imaginary component (several orders of magnitude).

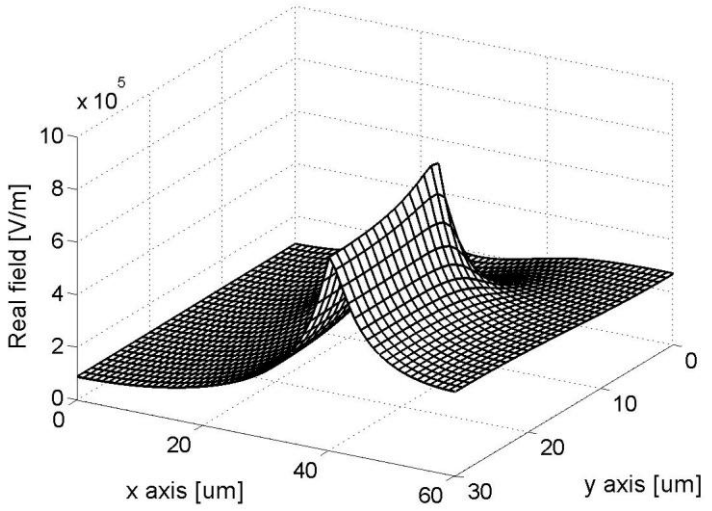

Figure 6.8. Real electric field magnitude

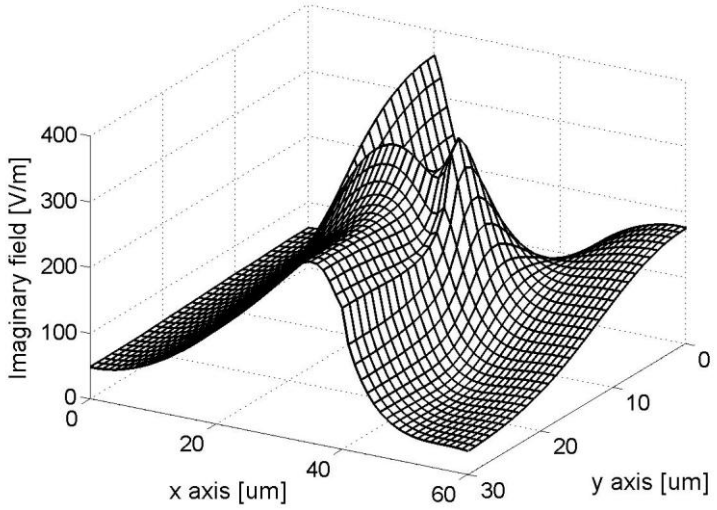

Figure 6.9. Imaginary electric field magnitude

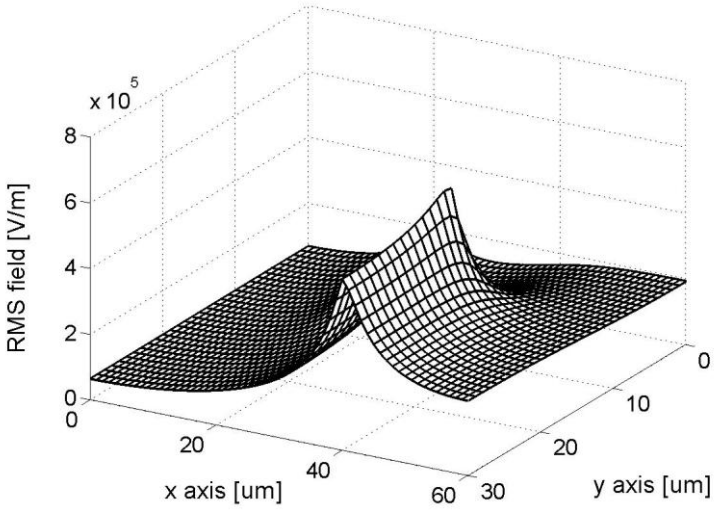

Figure 6.10. RMS value of the electric field

The following figures show the vector plots of the electric field. Figure 6.11 shows the electric field vector in the x-y plane 2 microns above the level of the microelectrodes. Figure 6.12 shows the electric field vector in the x-z plane which corresponds to y of 22 microns. These plots show the electric field vector point away from the microelectrodes, as expected based on the analytical calculation of

the electric field direction (the electric field is proportional to the negative gradient of the potential distribution).

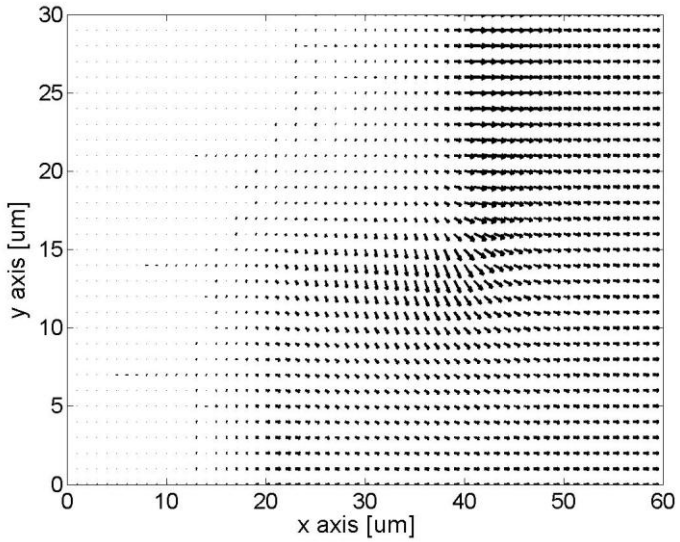

Figure 6.11. Electric field vector in the x-y plane 2 microns above the microelectrodes

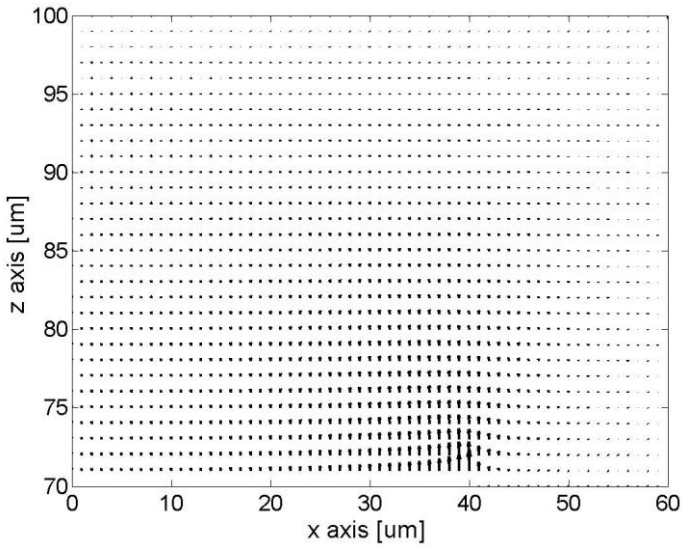

Figure 6.12. Electric field vector in the x-z plane (y equals 22 microns)

Figures 6.13 through 6.16 show the dielectrophoretic force in the system. Figure 6.13 shows the magnitude of the force, and figures 6.14 and 6.15 show the components in the x and z directions of the dielectrophoretic force.

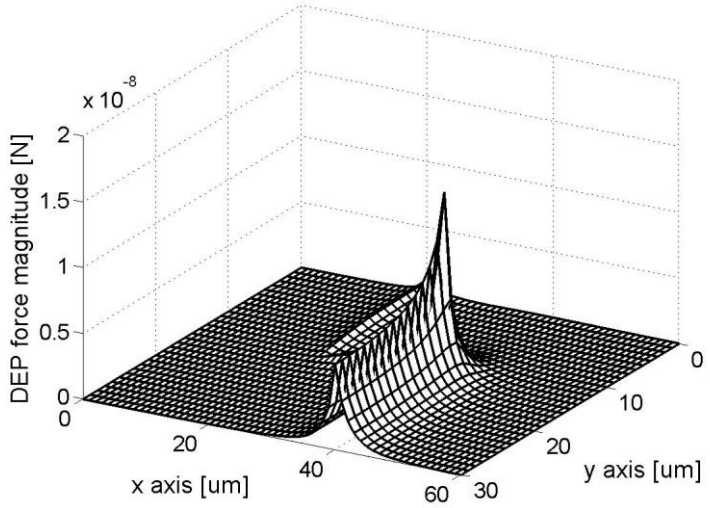

Figure 6.13. DEP force

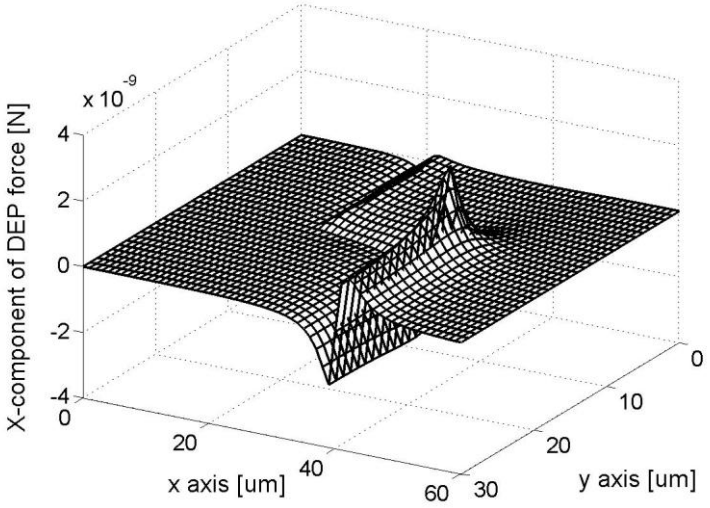

Figure 6.14. X-component of the DEP force

From the figures 6.14 and 6.15 it is obvious that the dielectrophoretic effect is negative in nature, as the direction of the dielectrophoretic force suggests that the particles subject to it would be pushed away from the edges of the microelectrodes where the electric field magnitude reaches its maximum. This effect can also be seen in figure 6.16, which shows the direction of the dielectrophoretic force vector is going from the edge of the microelectrodes outwards.

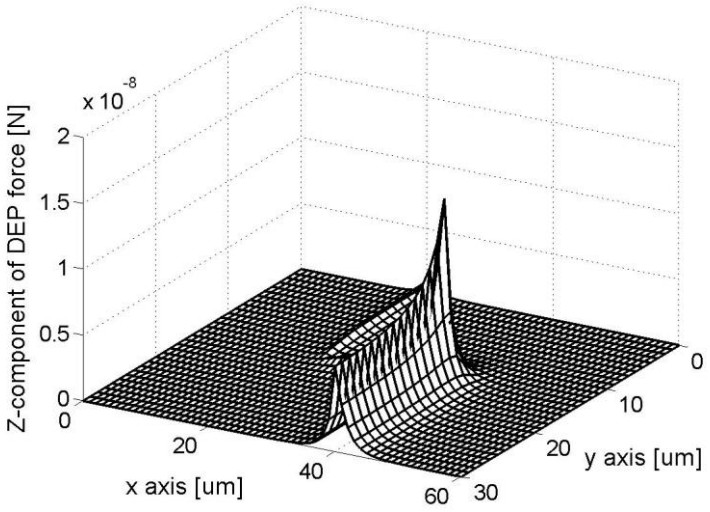

Figure 6.15. Z-component of the DEP force

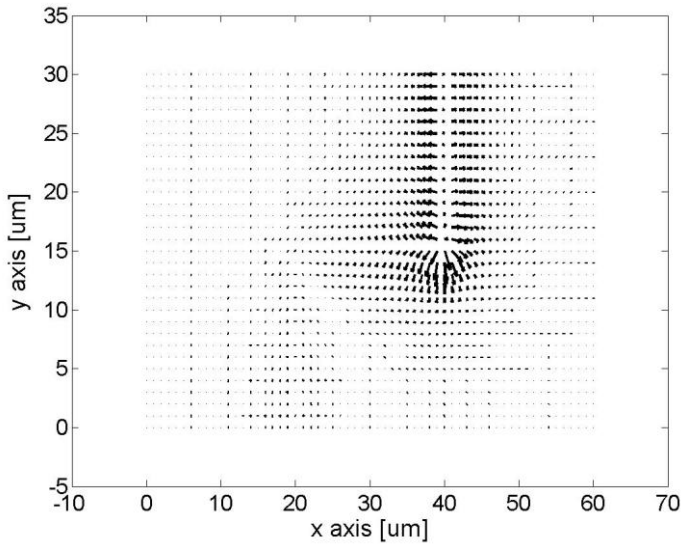

Figure 6.16. Z-component of the DEP force

6.2. Traveling wave dielectrophoretic array

This section shows the simulation of dielectrophoresis in a travelling wave dielectrophoretic field. The layout of microelectrodes is shown in figure 6.17. The four-phase voltage is applied to the microelectrodes, as shown in the figure.

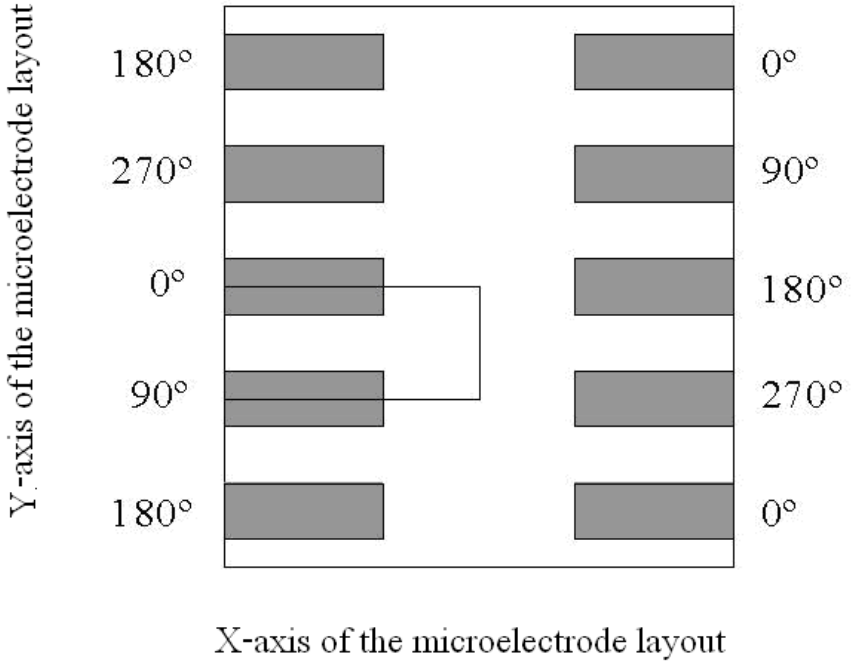

Figure 6.17. Layout of microelectrodes for the travelling wave field

The rectangle highlighted in figure 6.17 shows the area for which the modelling has been done. This appears to be the smallest area in the array of microelectrodes that can have its boundary conditions fully defined in terms of Neumann and Dirichlet boundary conditions, for both real and imaginary components of the electric potential. Figures 6.18 and 6.19 show the boundary conditions for the electrical and thermal problems. The system consists of the suspending liquid enclosed by two layers of glass, the bottom one being the base for the electrode fabrication and the top one being the cover slip. The bottom of the structure is arbitrarily placed at z = 0. The temperature in the planes z = 0 and z = 1200 μm is assumed to be equal to 300 K and these are represented as the Dirichlet boundary conditions for the thermal problem [199, 247]. The electrodes are omitted from the calculation in the thermal problem modelling, because they are assumed to have negligible thermal resistance in the z direction [199]. For the electrical problem, the potential distribution may be solved for the entire structure shown in figure 6.18, including the glass. However, if the conductivity and permittivity of the liquid are much greater than the conductivity and permittivity of glass, only the liquid can be included in the electrical problem, with the boundary conditions at the liquid-glass interface as shown in figure 6.19 [154].

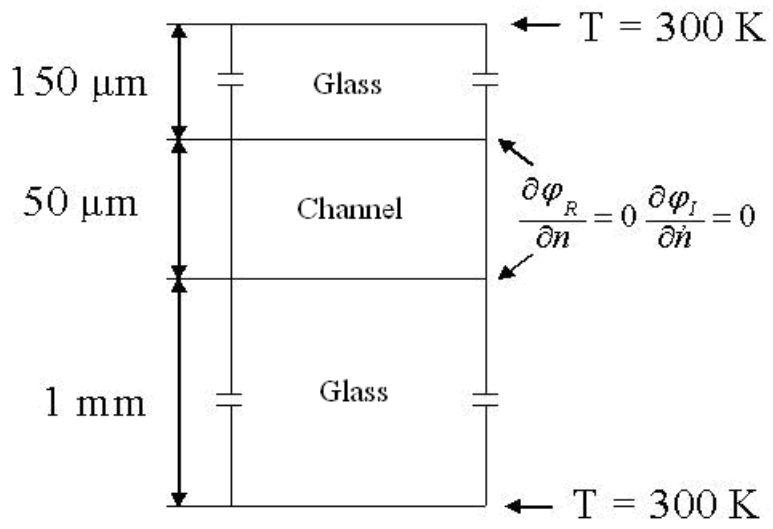

Figure 6.18. Electrical and thermal boundary conditions, z direction

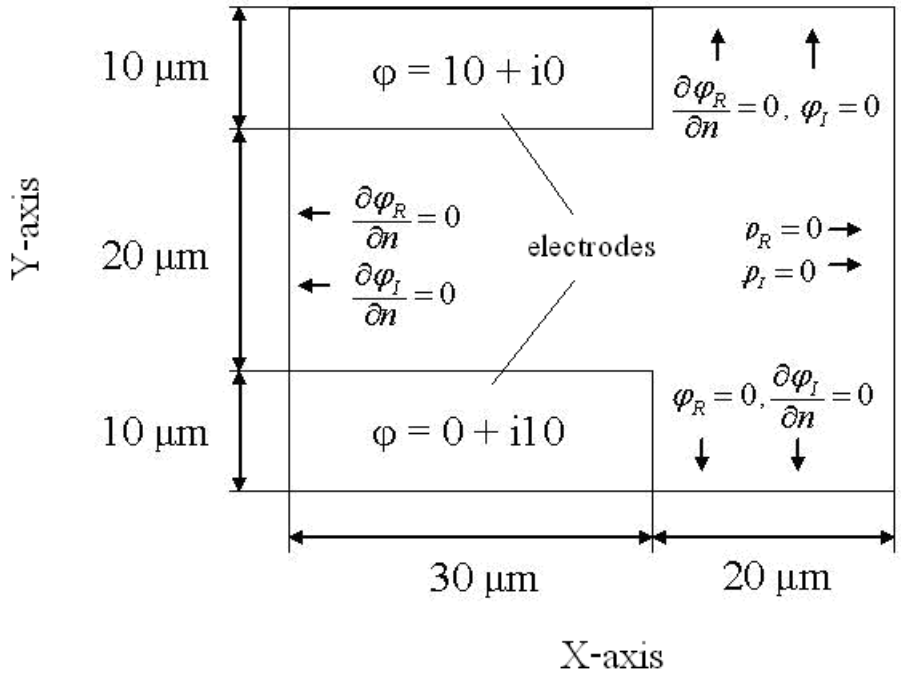

Figure 6.19. Electrical boundary conditions, the plane of the electrodes

For the thermal problem, Neumann boundary condition for the temperature is set on all four boundaries in figure 6.19. The top left corner is assigned x = 0 and y = 0. The frequency of the voltage is 1 MHz.

The potential distributions for φ_R and φ_I are shown in figures 6.20 and 6.21, respectively, in the plane 2 µm above the plane of the electrodes.

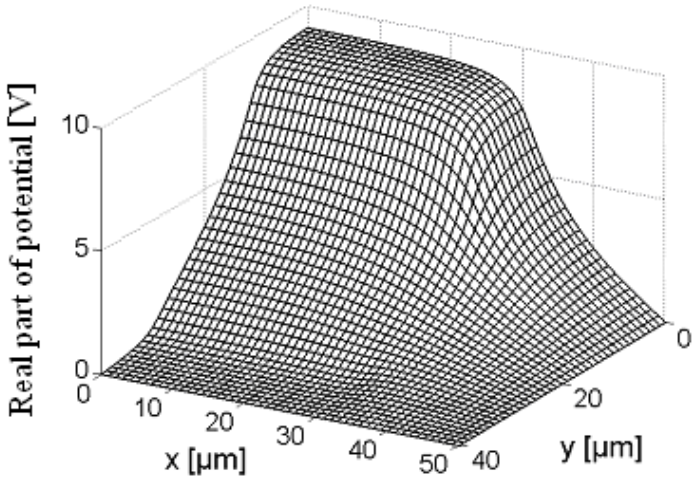

Figure 6.20. Real part of potential φ_R [V], z = 1002 µm

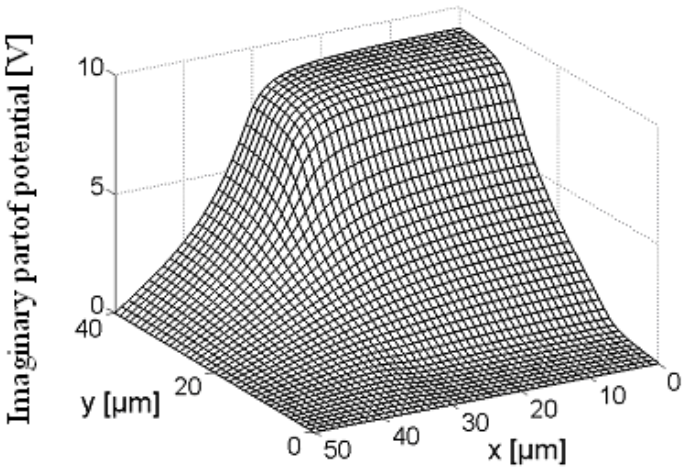

Figure 6.21. Imaginary part of potential φ_I [V], z = 1002 µm

Figure 6.22 shows E_{RMS} in the plane 2 µm above the plane of the microelectrodes. Figure 6.23 shows E_{RMS} in plane x = 25 µm, for the entire liquid, from z = 1000 µm to z = 1050 µm. As expected, the peaks of the electrical field are at the tips of the electrodes.

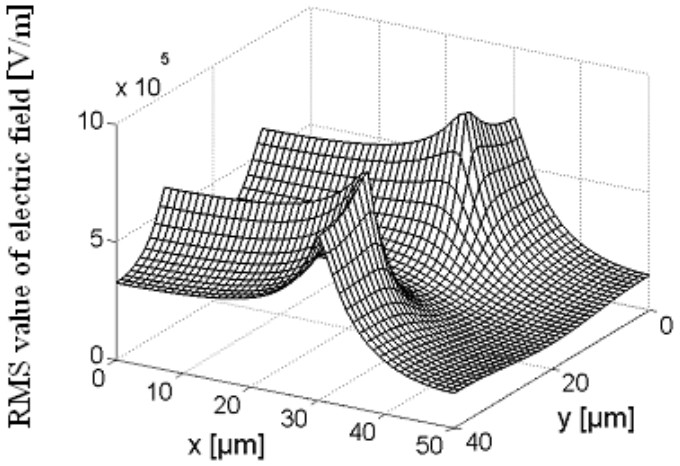

Figure 6.22. RMS value of electric field E_{RMS} [V/m], z = 1002 µm

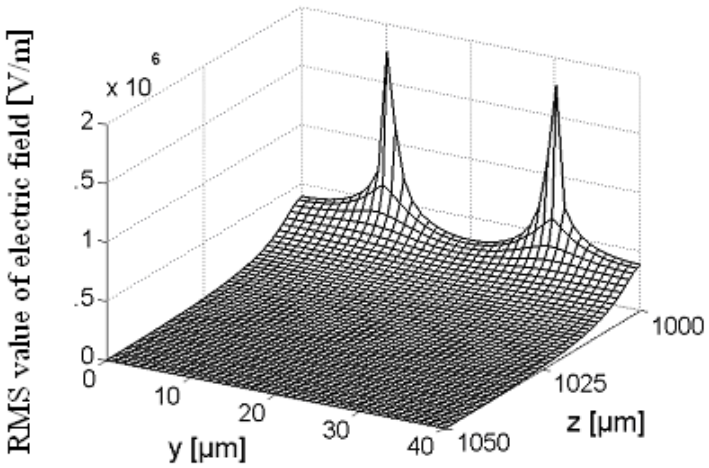

Figure 6.23. RMS value of electric field E_{RMS} [V/m], x = 25 µm

Figures 6.24 and 6.25 show the temperature distribution due to the non-uniformity of the electrical field. Figure 6.24 shows the temperature distribution just above the electrodes, in the plane z = 1002 µm, while figure 6.25 shows the temperature distribution in the plane x = 25 µm, for the entire structure shown in figure 6.18.

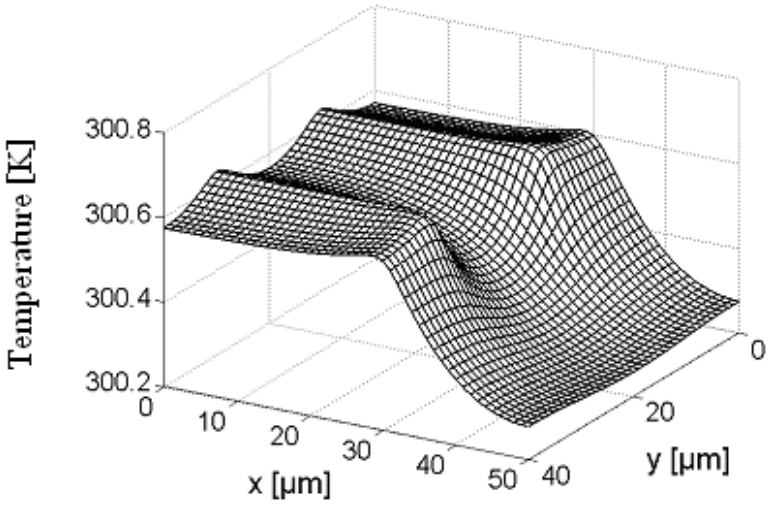

Figure 6.24. Temperature [K], z = 1002 µm

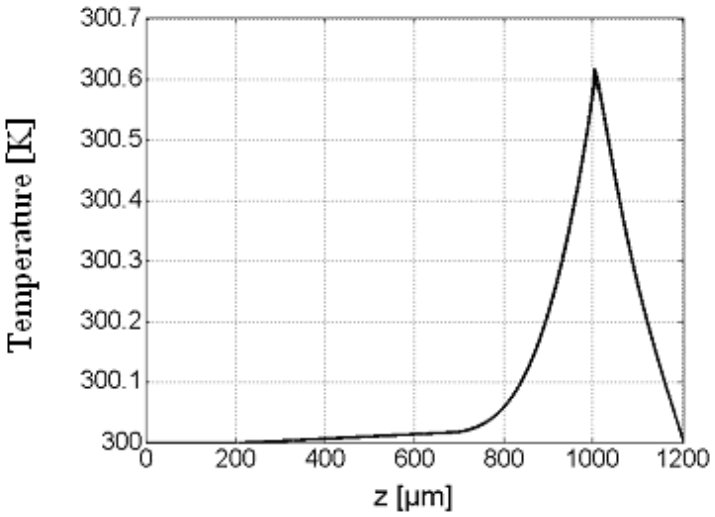

Figure 6.25. Temperature [K], x = 25 µm

As shown in [247], the travelling wave dielectrophoretic force consists of two parts which act independently on the particle and the overall force is a mere superposition of these two parts. In certain cases, one of them may be equal to zero, so it is interesting to observe the particle motion under the influence of the other, non-zero component of the force. For instance, if the imaginary part of the Clausius-Mossotti factor in equation (3.31) is equal to zero or is much smaller than the real part, the particle is subjected to the force that depends only on the gradient of E_{RMS}, while the second term on the right hand side of the equation may be neglected.

Similarly, if the real part of f_{CM} is equal to zero or negligible compared to the imaginary part, the first term on the right hand side may be neglected. In this case the particle is subjected to the force that depends only on the curl of the cross product between the gradients of the imaginary and real parts of the potential.

The case in which the imaginary part of f_{CM} is assumed zero is shown in figures 6.26 and 6.27. The real part of f_{CM} is assumed to be 0.5, and the radius of the particle is assumed to be 1 μm. With the real part of f_{CM} being positive, the particle is subjected to positive dielectrophoresis. As mentioned in [247], only the force on the dipole is taken into account, while the higher order forces have been neglected.

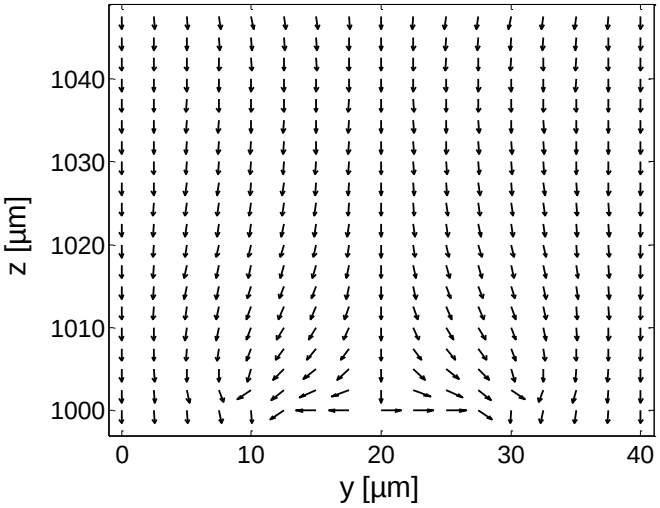

Figure 6.26. DEP force, x = 25 μm

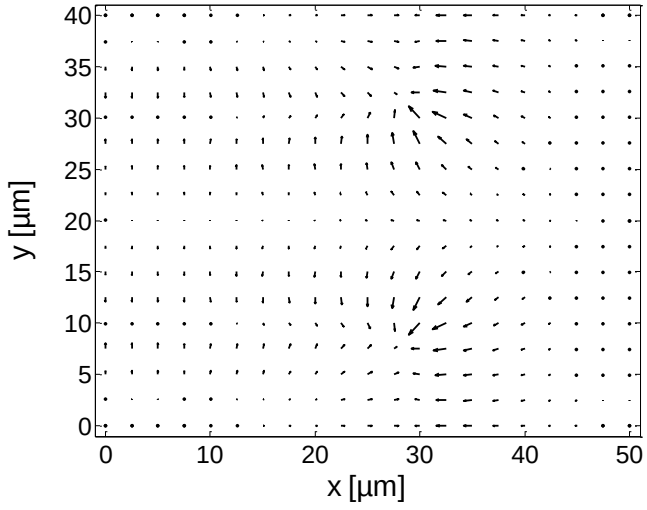

Figure 6.27. DEP force, z = 1002 μm

Figure 6.26 shows the direction of the force in the plain x = 25 μm, while figure 6.27 shows the magnitude of the force in the plain z = 1002 μm. The largest arrow in figure 6.27 corresponds to the force of approximately $5e^{-10}$ N. It can be seen that the particle experiences the positive DEP force, as the direction of the force is towards the tips of the microelectrodes, where the field is the strongest.

If the real part of f_{CM} was negative and of the same magnitude, i.e. -0.5, the magnitude of the force would be the same and the direction would be opposite to the one shown in figures 6.26 and 6.27 (in this case the particle would be subjected to the negative DEP force and repelled from the regions of high field strength at the electrode tips).

If we assume that the real-part of the f_{CM} factor is equal to zero and the imaginary part is equal to 0.5, the DEP force consists only of the component given by the second term on the right-hand side of the equation 3.31. The result is shown in figures 6.28 and 6.29. The former shows the direction of the force in the plain x = 15 μm, while the latter shows the direction of the force in the plain x = 35 μm.

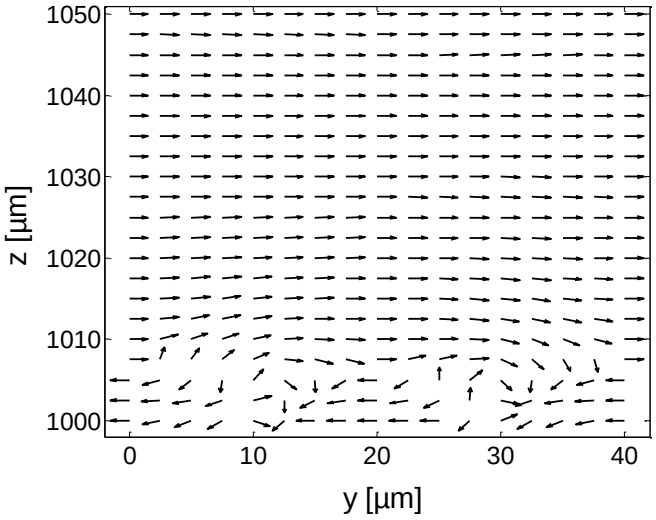

Figure 6.28. DEP force, x = 15 μm

The direction of the force is the same in both figures if the particle is levitated more than 10 μm above the electrodes. Figure 6.29 shows that the direction of the force does not change with the z co-ordinate if the particle is positioned in the gap between the sets of electrodes and not directly above the electrodes. In this case, the force always acts in the direction opposite to that of the travelling field (assuming that the imaginary part of f_{CM} is positive). If the particle is positioned

above the electrodes, the direction of the force depends on the height to which the particle is levitated, as shown in figure 6.28. Close to the electrode plane the force acts in the same direction as the travelling field, and away from the electrodes the force acts in the direction opposite to the field.

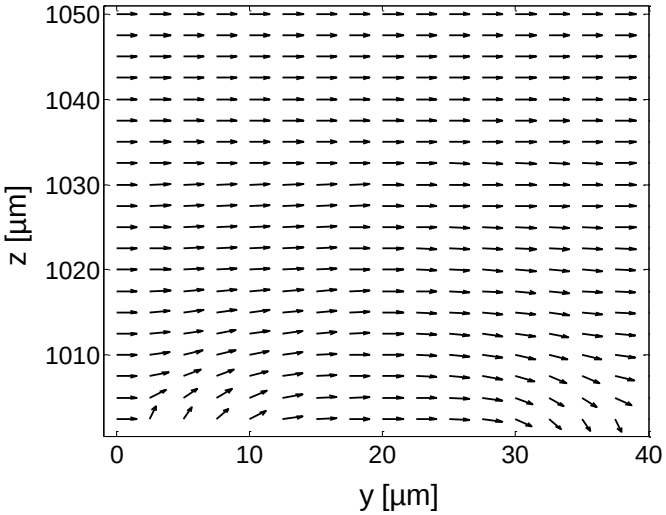

Figure 6.29. DEP force, x = 35 µm

The same behaviour of the force can be derived from Figures 6.30 and 6.31, which show the magnitude and the direction of the force in the plane 2 µm and 25 µm above the electrodes, respectively.

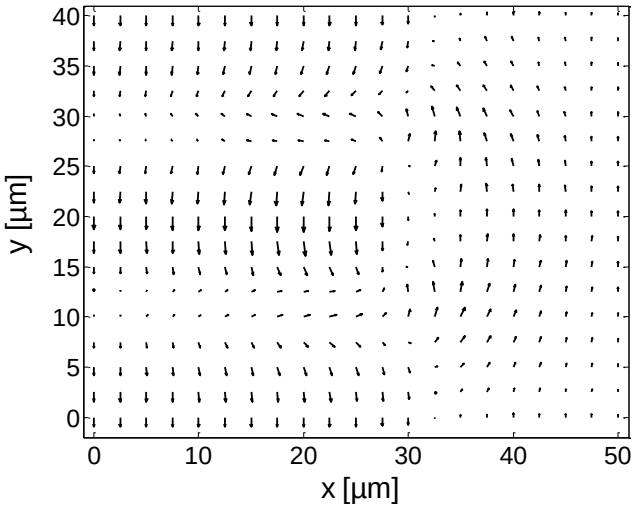

Figure 6.30. DEP force, z = 1002 µm

In the plane 25 μm above the electrodes, the direction of the force is the same in all of the points and the magnitude decreases away from the electrodes, being the smallest in the middle of the channel. In the plane 2 μm above the electrodes, both the direction and the magnitude depend on the position in the plane. In between the electrode sets, the direction of the force is the same as in the plane 25 μm above the electrodes, while directly above the electrodes the force acts in the opposite direction. The largest arrow in Figure 6.30 corresponds to the force of around $4e^{-11}$ N, and in Figure 6.31 to the force of around $2e^{-12}$ N.

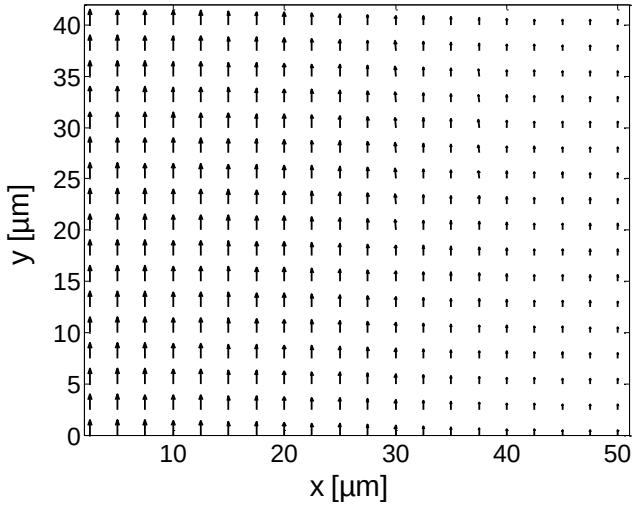

Figure 6.31. DEP force, z = 1025 μm

As already mentioned, in the case where both the real and imaginary parts of f_{CM} are not equal to zero and are of comparable absolute values, the total force will be the superposition of the two parts – the real one and the imaginary one – as shown in equation (3.31). An example of this situation is shown in figures 6.32 and 6.33. The real part of f_{CM} is assumed to be -0.5, so that the particle is repelled from the tips of the electrodes by the influence of negative dielectrophoresis. The imaginary part of f_{CM} is assumed to be 0.5.

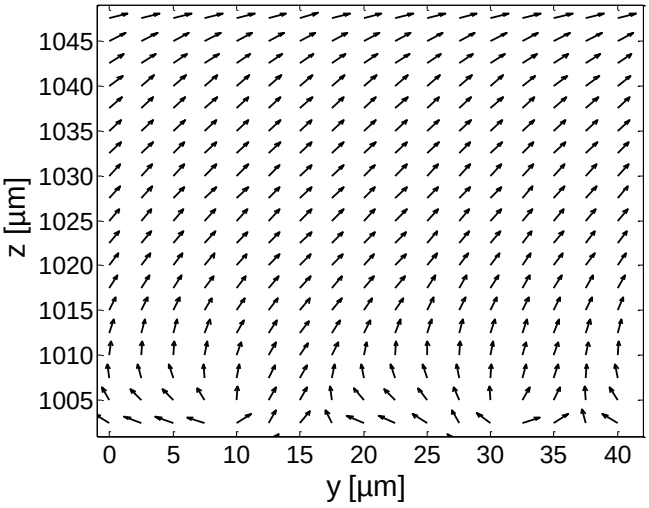

Figure 6.32. DEP force, x = 15 μm

Figures 6.32 and 6.33 show the direction of the force in the planes x = 15 μm (directly above the electrodes) and x = 35 μm (in between the electrode sets), respectively. It can be seen that in this case the particle will be levitated to a certain height above the plane of the electrodes and then forced to move along the electrodes in the direction opposite to the travelling field. If the imaginary part was assumed negative, the translational motion would be in the same direction as the travelling field.

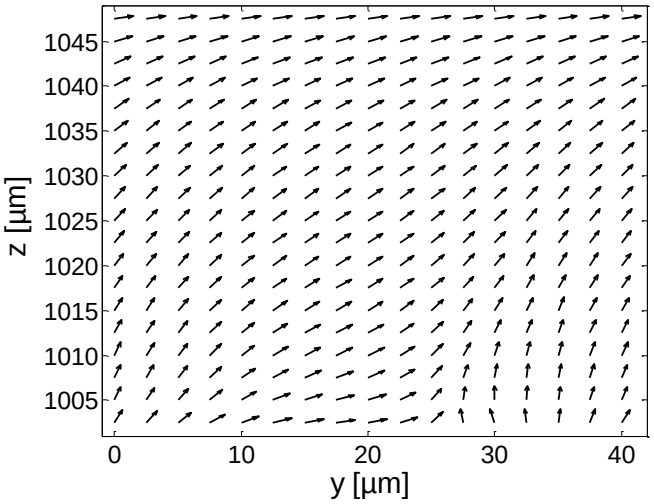

Figure 6.33. DEP force, x = 35 μm

The following figures show the logarithm of the ratio of the absolute values of the first and the second term on the right hand side of equation (3.31) in the

planes x = 15 μm and x = 35 μm, respectively. The real and imaginary parts of f_{CM} are assumed to be equal to -0.5 and 0.5, respectively. It can be seen that, depending on the height to which the particle is levitated, the dominant part of the DEP force given by equation 3.31 can be either given by the first or the second term on the right hand side. If we use the following notation:

$$F_1 = \mathrm{Re}(f_{CM}) \mid \nabla \vec{E}^2 \mid \qquad (6.1),$$

$$F_2 = 2\mathrm{Im}(f_{CM}) \mid \nabla x(\vec{E}_I x \vec{E}_R) \mid \qquad (6.2),$$

then the ratio between the first and the second term on the right hand side of equation (3.31) is equal to F_1/F_2.

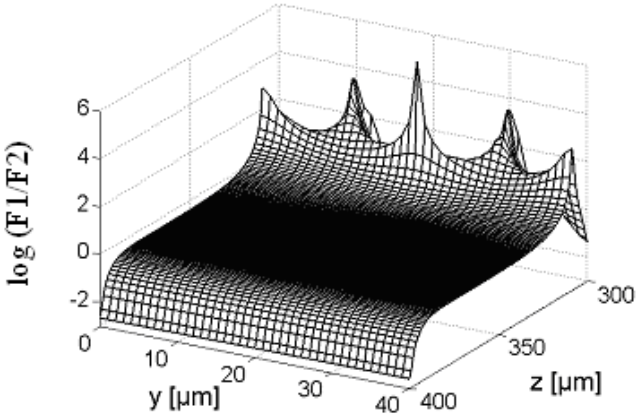

Figure 6.34. Logarithm of ratio F_1/F_2 as given with equations (6.1) and (6.2), x = 15 μm

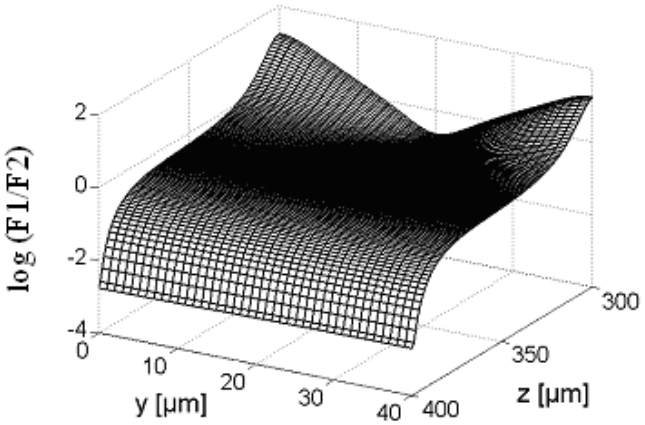

Figure 6.35. Logarithm of ratio F_1/F_2 as given with equations (6.1) and (6.2), x = 35 μm

It can be seen that in both cases the first term is dominant in the area less than 20 μm above the electrodes plane. Around that area the magnitude of both parts is of the same order. Farther above the electrodes plane the second term (corresponding to F_2) becomes dominant. This behaviour can also be seen in figures 6.32 and 6.33. As mentioned above, the particle is first levitated under the influence of the component of the force given by the first term in equation (3.31), and then forced to move along the electrodes under the influence of the component given by the second term (when away from the plain of the electrodes). The regions in which the first or the second term in the equation dominates depend on the dimensions of the electrodes layout (i.e. the gaps between the adjacent and opposite electrodes) and the ratio between the real and imaginary part of f_{CM}. For example, if the gap between the opposite sets of electrodes remains the same and the gap between the adjacent electrodes in the same set doubles, the second term in equation (3.31) will become dominant in the planes even closer to the electrodes than 20 μm. That means that the particle will be levitated to the smaller height before it starts to move along the electrodes. With the careful design of the microelectrodes, its efficiency for the separation of different populations of particles can be increased.

6.3. Impact of medium conductivity on its temperature

In this section, the impact of increase in the conductivity of the suspending medium on its temperature will be described. The castellated microelectrodes structure depicted in chapter 5 in figure 5.1 will be taken as an example. The only change to that structure, as specified in the input file, is the dimension of the problem in *z* direction, i.e. its height. The overall height of the structure is 1200 microns, where 600 microns is the thickness of the substrate, 30 microns is the height of the microchannel, and 570 microns is the thickness of the lid. The height of the problem has been changed to increase the distance between the channel and the top and the bottom of the structure, where temperature is constant due to the Dirichlet's boundary condition for the thermal problem. This should reduce the impact of these boundary conditions on the peak temperature in the channel, and increase the impact of the heating due to the electric field.

To model the dependency of the temperature on the medium conductivity and permittivity, the following two equations have been taken from [193]:

$$\sigma = C_T[1 + 0.022(T - 300)] \tag{6.3}$$

$$\varepsilon = \varepsilon_0 * \varepsilon_{300}\{1 - (T - 300) * [4.6 * 10^{-3} - 8.9 * 10^{-6}\,(T - 300)]\} \tag{6.4}$$

Here, T is the temperature in any given point in the medium, C_T is the suspending medium conductivity at the temperature of 300 K, ε_0 is the permittivity of vacuum, and ε_{300} is the permittivity of the suspending medium at the temperature of 300 K. In the simulations, equation (6.4) has all of its parameters constant, while in equation (6.3) C_T changes from 1 to 80 S/m. For these changes of C_T the temperature changes are observed in the channel, and consequently there are changes in the permittivity, electric field gradient and the magnitude of the dielectrophoretic force, as will be shown in the following figures.

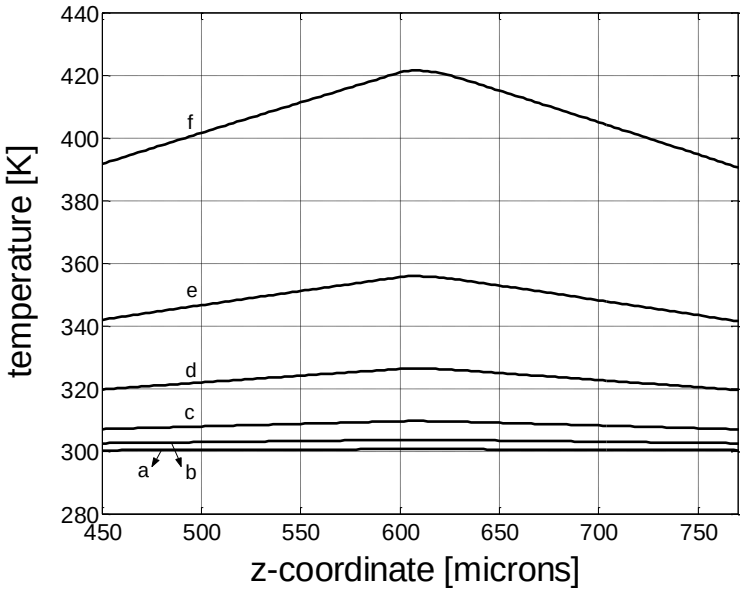

Figure 6.36. Temperature in z-direction for different values of C_T: (a) 1 mS/m, (b) 10 mS/m, (c) 20 mS/m, (d) 40 mS/m, (e) 60 mS/m, and (f) 80 mS/m

Figure 6.36 shows the temperature distribution in the z-direction for different values of C_T. As stated above, the microchannel lies between 600 and 630 μm. It is apparent that the peak temperature always appears right above the electrodes, which are located at z = 600 μm. This is expected, as similar results have been presented in section 6.2, in figures 6.24 and 6.25. In figure 6.37 the temperature dependence on C_T is shown such that for every value of C_T between 1 and 80 mS/m the temperature value is shown at the point 2 microns above the electrode plain. The temperature

dependence on C_T shows exponential behaviour. In other words, if the conductivity of the suspending medium is increased, the temperature of the medium increases exponentially. It can also be seen that by increasing C_T beyond 80 mS/m, the temperature of the medium quickly approaches 100 °C according to the model, so that range of C_T is omitted from the analysis.

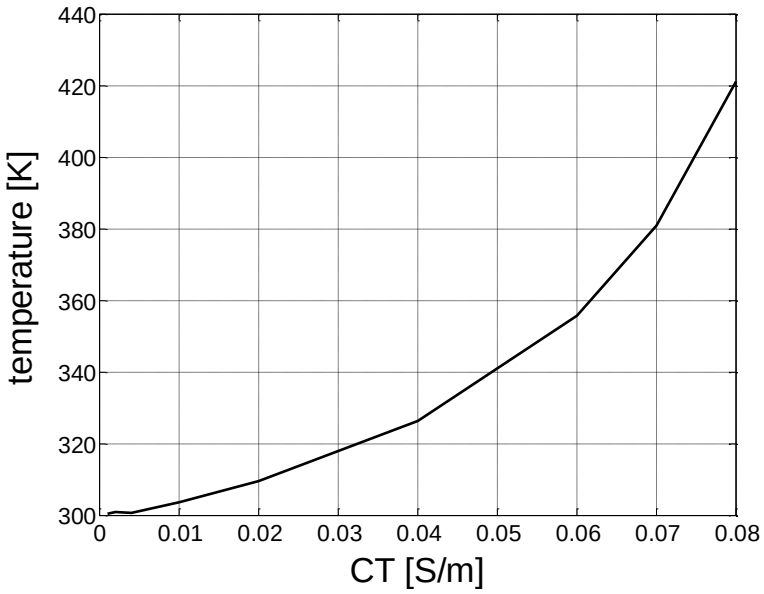

Figure 6.37. Temperature dependence on C_T in the plain 2 microns above the electrodes

Figure 6.38 shows the dependency of the medium conductivity on the parameter C_T. Similar to the temperature dependency, it also shows exponential behaviour, increasing rapidly as the value of C_T increases. Equation (6.3) suggests that the medium conductivity increases with both C_T and the temperature. Since the temperature increases exponentially with C_T, the conductivity shows similar behaviour, and hence the curves in figures 6.37 and 6.38 look very similar. On the other hand, figure 6.39 shows the dependency of the medium permittivity on the value of C_T. In this case, as suggested by the equation (6.4), the value of the permittivity decreases with C_T, since the permittivity decreases when the temperature increases, and the temperature increases exponentially with C_T, as shown in figure 6.37. The curve in figure 6.39 shows inverse exponential behaviour and the value of the permittivity falls rapidly with C_T as we approach larger values of C_T.

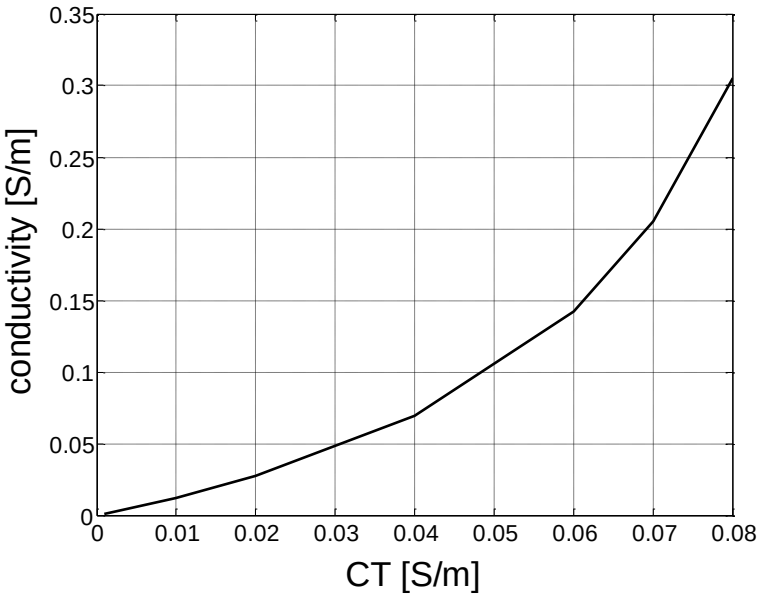

Figure 6.38. Conductivity dependence on C_T in the plain 2 microns above the electrodes

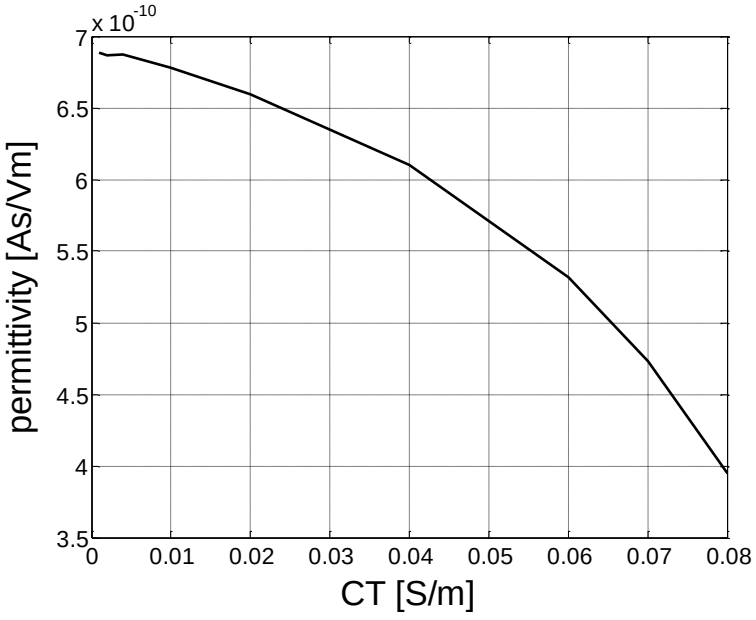

Figure 6.39. Permittivity dependence on C_T in the plain 2 microns above the electrodes

Figures 6.40 and 6.41 show the dependencies of the gradient of the root mean square of the electric field and the magnitude of the dielectrophoretic force on C_T, respectively. From figure 6.40 it is obvious that the gradient of squared E_{RMS} increases almost linearly with C_T, while the dielectrophoretic force in figure 6.41 decreases in a similar way as the medium permittivity in figure 6.39. The decrease in

the dielectrophoretic force magnitude can be explained with the help of equations (3.23) and (3.31) from chapter 3.

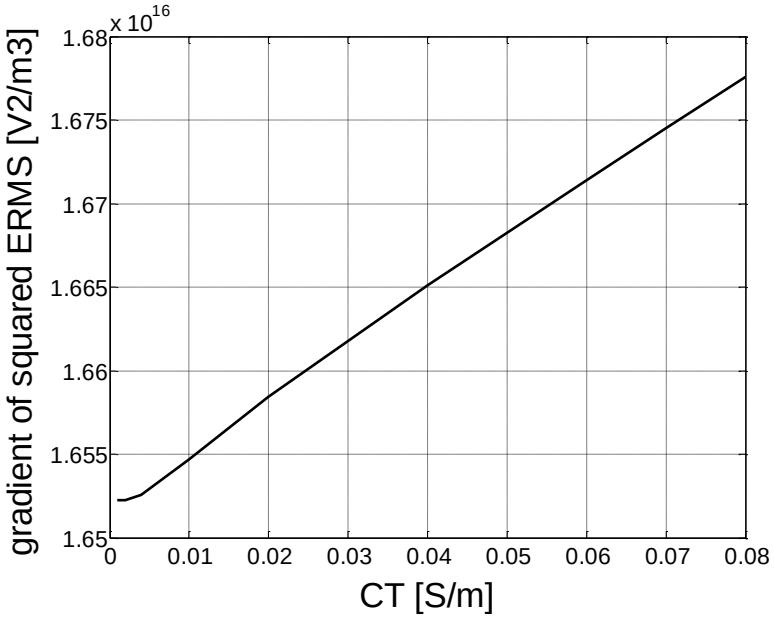

Figure 6.40. Dependence of ERMS squared [V^2/m^3] on C_T in the plain 2 microns above the electrodes

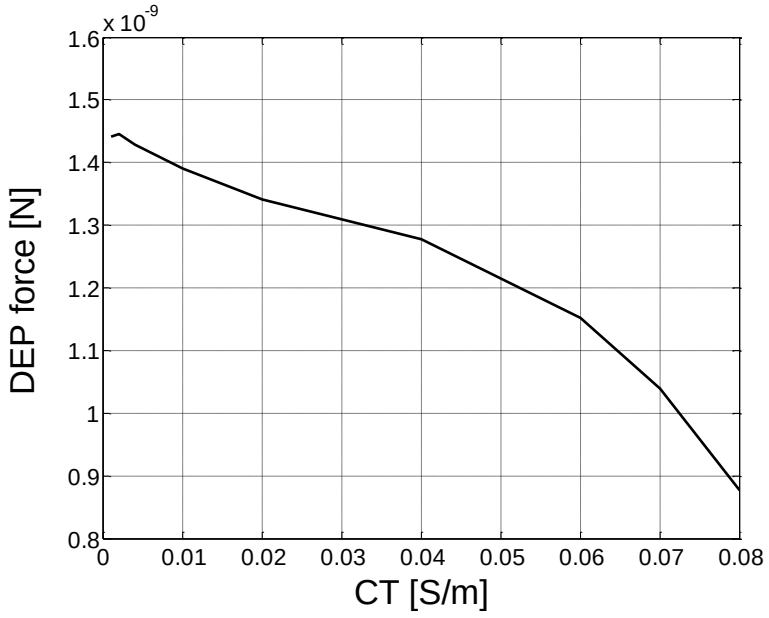

Figure 6.41. Dependence of the dielectrophoretic force on C_T in the plain 2 microns above the electrodes

It is apparent from equation (3.31) that the dielectrophoretic force depends on the medium permittivity, Clausius-Mossotti factor or f_{CM}, and the gradient of the

squared value of E_{RMS}. It should be noted that f_{CM} does not change value significantly with C_T, since it is always defined with the ratio of the conductivities and permittivities of the medium and the particles. Here, the assumption is that the particles in question are latex spheres with the radius of 1 μm, the frequency of the applied voltage is 10 MHz, and the conductivity and permittivity of the particles are smaller than the conductivity and permittivity of the medium by one order of magnitude [193]. From figure 3.16 and equation (3.2) in chapter 3 it is obvious that, with the changes in the medium conductivity and permittivity as described in figures 6.38 and 6.39, the real and imaginary parts of f_{CM} do not change significantly, which is also proven in this simulation. Therefore, if f_{CM} is constant, and if the gradient of squared E_{RMS} increases linearly with C_T, and if the medium permittivity decreases exponentially with C_T, it is expected that the magnitude of the dielectrophoretic force should also decrease with C_T, which is what figure 6.41 suggests. This is due to the fact that the decrease in the medium permittivity dominates over the increase in the gradient of E_{RMS} squared, resulting in overall decrease of the dielectrophoretic force magnitude.

In conclusion, this section analyzes the effect of increasing the medium conductivity on the temperature of the medium and the dielectrophoretic force. Several different simulations modelling different conductivity values of the medium have been performed and the impact on temperature and dielectrophoretic force has been analyzed using Matlab. The results suggest significant increase in the temperature of the medium in the microchannel above the microelectrodes, which in turn leads to decrease of the dielectrophoretic force due to decrease in the medium permittivity.

This chapter shows the results of the dielectrophoretic effect simulation in castellated microelectrodes and travelling wave dielectrophoretic field, by using the program described in chapter 5. The results show the distribution of the electric potential and temperature within the channel, and the resulting dielectrophoretic force magnitude and direction. The final section shows how the temperature of the suspending medium changes with the medium conductivity.

Chapter 7. Separation of latex spheres by using dielectrophoresis and fluid flow

This chapter shows the experimental and simulation results of separating two populations of latex spheres by using dielectrophoretic force and the drag force from the moving liquid. The layout of microelectrodes is the same as the one described in chapter 4, which is used in Doctor-on-a-Chip.

In [201] separation of two latex sphere populations using the dielectrophoretic force and the fluid drag force has been performed experimentally, and a three-dimensional numerical solution of the separation has been presented as well. Microelectrodes of a suitable layout shown in figure 7.1 are used to trap one population of spheres, while the other one is dragged away from the electrodes by the generated fluid flow.

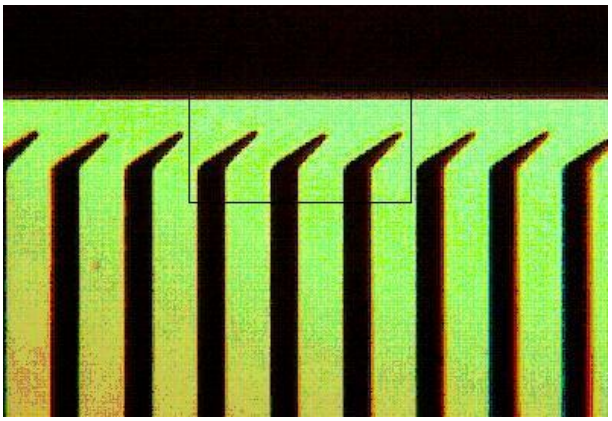

Figure 7.1. The layout of the electrodes used for particles separation.

This separation technique is based on the fluid flow fractionation already described in chapter 3. Microelectrodes are used to generate the electrical field within a closed microchannel, and hence the particles suspended within the liquid experience the DEP force. The resulting effect of having two different types of forces acting upon the particles can be different, depending on the setup.

Firstly, it is possible that the frequency of the applied voltage and the conductivity of the suspending liquid are adjusted in a way that all of the particles experience negative dielectrophoresis and are therefore levitated to a certain height above the electrodes plane. The height to which the particles are levitated is the height at which the DEP force and the gravitational force on the particles are in

balance. Therefore it depends on dielectric properties and mass density of the particles, but not the size, because both the DEP force and the gravitational force are proportional to the volume of a particle. For the particles separation, the fluid motion is generated across the electrodes and the particles are dragged along by the flow. The fluid flow profile is parabolic, and the particles experience the strongest drag force in the middle of the channel, while the force decreases towards the top and the bottom of the channel. The particles experiencing the strongest drag force will be the first to leave the microchannel and that results in the particles separation.

Secondly, a similar technique allows only one population of particles to be dragged away from the channel, while the other one remains trapped within the channel. This can be achieved with one population of particles being subjected to positive dielectrophoresis and the other one to negative dielectrophoresis. The first population is then attracted to the electrode tips and immobilised there under the influence of the strong DEP force, while the second population is levitated towards the middle of the channel and dragged away by the fluid flow.

Finally, in [201] both populations experience the negative DEP force and are therefore levitated above the electrodes. One population of particles experiences the strong force that pushes the particles against the top of the microchannel making them immobile. For this purpose, the microchannel is made only 10 μm deep. The other population is also subjected to the negative DEP force, but the particles leave the channel carried away by the liquid, because the DEP force is overcome by the drag force.

In [201], the electrodes are fabricated on the glass slide and the 10 μm thick insulating tape is used to form the microchannel, which contains the liquid and the particles. The channel is sealed with the glass cover slip. The potential distribution is obtained only for the liquid, with Neumann boundary conditions for the potential at the interfaces with glass and the insulating tape. This is a good approximation because it can be shown that the normal component of the electrical field in the liquid is negligible due to the large differences in the conductivity and permittivity values between the liquid and the surrounding materials. Double distilled water is used as the suspending medium, with the conductivity around 1 μS and the relative permittivity around 80. The conductivity of glass is around 10^{-10} S and the relative permittivity around 5. The voltage applied to the electrodes is a sine signal with the

magnitude of 20 V and the frequency of 6 MHz. This frequency is chosen to minimize EHD pumping of the liquid.

The particles used in the experiment are latex spheres 3 μm and 0.914 μm in diameter. For the DEP force calculation, the particles conductivity is modelled as $\sigma = 2K_S/r$ where K_S is the surface conductance r is the radius of the sphere. The relative permittivity of the spheres is taken to be 2.55. The surface conductance is of the order of 1-3 nS and it is different for spheres with different radii. In this case high accuracy of K_S is not necessary, since it has a little impact on the value of the Clausius-Mossotti factor.

The fluid flow profile within the microchannel is given by the following Navier-Stokes equation in the low Reynolds number approximation:

$$-\nabla p + \nabla^2 \vec{u} + \vec{f} = 0 \qquad (7.1).$$

Here *p* is the pressure, *u* is the fluid velocity, and *f* is the density of the body force on fluid. In this case we assume that the electrohydrodynamic force density is negligible in equation (7.1). The frequency dependence of this force is such that at high frequencies it seizes to be significant. Therefore, the fluid velocity profile is given only by the pressure difference. If the pressure gradient is constant along the channel in the direction from left to right in figure 7.1, the velocity profile is parabolic. The maximum velocity is in the middle of the channel, while at the bottom, top and side walls the velocity is equal to zero. The drag force on spherical particles of radius r can be calculated from the fluid velocity using the following equation:

$$\vec{F}_{drag} = 6\pi\eta r\vec{u} \qquad (7.2).$$

Here η is the viscosity of the fluid. From the observed fluid velocity, we can estimate the drag force on the particles and compare it with the calculated DEP force.

The first step towards the calculation of the DEP force on the particles is to solve the distribution of the electric potential. The domain for the solution is highlighted with the rectangle in figure 7.1, which encloses the three electrodes from the bottom set and 30 μm of the top electrode. All the important dimensions are

shown in figure 7.2. The bottom left corner is assigned x = 0 and y = 0, the plane of the electrodes is assigned z = 0 and the top of the microchannel z = 10 μm.

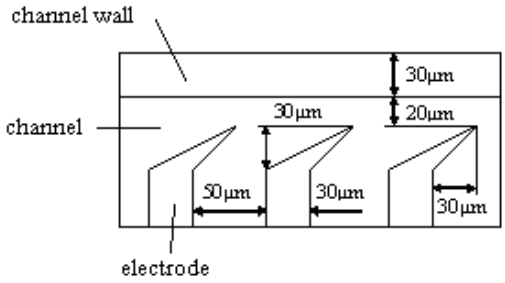

Figure 7.2. Dimensions of the electrode layout for numerical solution

Resulting potential distribution is shown in figure 7.3, while figure 7.4 shows E_{RMS}. Both of those figures show the results in the plane 2 μm above the electrodes.

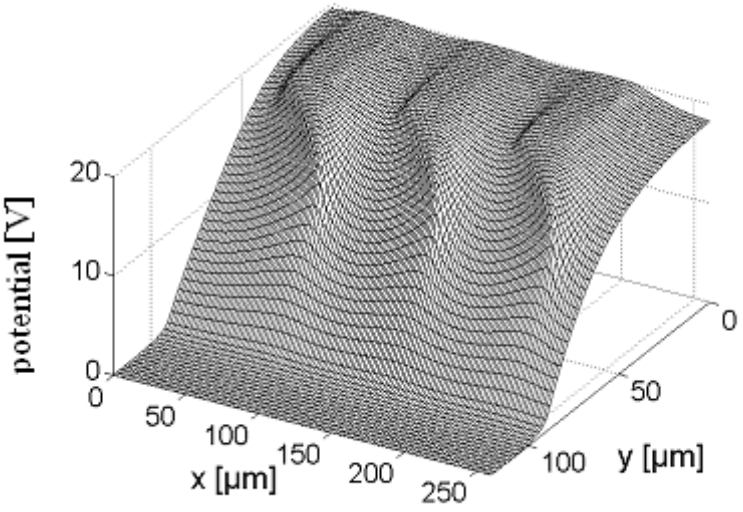

Figure 7.3. Potential φ at z = 2 μm

As expected, the peaks in the electrical field distribution are at the tips of the electrodes. Because of the shape of the electrodes, it is difficult to achieve high accuracy of the potential distribution with the limited number of mesh points near the tips. However, the important events in particle separation are taking place away from this region due to negative dielectrophoresis on the particles, so these probable inaccuracies are not very important.

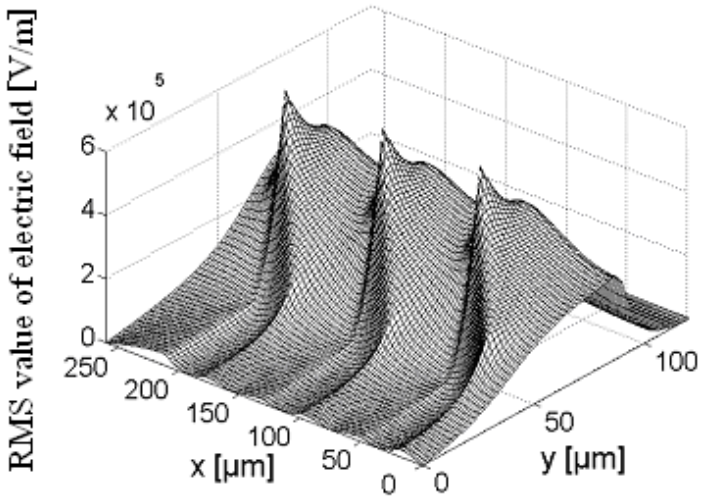

Figure 7.4. RMS value of electric field at z = 2 μm

Figures 7.5 and 7.6 show the magnitude of the DEP force on particles and its direction, respectively, in the plane z = 2 μm. As expected, the force is strongest at the tips of electrodes and weakest between the electrodes in the bottom set of electrodes (in the regions of the smallest gradient of potential).

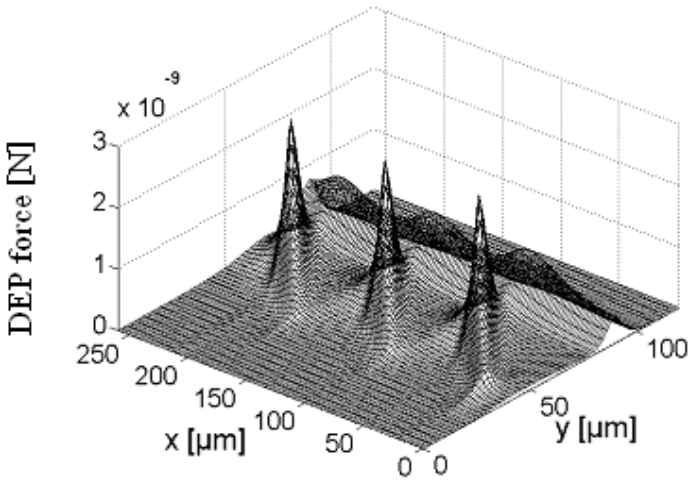

Figure 7.5. Dielectrophoretic force at z = 2 μm

Figures 7.5 and 7.6 show the simulation results for the larger particles (3 μm in diameter). For the smaller particles, the qualitative distribution of the DEP force is exactly the same, and the only difference in magnitude results from different particle volumes. The real part of the Clausius-Mossotti factor is of a similar value

for both particles. The DEP force on the smaller particles is therefore about 35 times weaker than for the larger particles.

When the particles were introduced in the system of microelectrodes shown in figure 7.1, we observed the motion of the liquid from the left hand side towards the right. The rate was the same after we have applied the voltage to the electrodes. Therefore, the assumption that the electrical body force on the liquid does not play a significant role on the liquid movement is reasonable.

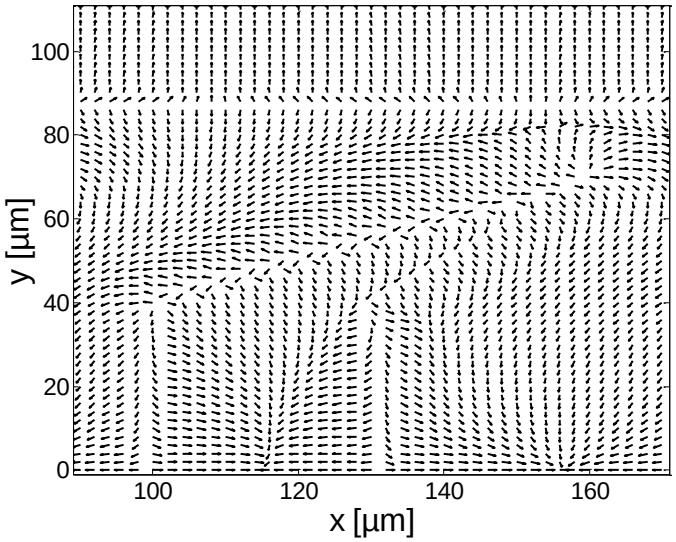

Figure 7.6. Direction of the DEP force vector at z = 2 μm

Figures 7.7.a-d show the sequence of the particles separation using negative dielectrophoresis and the fluid flow, as described in the text above. Figure 7.7.a shows the particles distribution within the channel before the voltage was applied to the electrodes. The dominant force on the particles is the drag force due to the fluid motion from left to right, and all the particles are carried away by the fluid at the rate of approximately 1 μm/s. It is very difficult to model the exact profile of the fluid velocity, because the particles diameter is comparable to the channel depth. The density of the particles is sufficient to break the regular parabolic profile of the fluid velocity. The smaller particles spin was noticed when they are found in the vicinity of the larger particles, probably due to the turbulence caused by the fluid flowing across the larger particles. However, the fluid velocity was estimated to be around 1 μm/s and use this value was used to estimate the drag force on particles and compare it to the calculated DEP force.

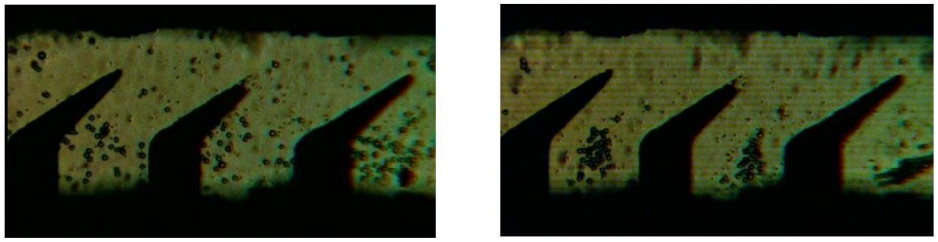

(a) (b)

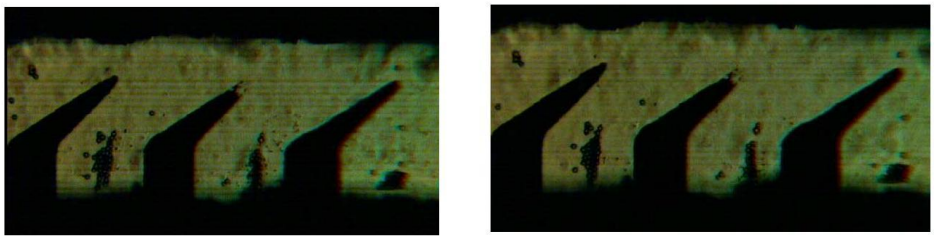

(c) (d)

Figure 7.7. The sequence of particle separation: **(a)** before the voltage was applied to the electrodes, **(b)** just after the voltage was applied to the electrodes, **(c)** smaller particles are being dragged out of the channel by the fluid flow, and **(d)** practically all of the smaller particles left the channel.

Figure 7.7.b shows the particle distribution just after the voltage has been applied to the electrodes. Both larger and smaller particles tend to move to the regions of low field strength, as shown in figure 7.6. The larger particles remain trapped in these regions between the electrodes, as shown in figures 7.7.b and 7.7.c, while the smaller particles are dragged away from the channel by the fluid flow. Initially, when the voltage was applied, the smaller particles had a tendency to move to the regions of low field strength as well as the larger particles, which means that they are also subjected to the negative DEP force. That confirmed the calculation, which showed that both populations experience the negative DEP force. However, the fluid drag force seems to govern the motion of the smaller particles. The rate at which they continued to move from the left to the right was slightly decreased, but not significantly. Figure 7.7.d shows that the majority of smaller particles eventually left the channel, while the larger particles remained trapped.

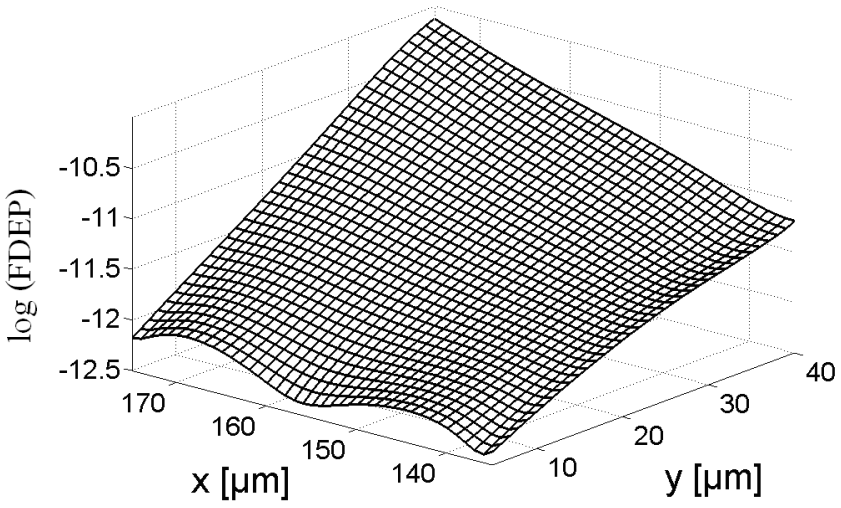

(a)

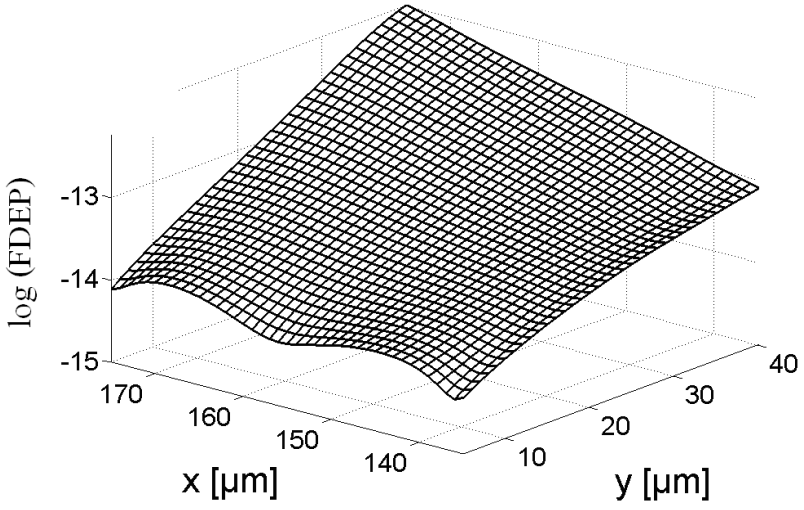

(b)

Figure 7.8. Logarithm of absolute value of dielectrophoretic force: (a) $\log(|\vec{F}_{DEP}|)$ for the larger particles at z = 8 μm, (b) $\log(|\vec{F}_{DEP}|)$ for the smaller particles at z = 9 μm.

To explain the background of the particles separation shown in figures 7.7.a-d, the DEP forces and the drag forces on the particles need to be compared. Figure 7.8 shows the DEP force on both populations of the particles in the region of the low field strength, where the larger particles accumulated in the experiments. The *x* and *y* components of the DEP force are such that the particles are pushed towards that region by the negative DEP force. Depending on the strength of that force, they will

either be held immobilized there, or washed away by the fluid flow, if the drag force overcomes the DEP force.

From equation (7.2) and the fluid flow rate of 1 μm/s, the drag force on the particles can be calculated. The viscosity of water is assumed to be $8.91*10^{-4}$ Ns/m^2. For both particles the drag force is in the order of magnitude of 10^{-14} N (the ratio between drag forces on spherical particles is equal to the ratio of their radii, which is only around 3.5 in this case). If we compare the drag forces on the particles with the calculated DEP forces in the regions of low field strength, we can see that the DEP force on the larger particles is two orders of magnitude stronger than the drag force, so they are trapped at the top of the channel. The fluid flow is not strong enough to overcome the DEP force and drag the particles away. For the smaller particles, the drag force and the DEP force are of the same order of magnitude, so that the particles are slowly dragged towards the right-hand side of the microchannel, hence the separation is possible. In the case of the larger particles, the dominant components of the DEP force are x and y component. Together with the cover slip they form a "wall" around the particles, and the drag force is not strong enough to push the particles "through" this "wall".

This chapter shows the results of the separation of two different populations of latex spheres by using dielectrophoresis and the fluid flow. The simulation results are presented by using the program described in chapter 5, and the experimental results are presented by using the layout of microelectrodes which is used in Doctor-on-a-Chip. It has been shown that the experimental results correlate well with the simulation results.

Chapter 8. Conclusion and recommendation for future work

In this work, a thorough feasibility analysis of dielectrophoretic separation of particles on a micro-scale was carried out. The overview was given of the relevant technologies required for the integration of the complete bodily fluid sample analysis for pathogens detection onto a single chip. This includes main microbiological concepts, PCR amplification, detection of DNA molecules, microfluidic technologies, and theory of dielectrophoresis. It should be noted that there was a significant time lag of about five years between the beginning of this research and the finalization of the thesis. In that period of time, the fields of microfluidics and MEMS have made tremendous progress, as significant financial and human resources continue to be invested into the research. Although some of the techniques and achievements presented in this thesis therefore seem a bit outdated, they present state of the art of these technologies in the first three to five years of the 21st century.

In chapter 1, the main aims and objectives of this research have been listed and the expectations have been set. In the following text, these objectives will be addressed again in the context of the previous 5 chapters, together with the recommendations for future work.

The overview of the microbiological techniques and methods for purification and amplification of the sample was given in chapter 2, together with the detection methods currently available for the final sample analysis. These components on the chip are crucial by means of enabling automated process of setting the stage for separation of pathogen DNA from the genomic DNA present in the sample. Automation means lower cost and higher reproducibility and reliability of the process. The main emphasis was given to possible integration of the existing technologies onto the chip, rather than investigating completely new principles.

The overview of the microfluidic components was given with a similar idea in mind: to show the existing technologies of manipulating liquids and particles through the microfluidic network on a microfabricated chip, in the reliable and reproducible manner. The emphasis was also given on handling biological materials, since some of the existing methods have been proved destructive due to, for example, increased temperature of the sample during manipulation of cells and DNA. Several viable solutions were presented in this work, and the main emphasis

in the future work related to this objective should be placed on coming up with the best possible one for this application. This aspect of the design probably has the most dependencies of all. For example, based on the details of the protocol for DNA extraction, purification and amplification, one solution to pump the liquids around the chip and transfer the DNA molecules might be more suitable than the other, which could potentially be more suitable with another protocol. Therefore, once the protocol for obtaining the DNA from a sample is clearly defined and verified, more detailed research should be performed of feasibility of different microfluidic techniques presented in this thesis in implementing that protocol on a chip. This will clearly have to involve a lot of experimental work, because of complexity of DNA transfer in microfluidic systems. Similarly, microfluidic techniques could potentially be related to DNA separation methods as well. In other words, if a technique similar to the separation technique described in section 5.4, which uses the combination of the fluid pumping and dielectrophoresis, would be used to separate DNA in DoC, the pumping technique and the DEP method of manipulating the DNA molecules with the electric field have to be investigated and defined together, as they need to work seamlessly during the sensitive process of the separation of micro and nano particles.

The overall design of the chip can be facilitated by using the computer aided design (CAD) methods and tools to evaluate certain aspects of the design. In particular, dielectrophoresis can be qualitatively and quantitatively analyzed given the layout of microelectrodes and the properties of the suspending liquid and the particles. It is apparently much more cost effective if a specific dielectrophoresis separation method would be analyzed and simulated by using a CAD tool prior to fabrication. In this way, spending time and financial resources on fabricating the design that does not work well could easily be avoided. Similarly, with the help of a CAD tool, any specific set of microelectrodes could be tuned in much faster and cost-efficient way, to improve the performance of separation early in the development cycle. For this purpose, the CAD tool should be robust, reliable, and capable of capturing all of the relevant effects in the particles manipulation with dielectrophoresis. In this work many of the relevant forces were described and analyzed qualitatively and quantitatively by using the numeric mathematical methods. The program for simulation of electric field and dielectrophoresis has shown good correlation with the real experimental data, as was presented in section

5.4. In the future, the main aspects of improving the program and making it more efficient, accurate and user friendly would include:

- Continue investigation of physical effects and forces that influence behaviour of particles in dielectrophoretic systems of microelectrodes, and incorporate them into the program for better accuracy. For example, fluid dynamics could be added to 3-D calculations to model the influence of the liquid pumping on the particles and vice-versa. This would clearly involve more experimental work to verify new features in the program.
- Add graphical user interface to enter the specification in a more efficient and user friendly way, and visualize the results at the end of the simulation without running multiple programs for analysis.
- Investigation of the algorithms used in the mesh generation and finite difference method calculations, and possible optimizations of the functions and algorithms for better performance and easier maintenance and upgrades.

Another important thing to note is that at the time this research was carried out, CAD tools for 3-D simulation of electric field were not easily available and customizable to a particular application. That is why the approach of developing the software for the purpose of simulating dielectrophoresis in three dimensions has been taken in the first place. Nowadays, it could be beneficial to again investigate available commercial CAD tools, and see if using any of them could be beneficial in long term, as opposed to keep maintaining and upgrading the existing simulation program described in this thesis. It should be emphasized again that the main goal of this research is development of DoC, and any tool that helps getting to the goal earlier should be evaluated and used.

The example of Doctor-on-a-Chip was also discussed and analyzed. As presented in chapter 3, it integrates the known methods of DNA extraction, amplification and manipulation on a single chip, but also introduces a novel approach to dielectrophoretic manipulation of DNA molecules (and other particles in general), by using a novel layout of microelectrodes described in section 5.4. As far as the sample preparation and DNA detection are concerned, Doctor-on-a-Chip should benefit from re-use of the existing methods relevant to those steps in the analysis. The main idea of this project, which was already emphasized, is not to

investigate all of the methods in the on-chip DNA analysis, but just the crucial one for DNA separation prior to analysis, which is dielectrophoresis, and its feasibility for this particular purpose. The other components, such as PCR for example, should be investigated for feasibility of integration onto a chip and compatibility with the idea of a total DNA analysis system. The recommendation should be drawn on the usability of these methods, but no significant effort should be put into discovering novel methods. In this particular case, figure 3.26 shows the components of the system which are reused for the purpose of analysis system assembly on a chip. The most notable reused components are the heated chambers for DNA extraction and PCR, the micropumps for fluid pumping and mixing, and the detectors of DNA based on the impedance measurement technique. All of these components are described in the text by quoting already published results of their research and development. In terms of the future work related to the chip integration, the challenges remain the same: making sure that the individual components can be put together on a single chip and work together seamlessly, to deliver the robust analytical method. The integration needs to be supported by a lot of experimental work, but probably one step at the time. For example, investigating integration of DNA preparation protocol and PCR on a single chip is challenging enough that it should be done separately, without introducing the complexity of dielectrophoretic separation and DNA detection into that same research. Only after DNA preparation and PCR have been successfully integrated, the microelectrodes should be added into the picture. In a similar way, dielectrophoretic separation chambers can be integrated with the detection of DNA, prior to integrating the whole system together, as described in chapter 3.

As far as investigating the dielectrophoretic methods for separation of DNA molecules is concerned, one novel method is described in details in section 5.4. The feasibility of the method, based on the novel layout of microelectrodes, has been experimentally proved as successful in separating small particles by using the dielectrophoretic force, and the experiment correlated well with the simulation performed on a computer. The next steps in the future work should involve separation of DNA molecules in the same or similar system of microelectrodes. Given the complexities that DNA brings to the table in terms of dielectrophoretic manipulation, this still remains the biggest challenge. In terms of DoC layout in chapter 4, the challenge is also to prove that several different pathogens can be

investigated for at the same time, by targeting a particular pathogen in a given array of microelectrodes, and by changing the setup in the microelectrode array in terms of the suspending liquid and voltage frequency.

In summary, this thesis has given a general overview of the technologies available for integration of DNA analysis onto a single chip. Already known methods of DNA sample preparation and transfer of molecules have been described in the context of DoC, and the novel method of dielectrophoretic separation of DNA molecules has been added as a method of detecting pathogens within the sample. The concept of the chip has been developed and described, and the foundation for the experimental work to prove the feasibility of these methods has been set. Specific to the dielectrophoretic manipulation of DNA, the 3-D simulation program has been developed to facilitate the experimental work by analysing dielectrophoresis on particles on a computer, and to facilitate the experimental work and increase the understanding of how particular microelectrode setup works. The simulation program has been successfully used to verify several experiments with different setup, and showed the correlation between the simulation data and the experiments.

References

[ref 1] Handbook of analytical techniques
Editors: Helmut Günzler, and Alex Williams
John Wiley, 2001

[ref 2] Proceedings of the μTAS 2000 Symposium, Enschede, Netherlands, 2000
Editors: A. van den Berg, W. Olthuis, and P. Bergveld
Kluwer Academic Pub, 2000

[ref 3] Proceedings of the μTAS '98 Workshop, Banff, Canada, 13-16 October 1998
Editors: D. J. Harrison and A. van den Berg
Kluwer Academic Pub, 2000

[ref 4] Development of a novel DNA chip based on a bipolar semiconductor microchip system
J. M. Song, M. S. Yang, and H. T. Kwan
Biosensors and Bioelectronics 22 (2007) 1447–1453

[ref 5] Nucleic acid techniques in bacterial systematics
Editors: Erko Stackebrandt and Michael Goodfellow
John Wiley, 1991

[ref 6] Microfluidic based lab-on-a-chip systems
B. H. Weigl
IVD Technology Magazine, Nov / Dec 2000

[ref 7] DNA-chip technologies, Part 1: Research fundamentals and industry catalysts
Cliffe Henke
IVD Technology Magazine, Sept 1998

[ref 8] DNA- chip technologies, Part 2: State-of-the-art competing technologies
Cliffe Henke
IVD Technology Magazine, Nov 1998

[ref 9] DNA- chip technologies, Part 3: What does the future hold
Cliffe Henke
IVD Technology Magazine, Jan 1999

[ref 10] Microfludic plastic chips by hot embossing and their application for DNA separation and detection
G. B. Lee, S. H. Chen, G. R. Huang, Y. H. Lin, W. C. Sung,
Microfluidic devices and systems, Proceedings of SPIE, 2004, Vol. 4177, 105-114

[ref 11] Design automation for microfluidic based chips
K. Chakrabarty and J. Zeng

ACM Journal on Emerging Technologies in Computing Systems, Vol. 1, No. 3, October 2005, 186-223

[ref 12] Molecular-Systems-on-Chip (MSoC): Steps forwards for programmable biosystems
P. Wagler, U. Tangen, T. Maeke, S. Chemnitz, M. Juenger, and J. McCaskill
Smart Structures and Materials 2004: Smart Electronics, MEMS, BioMEMS, and Nanotechnology, Proceedings of SPIE, Vol. 5389, 298-305

[ref 13] On-chip DNA band detection in microfabricated separation systems
S. Brahmasandraa, B. Johnson, J. Webster, D. Burke, C. Mastrangelo, and M. Burns
Microfluidic devices and systems 1998, Proceedings of SPIE, Vol. 3515, 242-251

[ref 14] Development of integrated microfluidic system for genetic analysis
R. Liu and p. Grodzinski
J. Microlith., Microfab., Microsyst., Vol. 2 No. 4, October 2003, 340-354

[ref 15] Electromechanics of particles
Thomas B. Jones
Cambridge University Press, 1995

[ref 16] A microchip-based DNA purification and real-time PCR biosensor for bacterial detection
N. Cady, S. Stelick, M. Kunnavakkam, Y. Liu, and C. Batt
Sensors, 2004. Proceedings of IEEE, Oct. 2004, Vol. 3, 1191-1194

[ref 17] Integrated microfluidic systems for DNA analysis
C. Lee, J. Lin, C. Liao, F. Huang, and G. Lee
Robotics and Biomimetics, 2004 IEEE International Conference**,** Aug 2004, 284 - 289

[ref 18] Electrical detection of viral DNA using ultramicroelectrode arrays
E. Nebling, T. Grunwald, J. Albers, P. Schaefer, and R. Hintsche
Anal. Chem., 76 (3), 2004, 689 -696

[ref 19] Integrated microfluidic biochips for immunoassay and DNA bioassays
Liu, R.H.
Engineering in Medicine and Biology Society, 2004, 26th Annual International Conference Proceedings, Vol. 2

[ref 20] Lab-on-a-chip based on BioMEMS
S. Kumar, R. Bajpai, and L. Bharadwaj
Proceedings of Intelligent Sensing and Information Processing Conference, 2004, 222-226

[ref 21] Microfluidic chips for DNA amplification, electrophoresis separation and on-line optical detection
G. Lee,C. Lin, C. Lin, F. Huang, C. Liao, C. Lee, and S. Chen
Micro Electro Mechanical Systems, 2003, IEEE The 16th Annual International Conference**,** 2003, 423 - 426

[ref 22] Microchip based purification of DNA from biological samples
M. Breadmore et al.
Anal. Chem., 75 (8), 2003, 1880 -1886

[ref 23] Fully electronic DNA detection on a CMOS chip: device and process issues
F. Hofmann et al.
Electron Devices Meeting, IEDM 2002 International Digest, 2002, 488-491

[ref 24] Heat properties of an integrated PCR micro-vessel
Z. Zhao, D. Cui, Z. Yu, L. Wang, and S. Xia
International Conference on Sensor Technology, ISTC 2001, 31-34

[ref 25] Closed chamber PCR chips for DNA amplification,
C. G. J. Schabmueller, M. A. Lee, A. G. R. Evans, A. Brunnschweiler, G. J. Ensell, and D. L. Leslie
Engineering Science and Education Journal, 9 (2000), 259-264

[ref 26] Real-time PCR analysis of nucleic acids purified from plasma using a silicon chip
P. Belgrader, R. Joshi, J. Ching, S. Zaner, D. A. Borkholder, and M. A. Northrup
Proc. of the μTAS Symposium, 2000, 239-242

[ref 27] Thermal management and surface passivation of a miniaturized PCR device for traditional Chinese medicine
I. K. Lao, T. M. H. Lee, M. C. Carles, and I.-M. Hsing
Proc. of the μTAS Symposium, 2000, 239-242

[ref 28] A micro cell lysis device
S.-W. Lee, and Y.-C. Tai
Sensors and Actuators A: Physical, 73 (1999), 74-79

[ref 29] Silicon microchambers for DNA amplification
J. H. Daniel, S. Iqbal, R. B. Millington, D. F. Moore, C. R. Lowe, D. L. Leslie, M. A. Lee, and M. J. Pearce
Sensors and Actuators, A 71 (1998) 81-88

[ref 30] Chemical amplification: continuous flow PCR on a chip
M. U. Kopp, and A. Manz
Science, 280 (1998), 1046-1048

[ref 31] Devilish tricks with tiny chips

Mark Ward
New Scientist, 6 June 1998.

[ref 32] Micromachined chemical reaction system
M. Koch, C. G. J. Schabmueller, A. G. R. Evans, and A. Brunnschweiler
Sensors and Actuators A: Physical, 74 (1999), 207-210

[ref 33] Development of biofactory-on-a-chip technology using excimer laser micromachining
D. Goater, J. P. H. Burt, and R. Pethig
Journal of Micromechanics and Microengineering, 8 (1998), 57-63

[ref 34] Making chips to probe genes
S. K. Moore
IEEE Spectrum, March 2001, 54-60

[ref 35] Molecular biophysics: structures in motion
Michel Daune
Oxford University Press, 1999

[ref 36] PCR
C. R. Newton, and A. Graham
Oxford Bios Scientific Pub., 1998

[ref 37] Microbiology
L. M. Prescott
William C Brown Publications, 1996

[ref 38] From Genes to Genomes: Concepts and Applications of DNA Technology
J. Dale, M. Schantz
Wiley, 2002

[ref 39] Molecular Biology of the Cell
B. Alberts et al
Garland, 2002

[ref 40] Microfluidic devices for biotechnology and organic chemical applications
H. Andersson
PhD Thesis, Royal Institute of Technology, Stockholm, Sweden

[ref 41] Microfluidic technology and applications
M. Koch, A. Evans and A. Brunnschweiler
Research Studies Press, 2000

[ref 42] Plastic-Silicon PCR amplification system made using microfabrication technologies
D. Lee, S. Park, K. Chung, and h. Pyo
5th IEEE Conference on Sensors, Daegu, Korea, 2006, 592-595

[ref 43] Micropumps, microvalves, and micromixers within PCR microfluidic chips: Advances and trends
C. Zhang, D. Xing, and Y. Li
Biotechnology Advances 25, 200, 483–514

[ref 44] Wafer level assembly methods for complex pathway microfluidic PCR reactor
N. Stoffel, A. Fisher, S. Tan, and M. Boysel
Electronic Components and Technology Conference, 2007, 1561-1566

[ref 45] Optimization of design and fabrication processes for realization of a PDMS-SOG-Silicon DNA amplification chip
S. Bhattacharya et al.
Journal of MEMS, Vol. 16, No. 2, 2007, 401-410

[ref 46] Microfluidic device for rapid detection of cytomegalovirus by sequence specific hybridization of PCR-amplified CMV-DNA
M. Briones et al.
Prceedings of 2006 International Conference on Microtechnologies in Medicine and Biology, Okinawa, Japan, 2006, 209-212

[ref 47] Real time PCR using a PCR microchip with integrated thermal system and polymer waveguides for the detection of campylobacter jejuni
Z. Wang, A. Sekulovic, J.P. Kutter, D.D. Bang, and A. Wolff
MEMS 2006, Istanbul, Turkey, 2006, 542-545

[ref 48] Fabrication of the multi-PCR chamber with inner heat-sink materials using a micro-blaster etching technique
H. Park, D. Eun, D. Kong, S. Kong, J. Shin, and J. Lee
Proceedings of the 2005 International Conference on MEMS, NANO and Smart Systems, Banff, Canada, 2005, 301-306

[ref 49] Cylindrical pillars in silicon PCR chip enhance the performance of DNA amplification
S. Park, M. Jung, T. Yoon, and H. Pyo
The 13th lntemational Conference on Solid-state Sensors, Actuators and Microsystems, Seoul, Korea, 2005, 1604-1607

[ref 50] A fully integrated microfluidic chip for RNA virus detection
F. Huang, C. Liao, and G. Lee
The 13th Intcmational Conference on Solid-State Sensors, Actuators and Microsystems, Seoul, Korea, 2005, 1624-1627

[ref 51] Simultaneous quantification for hepatitis B virus and hepatitis C virus using real-time PCR lab-on-a-chip
J. H. Chien et al.
Proceedings of the 1st IEEE International Conference on Nano/Micro Engineered and Molecular Systems, Zhuhai, China, 2006, 274-277

[ref 52] Fabrication of a three-dimensional multi-chamber using polymer bonding and MEMS technology
D. Eun et al.
International Microprocesses and Nanotechnology Conference, 2005, 214-215

[ref 53] Miniaturized independently controllable multichamber thermal cycler
Q. Zou, U. Sridhar, Y. Chen, and J. Singh
IEEE Sensors Journal, Vol. 3, No. 6, December 2003, 774-780

[ref 54] PCR array on chip – thermal characterization
V. Iordanov et al.
Sensors 2003, 1045-1048

[ref 55] Microfluidic chip for DNA amplification, electrophoresis, separation and online optical detection
G. Lee et al.
16th Annual Conference on MEMS, Kyoto, Japan, 2003, 423-426

[ref 56] PCR using electrostatic micromanipulation
M. Tokoro, T. Katayama, T. Taniguchi, T. Toni, and T. Higuchi
SICE, Osaka, Japan, 2002, 954-956

[ref 57] Design of a PCR protocol for improving reliability of PCR in DNA computing
M. Nakatsugawa et al.
Proceedings of the Congress on Evolutionary Computation, Honolulu, USA, 2002, 91-96

[ref 58] Closed chamber PCR chips for DNA amplification
C. Schabmueller, M. Lee, A. Evans, A. Brunnschweiler, G. Ensell, and D. Leslie
Engineering Science and Education Journal, December 2000, 259-264

[ref 59] Biochip for PCR amplification in silicon
Zhao Zhan, Cui Dafu, Yu Zhongyao, and Wang Li
1st Annual International IEEE-EMBS Special Topic Conference on Microtechnologies in Medicine & Biology, 2000, Lyon, France, 25-28

[ref 60] PCR biocompatibility of lab-on-a-chip and MEMS materials
T. Christensen et al.
Journal of Micromechanics and Microengineering 17, 2007, 1527–1532

[ref 61] PCR thermal management in an integrated Lab on Chip
J. Singh and M. Ekaputri
Journal of Physics Conference Series 34, 2006, 222–227

[ref 62] Integrated microfluidic systems for cell lysis, mixing/pumping and DNA amplification
C. Lee, G. Lee, J. Lin, F. Huang, and C. Liao

Journal of Micromechanics and Microengineering 15, 2005, 1215–1223

[ref 63] Development of a CMOS-compatible PCR chip: comparison of design and system strategies
Ivan Erill et al.
Journal of Micromechanics and Microengineering 14, 2004, 1558–1658

[ref 64] Design and theoretical evaluation of a novel microfluidic device to be used for PCR
M. Bu et al.
Journal of Micromechanics and Microengineering 13, 2003, S125-S130

[ref 65] Micropumps, microvalves, and micromixers within PCR microfluidic chips: Advances and trends
C. Zhang, D. Xing, and Y. Li
Biotechnology Advances 25, 2007, 483–514

[ref 66] PCR microfluidic devices for DNA amplification
C. Zhang, J. Xu, W. Ma, and W. Zheng
Biotechnology Advances 24, 2006, 243–284

[ref 67] Detection and monitoring of virus infections by real-time PCR
F. Watzinger, K. Ebner, T. Lion
Molecular Aspects of Medicine 27, 2006, 254–298

[ref 68] PCR Microchip Array Based on Polymer Bonding Technique
X. Yu, T. Li, L. Hao, and D. Zhang
Journal of Electronic Packaging, 2005, Volume 127, Issue 1, pp. 38-42

[ref 69] Development of a CCD-based fluorimeter for real-time PCR machine
D. Lee, B. Chang, and P. Chen
Sensors and Actuators B 107, 2005, 872–881

[ref 70] Microfluidic approaches to malaria detection
P. Gascoyne, J. Satayavivad, and M. Ruchirawat
Acta Tropica 89, 2004, 357–369

[ref 71] Convective polymerase chain reaction around micro immersion heater
M. Hennig and D. Brauna_
Applied Physics Letters 87, 2005,

[ref 72] Continuous flow, submicro-liter scale PCR chip for DNA amplification
W. Zheng and S. Chen
Proceedings of SPIE Vol. 4560, 2001, 256-262

[ref 73] Design and experiment of silicon PCR chips
Z. Cui, Z. Zhao, and S. Xia
Proceedings of SPIE Vol. 4755, 2002, 71-76

[ref 74] A rapid micro-PCR system for hepatitis C virus amplification

Y. Lin, M. Huang, K. Young, T. Chang, and C. Yi
Proceedings of SPIE Vol. 4176, 2000, 188-193

[ref 75] Design of a nanomechanical fluid control valve based on functionalized silicon cantilevers: coupling molecular mechanics with classical engineering design
S. Solares, M. Blanco and W. Goddard
Nanotechnology 15, 2004, 1405–1415

[ref 76] Characterization of micromachined cantilever valves
M. Koch, A. Evans, and A. Brunnschweiler
J. Micromech. Microeng. 7, 1997, 221–223

[ref 77] Processing and modeling of micromachined cantilever valves
M Koch, A G R Evans, and A Brunnschweiler
IEE Colloquium on Microengineered Components for Fluids, 1996, 1-3

[ref 78] A high-performance silicon micropump for an implantable drug delivery system
D. Maillefer et al.
12th IEEE Internatioanl Conference on MEMS, 1999, 541-546

[ref 79] Micro liquid handling using an I flow-regulated silicon micropump
V. Gas, B. van der Schoot, S. Jeanneret, and N. de Rooij
J. Micromech. Mcroeng. 3, 1993, 214-215

[ref 80] A low power MEMS silicone/parylene valve
X. Yang, C. Grosjean, and Y. Tai
Solid State Sensor and Actuator Workshop, 1998, 316-319

[ref 81] A Thermopneumatic Peristaltic Micropump
C. Grosjean and Y. Tai
Transducers ‘99, 1999

[ref 82] A high-performance silicon micropump for an implantable drug delivery system
D. Maillefer, H. van Lintel, G. Rey-Mermet, R. Hirschi
Proc. of the 12th IEEE MEMS, 1999, 541-546

[ref 83] A self-filling low-cost membrane micropump
K. Kaemper, J. Doepper, W. Ehrfeld, and S. Oberbeck
Proc of the 11th IEEE MEMS 1998, 432-437

[ref 84] Robust design of gas and liquid micropumps
M. Richter, R. Linnemann, and P. Woias
Sensors & Actuators A68, 1998, 480-486

[ref 85] A Piezoelectric micropump based on micromachining of silicon
H. van Lintel ,.F. van de Pol, and S. Bouwstra
Sensors & Actuators A15, 1988, 153-168

[ref 86] A valveless planar fluid pump with two pump chambers
A. Olsson, G. Stemme and E. Stemme
Sensors & Actuators A 46-47, 1995, 549-556

[ref 87] Miniature valveless pumps based on printed circuit board technique
N.-T. Nguyen, and X. Huang
Sensors and Actuators A: Physical, 88, 2001, 104-111

[ref 88] Fluidics and sample handling in clinical chemical analysis
D. D. Cunningham
Analytica Chimica Acta, 429, 2001, 1-18

[ref 89] Ultrasonic micromixer for microfluidic systems
Z. Yang, S. Matsumoto, H. Goto, M. Matsumoto, and R. Maeda
Sensors and Actuators A: Physical, 93, 2001, 266-272

[ref 90] A valve-less diffuser micropump for microfluidic analytical systems
H. Andersson, W. van der Wijngaart, P. Nilsson, P. Enoksson, and G. Stemme
Sensors and Actuators B: Chemical, 72, 2001, 259-265

[ref 91] Fabrication and characterization of electroosmotic micropumps
S. Zeng, C.-H. Chen, J. C. Mikkelsen, Jr., and Juan G. Santiago
Sensors and Actuators B: Chemical, 79, 2001, 107-114

[ref 92] Partial electroosmotic pumping in complex capillary systems; Part 1: Principles and general theoretical approach
W. E. Morf, O. T. Guenat, and N. F. de Rooij
Sensors and Actuators B: Chemical, 72, 2001, 266-272

[ref 93] Partial electroosmotic pumping in complex capillary systems; Part 2: Fabrication and application of a micro total analysis system (μTAS) suited for continuous volumetric nanotitrations
O. T. Guenat, D. Ghiglione, W. E. Morf, and N. F. de Rooij
Sensors and Actuators B: Chemical, 72, 2001, 273-282

[ref 94] Micromachined flow-through filter-chamber for chemical reactions on beads
H. Andersson, W. van der Wijngaart, P. Enoksson, and G. Stemme
Sensors and Actuators B: Chemical, 67, 2000, 203-208

[ref 95] Microactuators and their technologies
E. Thielicke, E. Obermeier
Mechatronics, 10, 2000, 431-455

[ref 96] Miniature valveless ultrasonic pumps and mixers
J. C. Rife, M. I. Bell, J. S. Horwitz, M. N. Kabler, R. C. Y. Auyeung and W. J. Kim
Sensors and Actuators A: Physical, 86, 2000, 135-140

[ref 97] Mixing in the offstream of a microchannel system
St. Ehlers, K. Elgeti, T. Menzel, and G. Wießmeier
Chemical Engineering and Processing, 39, 2000, 291-298

[ref 98] An active silicone micromixer for μTAS applications
P. Woias, K. Hauser, and E. Yacoub-George
Proc. of the μTAS Symposium, 2000, 239-242

[ref 99] Fabrication and test of a thermopneumatic micropump with a corrugated p+ diaphragm
O. C. Jeong, and S. S. Yang
Sensors and Actuators A: Physical, 83, 2000, 249-255

[ref 100] A high frequency high flow rate piezoelectrically driven MEMS micropump
H. Li et al.
Proc. IEEE Solid State Sensors and Actuators Workshop, 2000

[ref 101] Design, optimization and simulation on microelectromagnetic pump
Q. Gong, Z. Zhou, Y. Yang, and X. Wang
Sensors and Actuators A: Physical, 83, 2000, 200-207

[ref 102] Centrifugal microfluidics: applications
G. J. Kellog, T. E. Arnold, B. L. Carvalho, D. C. Duffy, and N. F. Shepperd
Proc. of the μTAS Symposium, 2000, 239-242

[ref 103] Microfabricated multi-frequency particle impedance characterization system
C. K. Fuller et al.
Proc. of the μTAS Symposium, 2000, 265-268

[ref 104] Liquid transport in rectangular microchannels by electroosmotic pumping
S. Arulanandam, and D. Li
Colloids and Surfaces A: Physicochem. and Eng. Aspects, 2000, 89-102

[ref 105] Resonantly driven piezoelectric micropump: Fabrication of a micropump having high power density
J.-H. Park, K. Yoshida, and S. Yokota
Mechatronics, 9, 1999, 687-702

[ref 106] A plastic micropump constructed with conventional techniques and materials
S. Böhm, W. Olthuis, and P. Bergveld
Sensors and Actuators A: Physical, 77, 1999, 223-228

[ref 107] Valveless diffuser pumps for liquids
Anders Olson

Submitted to the School of Electrical Engineering, Royal Institute of Technology, Stockholm, in partial fulfilment of the requirements for the degree of Licentiate of Engineering, 1998

[ref 108] Micronozzle/diffuser flow and its application in micro valveless pumps
X. N. Jiang, X. Y. Huang, C. Y. Liu, Z. Y. Zhou, Y. Li, and Y. Yang
Sensors and Actuators A: Physical, 70, 1998, 81-87

[ref 109] Micro mixer incorporated with piezoelectrically driven valveless micropump
Z. Yang, H. Goto, M. Matsumoto, and T. Yada
Proc. of the μTAS Symposium, 1998, 177-180

[ref 110] Membrane immobilization of nucleic acids, Part 1: Substrates
K. D. Jones
IVD Technology Magazine, Jul / Aug 2001, 6 pages

[ref 111] Membrane immobilization of nucleic acids, Part 2: Probe attachment techniques
K. D. Jones
IVD Technology Magazine, Sept 2001, 8 pages

[ref 112] Membrane immobilization of nucleic acids, Part 3: Covalent linkage and system manufacturability
K. D. Jones
IVD Technology Magazine, Nov / Dec 2001, 8 pages

[ref 113] A CMOS Image Sensor Utilizing Opacity of Nanometallic Particles for DNA Detection
Y. Wang, C. Xu, J. Li, and J. He
IEE Transaction on Electron Devices, Vol. 54, No. 6, 2007, 1549-1554

[ref 114] An Aligned Carbon Nanotube Biosensor for DNA Detection
J. Clendenin, J. Kim, and S. Tungs
IEEE International Conference on Nano/Micro Engineered and Molecular Systems, 2007, 1028-1033

[ref 115] An Inductance-based Sensor for DNA Hybridization Detection
S. M. Azimi, M. R. Bahmanyar, M. Zolgharni, and W. Balachandran
IEEE International Conference on Nano/Micro Engineered and Molecular Systems, 2007, 524-527

[ref 116] Microfluidic Three-Electrode Cell Array for Low-Current Electrochemical Detection
N. Triroj, M. Lapierre-Devlin, S. Kelley, and R. Beresford
IEEE Sensors Journal, Vol. 6, No. 6, 2006, 1395-1402

[ref 117] Microfluidic device for rapid detection of cytomegalovirus (CMV) by sequence-specific hybridization of PCR-amplified CMV-DNA

M. Briones, K. Yamashita, S. Numata, M. Miyazaki, Y. Nakamura, and H. Maeda
International Conference on Microtechnologies in Medicine and Biology, 2006, 209 - 212

[ref 118] Gold-nanoparticle-assisted oligonucleotide immobilisation for improved DNA detection
C. Minard-Basquin et al.
IEE Proceedings in Nanobiotechnology, Vol. 152, 2005, 97-103

[ref 119] Chip-based electrical detection of DNA
R. Moeller and W. Fritzsche
IEE Proceedings in Nanobiotechnology Vol. 152, 2005, 47-51

[ref 120] Comparison of DNA detection methods using nanoparticles and silver enhancement
B. Foultier, L. Moreno-Hagelsieb, D. Flandre, and J. Remacle
IEE Proceedings in Nanobiotechnology, Vol. 152, 2005, 3-12

[ref 121] Integrated circuit based biosensor technologies for DNA-microarray applications
M. Chan
7th International Conference on Solid-State and Integrated Circuits Technology, Vol. 3, 2004, 1755-1760

[ref 122] An interdigitated electrode detector for the identification of a single specific DNA molecule fragment
L. F. Fuller et al.
Proceedings of the 15th Biennial University/Government/Industry Microelectronics Symposium, 2003, 200-202

[ref 123] Design and fabrication of bio-magnetic sensors and magnetic nanobead labels for DNA detection and identification
S. X. Wang et al.
Intermag 2003, EC-01

[ref 124] Microfluidic chips for DNA amplification, electrophoresis separation and on-line optical detection
G. B. Lee et al.
16th Annual International Conference on MEMS, 2003, 423-426

[ref 125] Dielectrophoretic detection of molecular bindings
T. Kawabata and M. Washizu
IEEE Transactions on Industry Applications, Vol. 37, 2001, 1625-1633

[ref 126] Microcantilever resonance-based DNA detection with nanoparticle probes
M. Su et al.
Applied Physics Letters, Vol. 82, No. 20, 2006, 3562-3564

[ref 127] DNA microarrays on silicon nanostructures: Optimization of the multilayer stack for fluorescence detection
C. Oillic et al.
Biosensors and Bioelectronics 22, 2007, 2086–2092

[ref 128] Advances in on-chip photodetection for applications in miniaturized genetic analysis systems
Vijay Namasivayam et al.
Journal of Micromech. Microeng. 14, 2004, 81–90

[ref 129] High sensitive detection of biological cells using dielectrophoretic impedance measurement method combined with electropermeabilization
J. Suehiro, M. Shutou, T. Hatano, and M. Hara
Sensors and Actuators B, 2003, 1-8

[ref 130] Nanoparticle-based electrochemical DNA detection
J. Wang
Analytica Chimica Acta 500, 2003, 247–257

[ref 131] DNA detection by integrable electronics
C. Guiducci et al.
Biosensors and Bioelectronics 19, 2004, 781–787

[ref 132] Development of a new detection method for DNA molecules
S. Katsura, T. Yasuda, K. Hirano, A. Mizuno and S. Tanaka
Supercond. Sci. Technol. 14, 2001, 1131–1134

[ref 133] Detection of DNA Hybridization using Adjacent Impedance Probing (AIP) Method
K. Ma, H. Zhou, and M. Madou
JALA, Vol. 10, No. 4, 2005, 219-224

[ref 134] Recent trends in electrochemical DNA biosensor technology
K. Kerman, M. Kobayashi, and E. Tamiya
Meas. Sci. Technol. 15, 2004, R1–R11

[ref 135] Enhanced DNA detection based on the amplification of gold nanoparticles using quartz crystal microbalance
L. B. Nie et al.
Nanotechnology 18, 2007

[ref 136] Metal nanoparticles as labels for heterogeneous, chip-based DNA detection
W. Fritzsche and A. Taton
Nanotechnology 14, 2003, R63–R73

[ref 137] Selective detection of viable bacteria using dielectrophoretic impedance measurement method
J. Suehiro, R. Hamada, D. Noutomi, M. Shutou, and M. Hara
Journal of Electrostatics 57, 2003, 157–168

[ref 138] Impedance technique for measuring dielectrophoretic collection of microbiological particles
D. Allsopp et al.
Journal of Physics D: Appl. Phys. 32, 1999, 1066–1074

[ref 139] Optical particle detection integrated in a dielectrophoretic lab-on-a-chip
L. Cui, T. Zhang, and H. Morgan
J. Micromech. Microeng. 12, 2002, 7–12

[ref 140] DNA biochip arraying, detection and amplification strategies
M. Campas and I. Katakis
Trends in Analytical Chemistry, Vol. 23, No. 1, 2004, 49-62

[ref 141] Selective detection of specific bacteria using dielectrophoretic impedance measurement method combined with an antigen–antibody reaction
J. Suehiro, D. Noutomi, M. Shutou, and M. Hara
Journal of Electrostatics 58, 2003, 229–246

[ref 142] Evaluation of a dielectrophoretic bacterial counting technique A.P. Brown, W.B. Betts, A.B. Harrison, and J.G. O'Neill Biosensors & Bioelectronics 14, 1999, 341–351

[ref 143] Electrokinetic separation methods
P.G. Righetti, C.J. Van Oss and J.W. Vanderhoff.
Elsevier/North-Holland Biomedical Press, 1979

[ref 144] Field computation by moment methods
Roger F. Harrington
IEEE Press, 1993

[ref 145] Electrostatics and its applications,
A.D. Moore
Wiley-Interscience, 1973.

[ref 146] AC electrokinetics: a review of forces in microelectrode structures
A. Ramos, H. Morgan, N. G. Green, and A. Castellanos
Journal of Physics D: Applied Physics 31, 1998, 2338-2353

[ref 147] Applications of dielectrophoresis in biotechnology
Pethig R. and Markx G.H.
Trends in Biotechnology, Vol.15, No. 10, 1997, 426-432

[ref 148] A comprehensive approach to electro-orientation, electro-deformation, dielectrophoresis, and electrorotation of ellipsoidal particles and biological cells
Jan Gimsa
Bioelectrochemistry 54, 2001, 23–31

[ref 149] Multipolar dielectrophoresis and electrorotation theory
M. Washizu and T. Jones

Journal of Electrostatics 37, 1998, 121-134

[ref 150] Generalized multipolar dielectrophoretic force and electrorotation torque calculation
M. Washizu and T. Jones
Journal of Electrostatics 38, 1998, 199-211

[ref 151] Holding Forces of Single-Particle Dielectrophoretic Traps
J. Voldman et al.
Biophysical Journal Volume 80, 2004, 531–541

[ref 152] The influence of higher moments on particle behavior in dielectrophoretic field cages
T. Schnelle, T. Mueller, S. Fiedler, and G. Fuhr
Journal of Electrostatics 46, 1999, 13-28

[ref 153] Numerical calculation of electric field surrounding biological cells in three dimensions
G. Bartsch et al.
Bioelectrochemistry and Bioenergetics 42, 1997, 221-226

[ref 154] Numerical solution of the dielectrophoretic and travelling wave forces for interdigitated electrode arrays using the finite element method
N.G. Green, A. Ramos, and H. Morgan
Journal of Electrostatics 56, 2002, 235–254

[ref 155] Quantitative assessment of dielectrophoresis as a micro fluidic retention and separation technique for beads and human blood erythrocytes
J. Auerswald and H. Knapp
Microelectronic Engineering 67–68, 2003, 879–886

[ref 156] Sampling and monitoring in bioprocessing using microtechniques
G. Gastrock, K. Lemke, J. Metze
Reviews in Molecular Biotechnology 82, 2001, 123-135

[ref 157] Single micro electrode dielectrophoretic tweezers for manipulation of suspended cells and particles
T. Schnelle et al.
Biochimica et Biophysica Acta 1428, 1999, 99-105

[ref 158] Sub-micron sized biological particle manipulation and characterization
B. Malyan and W. Balachandran
Journal of Electrostatics 52, 2001, 15-19

[ref 159] Viability of dielectrophoretically trapped neural cortical cells in culture
T. Heida, P. Vulto, W.L.C. Rutten, and E. Marani
Journal of Neuroscience Methods 110, 2001, 37–44

[ref 160] Single particle characterization and manipulation by opposite field dielectrophoresis

R. Holzela
Journal of Electrostatics 56, 2002, 435–447

[ref 161] Accurate dielectric modelling of shelled particles and cells
M. Sancho, G. Martınez, and C. Martın
Journal of Electrostatics 57, 2003, 143–156

[ref 162] A 3-D microelectrode system for handling and caging single cells and particles
T. Mueller et al
Biosensors & Bioelectronics 14, 1999, 247–256

[ref 163] The ac and dc electric field effects on photoreceptor rods of *Xenopus laeĺis*
E. Kovacs and H. Berg
Bioelectrochemistry and Bioenergetics 47, 1998, 167–173

[ref 164] Characterization of biological cells by dielectric spectroscopy
K. Asami
Journal of Non-Crystalline Solids 305, 2002, 268–277

[ref 165] Dielectric spectroscopy of Schizosaccharomyces pombe using electrorotation and electroorientation
M. Kriegmaier
Biochimica et Biophysica Acta 1568, 2001, 135-146

[ref 166] Dielectrophoretic behavior of latex nanospheres: Low-Frequency Dispersion
M. Hughes
Journal of Colloid and Interface Science 250**,** 2002, 291–294

[ref 167] The Dielectrophoretic Behavior of Submicron Latex Spheres: Influence of Surface Conductance
M. Hughes, H. Morgan, and M. Flynn
Journal of Colloid and Interface Science 220, 1999, 454–457

[ref 168] Dielectrophoretic Detection of Molecular Bindings
T. Kawabata and M. Washizu,
IEEE Transactions on Industry Applications, Vol. 37, No. 6, 2001, 1625

[ref 169] Dielectric relaxation measurements of 12 kbp plasmid DNA
D. Bakewell, I. Ermolina, H. Morgan, J. Milner, and Y. Feldman
Biochimica et Biophysica Acta 1493, 2000, 151-158

[ref 170] Dielectrophoretic detection of changes in erythrocyte membranes following malarial infection
P. Gascoyne, R. Pethig, J. Satayavivad, F. Becker, and M. Ruchirawat
Biochimica et Biophysica Acta 1323, 1997, 240–252

[ref 171] Detection of cellular responses to toxicants by dielectrophoresis
K. Ratanachoo, P. Gascoyne, and M. Ruchirawat

Biochimica et Biophysica Acta 1564, 2002, 449– 458

[ref 172] AC Electrokinetics: colloinds and nanoparticles
H. Morgan and N. G. Green
Research Studies Press, England, 2001

[ref 173] Electrokinetic behavior of bacterial suspensions
J. Kijlstra and A. van der Wal Bioelectrochemistry
Bioenergetics 37, 1995, 149-151

[ref 174] Living cells in opto-electrical cages
G. Fuhr and Christoph Reichle
Trends in analytical chemistry, Vol. 19, No. 6, 2000, 402-409

[ref 175] The Influence of Stern Layer Conductance on the Dielectrophoretic Behavior of Latex Nanospheres
M. Hughes and N. Green
Journal of Colloid and Interface Science 250**,** 2002, 266–268

[ref 176] Measuring the dielectric properties of herpes simplex virus type 1 virions with dielectrophoresis
M. Hughes, H. Morgan , and F. Rixon
Biochimica et Biophysica Acta 1571, 2002, 1–8

[ref 177] Parasite viability by electrorotation
C. Dalton, A.D. Goater, J. Drysdale, and R. Pethig
Colloids and Surfaces A: Physicochem. and Eng. Aspects 2001, 263–268

[ref 178] Measurements of the dielectric properties of peripheral blood mononuclear cells and trophoblast cells using AC electrokinetic techniques
K.L. Chan, H. Morgan, E. Morgan, I. Cameron, and M.R. Thomas
Biochimica et Biophysica Acta 1500, 2000, 313-322

[ref 179] Dielectrophoretic manipulation of rod shaped viral particles
H. Morgan and N. Green
Journal of Electrostatics 42, 1997, 279-293

[ref 180] Precise measurements of the complex permittivity of dielectric materials at microwave frequencies
Jerzy Krupka
Materials Chemistry and Physics 79, 2003, 195–198

[ref 181] The dielectric properties of biological cells at radiofrequencies: Applications in biotechnology
G. Markx and C. Daveyb
Enzyme Microbial Technology 25, 1999, 161–171

[ref 182] Electric field calibration in micro-electrode chambers by temperature measurements
H. Glasser, T. Schnelle, T. MuÈller, and G. Fuhr

Thermochimica Acta 333, 1999, 183-190

[ref 183] A single-shell model for biological cells extended to account for the dielectric anisotropy of the plasma membrane
V. Sukhorukov, G. Meedt, M. Kuerschner, and U. Zimmermann
Journal of Electrostatics 50, 2001, 191-204

[ref 184] AC electrokinetics: applications for nanotechnology,
M. P. Hughes
Nanotechnology, Volume 11, 2000, 124-132

[ref 185] Separation of erythrocytes and latex beads by dielectrophoretic levitation and hyperlayer field-flow fractionation.
J. Rousselet, G. Markx, and R. Pethig
Colloids and Surfaces Physicochem. and Eng. Aspects 140, 1998, 209–216

[ref 186] Design and analysis of extruded quadrupolar dielectrophoretic traps
J. Voldmana, M. Tonerb, M. Graya, and M. Schmidt
Journal of Electrostatics 57, 2003, 69–90

[ref 187] Trapping in AC octode field cages
T. Schnelle, T. Mueller, and G. Fuhr
Journal of Electrostatics 50, 2000, 17-29

[ref 188] Manipulation and trapping of sub-micron bioparticles using dielectrophoresis
N.G. Green, H. Morgan, and J. Milner
J. Biochem. Biophys. Methods 35, 1997, 89–102

[ref 189] The Use of a Rotlin Field in the Dielectrophoretic Separation of Different Types of Bioparticles
J. Calderwood and E. Mognaschi
IEEE Trans. on Industry Applications, Vol. 37, No. 6, 2001, 1658-1662

[ref 190] Quadrupole levitation of microscopic dielectric particles
L. Hartley, K. Kaler, and R. Paul
Journal of Electrostatics 46, 1999, 233-246

[ref 191] Non-uniform spatial distributions of both the magnitude and phase of AC electric fields determine dielectrophoretic forces
X. Wang et al.
Biochimica et Biophysica Acta 1243, 1995, 185-194

[ref 192] Positioning and Levitation Media for the Separation of Biological Cells
W. Arnold
IEEE Trans. on Industry Applications, Vol. 37, No. 5, 2001, 1468-1475

[ref 193] Paired microelectrode system: dielectrophoretic particle sorting and force calibration
T. Schnelle, T. Mueller, G. Gradl, S.G. Shirley, and G. Fuhr

Journal of Electrostatics 47, 1999, 121-132

[ref 194] Separation of submicrometre particles using a combination of dielectrophoretic and electrohydrodynamic forces
N. G. Green and H. Morgan
Journal of Physics D, Applied Physics, 31, 1998, 25-30

[ref 195] Dielectrohpretic separation of bacteria using a conductivity gradient
G. Markx, P. Dyda, and R. Pethig
Journal of Biotechnology 51, 1996, 175-180

[ref 196] Large area microelectrodes for dielectrophoretic fractionation
N. Green, H. Morgan, M. Hughes, and W. Monaghan
Microelectronic Engineering 37, 1997, 421-424

[ref 197] An Integrated Microchip for Dielectrophoresis Based Characterization and Manipulation of Cells
E. Cen, L. Qian, and K. Kaler
Proceedings of the 25th Annual International Conference of the IEEE EMBS Cancun, Mexico, 2003, 3344-3347

[ref 198] Sub-micrometer AC electrokinetics
N. Green and H. Morgan
Proceedings of the 20th Annual International Conf. of the IEEE Engineering in Medicine and Biology Society, Vol. 20, No 6, 1998, 2974-2977

[ref 199] Electrothermally induced fluid flow on microelectrodes
N. Green, A. Ramos, A. Gonzalez, A. Castellanos, and H. Morgan
Journal of Electrostatics 53, 2001, 71-87

[ref 200] Numerical Modelling of Dielectrophoretic Effect for Submicron Particles Manipulation
B. Malnar, W. Balachandran, and F. Cecelja
IOP Conference Series, No. 178, 2004, 215-220

[ref 201] Separation of Latex Spheres using Dielectrophoresis and Fluid Flow
B. Malnar, B. Malyan, W. Balachandran, and F. Cecelja
IEE Proceedings on Nanobiotechnology, Vol. 150, No. 2, 2003, 66-69

[ref 202] Doctor on a Chip comes a step closer
W. Balachandran, B. Malyan, F. Cecelja, B. Malnar, and P. Slijepcevic
Pharmaceutical Visions Journal, 2002, 2-4

[ref 203] Doctor on a Chip
B. Malnar, B. Malyan, F. Cecelja, and W. Balachandran
MIPRO Proceedings, 2005

[ref 204] Centrifugal microfluidics: applications
G. Kellog, T. Arnold, B. Carvalho, D. Duffy, and N.F. Shepperd Jr.

Proceedings of the μTAS Symposium, 2000, 239-242

[ref 205] Dielectrophoretic transport and sorting of particles using an electrode micro-array
B. Malyan, J Kulon, and W. Balachandran
Proceedings of Electrostatics 2003, Edinburgh, UK, March 2003

[ref 206] Bio-nanotechnology of DNA
M. Washizu
2nd Annual International IEE-EBMS Special Topics Conference on Microtechnologies in Medicine and Biology, Madison, Wisconsin, 2002, 1-6

[ref 207] Design and simulation of dielectrophoretic based microsystem for bioparticles handling
F. Morales et al.
1st Annual Intemational IEEE-EMBS Special Topic Conference on Microtechnologies in Medicine & Biology 429, 2000, 429-433

[ref 208] A Dielectrophoretic Filter for Separation and Collection of Fine Particles Suspended in Liquid
G. Zhoue et al.
Proceedings of Joint Conference of ACED and K-J, 2002, 1404-1411

[ref 209] Trapping particles in microfluidics by positive dielectrophoresis
N. Markarian et al.
Proceedings of IEEE 29th Annual Bioengineering Conf., 2003, 152-153

[ref 210] Molecular Surgery of DNA Based on Electrostatic Micromanipulation
T. Yamamoto, O. Kurosawa, H. Kabata, N. Shimamoto, and M. Washizu
IEEE Transaction on Industry Applications, Vol. 36, No. 4, 2000

[ref 211] Microdevices for separation, accumulation, and analysis of biological micro- and nanoparticles
J. Kentsch et al.
IEE Proc.-Nanobiotechnology, Vol. 150, No. 2, 2003, 82-89

[ref 212] Dielectrophoretic Filter for Separation and Recovery of Biological Cells in Water
J. Suehiro and G. Zhou
IEEE Trans. on Industry Applications, Vol. 39, No. 5, 2003, 1514-1521

[ref 213] 3D focusing of nanoparticles in microfluidic channels
H. Morgan, D. Holmes and N.G. Green
IEE Proc.-Nanobiotechnology. Vol. 150, No. 2, November 2003

[ref 214] Dielectrophoretic manipulation of surface-bound DNA
W. Germishuizen, C. Walti, P. Tosch, R. Wirtz, M. Pepper, A. Davies, and A. Middelberg
IEE Proc. Nanobiotechnology, Vol. 150, No. 2, 2003, 54-58

[ref 215] Dielectrophoresis-Based Sample Handling in General-Purpose Programmable Diagnostic Instruments
P. Gascoyne and J. Vykoukal,
Proceedings of the IEEE, Vol. 92, No. 1, 2004, 22-42

[ref 216] Microdevices for Dielectrophoretic Flow-Through Cell Separation
D. Holmes, N. Green, and H. Morgan,
IEEE Engineering in Medicine and Biology Magazine, 2003, 85-90

[ref 217] Electrodeless Dielectrophoresis for Micro Total Analysis Systems
C. Chou and F. Zehnhausern
IEEE Engineering in Medicine and Biology Magazine, 2003, 62-67

[ref 218] Towards Single Molecule Manipulation with Dielectrophoresis Using Nanoelectrodes
L. Zheng, S. Li, P. James, and P. Brody
3rd IEEE Conference on Nanotechnology, 2003, Vol. 1, 437 – 440

[ref 219] Dielectrophoretic manipulation of DNA
R. H.olzel and F.F. Bier
IEE Proceedings in Nanobiotechnol.ogy, Vol. 150, No. 2, 2003, 47-53

[ref 220] The Potential of Dielectrophoresis for Single-Cell Experiments
T. Mueller et al.
IEEE Engineering in Medicine and Biology Magazine, 2004, 51-61

[ref 221] Calculation of the Electric Field for Lined-up Spherical Dielectric Particles
B. Techaumnat and T. Takuma
IEEE Trans. on Dielectrics and Electrical Insulation, Vol. 10, 2003, 623-633

[ref 222] Aggregation profile characterization in dielectrophoretic structures using bacteria and submicron latex particles
R. Casanella, J. Samitier, A. Errachid, C. Madrid, S. Paytubi and A. Juarez
IEE Proceedings in Nanobiotechnol., Vol. 150, No. 2, 2003 70-74

[ref 223] Characterization and Modeling of a Microfluidic Dielectrophoresis Filter for biological Species
H. Li, Y. Zheng, D. Akin, and R. Bashir
Journal of MEMS, Vol. 14, No. 1, 2005, 103-112

[ref 224] Electrokinetics in Micro Devices for Biotechnology Applications
P. Wong, T. Wang, J. Deval, and C. Ho
IEEE/ASME Transactions on Mechatronics, 2004, 366-376

[ref 225] Trapping of micrometre and sub-micrometre particles by high-frequency electric fields and hydrodynamic forces
T. Mueller et al.
J. Phys. D: Appl. Phys. 29, 1996, 340–349

[ref 226] The role of electrohydrodynamic forces in the dielectrophoretic manipulation and separation of particles
A. Ramos, H. Morgan, N. G. Green, and A. Castellanos
Journal of Electrostatics, 47, 1999, 71-81

[ref 227] Separation of sub-micrometre particles using a combination of dielectrophoretic and electrohydrodynamic forces
N. G. Green and H. Morgan
Journal of Physics D: Applied Physics, 31, 1998, 25-30

[ref 228] Electrohydrodynamics
A. Castellanos (editor)
Springer, New York, 1998

[ref 229] Electrohydrodynamics and dielectrophoresis in microsystems: scaling laws
A Castellanos, A. Ramos, A. Gonzalez, N. Green, and H. Morgan,
J. Phys. D: Appl. Phys. 36, 2003, 2584–2597

[ref 230] Finite element modeling of a 3-D DEP flow separator device for optimal bioprocessing conditions
H. O. Fatoyinbo and M. P. Hughes
Proceedings of the 26th Annual International Conference of the IEEE EMBS, 2004, 2587-2590

[ref 231] High-Speed Integrated Particle Sorters based on Dielectrophoresis
J. Nieuwenhuis, A. Jachimowicz, P. Svasek, and M. Vellekoop
Proceedings of IEEE Sensors, 2004, Vol. 1, 64-67

[ref 232] Understanding dielectrophoretic trapping of neuronal cells: modeling electric field, electrode–liquid interface and fluid flow
T. Heida,W. Rutten, and E. Marani
J. Phys. D: Appl. Phys. 35, 2002, 1592–1602

[ref 233] A combined travelling wave dielectrophoresis and electrorotation device: applied to the concentration and viability determination of cryptosporidium
A. D. Goater, J. P. H. Burt, and R. Pethig
Journal of Physics D: Applied Physics, 30, 1997, 65-69

[ref 234] Dielectrophoretic forces on particles in travelling electric fields
M. P. Hughes, R. Pethig, and X.-B. Wang
Journal of Physics D: Applied Physics, 29, 1996, 474-482

[ref 235] Electrokinetic system to determine differences of electrorotation and travelling-wave electrophoresis between autotrophic and heterotrophic algal cells
Y. Wu et al.
Colloids and Surfaces A: Physicochem. Eng. Aspects 262, 2005, 57–64

[ref 236] Electromanipulation and separation of cells using travelling electric fields
M. Talary, J. Burt, J. Tame, and R. Pethig
Journal of Physics D: Applied Physics, 29, 1996, 2198-2203

[ref 237] Design and fabrication of travelling wave dielectrophoresis structures
L. Cui and H. Morgan
Journal of Micromech. Microengineering 10, 2000, 72–79

[ref 238] Analysis of dielectrophoretic electrode arrays for nanoparticle manipulation
W. Li, H. Du, D. Chen, and C. Shu
Computational Materials Science 30, 2004, 320–325

[ref 239] Separation of bioparticles using the travelling wave dielectrophoresis with multiple frequencies
I. Mezic et al.
Proceedings of the 42nd IEEE Conference on Decision and Control, Maui, Hawaii USA, 2003, 6448-6453

[ref 240] A unified theory of theory of dielectrophoresis and travelling wave dielectrophoresis
X. Wang, Y. Huang, F. Becker, and P. Gascoyne
Journal of Physics D Applied Physics 27, 1994, 1571-1574

[ref 241] Numerical simulation of travelling wave induced electrothermal fluid flow
I. Nielsen, N. Green, and A. Wolff
J. Phys. D: Appl. Phys. 37, 2004, 2323–2330

[ref 242] Enhancing Travelling-Wave Dielectrophoresis with Signal Superposition
R. Pethig, M. Talary, and R. Lee
IEEE Engineering in Medicine and Biology Magazine, 2003, 43-50

[ref 243] The dielectrophoretic and travelling wave forces generated by interdigitated electrode arrays: analytical solution using Fourier series
H. Morgan, A. Izquierdo, D. Bakewell, N. Green, and A. Ramos
J. Phys. D: Appl. Phys. 34, 2001, 1553–1561

[ref 244] A combined dielectrophoresis, travelling wave dielectrophoresis and electrorotation microchip for the manipulation and characterization of human malignant cells
E. Cena, C. Daltona, Y. Lia, S. Adamiab, L. Pilarskib, and K. Kalera
Journal of Microbiological Methods 58, 2004, 387– 401

[ref 245] Large-area travelling-wave dielectrophoresis particle separator
H. Morgan, N. G. Green, M. P. Hughes, W. Monaghan, and T. Tan
Journal of Micromechanics and Microengineering, 7 (1997) 65-70

[ref 246] Travelling wave driven microfabricated electrohydrodynamic pumps for liquids
G. Fuhr, T. Schnelle, and B. Wagnert

J. Micromech. Microeng. 4, 1994, 217-226

[ref 247] 3D simulation of travelling wave dielectrophoretic force on particles
B. Malnar, W. Balachandran, and F. Cecelja,
Proceedings of the ESA-IEEE Conference on Electrostatics, vol. 1, U.S.A. 2003

[ref 248] Non-invasive determination of bacterial single cell properties by electrorotation
R. Holzel
Biochimica et Biophysica Acta 1450, 1999, 53-60

[ref 249] Electrorotation of liposomes: verification of dielectric multi-shell model for cells
K. Chan, P. Gascoyne, F. Becker, and R. Pethig
Biochimica et Biophysica Acta 1349, 1997, 182–196

[ref 250] A new microsystem for automated electrorotation measurements using laser tweezers
C. Reichle, T. Schnelle, T. Mueller, and G. Fuhr
Biochimica et Biophysica Acta 1459, 2000, 218-229

[ref 251] Electrorotation of colloidal suspensions
J. Huang, K. Yua, and G. Gu
Physics Letters A 300, 2002, 385–391

[ref 252] Electrorotation in octopole microcages
C. Reichle, T. Mueller, T. Schnelle, and G. Fuhr
J. Phys. D: Appl. Phys. 32 (1999) 2128–2135

[ref 253] Investigation of human malignant cells by electrorotation
C. Dalton et al.
2004 Report Conf. on Elec. Insulation and Diel. Phenomena, 485-488

[ref 254] Particle characterization by AC-electrokinetic phenomena: A short introduction to dielectrophoresis and electrorotation
J. Gimsa
Colloids and Surfaces A: Physicochem. and Eng. Aspects, 1999, 451-459

[ref 255] Differentiation of viable and non-viable bacterial biofilms using electrorotation
X. Zhou, G. Markx, R. Pethig, and I. Eastwood
Biochimica et Biophysica Acta 1245, 1995, 85-93

[ref 256] Automated electrorotation: dielectric characterisation of living cells by real-time motion estimation
G. De Gasperis, X.-B. Wang, J. Yang, F. F. Becker, and P. R. C. Gascoyne
Meas. Sci. Technol. 9, 1998, 518-529

[ref 257] Separation of sub-micron bioparticles by dielectrophoresis

H. Morgan, M. P. Hughes, N. G. Green
Biophysical Journal, Volume 77, 1999, 516-525

[ref 258] AC electric-field-induced flow in microelectrodes (letter to the editor)
A. Ramos, H. Morgan, N. G. Green, and A. Castellanos
Journal of Colloid and interface science, 217, 1999, 420-422

[ref 259] Computer-aided analyses of electric fields used in electrorotation studies
M. P. Hughes, X.-B. Wang, F. F. Becker, P. R. C. Gascoyne and R. Pethig
Journal of Physics D: Applied Physics, 27, 1994, 1564-1570

[ref 260] Examination of dielectrophoretic behaviour of DNA as a function of frequency from 30 Hz to 1 MHz using a flexible microfluidic test apparatus
S. M. Crippen, M. R. Holl, and D. R. Meldrum
Proc. of the μTAS Symposium, 2000, 239-242

[ref 261] Solid-phase nucleic acid extraction, amplification, and detection
R. R. Mondesire, D. L. Kozwich, K. A. Johansen, J. C. Gerdes, and S. E. Beard
IVD Technology Magazine, May 2000, 10 pages

[ref 262] Cell reactions to dielectrophoretic manipulation
S. Archer, T.-T. Li, A. T. Evans, S. T. Britland, and H. Morgan
Biochemical and Biophysical Research Comm., 257, 1999, 687-698

[ref 263] Novel separation method on a chip using capillary electrophoresis in combination with dielectrophoresis
K. Morishima, D. W. Arnold, A. R. Wheeler, D. J. Rakestraw, and R. N. Zare
Proc. of the μTAS Symposium, 2000, 239-242

[ref 264] Transportation of DNA molecule utilizing the conformational transition in the higher order structure of DNA
K. Morishima, F. Arai, T. Fukunda, H. Matsuura, and K. Yoshikawa
CCAB 97, mini review

[ref 265] Characterisation of the dielectrophoretic movement of DNA in micro-fabricated structures
D. Bakewell, H. Morgan, and J. J. Miller
Proc. Institute of Physics 163, 1999, 73-76

[ref 266] Particle characterization by AC electrokinetic phenomena: Dielectrophoresis of Latex particles measured by dielectrophoretic phase analysis light scattering (DPALS)
B. Prüger, P. Eppmann, and J. Gimsa
Colloids and Surfaces, A: Physicochem. and Eng. Aspects, 1999, 443-449

[ref 267] DNA SEQUENCING: Massively Parallel Genomics
M. Fodor

Science 18, July 1997

[ref 268] Parallel analysis of genetic selections using whole genome oligonucleotide arrays
R. Cho et al.
PNAS Vol. 95, Issue 7, 3752-3757, March 31, 1998

[ref 269] Frontiers in Biomolecular Diagnostics
V. Dinh, T. B.M. Cullum, and D.L. Stokes
Nanosensors and Biochips:, Sensors and Actuators, B 74, 2 2001

[ref 270] Electric field directed nucleic acid hybridization on microchips
C. Edman et al.
Nanogen, 10398 Pacific Center Court, San Diego, CA 92121, USA

[ref 271] Micro vials on a silicon wafer for sample introduction in capillary electrophoresis
M. Jansson et al.
Journal of chromatography, vol. 626, 1992

[ref 272] Mass spectrometry from miniaturized arrays for full comparative DNA analysis
D. Little et al.
Nature Med 3, 1413-1416, 1997

[ref 273] Integrated microanalytical technology enabling rapid and automated protein identification
S. Ekstroem et al.
Analytical chemistry, vol 72, 286-293, 2000

[ref 274] Generation and Screening of an Oligonucleotide-Encoded Synthetic Peptide Library
M. Needels et al.
Proceedings of the National Academy of Sciences, Vol 90, 1993

[ref 275] Advanced multiplexed analysis with the FLowMetrix System
R. Fulton, R. McDade, P. Smith, L. Kienker and J. Kettman
Clinical Chem. 43, 1997

[ref 276] DNA Electronics
V. Bhalla et al
EMBO Reports, Vol. 4, No. 5, 2003

[ref 277] Electronic detection of DNA by its intrinsic molecular charge
J. Fritz et al
PNAS, Vol. 99, No. 22, 2002

[ref 278] DNA electrical properties and potential nano-applications
M. Zhang and T. J. Tarn
IEEE Conference on Nanotechnology, San Francisco CA, USA, 2003

[ref 279] Introduction to modern virology
N. J. Dimmock, A. J. Easton, and K. N. Leppard
Wiley-Blackwell, 6th edition, 2007

[ref 280] Forensic DNA typing
J. M. Butler
Academic Press, 2nd edition, 2005

[ref 281] Molecular cloning: a laboratory manual
J. Sambrook
Cold Spring Harbor Laboratory Press, 3rd Lab edition, 2001

[ref 282] Faster Greedy Algorithms for Multiple Degenerate Primer Selection
S. Balla et al
8th IEEE International Conf. on BioInformatics and BioEngineering, 2008

[ref 283] Separation type multiplex PCR chip for detecting male infertility
S. M. Ha et al
Digest of papers on Microprocessor and Nanotechnology, 2007

[ref 284] Genomics
C. R. Cantor, C. R. Smith
Wiley-IEEE, 2003

[ref 285] Nucleic acid testing for human disease
A. Lorincz
CRC Press, 2006

[ref 286] World congress on medical physics and biomedical engineering
S. Kim et al
Springer, 2007

[ref 287] Evaluation of loop-mediated isothermal amplification (LAMP), PCR and parasitological tests for detection of *Trypanosoma evansi* in experimentally infected pigs
O. Thekisoe et al
Veterinary Parasitology, Volume 130, Issues 3-4, June 2005

[ref 288] Loop-Mediated Isothermal Amplification for Detection of African Trypanosomes
N. Kuboki et al
Journal of Clinical Microbiology, 41(12): 5517–5524, 2003

[ref 289] Development and Preliminary Evaluation of a Loop-Mediated Isothermal Amplification Procedure for Sensitive Detection of *Cryptosporidium* Oocysts in Fecal and Water Samples
P. Karanis et al
Applications of Environmental Microbiology, 73(17): 5660–5662, 2007

[ref 290] Micropump based on PZT uni-morph and one way parylene valves

G. H Feng and E. S. Kim
Journal of Micromech. Microeng. 14, 429-435, 2004

[ref 291] A review of microvalves
K. W. Oh and C. H. Ahn
Journal of Micromech. Microeng. 16, R13-R39, 2006

[ref 292] Piezoelectric unimorph valve assembled on an LTCC substrate
M. Sobocinski et al
Sensors and actuators A 149, 315-319, 2009

[ref 293] A High-Flow Thermopneumatic Microvalve With Improved Efficiencyand Integrated State Sensing
R. A. Collin and D. W. Kensall
Journal of Microelectromechanical Systems, Vol 12, No 2, April 2003

[ref 294] Fundamentals and applications of microfluidics
N. T. Nguyen and S. T. Wereley
Artech House Publishers, 2002

[ref 295] Microfluidic technologies for miniaturized analysis systems
N. T. Nguyen
Springer, 2007

[ref 296] Micromixers – a review
N. T. Nguyen and Z. Wu
Journal of Micromech. Microeng. 15, R1-R16, 2005

[ref 297] An effective passive microfluidic mixer utilizing chaotic advection
N. T. Nguyen et al
Sensors and Actuators B 132, 172-181, 2008

[ref 298] Active microfluidic mixer chip
X. Nie et al
Applied physics letters 88, 2006

[ref 299] Fluid micromixing technology and its applications for biological and chemical processes
Y. T. Chew et al
IFMBE Proceedings, Vol 15, 2007

[ref 300] Temperature-electrical conductivity relation of water for environmental monitoring and geophysical data intervention
M. Hayashi
Environmental Monitoring and Assessment, Kluwer Academic Pub, 2004

[ref 301] Computer methods for partial differential equations
Robert Vichnevetsky
Prentice Hall, Inc, 1981

[ref 302] Finite volume methods for hyperbolic problems
R. LeVeque
Cambridge University Press, 202

[ref 303] Applied engineering mathematics
X. Yang
Cambridge International Science Publishing, 2008

[ref 304] Numerical methods for exterior problems, volume 2
L. Ying
World Scientific, 2006

[ref 305] Microstructures in elastic media: principles and computational methods
P. Nhan and S. Kim
Oxford University Press, 1994

[ref 306] Preparation and hybridization analysis of DNA/RNA from E. coli on microfabricated bioelectronic chips
J. Cheng et al.
Nature Biotechnology, Volume 16, 541-546, 1998

[ref 307] Self contained fully integrated biochips for sample preparation, PCR amplification and DNA microarray analysis
R. Liu et al.
Integrated biochips for DNA analysis, Landes Bioscience, 2007

[ref 308] Microfluidic devices for sample pretreatment and applications
X. Chen and D. Cui
Microsystem Technology, vol 15, 667-676, 2009

[ref 309] Dielectric and dielectrophoretic properties of DNA
R. Hoelzel
IET Nanobiotechnology, vol 3, 28-45, 2009

[ref 310] Bio-nanotechnology of DNA
M. Washizu
2nd Annual Intenrational IEEE-EMBS Conference on Microtechnologies in Medicine, Madison, Wisconsin, 2002

[ref 311] Dielectrophoretic detection of molecular bindings
T. Kawabata and M. Washizu
IEEE Transactions on Industry Applications, vol 37, 2001

[ref 312] Electrostatic manipulation of DNA in microfabricated structures
M. Washizu and O. Kurosawa
IEEE Transactions on Industry Applications, vol 26, 1990

[ref 313] Electronic manipulation of DNA and proteins for potential nano-bio circuit
L. Zheng et al
Proc. of SPIE, vol 5331, 2004

[ref 313] Towards single molecule manipulation with DEP using nanoelectrodes
L. Zheng et al
Proc. of SPIE, vol 5331, 2004

[ref 314] Trapping of 27bp-8kbp DNA and immobilization of thiol-modified DNA using dielectrophoresis
S. Tuukkanen et al.
Nanotechnology 18, 2007

[ref 315] Dielectrophoresis of DNA: Time and Frequency Dependent Collections on Microelectrodes
D. Bakewell and H. Morgan
IEEE Transactions on Nanobioscience, vol 5, 2006

[ref 316] Size separation of DNA molecules by pulsed electric field DEP
S. Nedelcu and J. Watson
Journal of Physics D, vol 37, 2004

[ref 317] Dielectrophoretic manipulation of Avidin and DNA
D. Bakewell et al.
Proc. of 20th Annual International Conference of the IEEE Engineering in Medicine and Bilogy Society, vol 20, 1998

Appendix A: Prototypes of the functions of the program

The following text lists the prototypes of the functions used in the program. The functions are described in more details in section 5.1 of the thesis, and here the index of the prototype matches the index of the subsection of section 5.2. For example the function described in subsection 5.2.1 is listed in this appendix in A.1, the function described in subsection 5.2.2 is listed in A.2 and so forth.

A.1. Function read_main_input_file

```
void read_main_input_file (char fileName[], float &xWidth, float &yWidth, float &zWidth, float **xMesh, float **yMesh, float **zMesh, float **materialInterface, float &xMinEl, float &xMaxEl, float &yMinEl, float &yMaxEl, float &zMinEl, float &zMaxEl, int &numBoundsEl, int &numElecs, int &numVoltages, boundary **boundsEl_i, boundary **boundsEl_j, electrode **elecs, float **voltages, float &freq);
```

A.2. Function read_thermal_input_file

```
void read_thermal_input_file (char fileName[], float &xMinTh, float &xMaxTh, float &yMinTh, float &yMaxTh, float &zMinTh, float &zMaxTh, int &numBoundsTh, boundary **boundsTh, int &isElectrodeThermTransparent, float &tempError);
```

A.3. Function read_fluid_input_file

```
void read_fluid_input_file (char fileName[], float &xMinFl, float &xMaxFl, float &yMinFl, float &yMaxFl, float &zMinFl, float &zMaxFl, int &numBoundsFl, boundary **boundsFl_x, boundary **boundsFl_y, boundary **boundsFl_z, boundary **boundsFl_p);
```

A.4. Function rewrite_input_file

```
void rewrite_input_file (float xWidth, float yWidth, float zWidth, float *xMesh, float *yMesh, float *zMesh, float *materialInterface, float xMinEl, float xMaxEl, float yMinEl, float yMaxEl, float zMinEl, float zMaxEl, int numBoundsEl, int numElectrodes, int numVoltages, boundary *boundsEl_i,
```

boundary *boundsEl_j, electrode *elecs, float *voltages, float freq, float xMinTh, float xMaxTh, float yMinTh, float yMaxTh, float zMinTh, float zMaxTh, int numBoundsTh, boundary *boundsTh, int elThermTrans, float tempError, float xMinFl, float xMaxFl, float yMinFl, float yMaxFl, float zMinFl, float zMaxFl, int numBoundsFl, boundary *boundsFl_x, boundary *boundsFl_y, boundary *boundsFl_z, boundary *boundsFl_p);

A.5. Function create_mesh_lines

void create_mesh_lines (float **meshLines, float *mesh, char axis);

A.6. Function create_nonuniform_mesh

void create_nonuniform_mesh (float *mesh, int i, int &nPart, float **array);

A.7. Function calculate_number_mesh_points

void calculate_number_mesh_points (int &numPoints, int &numPointsEl, int &numPointsTh, int &numPointsFl, float xWidth, float yWidth, float zWidth, float *xMeshLines, float *yMeshLines, float *zMeshLines, float xMinEl, float xMaxEl, float yMinEl, float yMaxEl, float zMinEl, float zMaxEl, float xMinTh, float xMaxTh, float yMinTh, float yMaxTh, float zMinTh, float zMaxTh, float xMinFl, float xMaxFl, float yMinFl, float yMaxFl, float zMinFl, float zMaxFl);

A.8. Function calculate_number_mesh_lines

int calculate_number_mesh_lines (float beginPoint, float endPoint, float *meshLines);

A.9. Function create_mesh_distances

void create_mesh_distances (float **meshDistances_fbrlud, float **x, float **y, float **z, int numPoints, float xWidth, float yWidth, float zWidth, float *xMeshLines, float *yMeshLines, float *zMeshLines);

A.10. Function create_relative_index

void create_relative_index (int numPointsEl, int numPointsTh, int numPointsFl, float *x, float *y, float *z, int **index_El_Th, int **index_El_Fl, int

**index_Th_El, int **index_Th_Fl, int **index_Fl_El, int **index_Fl_Th, float xWidth, float yWidth, float zWidth, float *xMeshLines, float *yMeshLines, float *zMeshLines, float xMinEl, float xMaxEl, float yMinEl, float yMaxEl, float zMinEl, float zMaxEl, float xMinTh, float xMaxTh, float yMinTh, float yMaxTh, float zMinTh, float zMaxTh, float xMinFl, float xMaxFl, float yMinFl, float yMaxFl, float zMinFl, float zMaxFl);

A.11. Function find_type

char find_type (electrode *electrodes, int numElectrodes, int numBounds, boundary *bounds, float x, float y, float z, float xMin, float xMax, float yMin, float yMax, float zMin, float zMax);

A.12. Function iselectrode

int iselectrode (float x, float y, float z, electrode *electrodes, int numElectrodes);

A.13. Function isboundary

int *isboundary (float x, float y, float z, boundary *bounds, int numBounds);

A.14. Function convert_triangular_electrodes

void convert_triangular_electrodes (electrode *electrodes, int numElectrodes);

A.15. Function convert_circular_electrodes

void convert_circular_electrodes (electrode *electrodes, int numElectrodes);

A.16. Function create_electrical_problem

void create_electrical_problem (electrode *electrodes, boundary *boundsEl, int numElectrodes, int numBoundsEl, float *meshDistances_fbrlud, float *x, float *y, float *z, int *index_El_Th, int *index_Th_El, float *xMeshLines, float *yMeshLines, float *zMeshLines, float xMinEl, float xMaxEl, float yMinEl, float yMaxEl, float zMinEl, float zMaxEl, int numPointsEl, char **type_El, int **indexF_El, int **indexB_El, int **indexR_El, int **indexL_El, int **indexU_El, int **indexD_El, float **potential_coefficients_fbrlud, float

*voltages, float **potential_i, float **potential_j, float **field_i, float **field_j, float **rmsField);

A.17. Function create_thermal_problem

void create_thermal_problem (electrode *elecs, boundary *boundsTh, int numElecs, char *typeElecs, int numBoundsTh, float *meshIndexes_fbrlud, float *x, float *y, float *z, float xWidth, float yWidth, float zWidth, float *xMeshLines, float *yMeshLines, float *zMeshLines, float xMinTh, float xMaxTh, float yMinTh, float yMaxTh, float zMinTh, float zMaxTh, int numPointsTh, int numPointsEl, char **type_Th, int **indexF_Th, int **indexB_Th, int **indexR_Th, int **indexL_Th, int **indexU_Th, int **indexD_Th, float **temperature_coefficients_fbrlud, float **temperature, float **temperature_prev, float **conductivity, float **permittivity, float **thermal_conductivity, char *material, int elThermTrans);

A.18. Function calculate_potential

void calculate_potential (float *materialInterface, float *x, float *y, float *z, int numPointsEl, char *type_El_i, char *type_El_j, float freq, float *potential_i, float *potential_j, float *conductivity, float *permittivity, float *meshIndexes_fbrlud, int *indexF_El_i, int *indexB_El_i, int *indexR_El_i, int *indexL_El_i, int *indexU_El_i, int *indexD_El_i, int *indexF_El_j, int *indexB_El_j, int *indexR_El_j, int *indexL_El_j, int *indexU_El_j, int *indexD_El_j, float *potential_coefficients_fbrlud, float *temperature, char *material, int *index_El_Th);

A.19. Function calculate_field

void calculate_field (int numPointsEl, char *type_El, char *material, float *meshIndexes_fbrlud, int *index_El_Th, float *potential, float *field, int *indexF_El, int *indexB_El, int *indexR_El, int *indexL_El, int *indexU_El, int *indexD_El);

A.20. Function calculate_rms_field

void calculate_rms_field (int numPointsEl, float *field_i, , float *field_j, float *rmsField);

A.21. Function calculate_field_components

void calculate_field_components (float **gradFieldComponents, float **fieldComponents, int numPointsEl, float *currentVoltages, char *type_El, char *material, float *meshIndexes_fbrlud, int *index_El_Th, float *potential, float *field, int *indexF_El, int *indexB_El, int *indexR_El, int *indexL_El, int *indexU_El, int *indexD_El);

A.22. Function create_electrical_problem_files

void create_electrical_problem_files (float *potential_i, float *potential_j, float *field_i, float *field_j, float *fieldComponents_i, float *fieldComponents_j, float *rmsField, float *currentVoltages, int *indexF_El, int *indexB_El, int *indexR_El, int *indexL_El, int *indexU_El, int *indexD_El, int *indexF_El_j, int *indexB_El_j, int *indexR_El_j, int *indexL_El_j, int *indexU_El_j, int *indexD_El_j, int *index_El_Th, float *x, float *y, float *z, electrode *elecs, boundary *boundsEl_i, boundary *boundsEl_j, int numElecs, char *typeElecs, int numBoundsEl, float xWidth, float yWidth, float zWidth, float *xMeshLines, float *yMeshLines, float *zMeshLines, float xMinEl, float xMaxEl, float yMinEl, float yMaxEl, float zMinEl, float zMaxEl);

A.23. Function create_thermal_problem_files

void create_thermal_problem_files (float *temperature, float *conductivity, float *permittivity, float *thermal_conductivity, float *x, float *y, float *z, float *xMeshLines, float *yMeshLines, float *zMeshLines, char *material);

A.24. Function calculate_cond_perm

void calculate_cond_perm (int numPointsTh, float *temperature, float *conductivity, float *permittivity, float *thermal_conductivity, char *material, float *materialInterface, float *x, float *y, float *z);

A.25. Function calculate_temperature_maxerror

void calculate_temperature_maxerror (float &temperature_maxerror, float &max_temperature, int numPointsTh, float *temperature, float *temperature_prev);

A.26. Function calculate_grad_rms_field

void calculate_grad_rms_field (int numPointsEl, float *rmsField, int *indexF_El, int *indexB_El, int *indexR_El, int *indexL_El, int *indexU_El, int *indexD_El, float *meshIndexes_fbrlud, float *x, float *y, float *z, int *index_El_Th);

A.27. Function calculate_ temperature

void calculate_temperature (int numPointsTh, char *type_Th, int *indexF_Th, int *indexB_Th, int *indexR_Th, int *indexL_Th, int *indexU_Th, int *indexD_Th, float *temperature_coefficients_fbrlud, float *xTh, float *yTh, float *zTh, float *temperature, float *thermal_conductivity, int *index_Th_Fl, int *index_Th_El, float *conductivity, float *rmsField, int elThermTrans);

A.28. Function calculate_grad_temperature

void calculate_grad_temperature (float **gradTemperature_x, float **gradTemperature_y, float **gradTemperature_z, int numPointsTh, float *temperature, int *indexF_Th, int *indexB_Th, int *indexR_Th, int *indexL_Th, int *indexU_Th, int *indexD_Th, float *meshIndexes_fbrlud, float *x, float *y, float *z);

A.29. Function calculate_cm_factor

void calculate_cm_factor (float &cm_factor_i, float &cm_factor_j, float permittivity_medium_i, float permittivity_medium_j, float permittivity_particle_i, float permittivity_particle_j);

A.30. Function calculate_dep_force_components

void calculate_dep_force_components_1 (int numPointsEl, double **dep_force_1_x, double **dep_force_1_y, double **dep_force_1_z, float *fieldComponents_i, float *fieldComponents_j, float *fieldx_i_x, float

*fieldx_j_x, float *fieldx_i_y, float *fieldx_j_y, float *fieldx_i_z, float *fieldx_j_z, float *fieldy_i_x, float *fieldy_j_x, float *fieldy_i_y, float *fieldy_j_y, float *fieldy_i_z, float *fieldy_j_z, float *fieldz_i_x, float *fieldz_j_x, float *fieldz_i_y, float *fieldz_j_y, float *fieldz_i_z, float *fieldz_j_z, float cm_factor_i, float cm_factor_j, float permittivity_medium_i, float radius, float *x, float *y, float *z, int *index_El_Th);

A.31. Function calculate_dep_force_components

void first_order_derivatives (float **fieldx_i_x, float **fieldx_j_x, float **fieldx_i_y, float **fieldx_j_y, float **fieldx_i_z, float **fieldx_j_z, float **fieldy_i_x, float **fieldy_j_x, float **fieldy_i_y, float **fieldy_j_y, float **fieldy_i_z, float **fieldy_j_z, float **fieldz_i_x, float **fieldz_j_x, float **fieldz_i_y, float **fieldz_j_y, float **fieldz_i_z, float **fieldz_j_z, float *fieldComponents_i, float *fieldComponents_j, int numPointsEl, int numPoints, float *x, float *y, float *z, char *type_El_i, char *type_El_j, int *indexF_El_i, int *indexB_El_i, int *indexR_El_i, int *indexL_El_i, int *indexU_El_i, int *indexD_El_i, int *indexF_El_j, int *indexB_El_j, int *indexR_El_j, int *indexL_El_j, int *indexU_El_j, int *indexD_El_j, int *index_El_Th, float *meshIndexes_fbrlud);